A survey for pulsations in A-type stars using SuperWASP

Daniel L. Holdsworth

Doctor of Philosophy

December 2015

Keele University

Abstract

"*It is sound judgement to hope that in the not too distant future we shall be competent to understand so simple a thing as a star.*"

– Sir Arthur Stanley Eddington, The Internal Constitution of Stars, 1926

A survey of A-type stars is conducted with the SuperWASP archive in the search for pulsationally variable stars. Over 1.5 million stars are selected based on their $(J - H)$ colour. Periodograms are calculated for light curves which have been extracted from the archive and cleaned of spurious points. Peaks which have amplitudes greater than 0.5 millimagnitude are identified in the periodograms. In total, 202 656 stars are identified to show variability in the range $5 - 300\,\mathrm{d}^{-1}$.

Spectroscopic follow-up was obtained for 38 stars which showed high-frequency pulsations between 60 and $235\,\mathrm{d}^{-1}$, and a further object with variability at $636\,\mathrm{d}^{-1}$. In this sample, 13 were identified to be normal A-type δ Sct stars, 14 to be pulsating metallic-lined Am stars, 11 to be rapidly oscillating Ap (roAp) stars, and one to be a subdwarf B variable star. The spectra were used not only to classify the stars, but to determine an effective temperature through Balmer line fitting.

Hybrid stars have been identified in this study, which show pulsations in both the high- and low-overtone domains; an observation not predicted by theory. These stars are prime targets to perform follow-up observations, as a confirmed detection of this phenomenon will have significant impact on the theory of pulsations in A-type stars.

The detected number of roAp stars has expanded the known number of this pulsator class by 22 per cent. Within these results both the hottest and coolest roAp star have been identified. Further to this, one object, KIC 7582608, was observed by the *Kepler* telescope for 4 yr, enabling a detailed frequency analysis. This analysis has identified significant frequency variations in this star, leading to the hypothesis that this is the first close binary star of its type.

The observational results presented in this thesis are able to present new challenges to the theory of pulsations in A-type stars, with potentially having the effect of further delaying the full understanding of *'so simple a thing as a star'*.

Acknowledgements

Firstly I'd like to thank my supervisor, Dr. Barry Smalley, for his guidance throughout the course of my Ph.D. Without the hours of discussion spend on this project, it would not have been possible to complete it on time. He has developed quite a knack of keeping me from going too far down the rabbit hole. And of course, many thanks are due for the amount of red pens he sacrificed to the countless drafts of papers and this thesis!

Secondly I'd like to thank my family, in particular my parents, Lynne and John, for their support in my chosen career path, even if they didn't always understand what it was! Perhaps a read of this tome will help to enlighten them.

A special mention must go to my Godson, Harrison Chapman, who showed such determination in his first year of life. I have learnt, and many others should, from such an example.

To my collaborators, those who have been co-authors on publications, and those who have kindly donated some of their observing time to obtain the odd spectrum or light curve here or there. Both discussions and data have been useful in compiling this thesis.

And of course, all of my friends, old and new, near and far, that have helped me through. Be it a ear to listen with, a voice to advise with or a scrutinous eye to review with, your presence has been much appreciated. And along with that, the many nights (and some days!) spent in the KPA clubhouse relaxing with a beer, or two, or three...

Contents

List of Figures

List of Tables

1 Introduction

Periodic variability in stars was first observed in the 16$^{\text{th}}$ and 17$^{\text{th}}$ centuries by David Fabricius and Johann Holwarda in Mira stars (Hoffleit 1997), however it was not until the 19$^{\text{th}}$ century that these variations were suggested to be driven by pulsations (Shapley 1914).

Since that time, with the advancement of observational techniques and instrumental capabilities, a whole host of pulsationally variable stars has been found. These improvements have enabled more and more precise observations to be made, allowing for, with space-based telescopes, the discovery of pulsations with amplitudes of just a few micro-magnitudes (e.g. Hekker et al. 2010; Jiang et al. 2011; Kurtz et al. 2011; Hareter et al. 2014; Rodríguez-López et al. 2015).

In the opening paragraph of his work, *The Internal Constitution of the Stars*, Sir Arthur Stanley Eddington wrote (Eddington 1926):

> *At first sight it would seem that the deep interior of the sun and stars is less accessible to scientific investigation than any other region of the universe. Our telescopes may probe farther and farther into the depths of space; but how can we ever obtain certain knowledge of that which is hidden behind substantial barriers? What appliance can pierce through the outer layers of a star and test the conditions within?*

The answer to these questions lies in photometric and spectroscopic time-series analysis of pulsating stars. The study of periodic light variations at the surface of a star can be used to probe its internal structure and determine the fundamental stellar parameters in a way which is, almost, model independent. With the use of basic physical relations and well based assumptions, the density, pressure and temperature inside the star can be derived (e.g. Aguirre, Casagrande & Miglio 2014; Chaplin et al. 2014; Tian et al. 2014; Buldgen et al. 2015).

Such practices can be applied to a plethora of pulsating stars across the Hertzsprung Russell Diagram (HRD), from stars like the Sun, to the hottest O-type stars, the evolved giant stars and degenerate white dwarf stars. This thesis however has chosen to focus on the A-type stars.

1.1 Variability Across the HR Diagram

Figure 1.1 shows where many pulsating stars lie on the HRD. Particular regions of interest are where different types of pulsator overlap, especially if both p and g modes are present (see section 1.3). The discovery of both mode types in a star enables the entire interior to be probed from surface to core (e.g. Kurtz et al. 2014; Saio et al. 2015). Provided here is a summary of some pulsationally variable stars on the HRD.

1.1.1 Main-Sequence Variables

Solar-like Pulsators

Due to the nature of solar-like oscillations, it is expected that stars with an outer convective zone will display similar pulsations. However due to the stochastic processes which cause these oscillations, stars pulsate with very low amplitudes. For example, the solar oscillations peak at 8 ppm for the strongest ~ 5 minute pulsation. The first solar-like oscillations observed other than in the Sun came in 1995 with observations of η Boo by Kjeldsen et al. (1995). Their observations showed excess power at a frequency of $73.4\,\mathrm{d}^{-1}$ (~ 20 minute). The difference between η Boo and the Sun arises from the difference in sound speed and surface gravity between the main-sequence Sun and less dense sub-giant.

γ Doradus Stars

Named after their prototype, γ Doradus stars (Cousins, Caldwell & Menzies 1989) are non-radial, multiperiodic, g mode pulsators which oscillate with periods of between $0.5 - 3\,\mathrm{d}$ (Kaye et al. 1999). γ Dor stars have spectral type A7−F5 and luminosity class of either IV, IV-V or V and masses within the range of $1.5 - 1.8 \pm 0.03\,\mathrm{M}_{\odot}$ (Kaye et al. 1999). These stars are an interesting class of pulsator as they lie in the same region as p mode solar-like oscillators on the HRD, and are discussed in more detail in section 1.4.1.

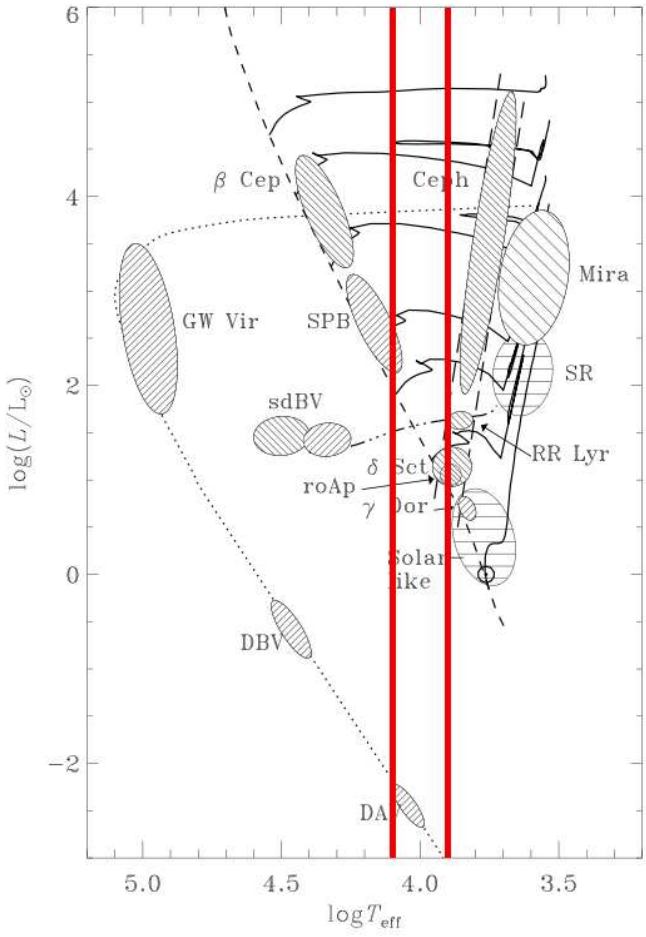

Figure 1.1: A pulsational HRD showing the positions of many pulsating stars. The diagonal dashed line represents the MS, the parallel dashed lines represent the classical instability strip, the dotted line represents the evolutionary track for white dwarf stars, and the solid lines represent evolutionary tracks to the MS. The vertical red lines indicate the temperature range of the A-type stars. Some classes are named for a star in that class, others are: rapidly oscillating Ap (roAp) stars; subdwarf B variables (sdBV); slowly pulsating B (SPB) stars; DBV stars are variable DB (helium-rich) white dwarfs and DVA are DA (hydrogen-rich) variable white dwarfs. The hatching indicates the types of modes and excitation mechanisms: up-left for opacity driven p modes; up-right for opacity driven g modes; horizontal for stochastically driven p modes. From Christensen-Dalsgaard (2003).

δ Scuti Stars

The δ Scuti stars are $1.5-2.5\,M_{\odot}$, p mode pulsators, with frequencies greater than $3\,d^{-1}$ and are found at the base of the instability strip (Breger 2000). Most δ Sct stars are multiperiodic pulsators, with a mixture of both radial and non-radial modes excited by the $\kappa-$mechanism (see section 1.3;Breger 2000). There exist several sub-groups of δ Sct stars: HADS (High Amplitude δ Scuti) stars which show amplitude variations of ≥ 0.3 mag, slow rotation rates ($v \sin i \leq 30$ km s^{-1}) and pulsate only in radial modes (Breger 2000); chemically unusual stars such as Am and λ Boo stars show δ Sct like pulsations but suffer amplitude variations due to their chemical abundance anomalies (Rodríguez & Breger 2001); and SX Phe stars which are the Population II equivalent of the standard δ Sct star (Frolov & Irkaev 1984). The δ Sct stars are discussed in more detail in section 1.4.2.

roAp Stars

Discovered by Kurtz (1982), rapidly oscillating chemically peculiar A-type (roAp) stars have strong magnetic fields, up to 24.5 kG (Hubrig et al. 2005), and pulsate in the frequency range $61-288\,d^{-1}$ with amplitudes on the order of 10 mmag in the $B-$band (Alentiev et al. 2012; Kurtz et al. 2006). Many modes of pulsation are aligned with the magnetic axis rather than the rotational axis of the star, leading to the oblique pulsator model of Kurtz (1982). Spectroscopic analysis of roAp pulsations can enable 3D mapping of the stellar atmosphere where chemical abundances effect the pulsations through chemical stratification (Kurtz 2005; Eyer & Mowlavi 2008).

Slowly Pulsating B Stars

The slowly pulsating B (SPB) stars are found on the upper-main-sequence, and show variability between $0.5-5$ d. The class was first observed photometrically by Waelkens (1991) who analyses several years of data for 7 SPB stars. It was found that these

stars can be monoperiodic or multiperiodic in nature with amplitudes up to 82 mmag in the $U-$band. They pulsate in high-order g modes which are thought to be driven by the $\kappa-$mechanism (Dziembowski, Moskalik & Pamyatnykh 1993).

β Cephei Stars

The β Cep stars are the hottest pulsating stars on the main-sequence, with masses up to about $18\,M_{\odot}$. They show mostly periodic light curves, with pulsations between $3-25\,d^{-1}$ (Stankov & Handler 2005). They have been shown to pulsate in both both p and g modes, with the $\kappa-$mechanism being the driving force (Moskalik & Dziembowski 1992). For the p mode pulsations amplitudes can reach 0.1 mag, whereas the g modes are observed to be about 0.01 mag (Stankov & Handler 2005).

1.1.2 Evolved Stars

RR Lyrae Stars

The RR Lyr stars are mostly monoperiodic radial pulsators, found in the classical instability strip and are extreme Population II stars. The RR Lyr stars are split into three sub-groups: RRa, RRb and RRc. The RRab group pulsate in the radial fundamental mode with an asymmetric light curve, whereas the RRc stars show sinusoidal variations and pulsate in the first overtone mode (Smith, Catelan & Kuehn 2011). The RR Lyr stars show an interesting modulation in their amplitudes which are about 100 times the period of the pulsation; this *Blazhko effect* was first observed by Blažko (1907), but has yet to be explained.

Semi-Regular Stars

The SR stars are stochastically driven p mode pulsators (Christensen-Dalsgaard, Kjeldsen & Mattei 2001) which show, as the name implies, non-regular light curve variations.

The SRs pulsate in the fundamental mode, as well as the 1st, 2nd and 3rd radial overtones (Wood 2000), and show amplitude less than 2.5 mag.

Mira Stars

The Mira variables are long period pulsators, with periods greater than about 80 d. Their amplitude variations are greater than 2.5 mag. They are situated at the red-edge of the instability strip, with temperatures between $2\,500 - 3\,500$ K (e.g. Feast 1996). The Mira stars pulsate in radial modes, driven in the H I-II and He I-II ionisation zones (Ostlie & Cox 1986).

Cepheids

The Cepheids have a long history, and are useful in astrophysics due to their well-known *period-luminosity* relationship discovered by Leavitt & Pickering (1912). The measurement of the period of a Cepheid star provides its absolute magnitude and thus the distance to the star. These stars pulsate in radial modes, most commonly in the fundamental mode. Some stars exhibit two or three pulsation frequencies which can allow for the determination of the mass and radius of the star – as first calculated by Petersen (1973). The periods of the Cepheid stars range between $1 - 50$ d, and they show amplitudes up to 1 mag.

sdBV Stars

Subdwarf B variable (sdBV) stars were first observed by Kilkenny et al. (1997). The prototype star, EC 14026, has two pulsation frequencies at about 600 and 645 d^{-1} with amplitudes of 12 and 4 mmag, respectively. The sdBV stars are sub-luminous B stars which show a lack of He in their spectra, they have masses less than 0.5 $\mathrm{M}_{\odot}$ and temperatures between 28 000 and 35 000 K (Kilkenny 2007). These stars pulsate in either p, g, or mixed modes with amplitudes between 0.001 and 0.3 mag and frequencies of between 144 and 1 080 d^{-1} (Kilkenny 2002; Kilkenny 2007).

White Dwarf Pulsators

The two largest groups of white dwarf pulsators are the DA and DB classes (Eisenstein et al. 2006). DA white dwarfs are classified such as they show only Balmer hydrogen lines in their optical spectra, they have temperatures in the range $11\,000 - 13\,000\,\mathrm{K}$ (Fontaine & Brassard 2008). Gravity mode pulsations have been observed over a wide frequency range from 62 to $823\,\mathrm{d}^{-1}$ in DAV stars (Fontaine & Brassard 2008; Bradley 1998).

DB pulsators have effective temperatures in the range of $22\,00 - 28\,000\,\mathrm{K}$ and show He I lines in their spectra (Beauchamp et al. 1996; Bergeron et al. 2011). They are again g mode pulsators with multiperiodic, low-amplitude, pulsations in the range $112 - 288\,\mathrm{d}^{-1}$ (Bradley 1995).

Summary

Many of the stars introduced here are long-period variable stars. As such, frequency analysis becomes difficult as variability signatures fall in the same region of a periodogram as many sources of noise (see section 1.6.1), thus causing confusion between real and false signatures. These stars also require long time-base observations to reliably extract a period, if a definitive period is even present.

The stars which show stochastically excited modes are intrinsically low-amplitude pulsators and, as such, are difficult to observe with ground-based telescopes. The stars which are most attainable from the ground, with short observing periods, are those which show higher amplitude, high-frequency pulsations. These types of pulsations are seen in the main-sequence A-type stars, and the hotter compact subdwarf and white dwarf pulsators. It is, therefore, these stars that this thesis focuses upon.

1.2 The A-type Stars

Unlike most other types of stars on the main-sequence (MS), it is hard to classify a set of 'normal' A-type stars. Cowley (1991) sums this up with a interesting comparison:

> *Normal A stars are rather like normal people. If you don't look too hard, there seem to be quite a few of them. After you get to know them well, most seem a little crazy.*

Typically, normal refers to the majority of stars in a particular spectral type (Wolff 1983), however in the A-type stars abnormalities seem to take a precedence. There are many subclasses of A-type stars which deviate from the norm: the Ap stars with their strong magnetic fields and peculiar elements (e.g. Eu, Cr, Pr, Nd), the Am stars with weak Ca II K lines compared to their metal line types, the λ Boo stars with their weak metal lines, and the pulsationally variable δ Sct stars, which are not spectroscopically defined and as such may cover all types of A star. A discussion of the abnormal A-type stars will follow shortly, but first an introduction to the A-type stars as a whole is needed.

The MS A-type stars are found in the HRD straddling the region where the classical instability strip intersects the MS. They have masses between about $1.5 - 2.9\,M_\odot$, radii of $1.5 - 2.2\,R_\odot$, and luminosities between $6 - 40\,L_\odot$. Their temperatures range from about 7 000 K to 10 000 K (Gray 2008). They have convective cores, with radiative envelopes, and two further convective zones just below the photosphere.

These convective zones (CZs) are the regions which play host to the two main ionisation zones within the A-type stars: the first zone, close to the surface of the star, lies at a temperature of about 14 000 K and is where neutral hydrogen and helium are ionised, with the second, the He II ionisation zone, much further into the star at about 50 000 K (Padmanabhan 2001; Antoci 2014). The outer CZs in the A-type stars account for just $1 - 1.5$ per cent of the stellar radius (Kallinger & Matthews 2010), whereas in the Sun, this accounts for about 30 per cent of the radius.

Figure 1.2 shows the change in the convection layers in zero-age main-sequence (ZAMS) stars from about G0 to A0, and how efficient convection is as a form of energy

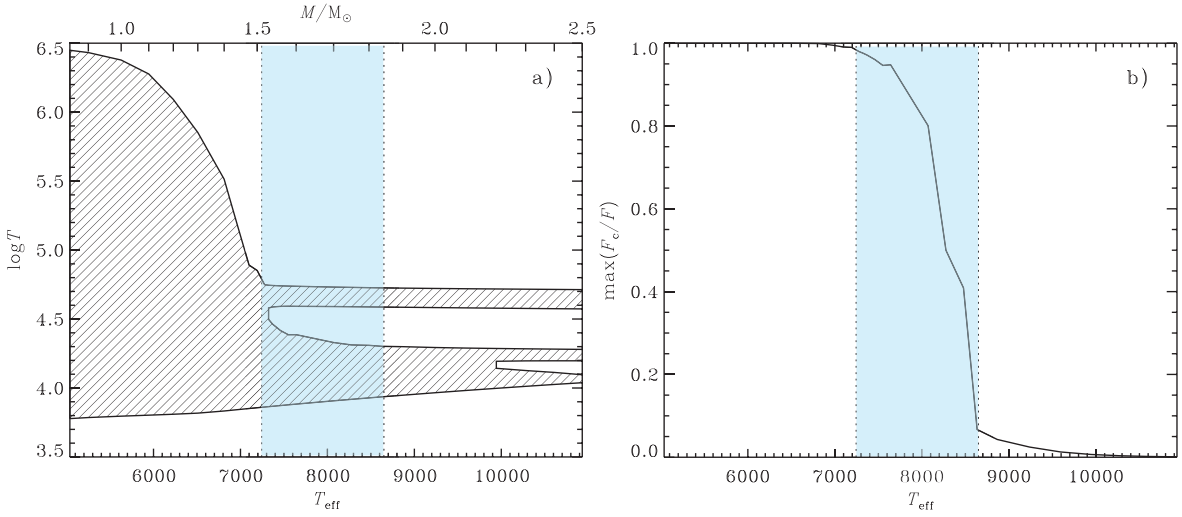

Figure 1.2: The envelope structure of the ZAMS stars. (a) The lined area represents the convective regions in the star as a function of $T_{\rm eff}$ and mass. It can be seen that the H and He I ionisation zones are combined for the A-type stars, and separate in the B-type stars, and are near the stellar surface, while the He II zone lies deeper in the star. (b) F_c/F represents the energy transferred by convection. The blue region in both panels indicates the area of the instability strip where significant changes in the convection zones and energy transfer take place. From Antoci (2014).

transfer within the star. There is a pronounced change in both of these factors in the temperature region where the instability strip crosses the MS as indicated by the blue shading. These CZs are key to the pulsational variability seen in the A-type stars.

The shallow CZs seen in the A-type stars are not efficient enough to produce a global magnetic field as in the case with less massive stars. There have been several studies of normal A-type stars in the search for magnetic fields (e.g. Shorlin et al. 2002; Bagnulo et al. 2006), however no stars have been found with field strengths above about 1 G. This is contrary to the Ap stars (see section 1.2.1) which have strong fields above 300 G. On the other hand, observations have been made of the magnetic field of the early A-type stars Vega (0.6 ± 0.3 G; Lignières et al. 2009; Petit et al. 2010) and Sirius (0.2 ± 0.1 G; Petit et al. 2011) which are much lower than the 300 G of the Ap stars, leading to a 'magnetic desert' in the A-type stars (Lignières et al. 2014). Detections

of such weak fields require very bright objects, thus limiting the sample available for study. Braithwaite & Cantiello (2013) suggest that these weak magnetic fields may be a result of inheritance or creation during, or shortly after, star formation rather than an ongoing dynamo effect. They suggest that all A-type stars have magnetic fields of this strength and that rapid rotators have stronger fields, accounting for the difference in field strength between Vega and Sirius, that younger stars have stronger fields which decrease over time, and that the field is strongest at the poles.

Despite the detection, or lack of, very weak magnetic fields in the normal A-type stars, Balona (2012) claims the detections of flares in *Kepler* observations of A- and F-type stars. This is not the first claim however, Wang (1993) claimed a detection in BD+47° 819, a star in the vicinity of the α Persei cluster. However, the *Kepler* observations presented by Balona (2012) do provide the best evidence, to date, of photometric flares in the A-type stars. Of the 7 137 F5–A0 stars searched, 33 were seen to show a flare-like brightening and decay. Consideration is made that the detected events may be a result of flares from an active cool companion, however this is ruled out due to the relative intensities of the companion flare and the dilution it would suffer from the A star flux: a companion flare would show an intensity 100 times less than those observed (Balona 2012; Balona 2015). However, some of the flares reported by Balona may be due to *Kepler* instrumental effects; Pedersen (2013) re-analysed the same candidate flare stars, but with more stringent criteria similar to those used in Walkowicz et al. (2011). She was able to confirm the presence of flare like signatures in some of the stars, but at a much lower rate than Balona (2012).

Linked to both the magnetic fields and flares observed in the A-type stars is the presence of starspots. Flares in the Sun are linked to the magnetic field, and the dynamo effect in the deep surface convective zone. As a result, they often occur in or near active regions/starspots as the magnetic field must be sufficient to suppress convective overturning of the material, causing flux blocking from below and allowing cooler, dark regions to form (Biermann 1948). It would therefore be reasonable to assume that the A-type stars, particularly those which show flares, will have starspots on their photospheres.

Balona (2011) conducted a study into low-frequency ($0.2 - 5\,\mathrm{d}^{-1}$) variability seen in A-type stars in the first release of the *Kepler* public archive. As well as finding evidence which supports the presence of convective cells in A-type stars (Kallinger & Matthews 2010), he proposes that 20 per cent of the A-type stars studied show evidence of rotational modulation. In this frequency range, one has to consider the possibility of low-frequency pulsations of the γ Dor type (see section 1.4.1). In this case, the stars studied have temperatures which place them hotter than the blue-edge of the γ Dor instability strip, suggesting that pulsations are not the cause of the variations. Further, the results of this study were compared to the rotation velocities of field stars, of the same effective temperature and luminosity, with agreement found between the two samples. It is proposed that, indeed, the A-type stars can show starspots, in much the same way as B-type stars are thought to (Degroote et al. 2009).

Finally, there is now evidence that A-type stars host transiting planets (e.g. Kalas et al. 2008; Lagrange et al. 2009). HD 15082 (WASP-33) is an Am (kA5hA8mF5) star with a transiting hot Jupiter planet, which also shows δ Sct pulsations (Christian et al. 2006; Collier Cameron et al. 2010). A further detection of an A-type star hosting a planet came from *Kepler* observations of the *Kepler* Object of Interest (KOI) 13 (Rowe et al. 2011; Barnes, Linscott & Shporer 2011). Balona (2014b) also suggests that 166 of 875 (19 per cent) of the A-type stars studied in Balona (2013a) may show signatures of synchronously orbiting planetary companions in their periodograms. However, this hypothesis is yet to be proven with high-resolution spectroscopy. If proven, the presence of a close-in planet may aid the understanding of the flares detected on A-type stars through reconnection events between the star and planet magnetic fields (Balona 2014b).

The projected rotation velocities, $v \sin i$, of the A-type stars are high, with equatorial rotation velocities $> 120\ \mathrm{km\,s^{-1}}$ (Adelman 2004). There is a subset of stars, however, that show significantly lower rotation velocities. The chemically peculiar (CP) A-type stars (see section 1.2.1) often do not show $v \sin i$ values greater than about $40\ \mathrm{km\,s^{-1}}$ (Abt & Morrell 1995). A detailed view of the rotation velocities of the A-type stars can be seen in Figure 1.3. The hotter stars show a broad range of rotational

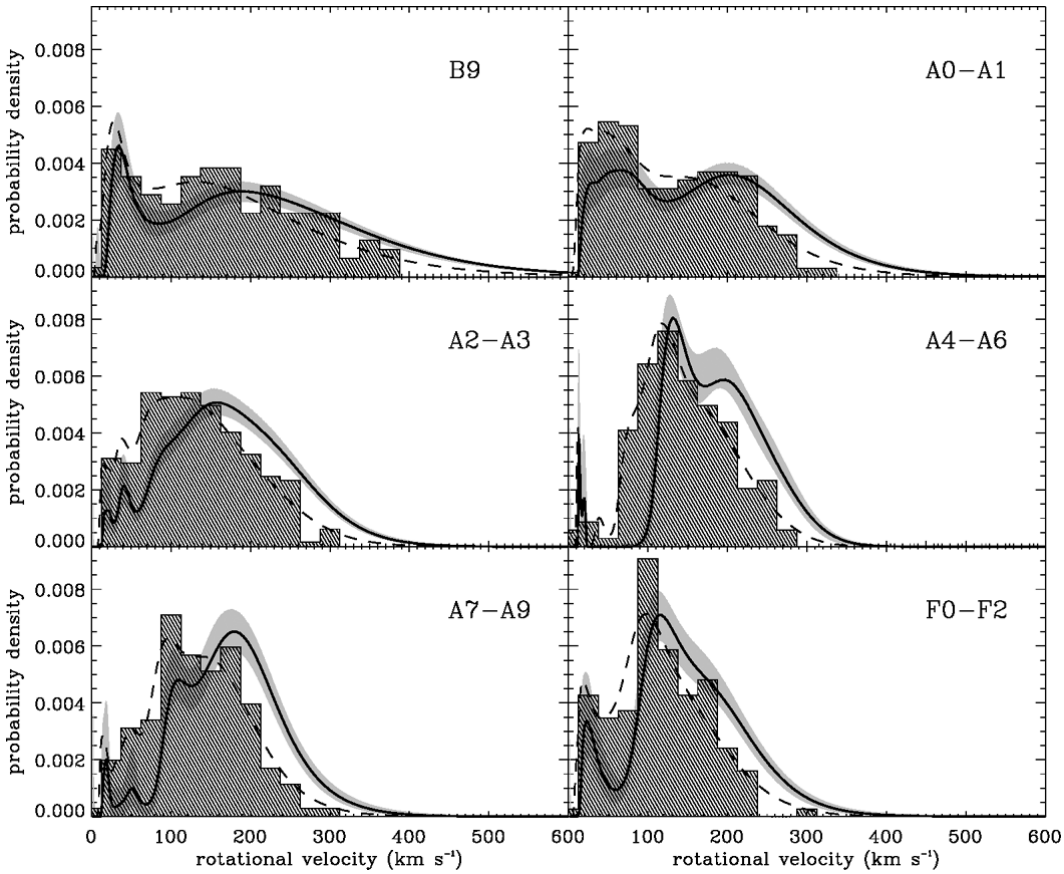

Figure 1.3: The rotation velocities of the normal A-type stars shown in spectral subclasses. Both binary and CP stars are removed from the sample. The histograms represent the observed $v \sin i$, the dashed line in the fitted $v \sin i$, the solid line is the deconvolved v distribution, and the grey shading represents the error on v. From Royer, Zorec & Gómez (2004).

velocities, with a rapid decrease in low velocity rotators between about A4−A9, and again an increase in the longer period rotators in the F-type stars. The study, by Royer, Zorec & Gómez (2004), removed known binary and CP stars from the sample which are known to be slow rotators, just retaining the MS normal A-type stars. Royer et al. (2014) found 17 slowly rotating normal A0−A1 type stars from a sub-set of a previous study. Their results suggest, along with the previous studies, that there is a sub-group of hot A-type stars that are intrinsically slow rotators.

The rotation velocities of the A-type stars are almost constant over their lifetime on the MS, with only a slight increase as they evolve from the ZAMS to the terminal-age main-sequence (TAMS) (Zorec & Royer 2012). This is opposite that seen in the B-type stars which show a significant shift to longer rotation periods as they evolve. The B-type stars also show a wider spread of rotation velocities than the A-type stars, as can be seen in Figure 1.3.

The rapid rotation in the A-type stars poses a problem when attempting spectral classification, as the rotation serves to broaden and weaken lines in the spectrum, giving the appearance of very few features beyond the strong Balmer lines (see Chapter 5 for examples).

Reiners & Royer (2004) claim the first detections of differential rotation in the A-type stars, previous to this they were thought to be rigid rotators. Balona (2011) also suggests this could be an explanation for travelling waves seen in *Kepler* light curves of A-type stars. Asteroseismic analysis of a late MS A-type star in the *Kepler* data, KIC 11145123 conducted by Kurtz et al. (2014), has shown that the radial rotation profile is almost constant, with a slightly faster rotating surface. Such an analysis has also been performed on a late MS F-type star, KIC 9244992 (Saio et al. 2015). In this case, the surface is seen to rotate more slowly than the core, but again by only a small margin. Kurtz et al. (2014) produced a model star based on KIC 11145123, and evolved it from the fully convective Hayashi phase, through the MS, to the TAMS, conserving angular momentum in the process. They found, that as the core contracts, the angular momentum here increases by a factor of five over the surface, leading to differential rotation from the core to the surface. There is, therefore, an effective method of angular momentum transport acting in these stars to allow for the near ridged rotation seen at these late stages of evolution. These results show the need for further examples of this type of asteroseismic analysis to further understand the evolution of the rotation profiles in the A- and F-type stars.

1.2.1 The Chemically Peculiar A-type Stars

As mentioned above, the A-type stars show many spectral abnormalities the with majority of the class not being 'normal' A-type stars. The following describes the characteristics of the two main classes of peculiar A-type stars, with a detailed spectroscopic approach given in Chapter 5.

The rotation velocities of the CP stars are much different than those of the normal A-type stars. Figure 1.4 shows the distribution of the rotation velocity for the two groups. There is a clear bimodal distribution between the two groups of stars. The causes will be discussed in the following sections.

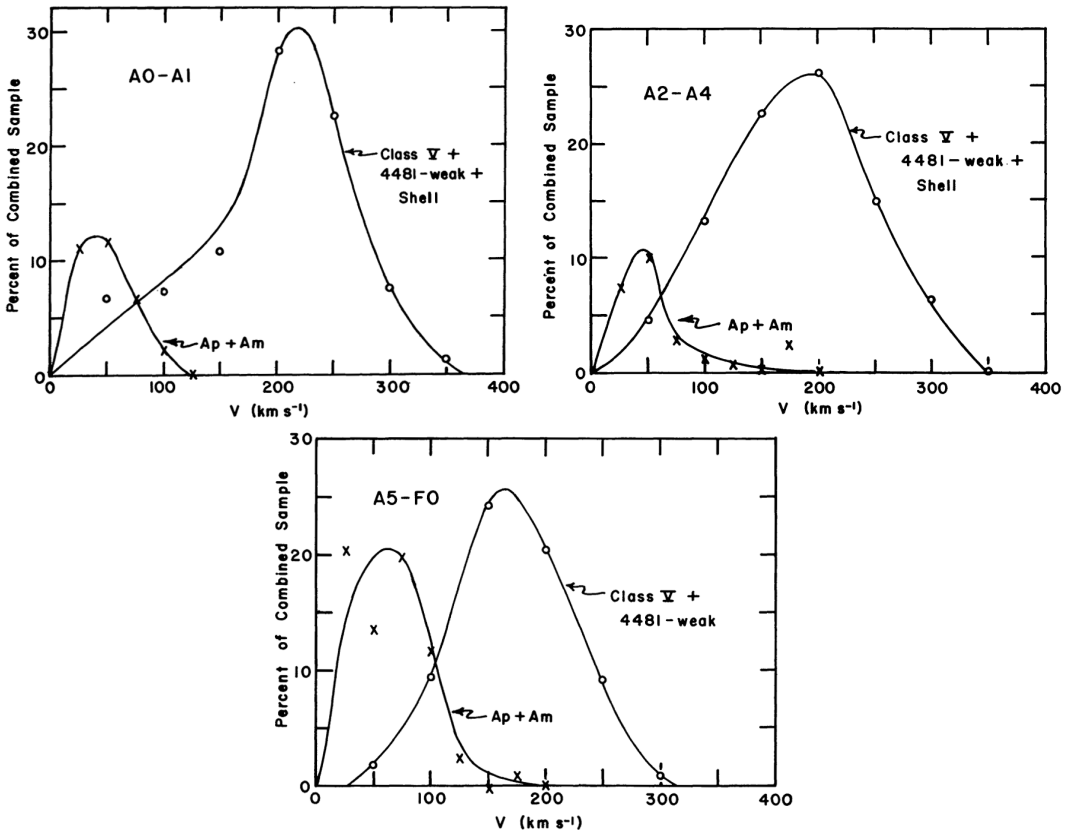

Figure 1.4: The rotation velocities of the normal and chemically peculiar A-type stars. From Abt & Morrell (1995).

1.2.2 Am Stars

The metallic-lined Am stars are a subgroup of A-type stars where the Ca II K line and the metallic lines show a difference in spectral type by five or more subclasses, with differences less than this leading to the marginal Am (denoted Am:) stars (Conti 1970). The Am stars appear to account for 50 per cent of the A-type stars which are classed as A8 and later (Smith 1973).

The Am stars are relatively slow rotators when compared to the normal A-type stars (see Figure 1.4), with a maximum rotation velocity of about 100 $\mathrm{km\,s^{-1}}$, and a mean value of 33 $\mathrm{km\,s^{-1}}$ (Abt & Moyd 1973). There are several theories for the reason of slow rotation in Am stars, but by far the most commonly occurring is binarity and tidal synchronisation. Early studies concluded that most, or all, known Am stars were in binary systems (Roman, Morgan & Eggen 1948; Abt 1961), but more recent studies place a more realistic limit of about 65 per cent on this number (Carquillat & Prieur 2007; Smalley et al. 2014).

The binary theory for Am stars, due to its link to slow rotation, was also used to explain the abundance anomalies in Am stars, as they are thought arise through radiative diffusion (Michaud 1970; Michaud et al. 1983). However, as there are still about 45 per cent of the Am stars not found in (close) binaries this theory may not hold true for the entire population (Balona et al. 2015).

In common with normal A-type stars, most of the Am stars do not show a strong magnetic field (Shorlin et al. 2002; Aurière et al. 2010). Mathys (1988) and Lanz & Mathys (1993) report detections of about 2 kG in the Am stars o Peg, HD 29173, and HD 195479A, however in the same study Lanz & Mathys (1993) do not detect fields in 16 other Am stars. However, later re-analysis of these stars by Shorlin et al. (2002) do not detect the same, or in fact any, field. Following the search for magnetic fields in Am stars, Blazère et al. (2014) found 'ultra-weak' magnetic fields in two further objects: β UMa and θ Leo. These fields resemble, in strength, those of Vega and Sirius, further suggesting that Am stars, as a group, host weak, possibly tangled (Böhm-Vitense 2006), magnetic fields.

Following on from this, Balona et al. (2015) have used *Kepler* and K2 data to study 29 Am stars at high photometric precision. Their observations suggest that two of these stars show possible flares, with 10 of 15 stars in the *Kepler* field showing a rotational modulation signal in their periodogram, and 1 of 14 doing so in the K2 data. Three of the detections in the *Kepler* data are at an amplitude of about 7 μmag or less, which is approaching the noise limits of the data. The K2 data used is from Campaign 0, and as such is only 45 d in length making detections of long rotation periods difficult due to the lack of sampling of the rotation signature. The noise level in the presented periodograms for the K2 data is much higher than the *Kepler* light curves, between about $0.5 - 2$ mmag in the low-frequency range. Therefore, some of the claimed detections may be a result of noise. The rotational modulation seen is proposed to be a result of starspots. Spots, coupled with flares, suggests that the Am stars have similar magnetic fields to the normal A-type stars. If this is the case, then the explanation of the presence of abundance anomalies must be rethought. The diffusion and gravitational settling of material in these slowly rotating, non-magnetic stars may not represent all of the process occurring in these stars, otherwise all A-type stars should show similar signatures. Rather, Balona et al. (2015) suggest that the abundance anomalies may arise from accretion from a debris disk, as with β Pic and other young A-type stars (Beust et al. 1996; Montgomery et al. 2015), or the in-fall of interplanetary dust and comets (Kumar, Davila & Rajan 1989).

The Am stars were once thought not to pulsate, or do so with small amplitudes (Breger 1970; Wolff 1983). However recent studies how shown this not to be the case (e.g. Smalley et al. 2011; Balona et al. 2011d; Holdsworth et al. 2014b). The pulsating Am stars pulsate with the same mechanism as the δ Sct stars and are, as such, discussed as part of the δ Sct stars in section 1.4.2.

1.2.3 Ap Stars

The chemically peculiar Ap stars are a rarer sub-class of A-type star than the Am stars. They show strong over-abundances of silicon, strontium, europium or chromium, or a

mixture of all, throughout their spectrum, but are classified using the blue region, where many strong lines are unblended. Only about 10 per cent of the A-type stars a known to be Ap stars (Wolff 1983).

Like the Am stars, the Ap stars are slow rotators, with periods up to decades (γ Equ; Bychkov, Bychkova & Madej 2006). Stępień (2000) proposed that the slow rotation is apparent at the ZAMS stage of evolution, with interactions between the magnetic field and the disk for only a short period of a long pre-main-sequence (PMS) life-time, causing breaking of the star. Observations of many young, slowly rotating, Ap stars have provided evidence for this (Pöhnl, Maitzen & Paunzen 2003; Bagnulo et al. 2003; Bagnulo et al. 2004), disputing previous theories that only after about 30 per cent of the MS life-time does the magnetic field develop and so magnetic breaking can slow the rotation velocity of the star (Hubrig, North & Mathys 2000).

The Ap stars show very strong dipole magnetic fields, much stronger than the tangled magnetic field seen in the Am and normal A-type stars. Observations by Aurière et al. (2004) suggest that all Ap stars have at least a magnetic field of 300 G, with some instances of very strong fields such as Babcock's star (HD 215441, 34 kG; Babcock 1960), HD 75049 (30 kG; Elkin et al. 2010b) and HD 137509 (29 kG; Kochukhov 2006). The magnetic fields in the Ap stars are mis-aligned with the rotational axis, and can be described by the rigid rotator model of Stibbs (1950). This model allows for the observations of a variable strength of the magnetic field as the star rotates. In this model, the field is presumed to be 'frozen-in' to the surface of the star, and so co-rotates with it. The angle between the magnetic and rotation axes is labelled as β, the angle of obliquity. Figure 1.5 shows the geometry of a rapidly oscillating Ap star.

The source of these strong magnetic fields is still debated. The current prevailing theory is that of fossil fields which have remained from the PMS stage of the star. However, recently both Ferrario et al. (2009) and Tutukov & Fedorova (2010) have, independently, proposed a scenario which involves the late merger of two proto-stellar objects. They suggest that binary stars, with masses between $0.7 - 1.5\,\mathrm{M}_{\odot}$ and a semi-major axis between $6 - 12\,\mathrm{R}_{\odot}$, coalesce through a result of mass-loss through magnetic stellar winds. The merger of two stars in this scenario would drive strong differential

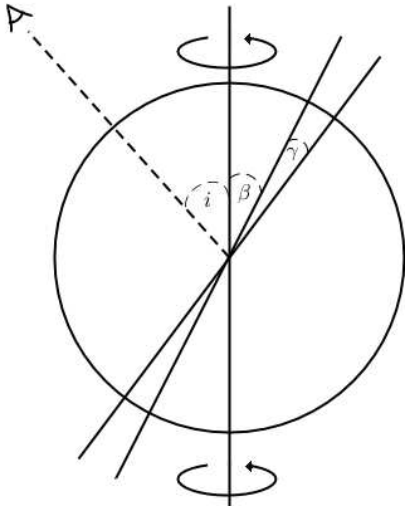

Figure 1.5: The geometry of a roAp star. The vertical line represents the rotation axis, the angle β is the angle between the rotation axis and the magnetic axis, and γ is the angle between the magnetic and pulsation axes (see section 1.4.3). The dashed line represents the line-of-sight, with i being the angle between the line-of-sight and the rotation axis.

rotation and a large-scale dynamo field. For this to occur, the merger must occur on the Henyey track of the PMS, as the radiative envelope is forming, rather than the Hayashi track where the star is fully convective. Both groups argue this scenario also accounts for the lack of close binary Ap systems, as systems with $P_{\rm orb} \leq 3\,{\rm d}$ would merge. Further evidence to support this theory is presented by Mathys (2014) who conducted a study on binaries with Ap components. He found a mutual exclusion of short rotation and orbital periods in the non-synchronised binary systems, and argues this supports the merger scenario as these now binary systems would have been triple stars until the merger, and that such a dynamical event would influence both the created Ap star and the third star in the system.

The first detailed study of Ap stars in binaries was conducted by Abt & Moyd (1973), who found just 20 per cent of the stars were in binary systems, compared to 47 ± 3 per cent of normal A-type stars which are spectroscopic binaries (Jaschek & Gómez 1970). They find a lack of close binaries (with separations of $10^6 - 10^9\,{\rm km}$)

but a normal incidence of wide binaries (with separations of $10^{10} - 5 \times 10^{11}$ km). More recently, North et al. (1998) found 27 per cent of the Ap stars to be in binaries, higher than that of the previous study, but still less than the normal stars. However, more importantly, they found a lack of short period binaries, with periods ≤ 3 d, which is consistent with the results of Gerbaldi, Floquet & Hauck (1985). Only one short period Ap star is found in their study, HD 200405 with a period of just 1.635 d. This is confirmed by Carrier et al. (2002), who also note the lack of short period binaries, except for HD 200405. For the wider binaries, Carrier et al. (2002) obtain a bias corrected result of 43 per cent for the Ap stars, a similar incidence as for the normal A-type stars.

As a result of the slow rotation, and the presence of a strong global magnetic field, the Ap stars often show chemical spots on their surface (Stibbs 1950). These spots can be stable for decades, allowing for a precise rotation period to be determined from a light curve. The cause of these spots is most likely a result of the slow rotation of the Ap stars, coupled with radiative levitation and gravitational settling in the presence of the strong magnetic field (Kochukhov 2011 and references therein). Detailed observations and mapping can now be achieved of the surface anomalies of the Ap stars using Doppler imaging and full Stokes parameters, with the ability to produce accurate 3D chemical spot structures (e.g. Kochukhov et al. 2004; Kochukhov et al. 2006; Kochukhov et al. 2015).

1.3 Pulsations

There are two main ways which pulsations can be characterised in stars, they are the pressure (p) modes and the gravity (g) modes. The p modes are acoustic waves which propagate through the star primarily in a vertical motion producing both radial and non-radial modes and have the pressure gradient as the restoring force when the star is out of equilibrium. The g modes primarily move horizontally in a star, and have buoyancy as the restoring force. The predominantly horizontal motion of the g modes

is a result of lateral infilling by the surrounding material of the volume vacated by a cell of plasma rising (or falling) away from equilibrium. High-degree p modes are most sensitive to the outer conditions of the star as they have small inertia with low-degree p modes able to probe into stellar cores, whereas the g modes probe deeper into their interiors (Kurtz 2005).

The p modes propagate between the surface of the star, where the density drops rapidly so they are reflected back into the interior, and a lower boundary limit, $r_{\rm t}$, where total internal reflection occurs (Figure 1.6). The boundary within the stars is described as

$$\frac{c^2(r_{\rm t})}{r_{\rm t}^2} = \frac{\omega^2}{l(l+1)} \tag{1.1}$$

where $c^2(r_{\rm t})$ is the adiabatic sound speed at $r_{\rm t}$, ω is the angular frequency of the wave, and l is the degree of the mode (see section 1.3.2 below).

The internal turning point for the g modes occurs when the buoyancy frequency, N, is equal to the angular frequency of the wave, ω. The parameter N, or more conveniently N^2, describes the motion of a small cell of plasma inside the star. In the case where $N^2 < 0$, the cell of material is less dense than its surroundings, and so is forced away from equilibrium, causing convective instability. However, if $N^2 > 0$, the cell is more dense than its surroundings and proceeds to sink. Buoyancy then forces the cell back towards the surface, causing an oscillation around its equilibrium position (Aerts, Christensen-Dalsgaard & Kurtz 2010). In the case of the A-type stars, the inner turning point is at the edge of the convective core, and the wave can propagate to nearly the surface (Figure 1.6).

1.3.1 Driving Mechanisms

There are two main driving mechanisms for the pulsations in stars, the *stochastic* and *opacity*, or κ, mechanisms. These processes occur in different types of stars, and are dictated by the stellar structure.

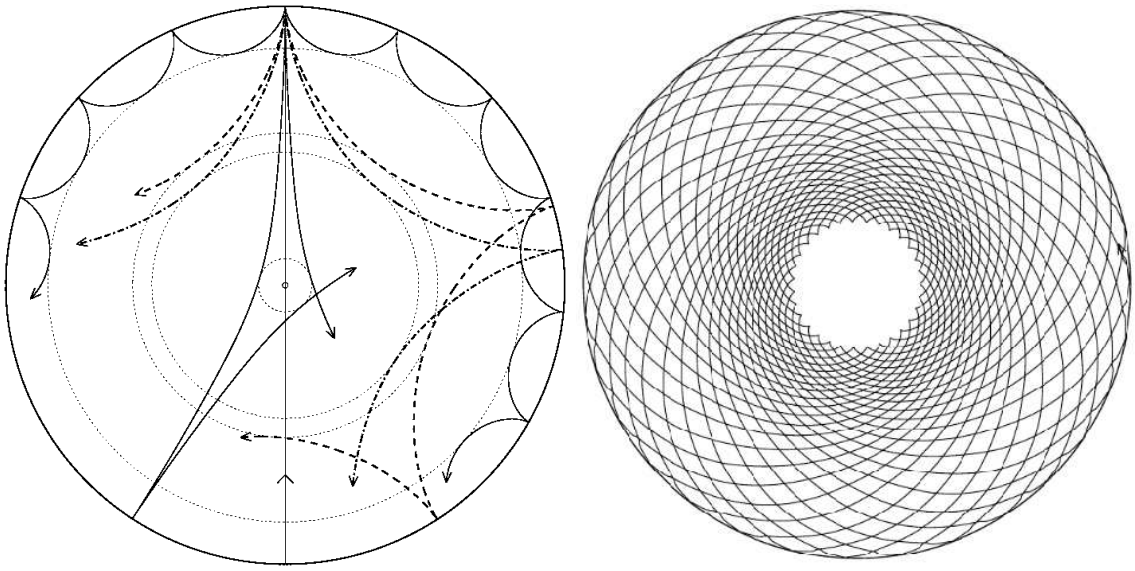

Figure 1.6: *Left*: The propagation of p modes for a Sun-like star. The acoustic waves are bent by the change of pressure until they undergo total internal reflection at boundaries described by the dotted circles. Reflection also occurs at the stellar surface due to a rapid decrease in density. The ray paths shown are for a frequency of $260\,\mathrm{d}^{-1}$ and degrees of $l = 75, 25, 20$ and 2 (in order of increasing penetration depth). From Cunha et al. (2007). *Right*: The propagation of g modes in an $8\,\mathrm{M}_{\odot}$ ZAMS star. The frequency of the mode is $4.32\,\mathrm{d}^{-1}$ with degree 5. As can be seen, the mode is trapped outside of the convective core. From Aerts, Christensen-Dalsgaard & Kurtz (2010).

Stochastic Process

The stochastic process operates in the Sun and solar-like pulsators, and relies on acoustic energy in the convective zone of the star exciting its natural frequencies (Belkacem et al. 2008). It was proposed that stable modes are a result of turbulent viscosity in the convection zone (Goldreich & Keeley 1977) and maintain the 5 min solar oscillations. Stochastic excitation relies heavily on the convective velocity near the outer boundary (Gautschy & Saio 1995). The amplitudes of stochastically driven p modes arise from the balance between excitation of modes and damping due to the acoustic noise (Houdek 2006).

$\kappa-$Mechanism

As a star pulsates there is an internal region that heats during compression while the remaining parts of the star cool. The cool regions of the star work to damp the oscillation, however if this is not possible then the star functions as a heat engine (Eddington 1919). The region which is heated during compression is a source of high-opacity in the star, and so this mechanism is referred to as the $\kappa-$*mechanism*. In most stars that pulsate under the $\kappa-$mechanism, the high source of opacity is hydrogen and helium, but can also be iron-group elements (Pamyatnykh 1999). In regions where the opacity is greatest, radiative flux becomes partially blocked and is converted into the kinetic energy of pulsations (Pamyatnykh 1999). This blocking of radiation causes the star to heat and swell beyond equilibrium, however the gas is re-ionised due to the increased temperature, reducing opacity allowing the radiation to escape and the star to cool and contract. On contraction, the ionised gas recombines and the process is repeated (Gautschy & Saio 1995).

1.3.2 Modes of Oscillation

There are three quantum numbers defining the modes of stellar oscillations: n is the number of radial nodes, l is the degree of the mode and denotes the number of surface nodes, and m is the azimuthal order of the mode, with $|m|$ specifying the number of longitudinal nodes. Different combinations of these quantum numbers result in various surface configurations (Figure 1.7).

Stars can pulsate in radial and non-radial modes. Radial modes consist of concentric shells of nodes, with the simplest being the fundamental mode with $l = 0$. In this case the centre of the star acts as a node, with the anti-node being the surface where maximum displacement occurs. This mode describes the pulsations seen in Cepheid variables and RR Lyrae stars. These stars, and δ Scuti stars, can also pulsate simultaneously in the first overtone, where a shell inside the star is a node and the surface is an anti-node. Comparison of the ratios of these two frequencies provides an indication of the internal structure of the star: for Cepheids the ratio is 0.71 and 0.77 for δ Sct (Aerts, Christensen-Dalsgaard & Kurtz 2010). The difference indicates a varying sound speed within the star, a direct measure of the temperature and/or chemical composition.

Non-radial modes only occur when $n \geq 1$. The simplest non-radial mode is the dipole mode where $l = 1$, $m = 0$, with the node being the equator. Visually, as the northern hemisphere contracts, the southern one swells. For high-degree l modes, the effects of oscillation are less evident as neighbouring sections have opposing intensity, this leads to *partial cancellation*. As we are currently unable to resolve the surface of a star we see the integrated intensity and so loose information from high l modes.

For a rotating star, it is possible to extract the angular velocity, Ω, through splitting of a multiplet. In a non-rotating, spherically symmetric star, the frequencies of a multiplet are the same, however a rotating star breaks symmetry and thus the multiplet may be resolved. In this case, frequency splitting by uniform rotation is given by (after Cunha et al. 2007)

$$\nu_{nlm} = \nu_{nl0} + m\beta_{nl}\Omega\,, \tag{1.2}$$

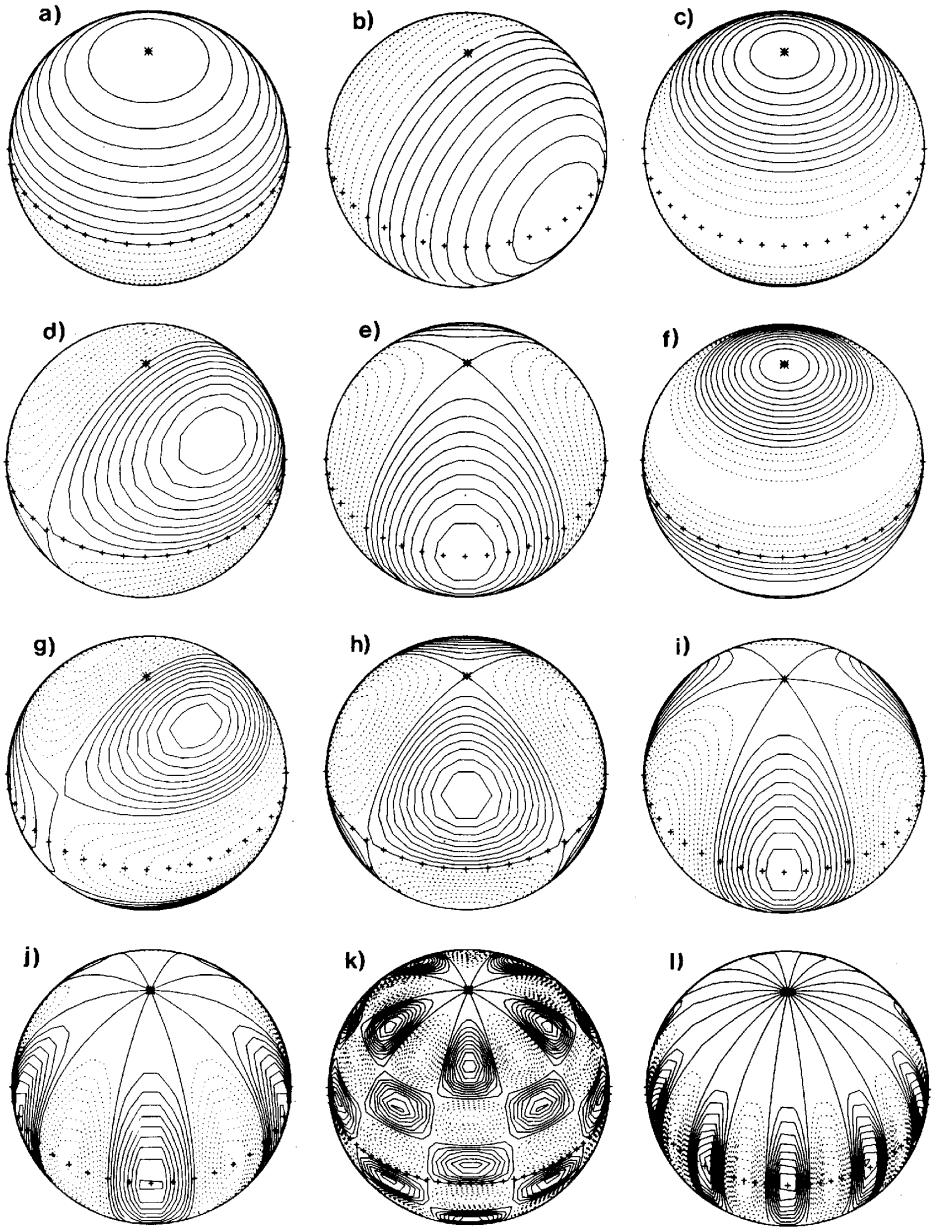

Figure 1.7: An example of some possible stellar pulsation modes. Solid lines indicate surface movement outwards, with dashed lines indicating recessive movement. The equator is represented with '++++' and the viewing angle is 45°. The following cases are illustrated: a) l = 1, m = 0; b) l = 1, m = 1; c) l = 2, m = 0; d) l = 2, m = 1; e) l = 2, m = 2; f) l = 3, m = 0; g) l = 3, m = 1; h) l = 3, m = 2; i) l = 3, m = 3; j) l = 5, m = 5; k) l = 10, m = 5; l) l = 10, m = 10. From Christensen-Dalsgaard (2003).

where ν_{nlm} is the observed frequency, ν_{nl0} is the rest frequency and β_{nl} is a constant containing the Ledoux constant which accounts for the model splitting due to rotation (Ledoux 1951). If multiplets of different l or n exist, then it is possible to probe the internal rotational profile of the star as has been done for the Sun (Thompson et al. 2003).

When $n \gg l$ there exists asymptotic relations for the spacing of p modes in frequency space, and for g modes in period space. Tassoul (1980) showed that these variations can be used to calculate the frequency spacing of p modes as

$$\nu_{nl} = \Delta\nu \left(n + \frac{l}{2} + \tilde{\alpha} \right) + \epsilon_{nl} \,, \tag{1.3}$$

where n and l are as before, $\tilde{\alpha}$ is a constant approximately 1, ϵ_{nl} is a small correction and $\Delta\nu$ is known as the large separation. This large separation is a measure of the sound speed in a star, from the surface to the core and back, which is given by

$$\Delta\nu = \left(2 \int_0^R \frac{dr}{c(r)} \right)^{-1} , \tag{1.4}$$

where $c(r)$ is the sound speed (Cunha et al. 2007). For stars near the MS, and more evolved red-giant stars, $\Delta\nu$ is a good estimation of the mean density of the star. The value ϵ_{nl}, from equation (1.3), gives rise to the small separation parameter which is a good indicator of stellar age as it is sensitive to core condensation (Aerts, Christensen-Dalsgaard & Kurtz 2010). This parameter is a measure of the frequency difference between adjacent odd or even modes (i.e. between modes of $\ell = 0$ and $\ell = 2$ or $\ell = 1$ and $\ell = 3$).

For g modes, Tassoul (1980) give the asymptotic relation, for nearly evenly spaced periods as

$$\Pi_{nl} = \frac{\Pi_0}{\sqrt{l(l+1)}} (n + \epsilon), \tag{1.5}$$

where n and l are as before, ϵ is a small constant, and Π_0 is given by

$$\Pi_0 = 2\pi^2 \left(\int \frac{N}{r} dr \right)^{-1} , \tag{1.6}$$

where N is the buoyancy frequency, and the integral is performed over the cavity in which the g mode is propagating. Deviations of the period spacing in g modes is a

diagnostic for stratification in stars as steep gradients in the mean molecular weight trap g modes. This relation is particularly useful when considering the γ Dor pulsators (see section 1.4.1), as their high-order pulsations allow the asymptotic relations to be used (Smeyers & Moya 2007), i.e. as $l/n \to 0$. These asymptotic relations can be used with the assumption that modes are linear, non-interacting (i.e. not perturbed by p modes, or *vice versa*), adiabatic, the pulsation cavity is uniformly mixed, and the star is spherically symmetric. It is assumed that the wavelength is much smaller than the pressure and density scale heights, so their derivatives can be neglected (although unphysical near the stellar surface).

1.4 Pulsations in A-type Stars

The A-type stars show a range of pulsational behaviours as these stars lie in the region of the HRD where the instability strip crosses the MS (cf. Figure 1.1). The stars in this region show both pressure and gravity modes across a wide range of frequencies.

Below is an in depth discussion on the MS, classically A-type, pulsators; the γ Dor, δ Sct and roAp variables. As the Cepheid variables are evolved stars, they shall not be discussed here, nor shall the solar-like stars. For a review of the the solar-like pulsators the reader is referred to Chaplin & Miglio (2013). There is no recent comprehensive review of the Cepheids, however Neilson & Ignace (2014) and Ripepi et al. (2015), and references therein, provide recent discussions on these stars.

1.4.1 γ Doradus Stars

The pulsation driving mechanism in the γ Dor stars is thought to be *convective blocking* at the base of the convective envelope, where the temperature is between 200 000 and 480 000 K and the change between radiative energy transfer and convection is abrupt (Guzik et al. 2000; Dupret et al. 2005). In modelling of these stars, changes in the convective luminosity are set to zero (frozen-in convection; Pesnell 1990; Guzik et al.

2000) in which case the convection does not transfer the additional luminosity during the pulsation cycle and is blocked at the base of the convection zone, thus driving the pulsations. This is only the case when the *local* convective time-scale is comparable to, or greater than, the pulsation period.

These stars are an interesting class of pulsator as they lie in the same region as p mode solar-like oscillators on the HRD. The presence of both the g and p modes in a single star allows for a fuller understanding of the stellar interior as the γ Dor g modes probe the core of the star, with the p modes originating much higher in the star (e.g. Miglio et al. 2008).

Ground-based observations of γ Dor stars are problematic as their intrinsic pulsation frequencies are close to 1 d periods, causing confusion between true pulsations and $1\,\mathrm{d}^{-1}$ aliasing. However, space-based observations with *Kepler* and *CoRoT* have confirmed many more detections (e.g. Uytterhoeven et al. 2011; Balona et al. 2011c; Hareter 2012).

The instability strip of the γ Dor stars is towards the red-edge of the classical instability strip. Figure 1.8 shows the instability strip for the γ Dor stars (red and blue dashed lines) as calculated by Dupret et al. (2005).

1.4.2 δ Scuti Stars

The pulsations in δ Sct stars are driven in the second ionisation zone of He, where changes in opacity act to regulate the flow of radiation. This zone occurs at a temperature of about 50 000 K (Chevalier 1971). The non-radial pulsations observed photometrically are low-degree ($l \leq 3$) and low-order ($n = 0 - 7$) modes (Breger 2000) whereas spectroscopic observations find high-degree ($l \sim 20$) modes (e.g. τ Peg; Kennelly et al. 1998).

As previously mentioned, the pulsations in the δ Sct stars are of the p mode type. However, recently Antoci et al. (2011) claimed to have found stochastically driven oscillations in the *Kepler* observations of HD 187547, as predicted by theory (Houdek et al. 1999; Samadi, Goupil & Houdek 2002). Later re-analysis with a longer data set

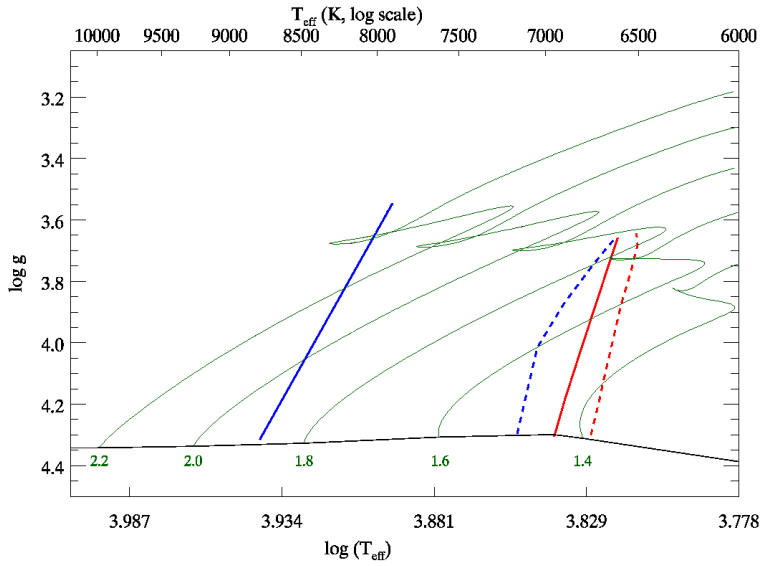

Figure 1.8: The red and blue edges of the γ Dor, dashed lines, and the δ Sct, solid lines, instability strips. Also included is the ZAMS (black line) and evolutionary tracks (green lines) from time-dependent convection models for a range of masses. Adapted from Murphy et al. (2015).

however has found this is not necessarily the case, but rather turbulent pressure in the surface convection zones (Antoci et al. 2014) may explain the observations, similar to the theory of Cunha et al. (2013) for the roAp stars (see section 1.4.3). If the presence of stochastically excited modes can be confirmed in the δ Sct stars, their occurrence with the opacity driven pulsations will allow for a mode identification of both oscillation types, and thus allow for deep modelling of the star. Such a task will result in the constraining of the overshooting parameter, $\alpha_{\rm OV}$, which is the main influence of a MS star's life-time with a convective core (Antoci et al. 2013).

Since the launch of the *Kepler* telescope, many studies have been conducted on δ Sct stars (e.g. Balona & Dziembowski 2011; Uytterhoeven et al. 2011; Balona 2014a; Bradley et al. 2015). That are two main points which can be drawn from these studies: that many stars lie outside the boundaries of the δ Sct instability strip, and that a hybrid between δ Sct and γ Dor pulsations is a common phenomenon in these stars.

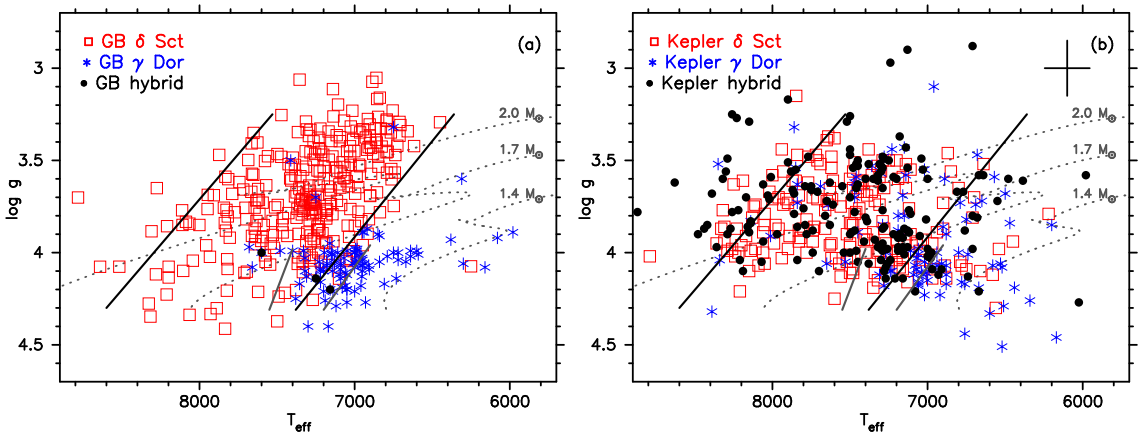

Figure 1.9: A comparison between (a) ground-based and (b) *Kepler* observations of δ Sct, γ Dor and hybrid pulsators. The red open squares are the δ Sct stars, the blue asterisks are the γ Dor stars and the filled circles are hybrid stars. The *Kepler* observations have widened the regions in which all stars are found. From Uytterhoeven et al. (2011).

Uytterhoeven et al. (2011) show a comparison between the ground-based observations and *Kepler* observations of δ Sct stars, and how they compare to the instability strip as calculated by Rodríguez & Breger (2001) (Figure 1.9). They show that many *Kepler* targets lie beyond the red-edge of the strip, even when the errors are taken into account. This was also the case for Bradley et al. (2015) and Balona & Dziembowski (2011).

As can be seen in Figure 1.8, the γ Dor and δ Sct instability strips have a region in common. It is therefore expected that there will be stars which exhibit both types of pulsation, the so-called hybrid stars. Previous to *Kepler* observations, only a small number of these stars were known (e.g. Henry & Fekel 2005; Uytterhoeven et al. 2008; Handler 2009), however hundreds have now been identified. They do not, as one would expect, lie solely in the over-lapping regions of the instability strip, or indeed are confined to either strip (however this could be a result of stellar parameter uncertainties). The wide spread of these hybrid stars though is questionable, as the convective flux blocking mechanism which drives the γ Dor pulsations is not effective at temperatures greater than about 480 000 K at the base of the convective zone (Guzik

et al. 2000). However, there is suggestion that chemical peculiarities may influence the hybridity of these stars (Uytterhoeven et al. 2011). Whatever the cause, the hybrid nature of these stars allows for a deeper analysis of the internal structure as the g modes probe deeper into the stellar interiors, whereas the p modes are confined to the surface layers (Grigahcène et al. 2010). It was the presence of these two mechanisms which allowed Kurtz et al. (2014) and Saio et al. (2015) to probe the rotation velocity profile of the A- and F-type stars, as previously discussed.

1.4.3 roAp Stars

The rapidly oscillating Ap (roAp) stars can be found at the base of the classical instability strip on the HRD, between the ZAMS and TAMS in luminosity. Since their first observation over 30 yr ago (Kurtz 1982), about 60 stars of this type have been discovered. The known roAp stars are presented in Table A.1, with information from the literature.

Most targets have been found through ground-based surveys of known Ap stars (e.g. Martinez, Kurtz & Kauffmann 1991; Martinez & Kurtz 1994), with recent additions from all-sky surveys (Holdsworth et al. 2014b) and space-based observations by *Kepler* (e.g. Kurtz et al. 2011; Balona et al. 2011a; Holdsworth et al. 2014c). Spectroscopy has also proved useful in the discovery of these stars, through observations of line profile variations (Elkin et al. 2010a; Elkin et al. 2011; Kochukhov et al. 2013).

Many modes of pulsation are nearly aligned with the magnetic axis rather than the rotational axis of the star, leading to the oblique pulsator model of Kurtz (1982) (cf. Figure 1.5). Such an orientation allows the pulsation modes to be viewed from different aspects over the stellar rotational cycle. The observations of roAp stars provide the best laboratory, beyond the Sun, to study the interactions between strong global magnetic fields and stellar pulsations. Although pulsating in roughly the same frequency range, the driving mechanisms differ between the Sun and the roAp stars: the κ-mechanism acting on the hydrogen ionisation zone is thought to be the driving force of the roAp high-overtone p mode pulsations, although recent models by Cunha et al. (2013) suggest

another excitation mechanism may be at work for a subset of roAp stars, similar to the solar pulsations which are stochastically driven in the convection zone.

To date there have been no roAp stars found in close binary systems. There are, however, three candidates which are strongly suspected of being in visual binary systems (i.e. HR 3831, γ Equ and α Cir). Schöller et al. (2012) conducted a study of known roAp stars in the search for companions using near-infrared imaging. They found six of their target roAp stars showed signs of companions, two of which were already known. However, from photometric data alone it is not possible to categorically determine whether the companions and the targets are gravitationally bound. Instead they calculate the probability of a chance projection, with their least certain companion having a chance projection probability of less than 2×10^{-3}. Regardless of whether they are gravitationally bound, the separation of visual binary stars means that stellar physics governing the individual stars is not affected. It is only in close binary systems that the components influence each other.

Photometric observations of roAp stars are best conducted through $B-$band filters, as this is the passband which the greatest amplitude of pulsations are observed (Medupe & Kurtz 1998), with amplitudes in the $B-$band up to a factor of 3 greater than the $R-$band. The pulsation amplitudes of roAp stars decreases rapidly with increasing wavelength (Weiss & Schneider 1984), which was once thought to be a result of limb darkening (Matthews et al. 1996). However, Medupe & Kurtz (1998) showed that limb darkening cannot account for the lack of amplitude at longer wavelengths, but rather a combination of this, the temperature structure and change in temperature of the pulsation period, and the fact that the continuum opacity increased with increasing wavelength (Kurtz & Medupe 1996).

Some roAp stars show highly stable pulsational frequencies, amplitudes and phases over time spans of years. Others have variable frequencies. Kurtz et al. (1994) and Kurtz et al. (1997) discussed frequency variability for the roAp star HR 3831 with ground-based data spanning 16 yr, albeit with large gaps through the years. While they originally suggested that the frequency variability could be cyclic, that was not supported by the later work. Similar frequency variability was reported for another

roAp star; Martinez, Kurtz & van Wyk (1994) discuss HD 12932 and identify seven further roAp stars for which frequency variability was known at that time.

More recently, Balona (2013b) shows an amplitude spectrum for KIC 10483436 where the largest amplitude pulsation mode has a frequency quintuplet, split by the rotation frequency ($P_{\rm rot} = 4.3\,{\rm d}$), caused by oblique pulsation. For the entire *Kepler* data set the amplitude spectrum can be described as 'ragged'; that is, the peaks of the quintuplet are composed of many closely spaced peaks in the amplitude spectrum. While this is typical for stochastically excited pulsators, stochastic excitation is not likely for roAp stars as there is no substantial convection zone near the surface of the star in which the modes can be excited to the amplitudes seen in the roAp stars. Thus the multiplicity of closely spaced peaks that make up each component of the oblique pulsator quintuplet must arise because of frequency, amplitude and/or phase variations over the time-span of the data set.

One source of these 'ragged' peaks may be binarity. Shibahashi & Kurtz (2012) and Murphy et al. (2014) introduce analysis of *Kepler* light curves in terms of light-time delays across a binary orbit for pulsating stars. The Frequency Modulation (FM; Shibahashi & Kurtz 2012) and Phase Modulation (PM; Murphy et al. 2014) techniques take the time delays, and as such frequency and phase variations, to determine the parameters of the binary system without the need for spectroscopy. These are excellent tools in the study of binary stars, as full sets of parameters, including the inclination i, the eccentricity e, the component masses, the mass function and ultimately radial velocities, can be extracted from photometry alone.

Further to the *Kepler* observations of variability, Kurtz et al. (2011) have now shown that multiple pulsation axes exist in a single roAp star, KIC 10195926. The oblique pulsator model suggests that the pulsation axis and rotation axis are aligned (Kurtz 1982). However, observations of α Cir have shown that the surface spots are not aligned with the pulsation axis (Bruntt et al. 2009). In KIC 10195926, Kurtz et al. (2011) show that the two pulsation modes which are detected are aligned to two separate spots. A revised version of the oblique pulsator model by Bigot & Dziembowski (2002) and Bigot & Kurtz (2011) supports this hypothesis. To rule out other explana-

tions, such as those presented by Cunha & Gough (2000) and Saio & Gautschy (2004) where modes of consecutive radial order are affected differently by the magnetic field, analysis of further *Kepler* Short Cadence observations, of this and other stars, need to be conducted.

With the addition now of highly precise space-based observations, the roAp stars are becoming ever more complicated to understand. With relatively few objects of this class to study, further targets need identifying to aid the understanding of this class of A-type pulsator as a whole.

1.5 Variability Detection Techniques

Many types of stellar variability are periodic in nature, at least on short time-scales, and thus can be extracted from a light curve via time-series analysis. However, such methods often require uniformly sampled, uninterrupted data, a luxury that astronomers rarely see. While it is possible to interpolate between data this method is not advisable, as observing gaps are often larger than data blocks, certainly for single site campaigns, and it is likely that errors will be introduced to the data. Discussed are various detection techniques.

1.5.1 Fourier Transforms

Fourier analysis of a data set involves fitting a harmonic model to the data. Such a technique works well then the variation in such that it can be described by combinations of sine/cosine functions. The output of a Fourier Transform (FT) is referred to as a periodogram. The fundamental FT has the form

$$F(\nu) \equiv \int_{-\infty}^{+\infty} x(t) \exp(2\pi \mathbf{i} \nu t) dt. \tag{1.7}$$

For this to be true, the function $x(t)$ must be continuous and infinite. In performing a FT we move from the *time domain* to the *frequency domain*. In reality, we are unable to

work with infinite continuous time series, thus the Discrete Fourier Transform (DFT) described by Deeming (1975) must be considered.

Fourier analysis produces a periodogram with power peaks at $\pm\nu_1$, $\pm\nu_2$, ..., etc. Application of a DFT results in frequencies $F_N(\nu)$ differing from $F(\nu)$ due to frequency interference, which is described by the *spectral window* such that

$$\frac{F_N(\nu)}{N} = F(\nu) * W_N(\nu), \tag{1.8}$$

where $W_N(\nu)$ is defined as

$$W_N(\nu) = \frac{1}{N}\sum_{i=1}^{N} \exp(2\pi \mathbf{i}\nu t_i). \tag{1.9}$$

$W_N(\nu)$ is solely calculated on the data spacings and is not effected by the measurement x. Besides a peaks at $\nu = 0$ a typical spectral window will show peaks at frequencies defined by the peculiarities in data spacing (Deeming 1975). The spectral window is key in determining if a peak in $F_N(\nu)$ is real or an artefact of data sampling. Single-site ground-based observations suffer from one day gaps in the observations which manifests itself as peaks in the spectral window at frequencies of $\nu_A = n\,\mathrm{d}^{-1}$ where n is from 1 to a large number. As a result, the periodogram shows sidelobes, or *aliases*, to a true peak at $\nu = \nu_{peak} \pm \nu_A$.

A detected peak in $F_N(\nu)$ must be compared to the spectral window to determine if the peak is real, especially if the peak falls on a frequency which suffers strong aliasing effects. In such cases, the shape of the peak is important in establishing its authenticity. Unequally sampled data can result in frequency shifts and amplitude variations in a DFT, as such efforts have been made to improve upon this method and provide a more reliable frequency search for unevenly sampled data. The window function however cannot distinguish between peaks which are due to physical variations such as airmass variations or instrumental artefacts, only peaks due to sampling aliases.

1.5.2 Lomb-Scargle Periodogram

Originally devised by Lomb (1976) and later refined by Scargle (1982), the Lomb-Scargle periodogram is widely used in stellar variability studies. This method, like the DFT, is applicable to unevenly sampled data. For N observations such that $(t_i, x(t_i))$ then the periodogram is calculated by

$$P_{LS}(\nu) = \frac{1}{2}\left\{ \frac{\left(\sum_{i=1}^{N} x(t_i)\cos[2\pi\nu(t_i-\tau)]\right)^2}{\sum_{i=1}^{N}\cos^2[2\pi\nu(t_i-\tau)]} + \frac{\left(\sum_{i=1}^{N} x(t_i)\sin[2\pi\nu(t_i-\tau)]\right)^2}{\sum_{i=1}^{N}\sin^2[2\pi\nu(t_i-\tau)]} \right\} \tag{1.10}$$

where τ is defined by

$$\tan(4\pi\nu\tau) = \frac{\sum_{i=1}^{N}\sin(4\pi\nu t_i)}{\sum_{i=1}^{N}\cos(4\pi\nu t_i)}. \tag{1.11}$$

It is more convenient to work in amplitude rather than power when considering astronomical variations as these have physical meanings, therefore we convert P_{LS} to amplitude via

$$A_{LS}(\nu) = \sqrt{\frac{4P_{LS}(\nu)}{N}}. \tag{1.12}$$

The parameter τ has been introduced so that if the values of t_i are replaced by $t_i + T$, where T is an arbitrary unit of time, then the periodogram remains unchanged, a useful result when dealing with multiple data sets per object.

1.5.3 Least-Squares

The least-squares method aims at modelling a set of x_i observations at times t_i as a function of sine and cosine to obtain $x_i(\nu)$. For a single frequency search, the aim is to minimise a likelihood function by finding free fitting parameters and evaluate a given test frequency, ν. The calculated $x_i(\nu)$ is compared to the measured x_i to find the residual which is then minimised (Lomb 1976).

To apply the least-squares method to multiple peak identification, one must, at each step, *pre-whiten* the data to remove all previously identified frequencies. Such a process cycle for the detection of multiple frequencies can be computationally costly.

This method is that used in the PERIOD04 program (Lenz & Breger 2005). In its basic form, PERIOD04 enables a user to perform quick frequency analysis on a set of data. Folded light curves of the object can be made, with the option to *pre-whiten* the data to extract further frequencies beyond the principle. Use of this program will enable analysis of small data sets, and for latter confirmation of frequencies, but is unsuitable for large data sets as human operation is required. PERIOD04 provides a useful visual and interactive interface for the analysis of time-series data. The code is well documented and often used in scientific publications (e.g. Díaz-Fraile, Rodríguez & Amado 2014; Maceroni et al. 2014), implying it is a reliable piece of software.

Another code that could be used is the SIGSPEC code of Reegen (2007). This code can be fully automated to pre-whiten a number of frequencies, or to a particular significance level. Although useful to extract every significant peak in the data, the code does not allow visualisation which can be key in identifying whether a peak is real or not.

1.5.4 Other Methods

The *String Length* or SL method was first introduced by Lafler & Kinman (1965) and later refined by Clarke (2002). The method uses a grid of search periods, $P_1, \Delta P, P_2$, which are applied to the original data. The phase of the data are then calculated, the original data is re-ordered and examined across the phase range $[0-1]$. The SL method is computationally intensive for large data sets and produces many low-frequency false peaks at the subharmonics of the true frequencies and their aliases – a general property of phase analysis methods. However, the method is useful in detecting non-sinusoidal variations with large amplitudes such as some binary systems. An extension of the SL method is the *Rope Length* method (Clarke 2002) which is concerned with the analysis of multivariate data such as multi-wavelength simultaneous observations, and operates in a similar way to the SL method.

The *Phase Dispersion Minimisation* or PDM technique was devised by Stellingwerf (1978) and aims to minimise the variance of the data with respect to the mean light

curve. A trial period, Π, is compared to a sub-sample of the data with the variance calculated and compared to the variance of the entire data set. If Π is a true period then a minima is seen in the periodogram. This would also be the case if two (or more) periods in the data were phased, producing many minima in the periodogram causing confusion between which minima to choose. The PDM technique simultaneously finds the best period and calculates a least-squares fit to the data. However, Stellingwerf (1978) comments that this method is well suited for small data sets with low levels of noise. It is also advised that the PDM technique first be used in a 'rough cut' regime with large bin sizes to identify the principle frequencies, with a second higher resolution pass over the periods of interest.

1.5.5 Chosen Method

For the work presented in this thesis, the Lomb-Scargle method of Press & Rybicki (1989) has been used to search for stellar variability in SuperWASP data. Use of the Lomb-Scargle periodogram is common practice in this field, suggesting its versatility and performance. There exists an optimised routine, FASPER (Press et al. 1992), coded in Fortran 77 which computes the periodogram. Use of this code has been proven to be effective in many variability studies (e.g. Durán-Rojas et al. 2009; Barclay et al. 2011; Smalley et al. 2011). Also included in the FASPER routine is a calculation of the false alarm probability (FAP; Horne & Baliunas 1986), the probability that a peak is appearing by chance in the periodogram, assuming that the data are pure noise in the normalised periodogram. This value takes into account any oversampling of the periodogram.

There exists a sensible upper limit to which to search for a frequency in a set of data. This frequency is dictated by the sampling of the data and is named the *Nyquist frequency*, ν_{Ny}. For evenly sampled data, $\nu_{Ny} = 1/2\Delta t$ where Δt is the sampling step. However, for unevenly sampled data, such as WASP, the calculation of the Nyquist becomes more complicated. It is suggested by Eyer & Bartholdi (1999) that one should take the Nyquist frequency to be $\nu_{Ny} = 1/2p$, where p is the greatest common divisor for

all differences consecutive observation times. This is not a hard and fast rule however, especially in the case for WASP data due to the observing strategy (see section 1.6). In essence, the WASP data do not have a definite ν_{Ny} due to the pseudo-random sampling of the pulsation signature leading to a comprehensive phase coverage, however caution must be exercised in the very high-frequency domain.

1.6 The WASP Project

The Wide Angle Search for Planets (WASP) project was established in 2000. The project is a two-site campaign in the search for transiting exoplanets. The first observatory, WASP-N, is located at the Observatorio del Roque de los Muchachos on La Palma and achieved first light in November 2003. The second instrument, WASP-S, is located at the Sutherland Station of the South African Astronomical Observatory (SAAO) and achieved first light in December 2005. The SuperWASP cameras observe a large portion of the sky with exception to the galactic disk due to the high-density of stars (Figure 1.10).

Each instrument consists of eight 200 mm, f/1.8 Canon telephoto lenses, mounted in a 2×4 configuration, backed by Andor CCDs of 2048×2048 pixels observing $\sim 61\,\mathrm{deg}^2$ each through broadband filters covering a wavelength range of $4000 - 7000$ Å (Pollacco et al. 2006). This set-up enables simultaneous observations of up to 8 fields with a pixel size of $13.7''$. The CCDs operate at $-50°$C, with a resulting dark current of $\sim 72\,e\,\mathrm{pixel}^{-1}\,\mathrm{hr}^{-1}$. The gain for the cameras[1] is $1.4\,e^-$, with a readout noise of about $10\,e$ per frame. After all overheads are taken into account, the dead-time between frames is less than 5 s (Pollacco et al. 2006).

The camera mount has a maximum slew speed of $10°\,\mathrm{s}^{-1}$ and a tracking accuracy of better than $0\farcs01\,\mathrm{s}^{-1}$. Such a configuration allows stable observations of the entire observable sky typically every 40 min, with typical cadences of around 10 min (Pollacco

[1] From the Andor CCD specification document.

et al. 2006). The observing strategy is to take two consecutive 30 s integrations at each of the pointings, before automatically changing fields from a predetermined list.

The images collected are passed through a custom-built reduction pipeline, where the data are corrected for primary and secondary extinction, the instrumental colour response and the system zero-point. The atmospheric extinction correction uses a network of stars with a known $(B - V)$ colour to determine the extinction terms, which are then applied to all extracted stars using an assumed colour of G-type stars. This process results in a 'WASP V' magnitude which is comparable to the Tycho-2 V_t passband. The data are also corrected for systematic errors using the SYSREM algorithm of Tamuz, Mazeh & Zucker (2005). Aperture photometry is performed at stellar positions provided by the USNO-B1.0 input catalogue (Monet et al. 2003). Stars brighter than $\sim 15^{th}$ magnitude are extracted and provided with a unique WASP ID of the format 1SWASPJ$hhmmss.ss \pm ddmmss.s$. For stars brighter than $V = 11.5$ WASP reaches photometric precision of 1 per cent and even better, 0.004 mag, for stars

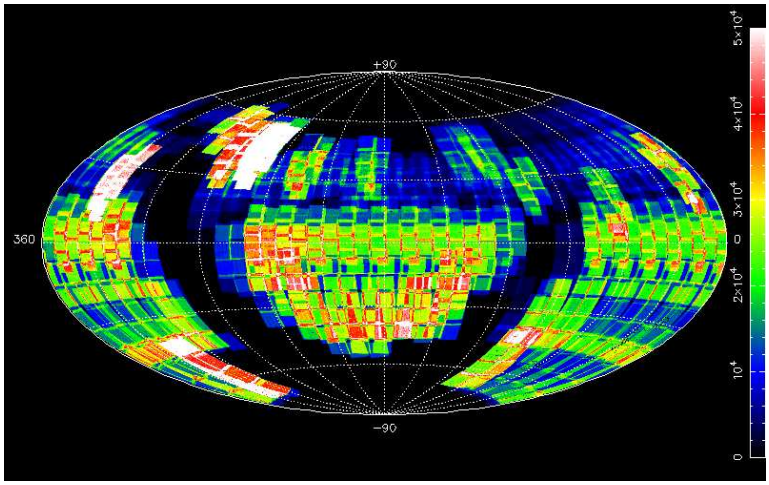

Figure 1.10: The extent of the WASP sky coverage as of 2014 November 20. The colour represents the average number of data points per star. Black regions show regions of sky where no data has been collected, principally the poles and galactic plane. White areas show the regions of intense observations, notably the *Kepler* field and the Magellanic clouds. Figure courtesy of WASP Consortium.

brighter than $V = 9.4$ (Pollacco et al. 2006). Data are stored in FITS format with labels of the observed field, camera and date of observation. Such a configuration and extended time-base allows the extraction of multiple light curves for each object based on either date, field or camera. As of 2015 Feb 24 there are over 428 billion data points in the archive covering over 31 million unique objects. With such a large database of objects it is possible to search for a wide variety of stellar variability.

1.6.1 Sources of Noise in WASP Data

WASP data is susceptible to large amounts of noise, especially with regards to the types of stars for which the reduction pipeline is not optimised for. Present in the data is uncorrelated 'white noise' which affects a periodogram uniformly across all frequencies and is mainly a result of photon statistics and sky background counts. The data also contains correlated 'red noise' which cannot be easily removed. The 'red noise' originates from trends in the changing airmass, changes in the atmospheric conditions, vignetting and flat-field errors. Finally, there is also stellar 'noise' in the data; low-frequency changes in stellar activity such as flare or spots produce noise in the FT of a light curve, as well as granulation on the stellar surface. Oscillations can also be classed as a source of noise, especially for studies in the search for planet transits. However it is the oscillations which are the signal here, rather than the noise.

In the WASP data, the correlated red noise combines with the white to produce 'pink noise', the most likely source of noise in WASP data (Smith et al. 2006). Smith et al. (2006) found that for bright stars ($V < 9.5$) there remains a noise level of ~ 3 mmag on times scales of 2.5 h after pipeline reductions. The study was conduced using unfiltered data, and since then broadband filters have been installed which may change the noise levels observed. The motivation for their study was concerned with the detection of exoplanets via the transit method, hence their choice of just 2.5 h of data. However, the more data included in the calculation of a periodogram reduces the final noise level, as will be the case for stellar variability studies here.

Noise also originates from variations in atmospheric transparency, scintillation

and seeing. Atmospheric variations operate at frequencies less than $90\,\mathrm{d}^{-1}$ and are more prominent at low frequencies, whereas scintillation is the dominant source of photometric noise above this frequency (Mary 2006). Scintillation originates in variations of atmospheric cells (of the order 10s of cm) resulting in different refraction degrees. The level of scintillation noise decreases with increasing wavelength and zenith angle (Dravins et al. 1997a; Dravins et al. 1997b).

Photon statistics are also present as a source of photometric error. WASP observations consist of 30 s integrations, which for faint objects can dramatically reduce the signal-to-noise ratio which goes as $\sqrt{N}$. This is seen in the photometric precision achieved by WASP, presented above. For example, for photon-dominated noise, the S/N for a light curve of an $m = 8$ magnitude star is about 30, whereas for an $m = 14$ magnitude star it is about 2, calculated using the WASP conversion between flux and magnitude, and a gain of $1.4\,e^-$ per count.

Aliasing arises from observing gaps in the data, as described in section 1.5. WASP data show strong one-day aliasing in a periodogram. For low-frequency peaks ($< 5\,\mathrm{d}^{-1}$) distinguishing between a true peak falling at an integer frequency and an alias becomes almost impossible. A careful analysis of the light curve, periodogram and window function are needed to identify a true pulsation peak. The right panel in Figure 1.11 shows the periodogram for the WASP object J0206 (HD 12932), a known roAp star. It is clear that a comb of peaks occur at integer frequencies from the true ν_{osc} at $124.14\,\mathrm{d}^{-1}$. The left panel of Figure 1.11 shows a periodogram of J0410 (HD 26400), a multi-frequency pulsator. The presence of the comb feature here can lead to confusion over the number of pulsation frequencies that are present. After an iterative process of pre-whitening, 4 frequencies are extracted.

This aliasing effect, however, can aid the detection of peaks in WASP data, especially at higher frequencies where there is less noise. True peaks in the periodogram are surrounded by $1\,\mathrm{d}^{-1}$ sidelobes decreasing in amplitude. This feature is utilised when distinguishing between true peaks and spurious peaks.

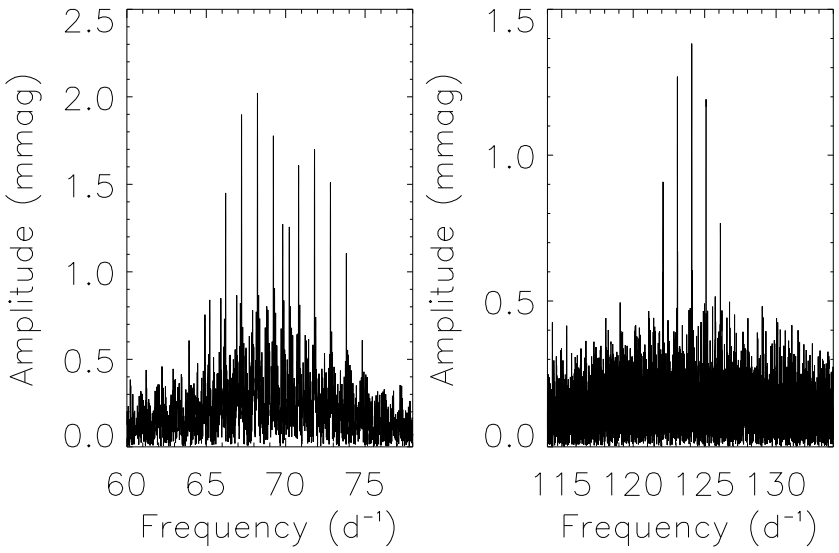

Figure 1.11: An example of aliasing effects on the periodogram. The left panel shows the periodogram of a multi-frequency pulsator, with 4 detected frequencies. The right panel shows the periodogram of a single frequency pulsator. As can be seen, the aliasing effects lie at $\pm n\,\mathrm{d}^{-1}$ from the true ν_{osc}. Before a process of iterative pre-whitening is performed, it can be hard to determine the number of pulsation frequencies present, especially in the left panel.

1.7 Thesis Overview

The next Chapter conducts an investigation into the detection limits of the SuperWASP data using results of the *Kepler* space telescope as a standard comparison. Chapter 3 discuss the methods of the archive search for pulsating A-type stars, with the results of Chapter 2 in mind. An overview of the results is then presented in Chapter 4. Chapter 5 presents a spectroscopic view of the A-type stars, and the classification techniques used to differentiate between normal and chemically peculiar stars. Chapter 6 discusses in detail several newly discovered pulsating stars on an individual basis. Chapter 7 presents an in depth analysis of a roAp star, discovered by SuperWASP, that has been observed by *Kepler* for the duration of the primary mission. Finally, Chapter 8 presents the conclusions of the thesis and describes the future work which it offers.

2 WASP Detection Limits – A *Kepler*-WASP Comparison

2.1 Introduction

Before any variability study can be undertaken with a data set, the instrumental characteristics of the data must be understood to ensure that reliable and useful results are produced by the study. In the context of variability studies with the WASP data, one requires a large test sample of stars for which the variability is already well characterised. To understand the capabilities of the WASP data, a subsection of the highly precise, space-based, observations by the *Kepler* satellite is used for comparison with WASP observations.

The *Kepler* mission, launched in March 2009, observed over 150 000 stars throughout its 4 yr life span. The telescope consisted of an array of 42 CCDs covering 115 $\deg^2$ of sky resulting in a pixel size of 3.98″, with observations being taken through a broad passband filter covering $4230 - 8970$Å (Koch et al. 2010), which is different from the WASP passband (Figure 2.1). The CCDs are read-out every three seconds to avoid pixel saturation, and are summed to the appropriate cadence. Each target in the *Kepler* field-of-view (FoV) has a unique identifier defined by the *Kepler* Input Catalogue (KIC).

The spacecraft was in a heliocentric orbit with a fixed pointing. As a result, every ∼90 d, the spacecraft paused observations and executed a 90° roll to keep the solar panels pointing in the direction of the Sun. During these rolls, the data were sent back to the ground stations to minimise interruptions to data collection. These regular gaps in the data allowed for an easy naming convention of the data: the data collected between each roll was assigned a Quarter, denoted QXX (from Q00, the 10 d commissioning run, to Q17, the last, not-complete, block).

The observations were taken in two cadence modes – the Long Cadence (LC) mode of 29.42 min was used for the majority of stars, with 512 stars observed in the

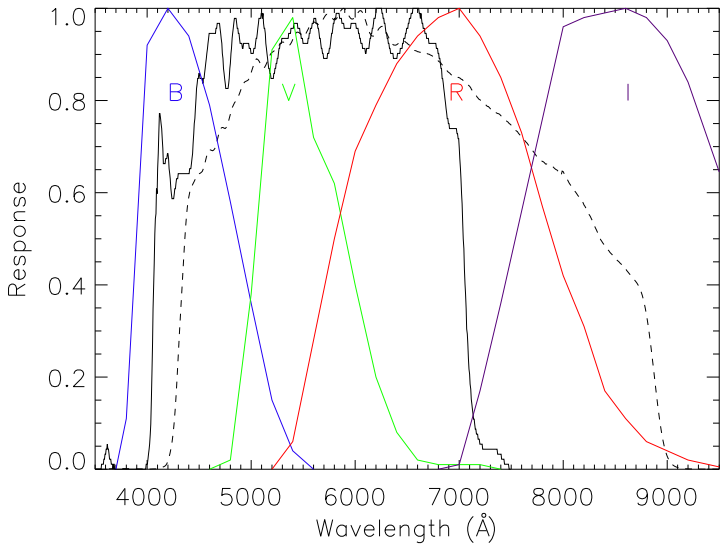

Figure 2.1: The normalised filter response functions of the WASP cameras (solid black line) compared to that of the *Kepler* instrument (dashed black line; *Kepler* Instrument Handbook), and the Johnson filters (coloured lines; Johnson & Morgan 1953).

Short Cadence (SC) mode of 58.85 s per Quarter (Gilliland et al. 2010). The Q01 observations achieved a duty cycle of 99.7 per cent (Gilliland et al. 2010). Not all Quarters were able to achieve such an impressive duty cycle: safe modes occur unexpectedly throughout the life-time of the craft and lead to further data gaps mid-way though Quarters.

The primary science goal of the *Kepler* mission was to discover ~ 50 Earth-like planets orbiting solar-like stars. Such a target requires photometric precision to 84 parts per million (Borucki et al. 2010; Koch et al. 2010). As a result, the instrument produced a wealth of high-cadence data at μmag precision; perfect conditions to search for stellar variability. As an example, early in the *Kepler* mission, Debosscher et al. (2011) conducted a full variability study on over 150 000 stars that had been observed during Q01 in, mostly, LC mode. They published their results as an online catalogue

accessible via the VizieR tool[1], detailing the first, second and third detected frequencies with corresponding amplitudes and significance.

The results of Debosscher et al. (2011) allow for the selection of a variety of variable stars for which comparison can be made between the WASP and *Kepler* periodograms, and thus determine reliable limits for the WASP data.

2.2 Initial Investigation

An initial selection of *Kepler* targets was made using the catalogue of Debosscher et al. (2011). The purpose of this smaller study is to provide an initial insight into the data characteristics of WASP observations compared to *Kepler*. Processing of a small number of targets allows for a more detailed study of light curves, periodograms and the final results. Targets were selected through a query requiring targets with an amplitude above 0.05 mmag. A selection of 50 targets was then made from the returned list to include a wide range of variability frequencies and amplitudes, however, with focus applied to stars classed a δ Scuti pulsators. The corresponding WASP target files were downloaded from the database and their light curves extracted. There existed no data for three targets in the WASP archive, resulting in a sample of 47. Due to the nature of the WASP data several light curves are available for each object resulting in a total of 209 data files. As well as the photometric data, the stellar position on the CCD and the sky count were also extracted. All WASP light curves were then analysed using the Period04 program (Lenz & Breger 2005) to extract the principle frequency and amplitude.

The results obtained for the WASP data were seen to be noisy and yielded few results. The analysis of a typical WASP light curve (Figure 2.2 top left upper panel) suggested that the outlying points strongly influence the resulting periodogram (Figure 2.2 top left lower panel), which shows high-amplitude low-frequency noise and a

[1] http://cdsarc.u-strasbg.fr/viz-bin/qcat?J/A+A/529/A89

high 'Fourier grass' level – the approximate background level of the periodogram which resembles mown grass – at higher frequencies. To remove the outliers, but retain signal, a resistant mean algorithm (Huber 1981) was tested with a variety of sigma cut values. The resistant mean trims outliers from the data using the median and median absolute deviation. The resistant mean, a form of robust statistics, is a very good method for the removal of outliers in the WASP data. The use of normal sigma clipping about the mean or median will result in outliers still being present in the final data. The absolute deviation is calculated as

$$\mathrm{ADev}(x_1 \ldots x_N) = \sum_{i=1}^{N} |x_i - x_{\mathrm{med}}| \ . \tag{2.1}$$

An observed value is then compared to the median of ADev value with a cut-off value, such that:

$$\mathrm{cutoff} = \sigma \times \mathrm{ADev}_{\mathrm{med}} \, , \tag{2.2}$$

and defined as 'good' if

$$\mathrm{ADev} \leq \mathrm{cutoff} \, . \tag{2.3}$$

In performing this step, significant outliers are removed from the light curve. A series of trial sigma values were tested between 2 and 6 to determine the most effective cut-off level. It was found that to best remove major outliers from the data, a sigma value of 4.0 was required. A value lower than this removed signal from the data, with values higher leaving too many outliers in the final light curve. The resulting light curve and periodogram (Figure 2.2 top right) are consequently much cleaner, with the correct peaks being detected, when compared to the *Kepler* periodogram of the same star (Figure 2.2 bottom). Subsequently the resistant mean algorithm was incorporated into the FITS extraction routine, with the WASP light curves re-extracted and analysed with PERIOD04. Although this technique significantly reduces noise in the data, the routine can also remove evidence for eclipses in binary systems, especially those with long periods and few eclipses per WASP data set, as the median will be closer to the out-of-eclipse value. It is therefore suggested that this noise reduction method be reserved for searches of low-amplitude variability.

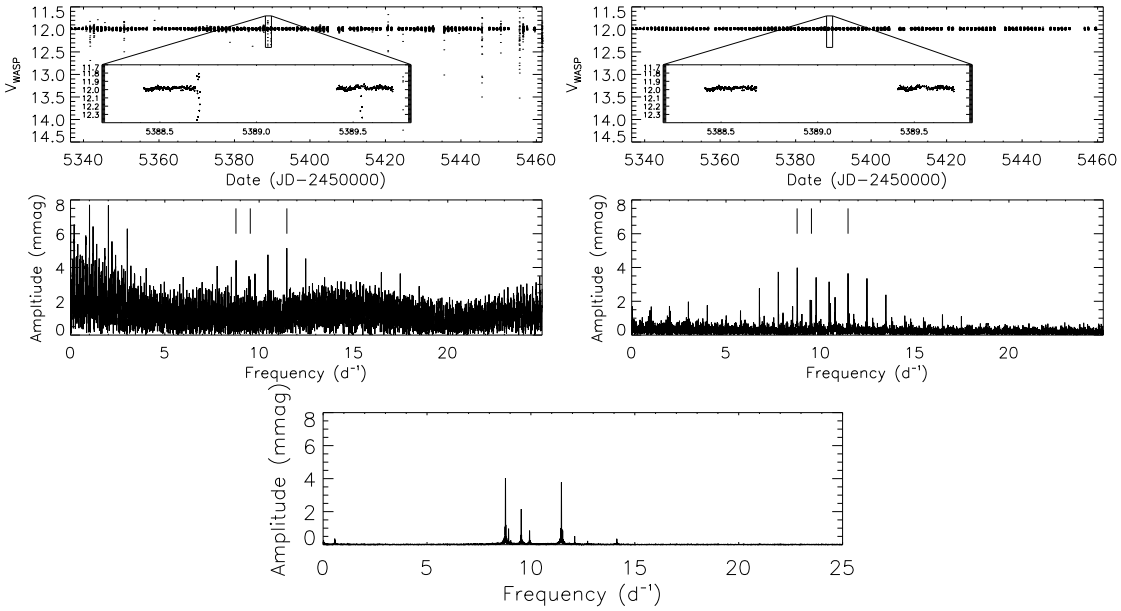

Figure 2.2: A comparison of the raw (top left), 14 659 data points, and cut (top right), 13 970 data points, light curves and corresponding periodograms for 1SWASPJ192444.63+490052.2. The much cleaner light curve, shown in the top right plot, results in a clean periodogram, with a Fourier grass level of about 0.5 mmag, which clearly shows the principal frequency at $8.77\,\mathrm{d}^{-1}$, a secondary peak at $11.47\,\mathrm{d}^{-1}$ and a third peak at $9.53\,\mathrm{d}^{-1}$. The periodogram of the raw data does not identify the principal frequency correctly due to high-amplitude, low-frequency noise; the Fourier grass level is about 2.5 mmag with the amplitudes of the peaks also much higher here. It is clear that the use of resistant mean clipping greatly enhances detection probability. The three pulsation frequencies are marked with vertical lines. The bottom panel shows the corresponding *Kepler* data of KIC 11295729 for comparison.

The extracted peaks for each object were compared between the two data sets and were said to agree if the WASP peak fell within $\pm 0.01\,\mathrm{d}^{-1}$ of the *Kepler* peak. This tolerance was chosen as it represents the typical Rayleigh criterion of a WASP season (i.e. $\Delta\nu = 1/\Delta T$, where ΔT is the season duration of 100 d). The WASP and *Kepler* Rayleigh criterion are about the same, as a *Kepler* Quarter is approximately 90 d in duration. Of the 209 WASP light curves 68 (33 per cent) were found to agree with *Kepler* observations. These 68 light curves belong to 18 unique objects (38 per cent of the total sample). Of the 18 objects, 16 were found to agree in multiple light curves with 2 agreeing in only one. One of the detections of a peak in only one light curve appears to be a spurious signal within the tolerance; with only 234 data points in the light curve and a S/N of 2.1, this peak would be disregarded if found in a large scale survey. It also shows an amplitude over 5 times that seen in the *Kepler* data which is unrealistic when considering the filter differences. The other signal found in only one data set is because there is only one data set extracted for this object.

The agreement in multiple light curves is an important point; the ground-based observations of SuperWASP lead to many artefacts in the data which can produce a spurious signal. These spurious signals may, in this case, coincide with a known-to-be real peak (as shown by the *Kepler* data). In a blind study it is not possible to distinguish between a real peak and a spurious peak, therefore multiple detections of a peak, from either the same or different seasons, will be required to determine if it is a true signature. As has been shown above, this may lead to the disregarding of some true peaks, but without *a priori* knowledge of the star, it is not sensible to include all single significant peaks.

Of the other 29 undetected objects, 12 targets have a *Kepler* amplitude of $\leq$ 1.0 mmag which puts them close to the previously assumed detection limit (Smalley et al. 2011). As well as being close to the limit, these and the other 17 objects suffer from a combination of a low number of points in their light curves and increased noise levels dictated by the sky brightness.

As previously mentioned, the CCD position of the target was also extracted from the FITS file to test if sensitivity variations, PSF variations, flat-fielding or vignetting

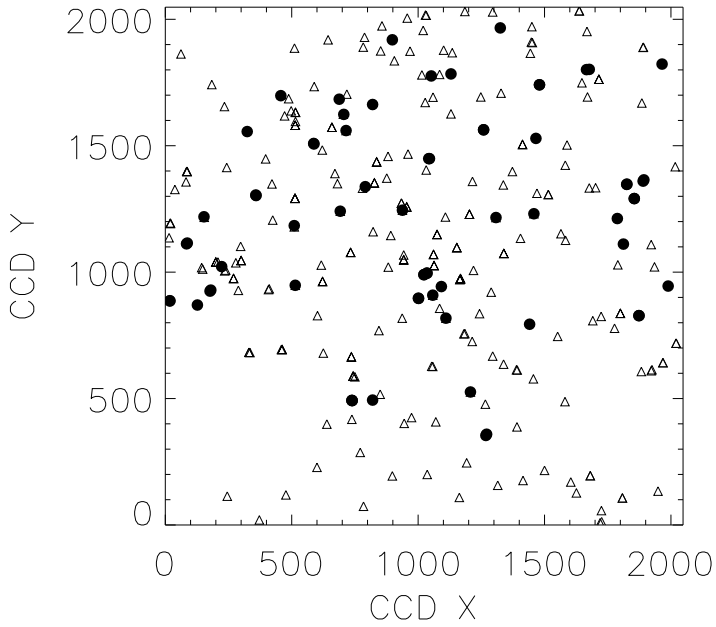

Figure 2.3: The WASP CCD position of detected (filled circles) and undetected (open triangles) peaks. There is no clear dependence on CCD position for detectability.

influenced the detectability of the known pulsations. Figure 2.3 shows the detected (filled circles) and undetected (open triangles) peaks as a function of their position on the WASP CCD. As can be seen, the sample covers a wide range of CCD position. Overall, there is no dependence on CCD position on the detectability. There is a region along the bottom of the CCD ($y \leq 300$ pixels) that is void of detections. The other three boarders, within 300 pixels of the CCD edge, show a detection rate of between $20.7 - 28.6$ per cent, however with such a small region and sample this result is not statistically significant. The exclusion of this region in the selection of targets at a later date would not be justified as the region accounts for just 10.7 per cent of the sample. The potential loss of detection far out weighs the computing time required to analyse the stars in this region.

Also extracted from the WASP FITS files was the sky count. Each point in the data set is assigned a value for the sky background count. An average value is then calculated for the entire light curve. Figure 2.4 shows the average sky count for each

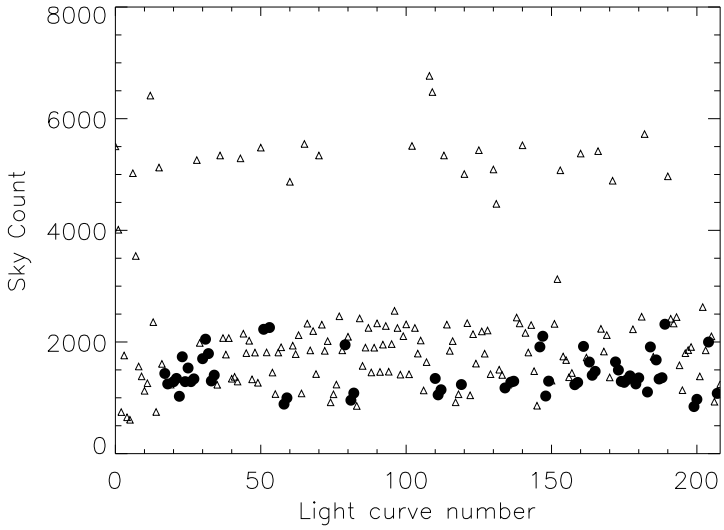

Figure 2.4: The average sky count for each of the 209 light curves. Those marked as filled circles are where detections are made. It is clear that sky counts above about 5 000 inhibit the detection of peaks; these data were collected in 2004, when no filters were used on the instrument.

of the light curves. The open triangles indicate the light curves for which a detection was not made, whereas the filled circles show the light curves which led to a correct detection. There are clearly two distinct regions in the plot: non-detections above about 4 500 counts and a mixture of detections and non-detections below 2 500 counts. It is then possible to place a conservative upper limit of the sky count of 5 000 counts: it is not expected that detections will occur above this limit.

Finally, the number of points per light curve are counted to determine if there is a lower limit on the number of points required for a detection (Figure 2.5); the number of points from which a periodogram is calculated plays an important role in the frequency resolution. Analysis of this parameter shows that about 40 per cent of the non-detected peaks have less than 1 000 data points in their light curve. Although there is one detection based on a light curve of just 234 data points, inspection of the periodogram showed that this is an under-sampled signature and appears to be a

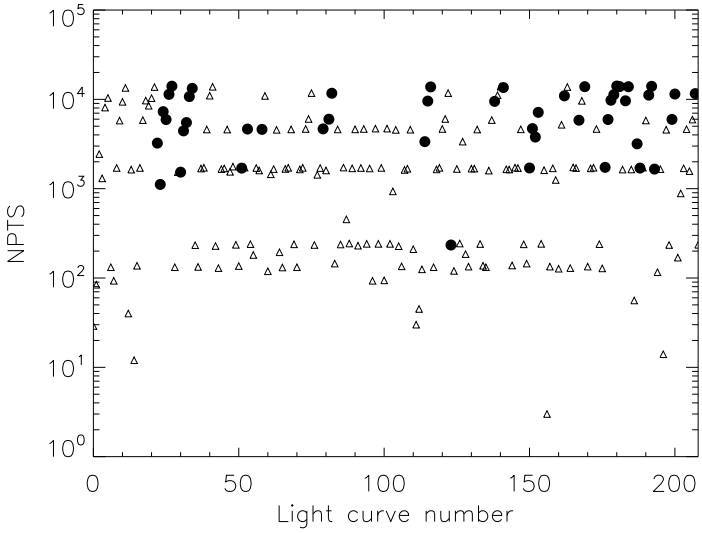

Figure 2.5: The number of points for each of the 209 light curves. Those marked as filled circles are where detections are made. An obvious lower limit on the number of points per light curve required for a detection is 1 000.

spurious peak. There are 6 other seasons of WASP data for this target which do not show the expected frequency. This reaffirms the need to have multiple detections of a frequency to make it believable.

In summary, 17 of the 47 stars were detected to vary with the same frequency as the *Kepler* observations show. No detection was made for the other 30 stars. Of these 30 stars, 11 have *Kepler* amplitudes below the expected detection limit of the WASP data, namely 1.0 mmag (Smalley et al. 2011), 4 have less that 1 000 data points in their light curves, and one has a very low-frequency signal which is lost in the WASP noise. This leaves 14 stars with unexplained non-detections.

Investigating the photometric aperture used to extract the photometry of theses stars show that there are multiple objects in the aperture which dilute the signal from the target star. This parameter will be incorporated in a wider study with a larger number of stars which are more representative of the targets in the SuperWASP archive.

2.3 A Broader Survey

To expand the initial study, a selection of 59,737 *Kepler* targets was made again using the catalogue of Debosscher et al. (2011). The only constrain applied required the amplitude of the principle frequency to be ≥ 0.1 mmag, this unrealistically low limit was to ensure that no bias effects were introduced into the sample. It is also worth remembering here that the maximum frequency sampled by Debosscher et al. (2011) is the Nyquist of the LC data, namely $24.4\,\mathrm{d}^{-1}$. However, it will be shown later, in section 2.4.2.4 and Figure 2.19, that information beyond this Nyquist frequency can be extracted. The matching targets were tabulated, detailing their unique KIC number, principle frequency and corresponding amplitude. Corresponding WASP targets were identified in a database query centred on the *Kepler* coordinates with a cone search of 14″. The extraction of the WASP targets required a $(J-H)$ colour of ≤ 0.4 so to select F-type stars and hotter. Such a colour cut restricts, loosely, the sample to the region in the HRD where the instability strip intersects the main-sequence – a region where high-amplitude p mode pulsations are found. This resulted in a final sample size of 13 060 unique *Kepler* targets and 12 779 unique WASP targets. It must be noted here that there is a difference in the point spread functions (PSFs) of the WASP and *Kepler* instruments; the WASP PSF is 41″, with the *Kepler* PSF being at most 7.5″. The PSF for the WASP data is close to the aperture size used for photometry (48″), and as such does not increase the effects of blending of stars. The difference means that the *Kepler* data will provide more accurate measures of individual stars, avoiding contamination from nearby targets.

Figure 2.6 shows the distribution of the sample in frequency-amplitude space, as well as the different types of class included in the sample. The class abbreviations are explained in Table 2.1, where the number of stars belonging to each class is also displayed. The discrepancy in the final sample sizes, between the WASP and *Kepler* datasets, results from the differing resolving power of the two instruments; *Kepler* has the power to resolve close objects which may only appear as one in both the WASP and USNO-B1.0 catalogues. This may result in multiple *Kepler* targets having only a

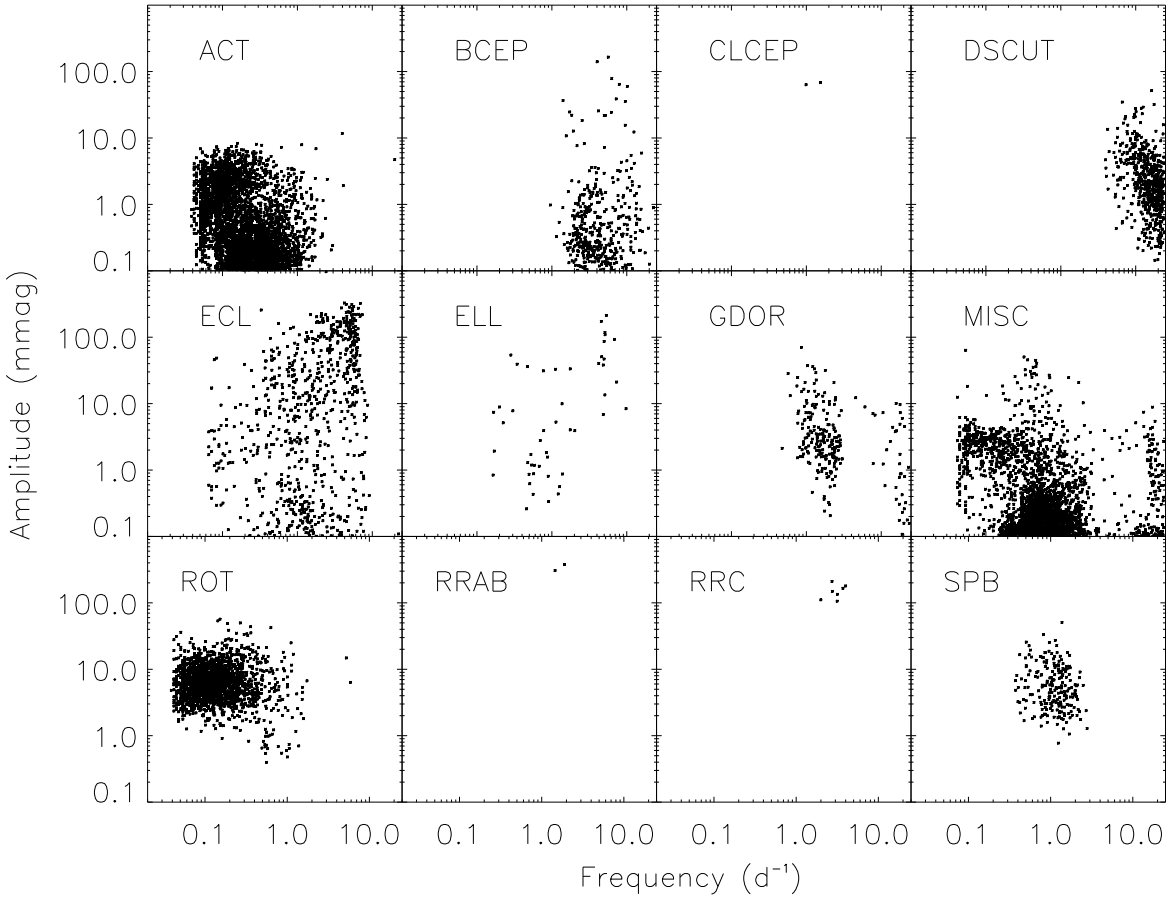

Figure 2.6: The distribution of stars used for the full detection limits survey. The abbreviated names are shown in Table 2.1 with the number of stars used.

single WASP designation (see section 2.4.2.3 and Figure 2.16 for further details).

For such a large sample it is not practical to manually perform Fourier analysis using Period04, as such, the Lomb periodogram method of Press & Rybicki (1989) was adopted as in the Numerical Recipes routine fasper (Press et al. 1992). Using the results of the initial sample, any data sets which contain less than 1 000 data points were rejected before the periodogram was calculated to save computational time, as well as data points with a sky count of >5 000. These cuts were based on the results of the initial investigation.

Table 2.1: The variability types and number of stars used for the detection limit study.

Variability Type	Number in Sample
Active Stars (ACT)	5074
β-Cephei Stars (BCEP)	424
Classical Cepheids (CLCEP)	2
δ Scuti stars (DSCUT)	583
Eclipsing Binaries (all types) (ECL)	774
Ellipsoidal Variables (ELL)	49
γ Doradus stars (GDOR)	239
Miscellaneous (MISC)	3589
Rotational Modulation (ROT)	2094
RR Lyrae stars, subtype ab (RRAB)	2
RR Lyrae stars, subtype c (RRC)	7
Slowly Pulsating B stars (SPB)	223

To determine if a peak in the periodogram can be deemed as significant, i.e. not due to noise, the signal-to-noise ratio (S/N) was also calculated. To determine the noise level, the periodogram is calculated up to $300\,\mathrm{d}^{-1}$, to increase the chance of a stable region being found, and is split into sections of $10\,\mathrm{d}^{-1}$ with the arithmetic mean of each section calculated. The noise level is then taken to be the lowest value calculated. That is to say, the noise is estimated to be half of the base of the 'Fourier grass' level of the most stable section. This value is then used for the entire periodogram (Figure 2.7). Although not the conventional method to calculate Fourier noise, which is to compare the peak amplitude to the residuals in a frequency range about the peak, the method adopted here is computationally fast as no pre-whittening is required and provides a measure that can be used as a noise indicator for peak identification purposes.

Storage of the entire periodogram is not practical due to the large data files. Therefore, only the 'most' significant peaks are saved. Typically, peaks with a S/N of 4 and above (Breger et al. 1993; Koen 2010) are deemed to be significant. However, with the noise calculation adopted here, such a value would result in the loss of many real peaks. As such, a revised value of 2.5 is used to ensure the lower limits of the data are truly tested. To visualise this, Figure 2.7 is plotted with the S/N thresholds of 4 (green line) and 2.5 (blue line) to show the number of peaks that would be discarded.

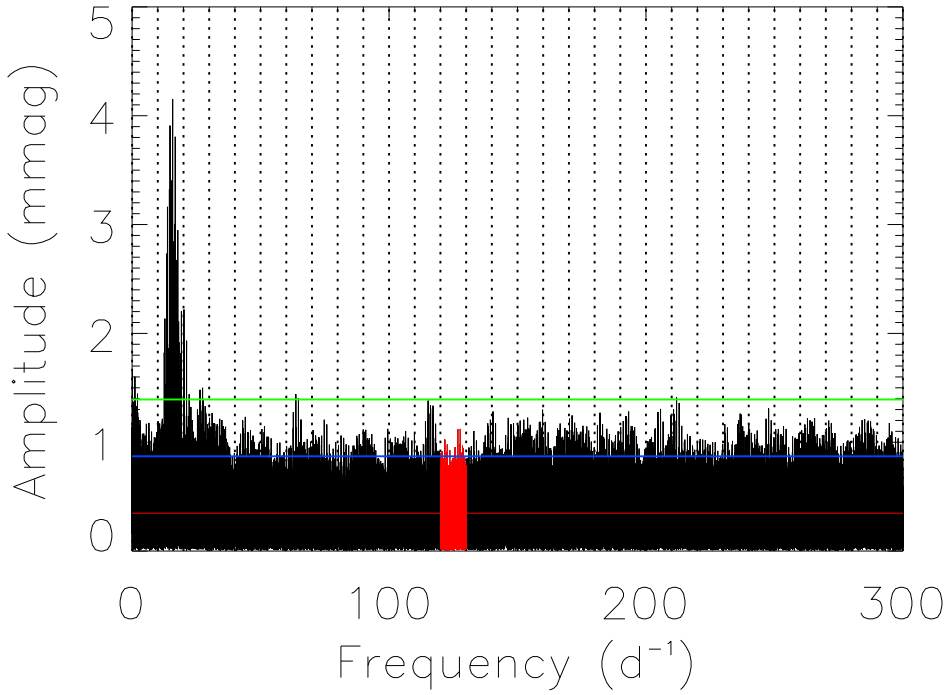

Figure 2.7: An example of the noise calculation for a periodogram (1SWASPJ005721.27+083004.1). The most stable section is shown in red, with the red horizontal line indicating the noise level used for the entire periodogram. In this example, the pulsation at 15.8 d^{-1} has a S/N of 11.9, whereas the highest peak in the highlighted region is just 3.2. The green line represents a S/N of 4.0 with the blue line representing 2.5.

With all significant peaks stored, a cross-comparison between the principle *Kepler* peaks and the extracted WASP peaks was conducted. To detect a match, a peak in the WASP data had to agree with the *Kepler* peak to within $\pm 0.01\,\mathrm{d}^{-1}$, as required in the initial study. If more than one peak fell within this range, the WASP peak with an amplitude closest to that in *Kepler* was chosen. As previously mentioned, matches from multiple WASP datasets were required to confirm that WASP had observed the same pulsation as *Kepler*. The final number of matches produced by these criteria was 10 061 individual WASP objects.

2.4 Results

With the results of a large, broad survey it becomes possible to view the results in a statistical manner and deduce further global constraints on the reliability of peaks extracted from WASP data. Below are presented the results of the survey, with a discussion of the detected peaks, and thus constraints on the detectability of pulsations in WASP data, and a discussion on why a small number of peaks were not matched between the two data sets.

2.4.1 The Detected Peaks

As stated, there were 10 061 principle frequency peaks that were matched between the *Kepler* and WASP data sets. This represents 78.7 per cent of the unique WASP targets that were used for the study. On the surface, such a statistic shows that WASP data is ideal for searching for, and studying, variations in mid F-type stars and hotter. However, detailed analysis shows that this fraction of detections may not be fully representative of the results.

The first logical test of the results is to compare the WASP frequencies and amplitudes to those expected from the *Kepler* data. Ideally, these two parameters should follow a 1 : 1 ratio, within the photometric errors. Obviously this will be the

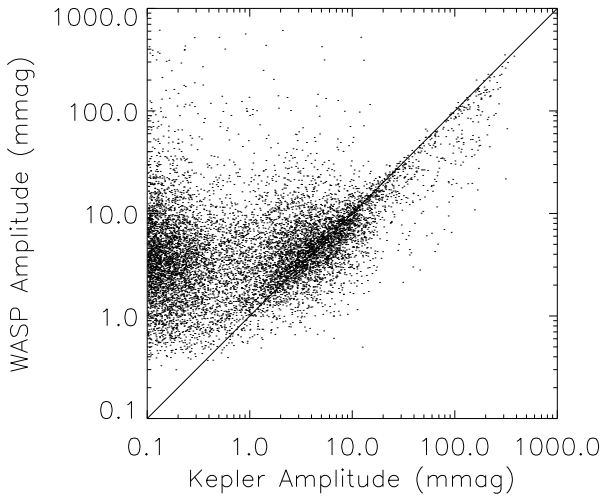

Figure 2.8: A comparison between the expected *Kepler* amplitudes and the extracted WASP amplitudes. It is clear that there are large discrepancies between the low-amplitude *Kepler* peaks and the extracted WASP peaks. The solid line shows the 1 : 1 ratio.

case for the frequencies, as the matching algorithm required the maximum separation to be $0.01\,\mathrm{d}^{-1}$. The amplitude however is allowed to vary to find the best matching peak. Figure 2.8 shows the comparison between the *Kepler* and WASP amplitudes. It is clear that the low-amplitude *Kepler* peaks are hard to extract from the WASP data. It is in this region that noise will be fitting the criteria set by the matching algorithm. These points will be identifiable by their low S/N and large False Alarm Probability (FAP) flag. From Figure 2.6 it is also possible to see that many of the low-amplitude peaks are in the low-frequency regime, the region where the WASP data suffers most from noise.

To combat these obvious mis-matches, the matching algorithm was adapted to require the amplitude of the WASP peak to be less than 2 times the *Kepler* peak, but with no lower limit. The implementation of the upper limit arises from the wavelength differences of the filters used for the two instruments. The central wavelength of the

Kepler filter is 6000 Å whereas the WASP central wavelength is 5500 Å. These central wavelengths are similar to those of the $R-$ and $V-$bands, respectively (cf. Figure 2.1). A study by Medupe & Kurtz (1998) looked into the wavelength dependence of the pulsation amplitude of the roAp stars. They found that the amplitude difference between the $V-$ and $R-$bands was up to about 2 times higher in the V. Although the sample here does not contain roAp stars, they do however occupy the same region in the HR diagram as the sample. The wavelength difference between the $V-$ and $R-$bands is 930 Å whereas the difference between WASP and *Kepler* is just 150 Å, thus the use of 2 times is more than adequate to account for any differences in amplitude due to filter responses. No lower limit was added to the extraction as, previously shown, the WASP data suffers from dilution effects from other objects in the photometric aperture which results in a lower amplitude than would be expected. These conclusions are clear from Figure 2.8: the low-amplitude *Kepler* peaks are over estimated and the high-amplitude *Kepler* peaks are underestimated by WASP. Having applied these constraints, the final matched sample is 4 416 peaks, with the matched points highlighted in red in Figure 2.9.

Form here, reference will be made to both matching routines with the following nomenclature and definitions:

- **Method A** – The initial method used to match peaks where only the frequency of the WASP peak was required to match the *Kepler* peak to within $0.01\,\mathrm{d}^{-1}$. There is no constrain on amplitude of the peak.

- **Method B** – Both the frequency and amplitude have constraints. The frequency constraint is as in the first method, whereas the amplitude must be no larger than twice the *Kepler* value, with no lower limit.

These cuts can also be used to inform on the type of stars likely to be detected from a blind study of the WASP archive. Repeating Figure 2.6 with the results of the matched peaks will show the populations of the classes of stars which were extracted. Figure 2.10 and Table 2.2 detail the resulting sample population.

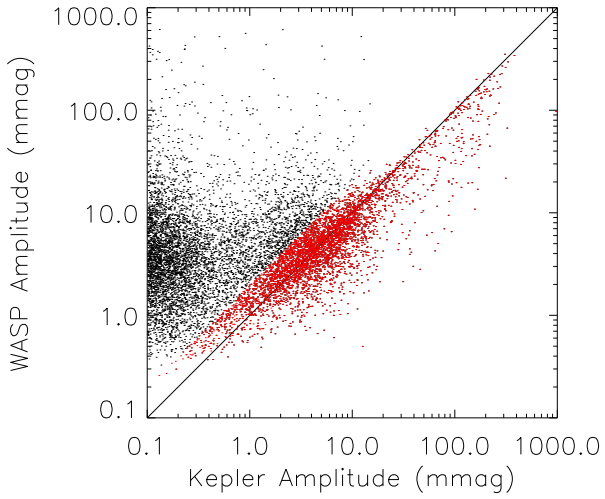

Figure 2.9: A comparison between the expected *Kepler* amplitudes and the extracted WASP amplitudes after the constraint of Method B is applied. The red points represent the matched peaks. The points now more closely follow the solid line showing the 1 : 1 ratio.

Table 2.2: The variability types and number of stars after peak matching with the two algorithms. The second column relates to Method A, and represent the black points in Figure 2.10, and the third column is Method B, shown in red in Figure 2.10. The numbers in brackets represent the percent of the original sample that was matched.

Variability Type	Number from Method A	Number from Method B
Active Stars (ACT)	3831 (75.5%)	801 (15.8%)
β-Cephei Stars (BCEP)	273 (65.4%)	98 (23.1%)
Classical Cepheids (CLCEP)	2 (100%)	2 (100%)
δ Scuti stars (DSCUT)	424 (72.7%)	385 (66.0%)
Eclipsing Binaries (all types) (ECL)	664 (85.8%)	493 (63.7%)
Ellipsoidal Variables (ELL)	45 (91.8%)	33 (67.3%)
γ Doradus stars (GDOR)	212 (88.7%)	178 (74.5%)
Miscellaneous (MISC)	2495 (69.5%)	538 (15.0%)
Rotational Modulation (ROT)	1899 (90.7%)	1682 (80.3%)
RR Lyrae stars, subtype ab (RRAB)	2 (100%)	2 (100%)
RR Lyrae stars, subtype c (RRC)	7 (100%)	7 (100%)
Slowly Pulsating B stars (SPB)	207 (92.8%)	197 (88.3%)

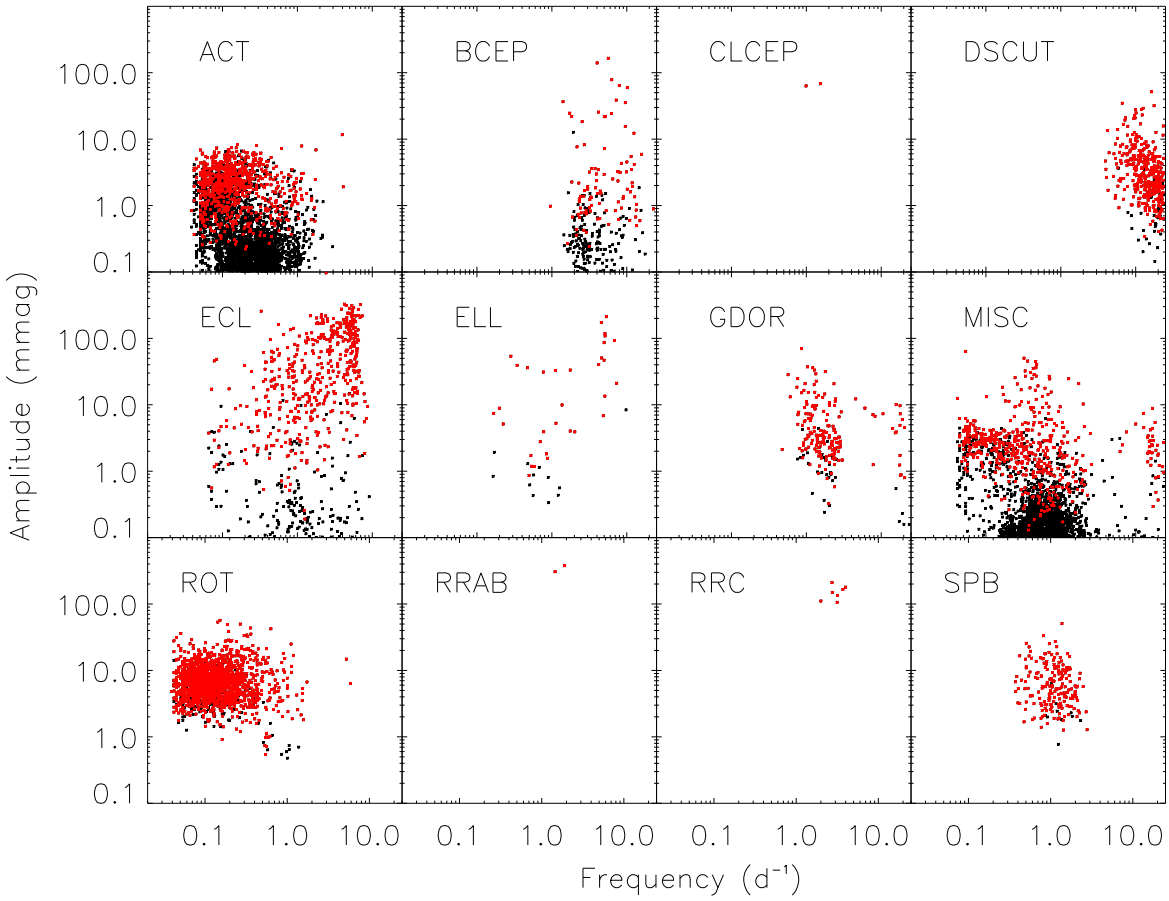

Figure 2.10: The final sample population after Method A is used (black points) and after Method B is used (red points). The number of points is detailed in Table 2.2.

It is evident that the stars with low-amplitude and low-frequency variations are difficult to detect in the WASP data. It was never expected that the quality of the WASP data would allow for the firm detection of low-amplitude variations. A study by Smalley et al. (2011) searched for pulsating Am stars in the WASP archive, and adopted a threshold for low-amplitude detections at 1 mmag. However this thesis suggests that under certain circumstances, this threshold can be pushed lower. In Figure 2.11, the dark blue and purple points represent the peaks which have the lowest FAP values. The lowest amplitude peak (KIC 6273239), with a FAP of zero, has a *Kepler* amplitude of 0.4 mmag, which was detected in the WASP data with an amplitude of 0.72 mmag and a S/N value of 7.9. This peak belongs to a δ Scuti star pulsating with a frequency of 20.3 d^{-1}. This shows that to adopt a limit of 1 mmag will result in the loss of the detection of some peaks. To avoid any further loss of detection, it is suggested that the lower limit of WASP detectability is 0.5 mmag as the detection is more closely related to the S/N rather than the absolute amplitude of the peak. Using a combination of the amplitude and S/N value will provide the most reliable results.

This lower limit, of course, is dependant on the magnitude of the host star however. Bright stars provide an easier target to detect variability, and as the magnitude of the stars fade, the ability to detect low-amplitude variations is greatly reduced. Figure 2.12 shows this effect with the sample used here. Method A, shown in blue, covers the full range of amplitude and magnitude of the targets, with no bias on the detection rate. However, the red points, representing Method B, show there is a clear dependence of detection rate on amplitude of variation and magnitude of the host star. The magnitudes of the targets have been collated from the NOMAD catalogue (Zacharias et al. 2005).

The cause of these non-detections in Method B can be attributed to the photometric precision of the WASP data at lower magnitudes. For stars fainter than $V \sim 11.5$ the photometric precision decreases from the 1 per cent accuracy achieved for the brighter targets (Pollacco et al. 2006). At this magnitude the sky brightness dominates the noise and so the detection probability. As well as this, many of the undetected peaks are of very low-amplitude, ≤ 0.5 mmag, and in the low-frequency range

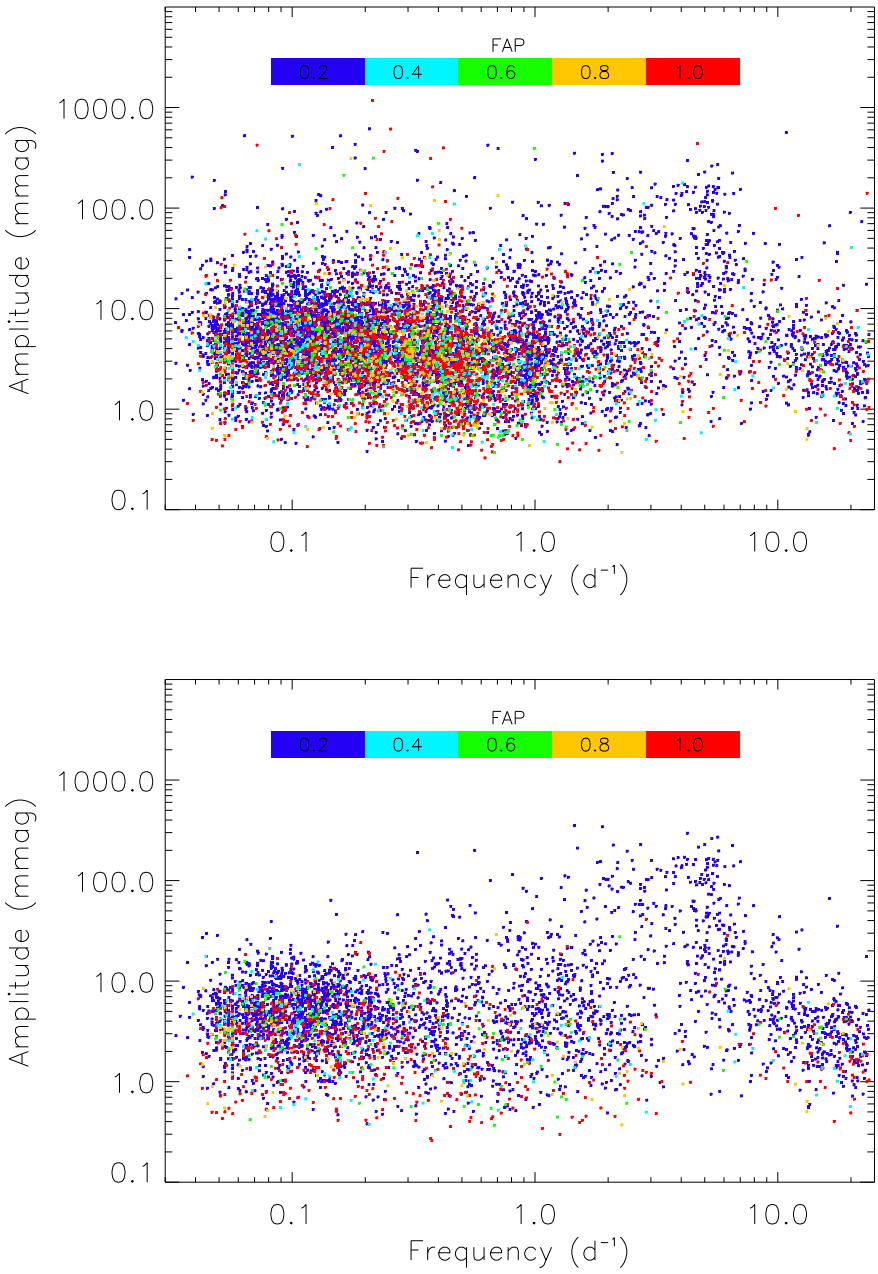

Figure 2.11: The frequency and amplitude of the remaining peaks after Method A (top) and Method B (bottom) are applied. Method B removes many of the peaks which have a large FAP value. The FAP values, as calculated with the periodogram, are binned in bins of 0.2 wide, the value on the colour index is the upper value for each bin.

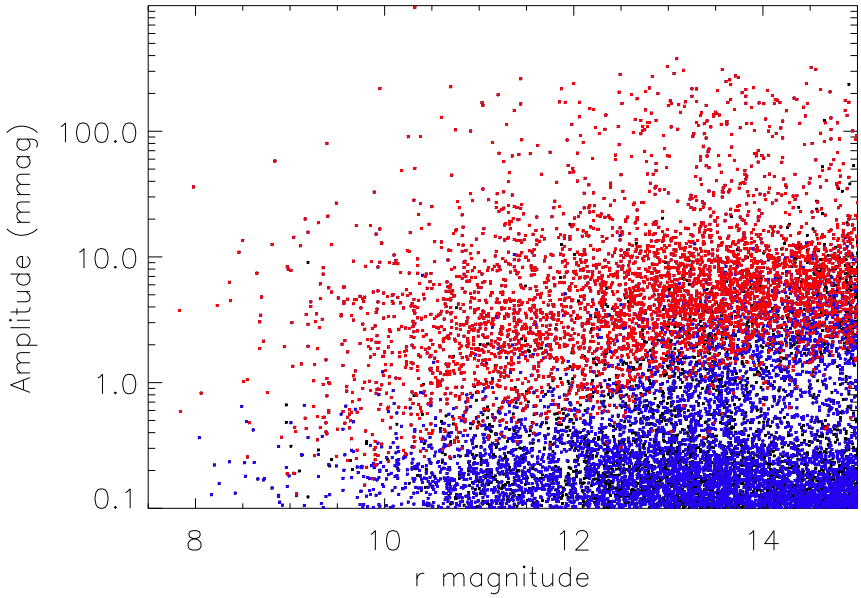

Figure 2.12: The amplitude and magnitude of the original sample (black), the results from Method A (blue), and the results from Method B (red). There is a clear dependence on both the amplitude and magnitude with regards to detectability.

(cf. Figure 2.10) where the red noise is dominant and is dramatically more significant than the pulsation amplitude. Finally, these faint targets are also more greatly affected by contamination caused by other stars in the photometric aperture which cause the pulsation amplitudes to be diluted. This is addressed further in section 2.4.2.3.

2.4.2 Non-Detections

Having discussed the detected peaks, and concluding a minimum detection limit of 0.5 mmag for the WASP data, the non-detected peaks must now be addressed. Already discussed are the effects of peak amplitude, target magnitude and the S/N of the peaks. However, there are further considerations to be made with regards to the undetected peaks. These include WASP noise, frequency differences beyond $0.01\,\mathrm{d}^{-1}$, incorrect catalogue data and dilution effects.

2.4.2.1 Noise

As discussed in section 1.6.1, despite best efforts to remove instrumental and photometric sources of noise from the WASP data, there is still evidence for noise in the periodograms. Most noise, in well sampled light curves, appears in the low-frequency domain below about $10\,\mathrm{d}^{-1}$. This is where night-to-night variations influence the light curve, changes in atmospheric and seeing conditions cause noise and changes in airmass are apparent. Below about $10\,\mathrm{d}^{-1}$ is also where we see the strong effects of the window function. The daily gaps in the data produce strong signals in a periodogram on, or very close to, integer d^{-1} values. This is not to say, of course, that above this frequency the periodogram is 'clean' with only real frequencies present. There is a constant Fourier 'grass' present in the data, with occasional strong peaks above this background level. Further to this, light curves with fewer data points produce real peaks with lower S/N which may be lost amongst the background level.

As an example, take the star KIC 10253676. In the Q01 *Kepler* data, the star is listed in Debosscher et al. (2011) as a 'Miscellaneous' variable with a frequency of

$0.73\,\mathrm{d}^{-1}$ and an amplitude of 0.533 mmag. In the WASP data, however, there are strong signatures in the low-frequency range, with the strongest peak at $3.00\,\mathrm{d}^{-1}$ with an amplitude of 6.91 mmag (Figure 2.13). This strongest peak is a result of ground-based observations, due to the daily gaps (see section 2.4.2.2), but the background to these peaks is raised above that at higher frequencies. It is in this region where many of the non-detections lie with low-amplitudes. The original method, A, to match the WASP and *Kepler* peaks had a greater tendency to match peaks that were high-amplitude noise peaks as they were close to the *Kepler* frequency, as was the case with this example. This is evident from Figure 2.8 were many of the low-amplitude peaks in *Kepler* are thought to be of a much higher amplitude in WASP, in some cases well over 1 000 times higher. It is hard to remove these mismatches using either the S/N criteria or the lower limit cut-off. The ability of WASP data, reduced in the described way, to detect low-frequency, low-amplitude stellar variations is severely hampered by noise.

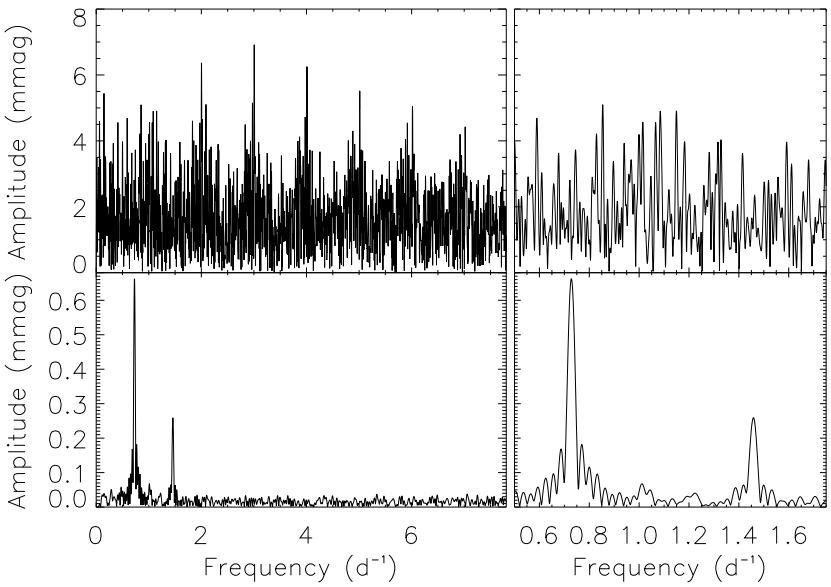

Figure 2.13: The WASP (upper) and *Kepler* (lower) periodograms of the same star (KIC 10253676), note the vast difference in scale. Method A identified this as a matched peak, however the revised algorithm in Method B correctly identified this as a false-positive.

The magnitude of the star also has an impact on the noise in the calculated periodogram. The photometric noise effecting the light curve goes as $\sqrt{N}$, where N is the number of photons detected, and the S/N goes as $N/\sqrt{N} = \sqrt{N}$. WASP observations are set at a given 30 s exposure, thus the number of photons from a faint star are fewer than from a bright star, leading to a more noisy light curve (as demonstrated in section 1.6.1).

The effect of this can be seen in Figure 2.14. Plotted are the S/N for the matched peaks using both methods. The number of stars in the sample increases with increasing magnitude, as would be expected. The black line in panel (a) represents the original sample, the the blue and red lines indicating the refined samples using Method A and B, respectively. The subsequent panels show a series of different S/N bands (see figure caption), with fewer detections of high S/N peaks for fainter stars. There remain a few strong detections in stars with $m > 14$, but these represent a small fraction of the total number of stars in this magnitude range. It is clear that for the most reliable detections, the stellar magnitude is required to be less than 14. Method B is prone to pruning out the low S/N peaks, but leaves the high S/N detection in the sample.

2.4.2.2 Aliasing

Also discussed in section 1.6 was the aliasing effects which affect periodograms, especially ground-based data. The strongest aliasing in the WASP data arises from the daily gaps in the observations, and as such, strong peaks are present in periodograms at integer d^{-1} values. This is evident in Figure 2.13, with the strongest peak at $3\,\mathrm{d}^{-1}$ and tailing off in power to about $8\,\mathrm{d}^{-1}$. These alias peaks pose a problem when trying to match with *Kepler* peaks which are close to an integer d^{-1} value. Fortunately, in the case of this sample, there are only 82 peaks that fall within $0.01\,\mathrm{d}^{-1}$ of an integer d^{-1} value.

Although not greatly influencing this sample, aliasing effects are hard to treat in a blind study of the WASP archive. Without a known frequency it is almost impossible to distinguish between a true peak and an alias at low-frequencies. One method to deal

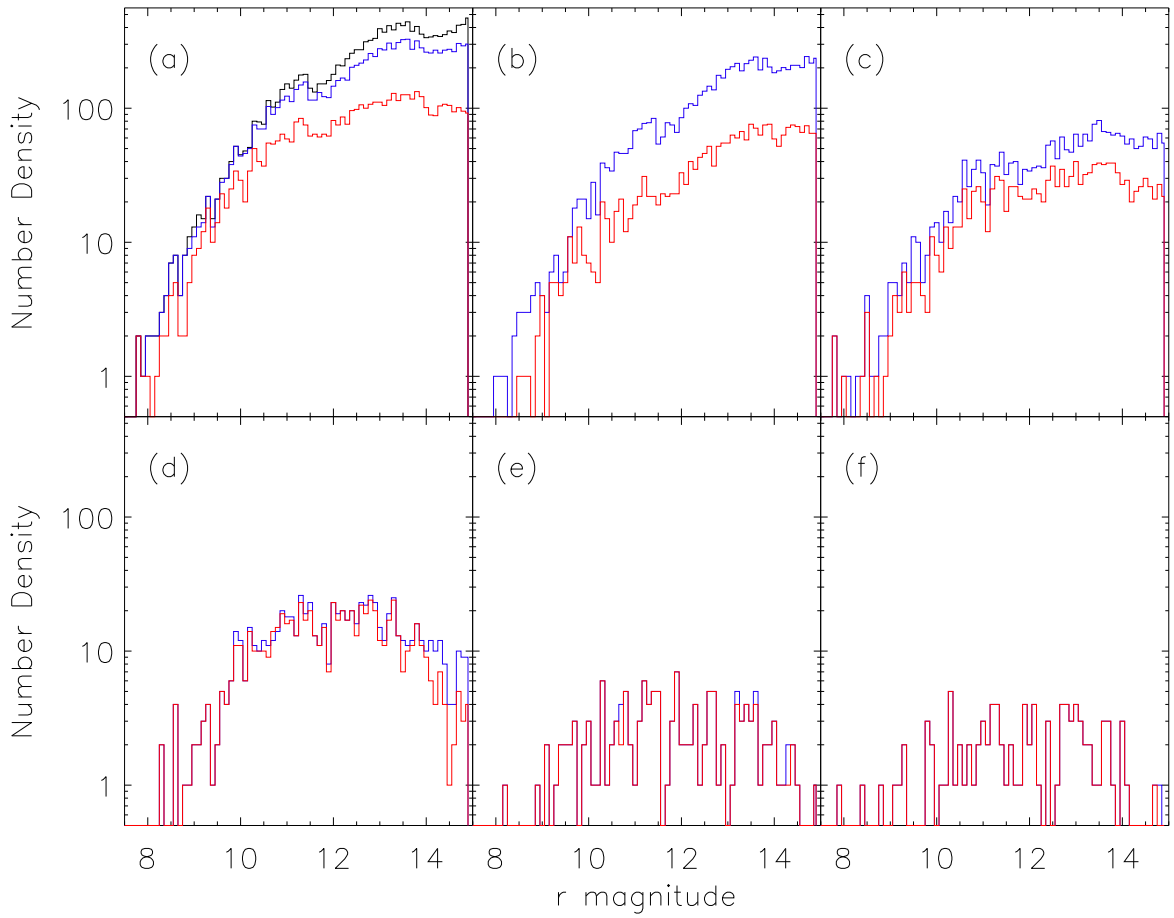

Figure 2.14: The S/N as a function of r magnitude, in bin sizes of 0.1 mag. The fainter stars clearly show a tendency to have a lower S/N, as expected from the photon statistics. The blue lines are Method A results, the red lines are Method B results. The panels are: (a) original sample (black) and the refined samples; (b) $2.5 \leq S/N < 5$; (c) $5 \leq S/N < 10$; (d) $10 \leq S/N < 30$; (e) $30 \leq S/N < 50$; (f) $S/N \geq 50$. The two methods vary greatly at low S/N, but agree when signal detection is more certain, as would be expected.

with this is to only search for variations occurring with a frequency greater than a lower cut-off, or to ignore peaks within a certain frequency range of the integer d^{-1} values at low-frequencies. This will evidently lead to the reduction of real peak identification, but greatly reduce the number of false positive detections.

Finally, aliases are also reflected at the boundaries of the periodogram, i.e. about the Nyquist frequency (ν_{Ny}) and about $0\,\mathrm{d}^{-1}$. As the Fourier transform also has a negative component, it is possible to have a peak in the positive domain (ν) and a corresponding peak in the negative domain ($-\nu$). This occurs most prominently close to the boundary so that aliases of $-\nu + n\,\mathrm{d}^{-1}$ still have enough power to be visible in the positive periodogram. Similarly, at the Nyquist, peaks with $\nu > \nu_{\mathrm{Ny}}$ show aliases of $\nu - n\,\mathrm{d}^{-1}$ which can be mistaken for a real peak in the sampled domain. In this case, the star will be seen to be variable, but the automatic selection of the incorrect frequency may occur.

2.4.2.3 Dilution and Target Blending

Due to the large pixel size of the SuperWASP cameras, many targets suffer from an amount of dilution from nearby stars. With non-isolated stars, many other foreground or background objects may contribute to the photometric counts of the target, diluting the power of the target's variability. To quantify the amount that a target star is diluted, the following relation is used:

$$Dilution\,Factor = \left[1 - \left(\frac{F_{target}}{F_{blends} + F_{target}}\right)\right] \times 100. \tag{2.4}$$

The dilution factor considers the flux of stars within $48''$ of the target (the photometric aperture, F_{blends}) and compares this to the flux of the target (F_{target}). The fluxes are extracted via an automatic PHP query which searches the NOMAD catalogue through the VizieR service. The blend flux is then composed of the r magnitude fluxes from stars brighter than 20^{th} magnitude.

The formula gives a percentage of how much the target star is diluted, and by extension, the variability. Low-amplitude variations in faint stars are susceptible to

dilution in crowded fields. Figure 2.15 shows the variation of dilution with stellar magnitude and variation amplitude; it is evident that dilution has a greater effect on faint stars, particularly those fainter than $\sim 14^{\text{th}}$. Stars with low values of dilution are shown in purple and blue, whereas those with a large dilution factor are shown in orange and red. Dilution starts to become a factor around 13^{th} magnitude, which accounts for, as well as the noise, the number of incorrect detections when using Method A of detection. This also accounts for why there are peaks which are below the 1 : 1 ratio in Figure 2.8. It is hard to quantify exactly how many objects are not detected due to dilution alone, as other factors such as amplitude and magnitude need to be taken into account. However, removing stars with amplitudes below 0.5 mmag, and assuming dilution greater than 80 per cent leads to non-detection, dilution accounts for the non-detection of 154 stars from Method A and 411 stars from Method B.

Dilution can also be a problem for *Kepler* data, as can be seen with KIC 10002787, and KIC 10002792. Figure 2.16 shows the WASP photometric aperture in which the two stars lie (with $J = 10.12$ and 11.20; Skrutskie et al. 2006). In the WASP data only one of which is resolved. However *Kepler* resolves both stars which have individual masks, as shown in Figure 2.17. Debosscher et al. (2011) suggest that KIC 10002787 has a principle frequency at $0.86\,\mathrm{d}^{-1}$ with an amplitude of 0.2 mmag, and that KIC 10002792 has a principle frequency at $0.86\,\mathrm{d}^{-1}$ with an amplitude of 13.1 mmag. Given that the period is the same for both targets, it is clear the the stars are not fully resolved, but that the pulsation is in the fainter star, KIC 10002792. Analysis of WASP data suggests that within the aperture a star varies at $0.86\,\mathrm{d}^{-1}$ with an amplitude of 6.3 mmag. Although the WASP ID, through the USNO-B1.0 catalogue, is associated with the brighter object, the variation is in fact originating from the fainter star. This is a key point. WASP has the ability to detect stellar variability, however when multiple objects fall within its aperture it is not possible to determine which star is the source of the variability. This case shows that it cannot be assumed that the brightest star is the source; only targeted photometry can determine this.

This also demonstrates the dilution of blended targets in the WASP data. Using the J magnitudes from Skrutskie et al. (2006), the dilution of the target can be calcu-

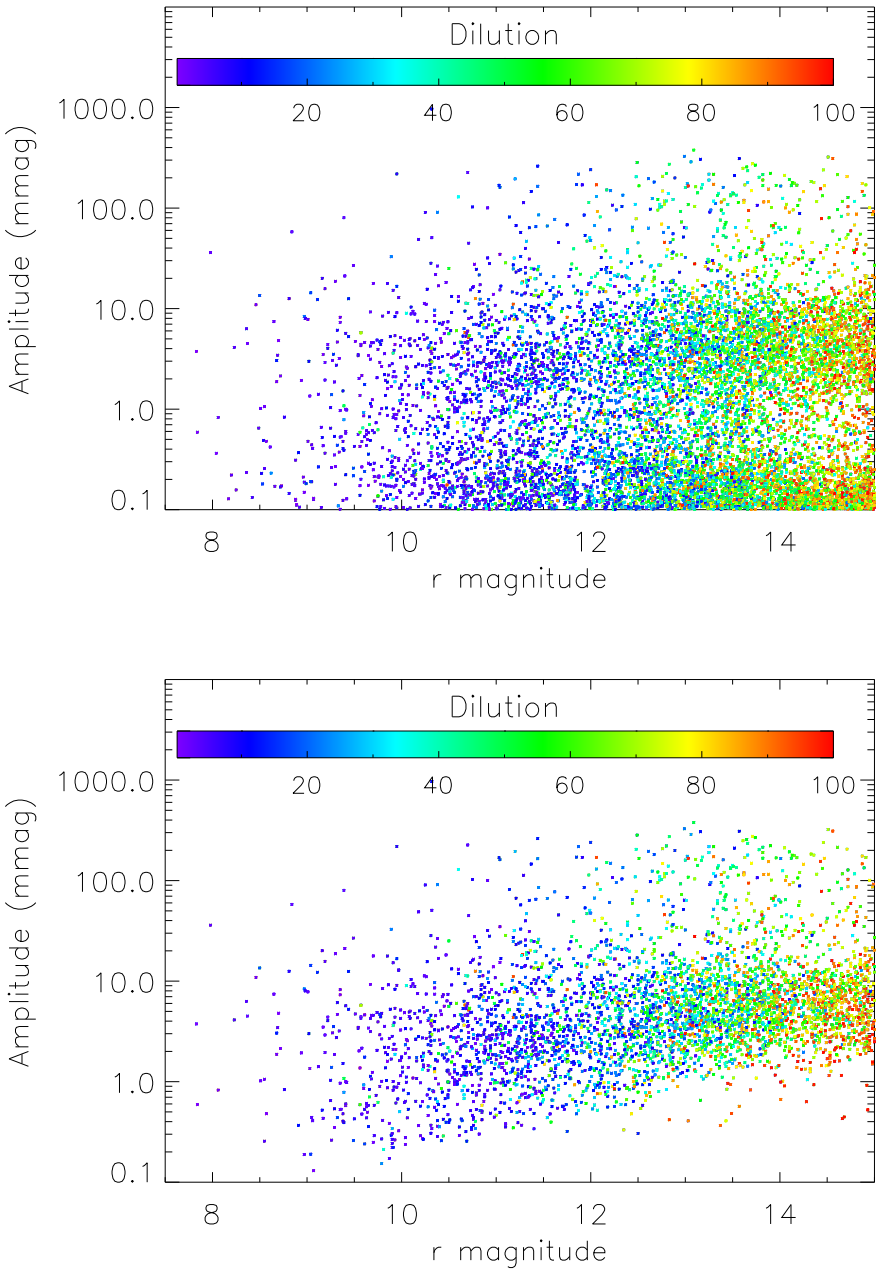

Figure 2.15: The magnitude and amplitude of the remaining peaks after Method A (top) and Method B (bottom) are applied. Method B removes many of the peaks which have a high dilution value, suggesting that Method A detects spurious peaks rather than a heavily diluted one. As expected, the dilution increases for the fainter objects.

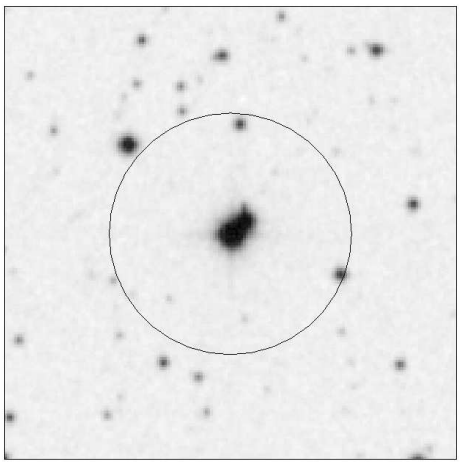

Figure 2.16: DSS image of 1SWASPJ191127.61+465853.7 (3′×3′). The two stars in the centre of the image are separately resolved by *Kepler* (see Figure 2.17) but are classed as one star in the WASP database. The brighter star on the lower left is identified as KIC 10002787, the fainter star on the upper right of the pair is KIC 10002792. The annulus, with a radius of 48″, is the aperture over which photometry is performed and the dilution factor is calculated. The annulus is 3.5 WASP pixels in radius.

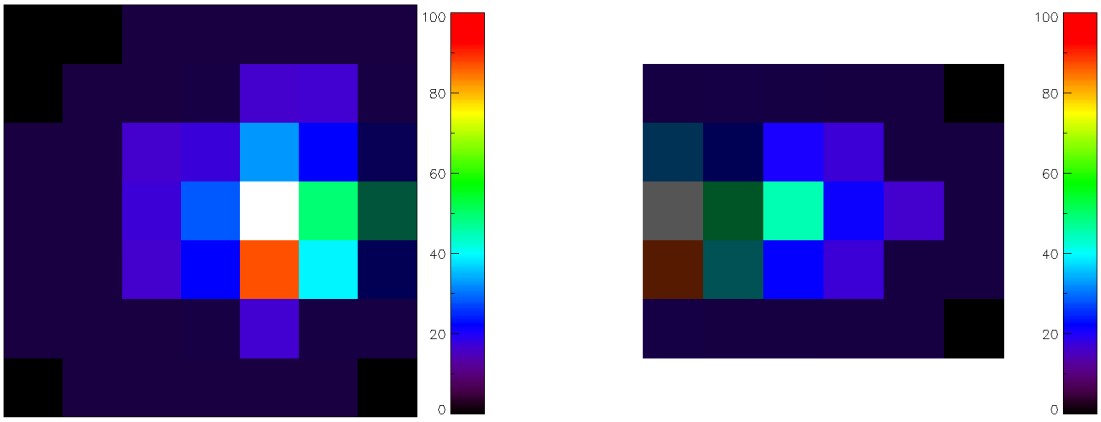

Figure 2.17: The *Kepler* pixel images and masks used for the pipeline extraction of KIC 10002787 (left) & KIC 10002792 (right). The full image is the extent of the pixel coverage of each star, the brightest colours form the pixel mask, other pixels have been shaded. The white pixel on the left and grey pixel on the right are the same pixel. The colour indicates the counts in the pixel scaled to be white for the largest and black for zero counts. The pixel sizes are 3.98″, while the stars are separated by 7.48″.

lated using equation (2.4) to be 70 per cent. This implies that the undiluted amplitude in the WASP data would be of the order 23 mmag. It is expected that the *Kepler* amplitude would be similar to this undiluted WASP amplitude, but it is not: a further example of the blending and dilution present in the *Kepler* data.

2.4.2.4 *Kepler* Data Artefacts

Two examples have been found that demonstrate errors in either the *Kepler* data itself, or the catalogue compiled by Debosscher et al. (2011). Figure 2.18 is an example of the former problem. The figure shows data of KIC 7950964; the green curve shows a normal, phase folded light curve of the eclipsing binary system. Fourier analysis of this data set suggests an orbital period of 0.41 d with an amplitude of 0.97 mag (this peak does appear in the WASP data, but only at 0.097 mag). The red curve is dramatically different; during the eclipse, the spacecraft seems to loose and regain sensitivity. This affects the Fourier result, suggesting a much deeper eclipse of 1.33 mag. It is therefore assummed that the red curve is a result of errors in the *Kepler* reduction pipeline, which have subsequently been rectified. Although the erroneous data presented here is for Q03 this effect may be present in the Q01 data used by Debosscher et al. (2011). Such problems with the public archive data used in this study may result in the identification of correct peaks in the WASP data, but are disregarded as the peak does not meet the required criteria. Over or under estimating the amplitude may push the peak beyond the amplitude observed by WASP. This example shows that *Kepler* data requires in-depth analysis to avoid incorrect conclusions, something which unfortunately a global study cannot afford.

The second source of error related to the *Kepler* data are the published catalogue values. Three examples have been found where the published value of the pulsation amplitude is much greater (by a factor of $\sim 10^5$) than that seen in the *Kepler* periodogram. These targets (KIC 5872403, KIC 6351577, KIC 11509767) have all been identified to have a principle frequency of 16.31 d^{-1} and amplitudes greater than 1 mag. Inspection of the Q01 light curves and periodograms (from data release 21) show that, although

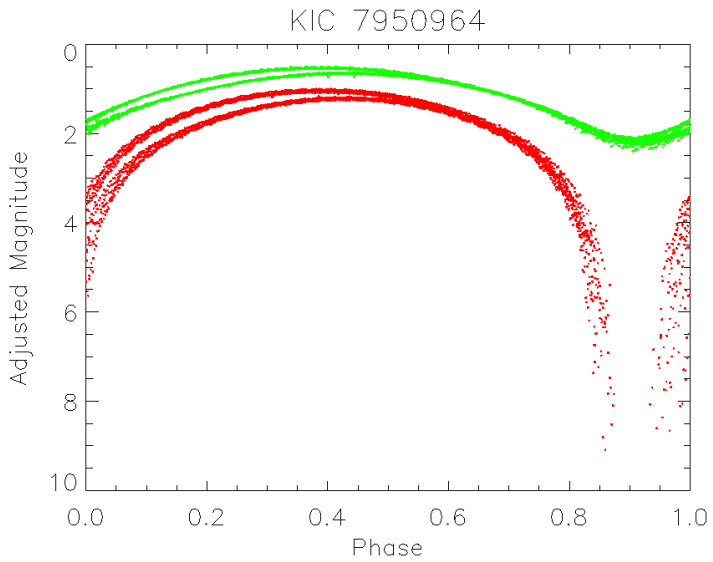

Figure 2.18: An example of inconsistent *Kepler* data. This example shows how *Kepler* data is variable from Quarter-to-Quarter. The green curve is Q01 data for an eclipsing binary system. Fourier analysis suggests this light curve has a period of 0.4 d and an amplitude of 0.97 mag. The red curve is for the same star, but from Q03. Clearly there is a difference between the two curves. The sensitivity of *Kepler* appears to decrease during eclipse, leading to a much higher amplitude of 1.33 mag.

there is a peak at the expected frequency, the maximum amplitude of the three is just 45.9 μmag. All show low-frequency peaks between 0.028 and 0.081 d^{-1}, which are greater than the quoted value. These targets have been re-analysed here using the PDC SAP flux data, the same as by Debosscher et al. (2011), however using a different data release. The fact that these three anomalous peaks all occur at the same frequency, and with similar amplitudes, suggests that this is not a transcription error in the catalogue, but data artefacts in the *Kepler* data itself. However, no record can be found in the literature of this frequency. Either way, errors as such will cause the non-detection of some peaks, and may be more subtle than the examples discussed here.

Further to this, most targets in the Debosscher et al. (2011) catalogue were studied with the LC *Kepler* data which has a Nyquist frequency of about 24 d^{-1}. In the temperature range which was selected for the comparison study there are many pulsators which show frequencies higher than this value and have high amplitudes (e.g. Smalley et al. 2011). As a result, there are peaks which appear in the LC periodograms which are in fact aliases of peaks above the Nyquist frequency which have been reflected into the lower frequency range. An example of this is KIC 8623953 (Figure 2.19). The star was observed in LC mode for the duration of the mission, and in SC mode during Q02, Q05, and Q10. Analysis of the LC data shown there to be a peak at 21.68 d^{-1} with an amplitude of 9 mmag, as shown in red in Figure 2.19. However there was no detection of this peak in the WASP data. With an amplitude and frequency with these values in a bright star ($r = 9.2$) which suffers little dilution (3.8 per cent) it would be expected that the peak would be seen in the WASP data. Therefore, investigation of the SC data was conducted and shows that the true pulsation in this star is seen at 27.26 d^{-1} with an amplitude of 18.3 mmag (also seen in WASP data), and the one seen in the LC data is an alias reflected about the Nyquist. In reality, the peak is recoverable from the LC data, despite being above the Nyquist frequency, using the method described by Murphy, Shibahashi & Kurtz (2013) (the technique will be described and used is Chapter 7). Again, this is just one example which was found as part of the survey, and may account for further non-detections of high-amplitude peaks, especially in the higher frequency range where the δ Sct stars are found.

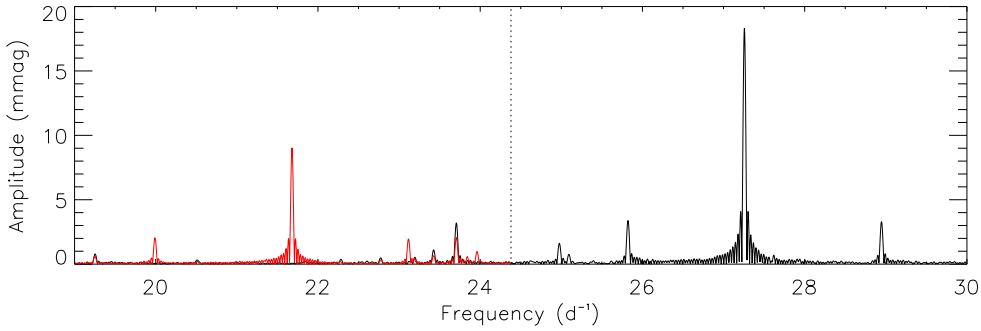

Figure 2.19: An example of how the LC data can show aliases of higher frequency peaks. The Q01 LC data is shown in red, with the SC Q10 data shown in black. The vertical dotted line is the LC Nyquist frequency which the peaks are reflected about. The highest peak in the LC data is quoted as real by Debosscher et al. (2011), but is in fact an alias of the peak at $27.5\,\mathrm{d}^{-1}$ seen in the SC data. This is another example of why there is no match to the LC peak in WASP data.

2.4.2.5 Airmass Effects

As is common with most ground-based observations, WASP observations require that the target's airmass, X, is less than 2 so to avoid ingesting unreliable and noisy data to the archive. As the airmass increases, the path-length which the light travels through the Earth's atmosphere increases. In doing so, the extra column density of air causes diffraction of the photons away from the telescope aperture, thus resulting in the star appearing fainter with higher statistical noise as a result. Over the course of a night the airmass varies with zenith angle, z, such that in the simplest form $X = \sec z$. Although best efforts are made to correct for the airmass, this is done for the centre of each frame, rather on an individual star basis, as a result there are residual airmass effects remaining in the final light curve. The airmass is also corrected for using an assumed colour term, based on G-type stars.

The period at which the airmass variation is expected to peak is 8 hours, the approximate observing period for a night. The bottom panel in Figure 2.20 shows a Fourier transform of the airmass variations for the object 1SWASPJ184640.29+472230.2

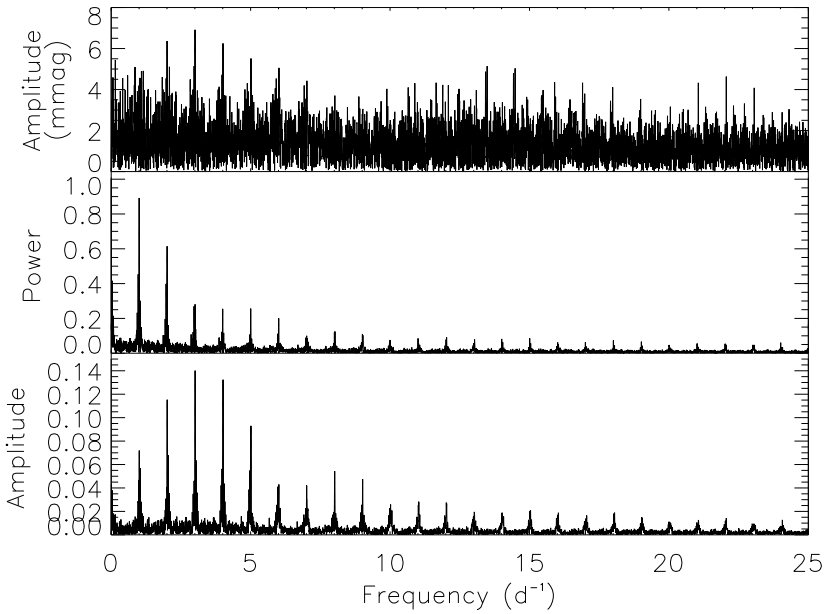

Figure 2.20: An example of aliasing and airmass effects on the periodogram. Top panel: periodogram of WASP data for KIC 10253676. Middle panel: corresponding window function. Bottom panel: periodogram of the airmass variations. The window function shows the dominance of the observing gaps. The periodogram of the airmass variations show a dominant peak at $3.01\,\mathrm{d}^{-1}$ corresponding to the nightly variation. The coincidence of the peaks in airmass and periodogram occurring at the same frequency implies there are residual airmass effects remaining in the light curve.

(KIC 10253676) observed in 2010. The principle frequency falls at $3\,\mathrm{d}^{-1}$ as expected, with a secondary peak at $8\,\mathrm{d}^{-1}$ which is a result of sampling (and in also evident in the window function of this periodogram). Also clearly evident are the effects of aliasing discussed previously. This peak in the airmass variations coincides with the peak seen in the periodogram of the light curve, indicating that there are still residual airmass effects present. This residual airmass with add further noise to the periodogram, contributing to problems of identifying low-amplitude, low-frequency pulsations in WASP data. However, as Figure 2.20 shows, the effect is very small when compared to the pulsation amplitudes involved.

2.5 Variable Variables

There are stars which exhibit intrinsic amplitude variations which are included in the sample. These stars change the amplitudes of their peaks over time, often swapping power between different pulsation modes (e.g. Breger & Montgomery 2014). The variations may, therefore, push the amplitude of a peak into the WASP noise level. A unique example of this can be seen in KIC 7106205 (Bowman & Kurtz 2014). This is a hybrid star which shows both δ Sct and γ Dor pulsations, with 8 significant g modes (≥ 0.01 mmag) and 9 p modes (≥ 0.1 mmag). All but 1 of the modes show highly stable frequencies and amplitudes over the entire duration of the *Kepler* observations, 1400 d. The one varying mode is a p mode, $\nu_{\rm mod} = 13.39\,{\rm d}^{-1}$, which shows an amplitude which varies by almost an order of magnitude over the 4 yr observations. Initially, at the start of *Kepler* observations, this mode has the highest amplitude at 5.16 mmag, but after about 500 d the amplitude has dropped to just 0.53 mmag (Bowman & Kurtz 2014). Figure 2.21 shows the mode that varies and a stable mode in the same star over 17 Quarters.

WASP data from 2007 shows that KIC 7106205 has a principle frequency at $13.39\,{\rm d}^{-1}$ and a WASP amplitude of 5.6 mmag. In 2009 data, the peak is no longer the principle frequency, but is present with an amplitude of 2.63 mmag, however the 2010 season of data does not show the pulsation. To study this star in more detail, Bowman, Holdsworth & Kurtz (2015) combined the available WASP and *Kepler* data to push the time base of observations to 2 yr prior to the launch of *Kepler*. They successfully correct the data for passband differences, integration time differences, and target blending using simultaneous WASP and *Kepler* data to reliably compare the two data sets. In doing so, their results show that the amplitude of KIC 7106205 has changed even more significantly than first thought by Bowman & Kurtz (2014) (Figure 2.22).

This star is an example of how a varying amplitude in a star may push the peak below the WASP detection limit. The predicted amplitude, in the WASP passband, for KIC 7106205 in 2010 is 0.87 mmag (Bowman, Holdsworth & Kurtz 2015), below

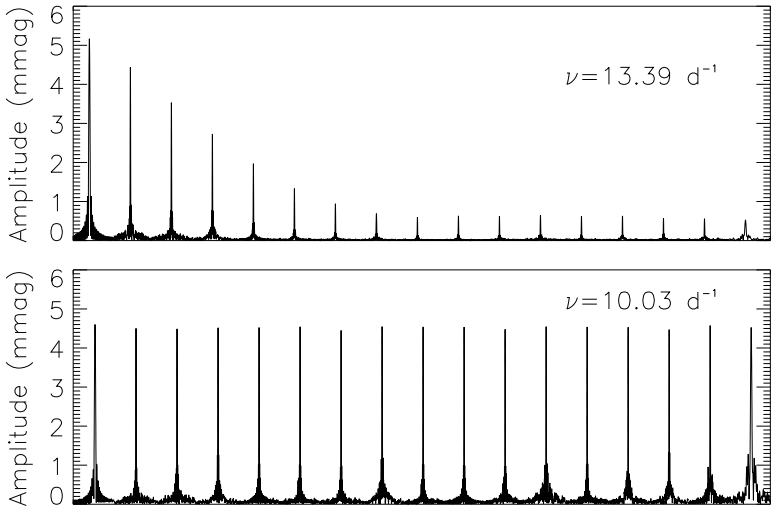

Figure 2.21: The amplitude variation of the 13.39 d^{-1} mode in KIC 7106205 (top) and a stable mode at 10.03 d^{-1} for comparison (bottom). Each peak corresponds to a different Quarter of LC data, from Q01 to Q17. Early observations of the mode show that it is in the WASP detection amplitude range, but begins to fall into the region where noise dominates the WASP periodogram.

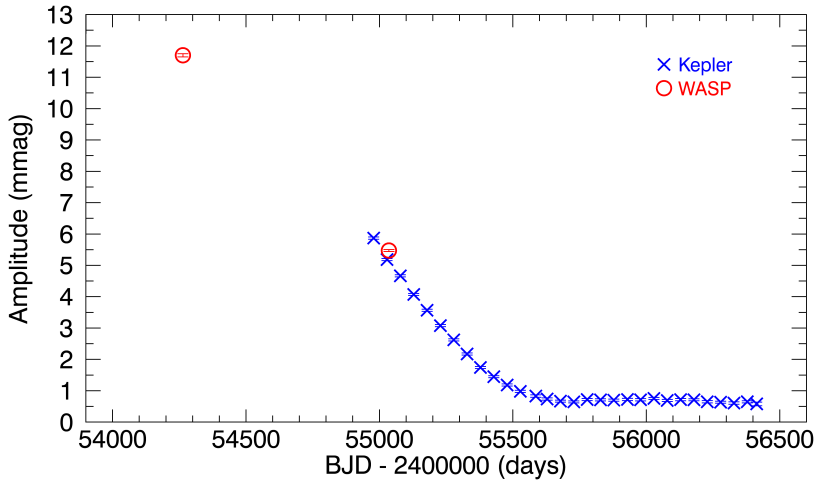

Figure 2.22: Corrected and calibrated WASP (red circles) and *Kepler* (blue crosses) amplitudes for the ν_{mod} peak in KIC 7106205. This shows the dramatic decrease in pulsation amplitude of this mode over time, and shows how ground-based observations can complement *Kepler* data. From Bowman, Holdsworth & Kurtz (2015).

the noise level for this periodogram. If the 2007 data did not exist for this star, no reliable detection of the pulsation would be made in the WASP data. Although this is currently the only known example in the *Kepler* data, there maybe other stars in this sample which show this phenomenon, thus causing non-detection in the WASP data.

2.6 Conclusions

This study has conducted a thorough investigation in to the feasibility of using SuperWASP observations to search for stellar variability in A-type stars. Previous studies of pulsations in the WASP archive (Smalley et al. 2011) have only used a rough estimate of the detection limits, however an extensive understanding of the WASP data characteristics has enabled the optimum detection limit to be set at 0.5 mmag. This limit however is a variable with regards to stellar magnitude, the number of observations and the crowding of the WASP photometric aperture.

Reliable peaks can be extracted for stars with more than 1 000 data points, below this number peaks become less well defined and dominated by noise in the periodogram. As well as this, observations with sky background counts greater than 5 000 are disregarded from the light curve as they do not lead to detections. After these exclusions have been made, periodograms with weak signals should have the characteristics of the stars investigated before being accepted or discarded as a real signal. Aliasing effects, and residual airmass effects, also need to be considered in the low-frequency regime when identifying peaks. The noise introduced by these effects often dilutes or disguises peaks of true variability in the star. With peaks in the low-frequency regime in particular, the window function of the data needs to be carefully compared to the periodogram to ensure the correct peak is identified.

The comparison of the WASP data to *Kepler* periodograms had highlighted most of the issues associated with frequency analysis of WASP data. The many non-detections can be explained by the derived detection limit of this study. Of the undetected peaks there are 6 246 peaks in the *Kepler* data with amplitudes below 0.5 mmag,

Table 2.3: The final selection criteria on the light curve data and calculated peaks.

Parameter	Value
Light curve points	$> 1\,000$
Sky Count	$< 5\,000$
Magnitude	$14 \leq r \leq 7$
Amplitude (mmag)	> 0.5
Frequency (d^{-1})	> 0.5
S/N	> 2.5
FAP	< 0.8

this accounts for 72.3 per cent of the undetected peaks when using Method B for detection. Of the remaining non-detections, 1 756 have a *Kepler* frequency below $0.5\,d^{-1}$, a region which has been shown to suffer greatly from the low-frequency WASP noise. This leave just 641 peaks that fall within the detectable parameter space of the WASP data. However, as has been shown in this Chapter, there are many reasons which these peaks may not have been identified in the WASP data.

Table 2.3 show the final results of the light curve selection criteria, and the peak extraction criteria. A constraint on the dilution can not be applied to the data as detections occur across the entire dilution range. If this is also considered astrophysically, a high-amplitude pulsator, such as a white dwarf or sdBV star, may have a brighter, in the $r-$band, companion or background object which would dilute the signal, but due to its pulsation strength, would still be detectable.

With this study complete, it is now possible to conduct a full and reliable survey of the A-type stars in the WASP archive in the search for pulsations.

3 The WASP Archive Survey

3.1 Introduction

With the detection limits determined (Chapter 2), attention must now turn to a survey of the SuperWASP archive. As previously discussed, the focus is on the F-, A-, and B-type stars where the p mode pulsations can have amplitudes above the determined detection limit. This range of spectral type allows for the discovery of a whole host of pulsating stars, from the slowly pulsating B (SPB) stars to the classical δ Scuti pulsators, the pulsating Am stars and the rapidly oscillating Ap (roAp) stars. The survey is also not bound to the main-sequence stars, with sub-dwarf and white dwarf stars being found in this region, along with other pre- and post-main sequence stars.

Previous surveys for pulsations in the A-type stars have targeted objects that were already known to be spectroscopically interesting A stars (e.g. Smalley et al. 2011; Paunzen et al. 2012; Kochukhov et al. 2013). Such an approach limits the results to specific types of pulsators. There is also the possibility of introducing biases into the detections and understanding of the observations. For example, if low-frequency pulsations are seen in an Ap star it would be natural to assume that there is a companion or error in the data as the theory does not predict the excitation of low-overtone p modes in these stars (Saio 2005). However, the approach adopted in this study requires no previous knowledge of the targets, except for a rough photometric spectral type. This has allowed for the search of all types of pulsations in F-, A- and B-type stars and will permit the possible discovery of new types. Such a method removes most biases and preconceptions of what types of variability will be found.

The motivation, therefore, for this study is to identify further cases of pulsating A-type stars with no biases in the selection of targets. The data which SuperWASP collects provides approximately uniform sky coverage, thus removing biases, for example, in the search for roAp stars which as been mainly conducted from the Southern Hemisphere (Martinez & Kurtz 1990b; Martinez & Kurtz 1994; Kochukhov et al. 2013).

This also allows for follow-up observations to be made of discoveries using a selection of telescope/instrument set-up, thus not requesting a significant amount of time from just one organisation.

3.2 Target selection

At the time of writing (2015 February), the WASP archive holds are over 428 billion data points covering over 31 million unique objects. This, of course, is mostly populated to the late-type cool stars which are the most likely candidates to host easily detectable extrasolar planets. To extract the stars of interest to this study a colour cut is performed based on the 2MASS photometry held in the archive. Stars were required to have a $(J-H)$ colour index of < 0.25 to be considered for the study. This corresponds to stars of spectral type F6 and hotter. This cut includes stars which are not expected to show pulsations in the detection range, but this cooler cut accounts for a small amount of reddening suffered by the hotter stars and enables the detection of pulsations in stars which are not expected to pulsate. It is also stipulated here that the targets must have a USNO magnitude of $14 \leq r \leq 7$, which are the approximate detection limits of the WASP instruments, and as has been shown in Chapter 2 stars fainter than about 14^{th} often shown heavily diluted amplitudes and few reliable detections. Finally, following Chapter 2, stars are rejected if they have fewer than 1 000 data points.

Using the $(J-H)$ colour as an indication of spectral type, and the conversion table of Tokunaga (2000), the distribution of the survey sample can be shown in terms of the spectral type (Figure 3.1). As one would expect, there are a larger number of stars in the sample for the later type stars, which are more common than the earlier type stars in the sample. The small number of F6 stars compared to the F5 stars is a result of the colour cut applied to the whole sample: a colour $(J-H)$ of 0.25 falls in the middle of the F6 range.

The subset of stars extracted from the archive amounts to about 1.5 million ob-

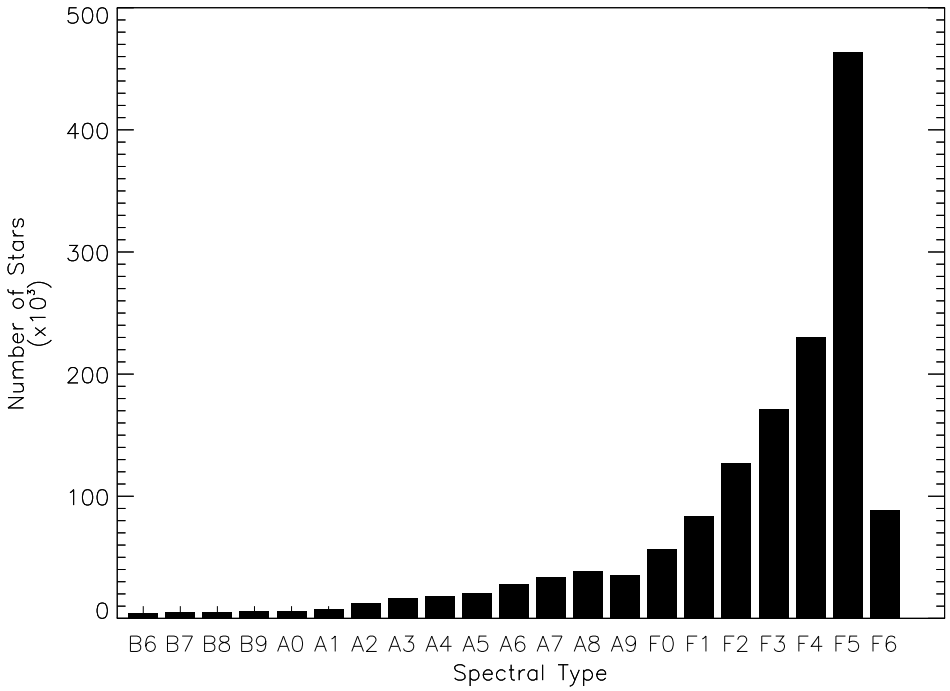

Figure 3.1: Distribution of the survey sample with spectral type. As expected, there is an increase in the number of stars for the later spectral types. The lack of F6 stars is a result of the $(J - H)$ cut applied to the sample, which falls in the F6 band.

jects, with the space required to hold such a large set of data totalled just under 2 TB. Handling such large volumes of data requires a local storage structure to split the data into more manageable sizes. To this end, two 2 TB disks we designated to store the northern and southern hemisphere data separately. The data were then subdivided into directories of R.A. hours and every 10° in Declination. Most directories then held about 5 000 star files, with a maximum of 38 000. The use of two disks enabled the future storage of the results in a similar structure based on northern and southern hemisphere.

3.3 Data Processing

The volume of data that required processing meant that single machine processing was not an option. Previous tests had shown that to read a single FITS file and calculate a periodogram for each of the seasons, required about 6 s to run. Such a rate on a single CPU would require over 100 d of continuous processing. As such, the data storage areas were mounted, through a departmental server, on all available machines in the department. This gave access to about 50 CPUs ranging from 2.0 to 3.2 GHz processors and 2 to 8 GB of RAM. In this way, the extraction and calculation took about 2 weeks to complete, and was restricted by disk access though I/O processes and job queuing rather than the available computing power.

From the subset of stars, a single code is run to extract each season of data and calculate a Lomb-Scargle periodogram up to a maximum of $300\,\mathrm{d}^{-1}$. The value of $300\,\mathrm{d}^{-1}$ is chosen to provide a wide range of frequencies over which to calculate the noise level, and to maximise the number of detections whilst trying to balance the computational time required. The code is initialised with a BASH script which supplies the FORTRAN code with the input file name and output destination. The script is run from the individual R.A. and Dec. directories, enabling several to the initialised at the same time.

The code first extracts the light curve from the WASP FITS file, selecting the

processed flux from the pipeline converting it to a WASP magnitude, and converts the time from seconds to days from a given reference point. Data points are then tested to determine if they fit certain criteria and rejected if they fail. The data are required to: be within a magnitude range of $5 < V_{\rm wasp} < 15$ to exclude saturated points and unrealistically faint points; have a sky count less than 5 000 to remove low S/N data; show a $\sigma^2_{t(i)}$ value below 0.1, which is the systematic error for each data point caused by wisps of clouds, Sahara dust and other transient events (Collier Cameron et al. 2006). The value is calculated by summing over all stars, j, in a frame, i, holding $\sigma^2_{s(j)}$ fixed, such that

$$\sum_j \frac{1}{\sigma^2_{ij} + \sigma^2_{t(i)} + \sigma^2_{s(j)}} = \sum_j \frac{m_{ij} - \hat{m}_j - \hat{z}_j}{\left(\sigma^2_{ij} + \sigma^2_{t(i)} + \sigma^2_{s(j)}\right)^2}, \tag{3.1}$$

where σ^2_{ij} is the formal error on the data, $\sigma^2_{s(j)}$ is variance caused by stellar variability, m_{ij} is the magnitude of a star, $\hat{m}_j$ is the mean magnitude of a star, and $\hat{z}_i$ is the zero-point correction for the frame. Essentially, for each star in a frame, the sources of variability are compared to the residual magnitude of the star, after taking into account the stellar variability and systematic offsets. Any difference in the the two values must be accounted for in frame to frame variability due to sky variability.

From there, the data are trimmed using a resistant mean algorithm, as described in section 2.2, with a sigma cut of 4.0. Finally the processed light curve is passed to the Lomb-Scargle routine FASPER of Press et al. (1992).

The FASPER routine requires, beyond the light curve, two further input parameters to be specified. In the code these are: *hifac* and *ofac*. The *hifac* value is calculated by:

$$hifac = \frac{\nu_{\rm max}}{\nu_{\rm Ny}}, \tag{3.2}$$

where $\nu_{\rm max}$ is the maximum frequency to be tested and $\nu_{\rm Ny}$ if the Nyquist frequency if the data were evenly sampled. This value is used to tell the code how much higher, or lower, than the Nyquist frequency the periodogram should be calculated. The *ofac* quantity is the oversampling factor of the periodogram. It is suggested by Press et al. (1992) that this value should be about 4, however it was found that a lower value of 2.5 gave comparable results and was 2 s faster per light curve to compute. The outputs of

the FASPER routine are: frequency (d^{-1}), amplitude (mag), S/N, and the false alarm probability (FAP) of Horne & Baliunas (1986). The calculation of the FAP accounts for the oversampling of the periodogram, thus providing a realistic estimate of the parameter.

Finally, the code calculates the noise level of the periodogram as described in section 2.3, to be able to calculate the S/N level for the peaks in the periodogram. Peaks with a S/N > 2.5 are written to the output file provided by the initial BASH input. In all, over 9 million individual periodograms were calculated.

3.4 Peak Extraction

With the periodograms calculated, the extraction of the most likely peaks must also be automated. For each WASP ID, the significant peaks from each season were read into arrays and cross identified, in frequency, to find peaks which were within a tolerance of $0.01\,d^{-1}$ as was used before (cf. Chapter 2). Peaks with false alarm probability (FAP) values of 1.0 were not included in the matching routine. This will reduce the number of spurious matching peaks above the 2.5 S/N limit. In requiring more than one peak in the given range ensures that the peak is present in more than one WASP season, thus making the detection more reliable. There is no constraint on the amplitudes of the the multiple peaks as the pulsation amplitude may not be stable between seasons (see section 2.4.2). Any matched peaks are then printed to file. The sample was then further reduced by removing peaks which had a FAP flag greater than 0.1, i.e. excluding peaks which have a 90 per cent chance of arising from noise. The reduction of the FAP limit at this stage allows for the chance that true peaks, in noisy data sets, lie in the $0.1-1.0$ range can be matched with the same signal in higher quality data sets.

The remaining peaks were then divided into two groups: peaks seen between 5 and $50\,d^{-1}$ and peaks above $50\,d^{-1}$. The matches below $50\,d^{-1}$, will account for many of the δ Sct stars in the sample, as well as the SPB stars, RR Lyrae stars, binaries and γ Dor stars. At the very low-frequency range, between $0-5\,d^{-1}$, many data artefacts

that will be matched, such as low-frequency noise and aliasing effects are present. This range is therefore fully excluded from the results. A future analysis of the low-frequency signatures in SuperWASP data is needed to fully understand and exploit this frequency range. The higher frequency range, above $50\,\mathrm{d}^{-1}$ is where the younger δ Sct stars are found, as well as the roAp stars and the compact variables. It is the higher frequency subset where most focus was applied as it is this domain which presents rarer stars and exploits the SuperWASP capabilities. These stars had their periodogram re-calculated, with all peaks being stored. At a later date they were plotted and inspected by eye to select the targets which showed true pulsations in multiple seasons. Through manual inspection, it becomes obvious that there are still many mis-matches made by the code, making human inspection vital in distinguishing between real peaks and noise.

During this selection process effects of blending or overcrowding of the WASP aperture are not considered. Due to the large pixel size of the WASP detectors this can be a common occurrence, with an estimated 12 per cent of targets suffering ≥ 50 per cent dilution. However, at the detection stage, variability is the sole interest, with later diagnostics used to resolve blends or confusion being conducted to ensure the variability is attributed to the correct target (see section 6.5 for an example).

3.4.1 Peak Extraction Testing

To test the robustness of the methods outlined above, and in particular in comparison to the 'standard' S/N detection limit of 4.0, 1 000 artificial light curves were created with the same time sampling as a typical WASP data set, but with Gaussian (i.e. white) noise as the signal. The time series were analysed in the same way as the real observations, with the aim of identifying if the methods outlined above will give rise to false-positive detections.

For real data, initially, a coarse cut using the FAP is made; this first selection requires peaks to have a FAP < 1.0. Then, all the periodograms of a single target, i.e. periodograms from multiple seasons, are compared in the search for matching peaks. Allowing peaks with a large FAP value at this stage aims to account for noisy

periodograms where a real signal might be hiding in, or close to, the noise. Once matches have been made, a second cut is made, requiring the FAP to be ≤ 0.1. This selects the periodograms with the highest likelihood of real detections. These are then set aside for human inspection.

For the test data, using the initial criterion that peaks must have a FAP value < 1.0, a S/N detection threshold of 2.5 gave rise to 28 568 false-positive peaks, with a limit of 4.0 leading to only 3421 peaks being flagged. It is clear that the 4.0 S/N threshold greatly reduces the number of false-positive peaks extracted from a purely white noise periodogram.

However, with the second cut which is applied to the real data, i.e. requiring the FAP value to be less than 0.1, both the 2.5 and 4.0 S/N thresholds identify just 135 peaks belonging to 55 unique objects. This demonstrates that the combination of a low FAP value and a S/N of 2.5 will not increase the number of false-positive detections over a S/N cut of 4.0, and it can be expected that 5.5 per cent of the flagged objects will be due to noise. It must be noted, however, that the noise in the WASP periodograms is not purely Gaussian but also has a component of red noise affecting the low-frequency domain.

3.5 Renson & Manfroid catalogue search

To further understand the capabilities of the WASP data with regards to finding high-frequency pulsators such as roAp stars, a test using the catalogue of Renson & Manfroid (2009) was conducted. All stars identified as Ap were cross-checked with the WASP database, and extracted with the same criteria as in section 3.2. This amounted to 543 Ap stars. Periodograms were calculated using the aforementioned method, and examined if the above criteria were fulfilled. The automatic search resulted in the extraction of just 1 known roAp star (HD 12932), out of a possible 15 known roAp stars in the subset that was searched (Table 3.1).

Table 3.1: Renson and WASP coincident roAp stars. Columns $9-16$ are a measure of the quality of the WASP data for each season.

HD	Literature Data			WASP Data										
	Mag (B)	ν (d^{-1})	ΔB (mmag)	Mag (V_{WASP})	ν (d^{-1})	ΔV (mmag)	N° of Seasons	χ^2/n						
6532	8.60	202.82	5	8.38	–	–	2	42.43	2.33					
9289	9.63	137.14	3.5	9.42	–	–	4	7.46	14.93	3.73	2.66			
12098	8.46	189.22	3	8.23	–	–	1	1.82						
12932	10.56	124.14	4	10.28	124.10	1.03	5	1.18	1.07	0.99	1.17	0.97		
84041	9.74	96.00	6	9.25	–	–	5	44.65	9.52	3.95	7.76	6.29		
99563	8.90	134.58	10	8.50	–	–	4	12.28	204.96	11.33	2.65			
101065	8.73	119.01	13	8.27	–	–	2	2.44	5.65					
119027	10.41	165.52	2	10.19	–	–	4	1.58	1.27	8.69	1.79			
122970	8.70	129.73	2	8.33	–	–	4	2.89	4.60	6.95	3.90			
185256	10.37	141.18	3	10.10	–	–	7	3.77	2.18	0.934	1.47	2.91	1.43	37.82
193756	9.56	110.77	1.5	9.27	–	–	5	3.29	0.95	1.82	4.25	3.10		
196470	10.14	133.33	0.7	9.84	–	–	6	3.02	4.10	3.53	4.91	2.58	4.48	
203932	9.10	244.07	2	8.92	–	–	4	23.25	3.80	0.66	17.62			
213637	10.05	125.22	1.5	9.73	–	–	8	1.52	1.63	1.53	2.06	1.52	1.42	0.89	1.36
218495	9.62	194.59	1	9.43	–	–	4	7.95	6.41	5.62	7.81			

To decipher why only one object was recovered from the WASP data the spectral response of the WASP instruments is considered. Designed for exoplanet detection, the broad spectral response dilutes the pulsations which are strongest in B-band photometry (Kurtz, Shibahashi & Goode 1990). Comparing WASP observations of HD 12932 with those in the literature, the WASP data suffers an amplitude decrease of ~ 75 per cent. Given the WASP detection threshold is nominally 0.5 mmag, we expect the lower limit in B-band photometry to be between $2-4$ mmag, thus accounting for the non-detection of 10 targets.

To further investigate why no pulsations are detected for the remaining 4 targets, a weighted reduced-χ^2 (Bevington 1969) is calculated for each season of data which aims to characterise the light curve by accounting for the number of data points and the scatter in the light curve i.e.

$$\chi^2/n = \frac{\Sigma((\mathrm{mag} - \mathrm{median(mag)})/\sigma)^2}{(n-1)}. \tag{3.3}$$

With this taken into account, it becomes more clear why no detections are made for the roAp stars with amplitudes above the expected amplitude threshold. For the four non-detected targets above the threshold, the χ^2/n value suggests the data are not of high enough quality to consistently detect pulsations.

This suggests that only a small fraction of the roAp stars that exist in the WASP database will be extracted. The main reason for the lack of detections of the known targets is the colour response of the WASP instruments.

Of the 543 Ap stars studied, no new roAp stars were detected amongst the sample. Of course, the survey is limited by the 0.5 mmag threshold, providing a lower limit on any pulsations in the WASP V-band photometry.

3.6 Summary

This survey of the SuperWASP archive adopts a new approach in the search for variability in the A-type stars, thus removing any preconceptions of the types of variability

that might be detected. This provides the opportunity to discover a host of variable stars, with the potential to find new observations which test the current theory of pulsations in A-type stars.

The targets selected for the study cover spectral types hotter than F6, thus including the δ Sct stars in the low-frequency, $5 - 50\,\mathrm{d}^{-1}$, range, and the roAp and compact pulsators above $50\,\mathrm{d}^{-1}$. Due to the complexity of the very low-frequency range (below $5\,\mathrm{d}^{-1}$), it has been decided that detections in this region shall be set aside, with the potential for later study. The interaction of the noise characteristics, alias effects and binary signatures in this range will make the detections of pulsation very difficult.

To increase the speed of calculation to the periodograms, the parameters of the FASPER code have been changed, and shown to almost half the computational time, with little effect on the resulting periodogram. Also, as the method of noise calculation is non-conventional (see section 2.3), further time has been saved.

In relation to the noise, peaks in the periodogram are only saved for later comparison if they fall above a S/N limit of 2.5. This lower value than the 'standard' 4.0 (Breger et al. 1993; Koen 2010) accounts for the way in which the noise is calculated. In not saving the entire periodogram, both I/O time and disk space are saved. Comparison of these peaks in then made in the frequency domain, requiring peaks to match with a tolerance of $\pm 0.01\,\mathrm{d}^{-1}$ which is the Rayleigh criterion of a WASP season. A match in amplitude is not required, at this stage, as the variable nature of the WASP data can lead to amplitude changes in the observed peaks.

Finally, to test the capabilities of the methods presented in relation to the detection of high-frequency peaks, the stars listed as Ap in the Renson & Manfroid (2009) catalogue were extracted from the archive and tested for pulsational variability. Of the known roAp stars, only one was detected, with no new detections made. The non-detection of the other roAp stars is a combined effect of amplitude dilution in the broad WASP passband, and the quality of the data in the WASP archive. However, even the detection of one of these stars show the capabilities of the archive, and the survey methods, to detect and extract high-frequency pulsations.

4 WASP Archive Survey Results

This work was partially published in Holdsworth et al. (2014b).

4.1 Introduction

In this Chapter, the results of the pulsation search in the 1.5 million stars are presented. In total, 202 656 unique targets have been identified to vary between $5 - 300\,\mathrm{d}^{-1}$. Included in this frequency range are, as discussed in Chapter 1, the δ Sct stars, roAp stars, pulsating Am stars, pre-main-sequence stars, β Cep stars, sdBV stars and white dwarf pulsators.

Due to the large number of targets with detected variability, it is not possible to perform an in-depth study on an individual basis, or a entire pulsation class. However, to study the results in a more meaningful manner, the detections have been separated into two main frequency groups: targets between $5 - 50\,\mathrm{d}^{-1}$ and targets between $50 - 300\,\mathrm{d}^{-1}$. In doing this, it is possible to separate the main bulk of the detections, namely δ Sct stars, and the higher frequency stars which are rarer in comparison. This is seen in the number of targets which fall into each of the frequency ranges: 202 281 stars in the low-frequency range and just 375 in the high-frequency range. The low-frequency range presents many difficulties for classifying the variability types, as in this range there are signatures from binaries, harmonics and aliasing effects.

There is, of course a distribution of pulsation frequencies which each type of pulsating class shows and so some of the classes will have examples in both of the regions. However, without a detailed analysis of the light curves and a full spectroscopic survey of the results, it is not possible to classify every individual star.

4.2 The 5–50 d^{-1} Range

The low-frequency domain covers the frequency range from $5 - 50\,\mathrm{d}^{-1}$. The lowest frequencies, below $5\,\mathrm{d}^{-1}$, have been excluded from the results as many of the detected frequencies in this range will be a result of noise, binarity or strong alias features. Although in this region the γ Dor and SPB stars are found, it is not possible to distinguish been these pulsation signals and noise without a thorough investigation of the light curve and periodogram. Inclusion of this range will inevitably skew the results in favour of noise rather than signal. Work on this range would be constitute an entirely separate project.

Of the 1.5 million stars surveyed, 202 281 stars were identified with variations in the low-frequency range. Again, it must be made clear that there will be contamination of this number from mis-identified peaks which are actually due to noise or other forms of low-frequency variability, or harmonics of $< 5\,\mathrm{d}^{-1}$ variability. The daily aliases can still be strong features out to about $16\,\mathrm{d}^{-1}$. To combat this issue, peaks that are within a tolerance of $\pm 0.01\,\mathrm{d}^{-1}$ (the approximate Rayleigh criterion of WASP data) of an integer frequency have been excluded from the analysis. Although this procedure will remove real signal, the remaining results will be more robust. Despite these efforts, this aliasing problem can be seen in Figure 4.1 which shows the distribution of the detections with frequency. The histogram bars are above the background for the low-frequency integer frequencies. This is a result of a slight deviation of peaks away from integer frequency values as the gaps in the data are not exactly day values. In removing the majority of false detections, there are now 51 375 stars which show variability in the range of 5.1 to $50\,\mathrm{d}^{-1}$.

To understand this group of pulsators, which will mostly consist of δ Sct stars, the $(J - H)$ colour, used for the initial selection, has been used to estimate a spectral type for the star, based on the table of Tokunaga (2000). The distribution of the targets is shown in Figure 4.2, and mirrors that of the entire sample shown in Figure 3.1. As the figure shows, there are very few B-type stars which have been detected to vary,

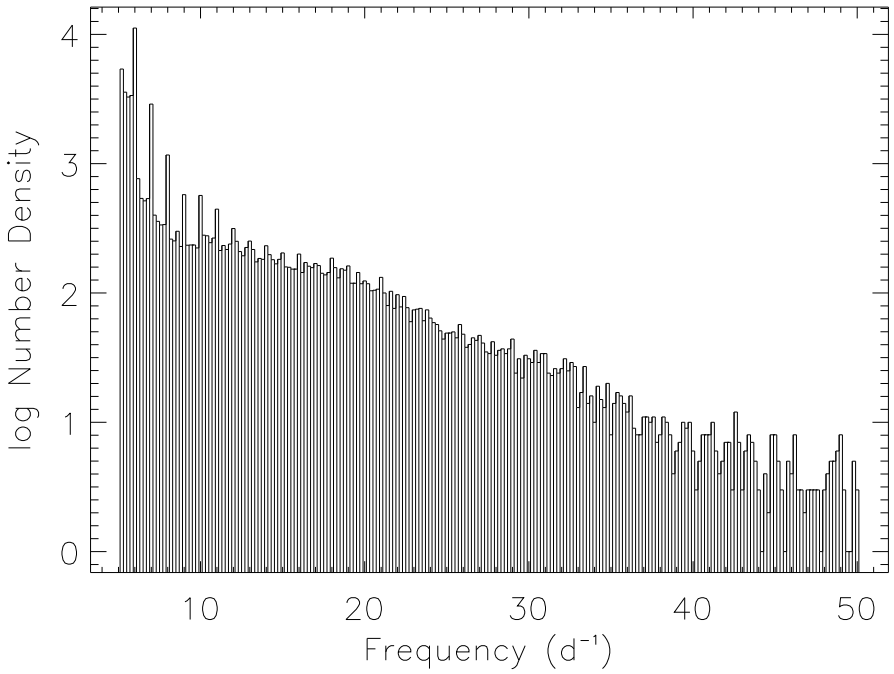

Figure 4.1: Histogram of the low-frequency peaks in frequency bins. The data are shown in bins of $0.2\,\mathrm{d}^{-1}$. Clearly evident are the $1\,\mathrm{d}^{-1}$ aliases which occur most prominently between $6-11\,\mathrm{d}^{-1}$. Note the number density is displayed in logarithmic format for clarity.

with a steady growth in detection through the A-type stars, and a significant number of detections in the F-type stars. The lack of detections in the F6 stars compared to the F5 and hotter F-type stars is a result of the colour cut of the original sample ($(J-H)<0.25$), which falls within the F6 spectral type band. In the estimation of the spectral type, the reddening along the line-of-sight has not been accounted for, and as such stars may be estimated to be a cooler spectral type than they actually are.

To understand what type of pulsation is originating from the different types of stars, Figure 4.3 shows the frequencies and amplitudes of the detected peaks with respect to the spectral type. As the temperature of the stars decreases, there are many more stars showing peaks at higher frequencies, and a wide spread of frequencies

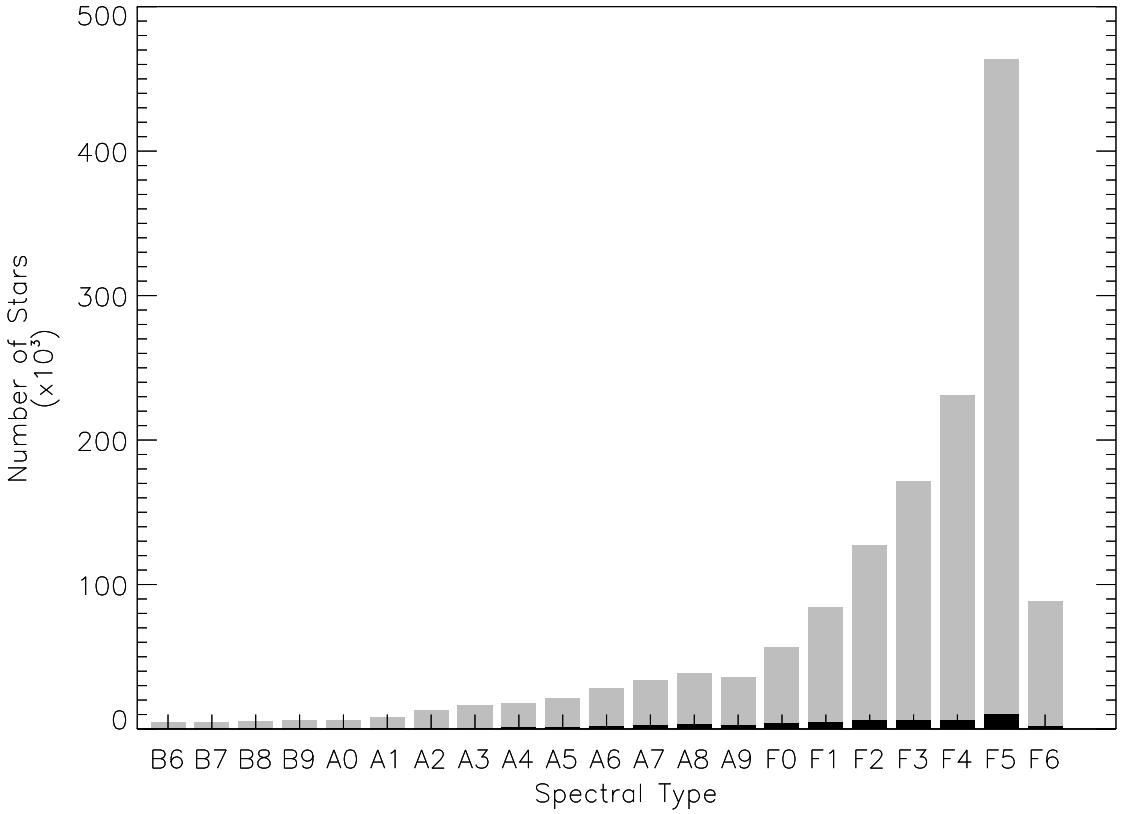

Figure 4.2: Distribution of the low-frequency pulsators, black bars, with spectral type, derived from $(J - H)$, compared to the total sample, grey bars. The lack of F6 stars is a result of the $(J - H)$ cut applied to the sample.

throughout the spectral type. The most comprehensive spread in the peaks is found to be in the A5–A9 stars, with the peak in mean frequency at A7. Here there are many peaks from the $5\,\mathrm{d}^{-1}$ lower limit to the $50\,\mathrm{d}^{-1}$ upper limit.

The amplitude plot in Figure 4.3 shows many of the peaks to have amplitudes less than about 400 mmag. Above this value, the detections are most likely a result of harmonics of eclipsing binary systems which fall above the $5\,\mathrm{d}^{-1}$ cut (they will also be present below 400 mmag). As indicated by the red line in this plot, the mean of the detected amplitudes increase, from about B9, to a peak in the F6 stars. This is an interesting result as the primary influence on the amplitude of a pulsation in the δ Sct stars is the rotation velocity (Breger 2000); the slower the rotation, the higher the amplitude that is observed. It is also the case that the slow rotators pulsate in radial modes, a combined effect which is observed predominantly in the high-amplitude δ Sct (HADS) stars. Figure 4.4 shows the rotation velocity of the A-type stars as a function of spectral type (Royer 2009). As the figure shows, the projected rotation velocity decreases rapidly in stars later then F0, which is consistent with the increase in amplitude seen in Figure 4.3. These results therefore provide further evidence to support theory.

The classical instability strip, as shown in Figure 1.8, ranges from about A2 to F4 in spectral type. The majority of the detected peaks in Figure 4.3 occur within these boundaries, with some spilling over into the hotter and cooler regions. This is somewhat reminiscent of the results from *Kepler* observations (e.g. Uytterhoeven et al. 2011; Bradley et al. 2015) suggesting that the boundaries are wider than currently calculated from theory.

Included in these observations there maybe present a number of examples of the HADS stars. The are know to show pulsations between $4 - 24\,\mathrm{d}^{-1}$ with amplitudes greater than 300 mmag (McNamara 2000; Balona et al. 2012b). They are found in the centre of the instability strip, from around A6 to F1 (McNamara 2000), where many detections of high-amplitude peaks have been made here. However, without inspection of the targets on an individual basis, confirmation cannot be sought of the nature of this variability.

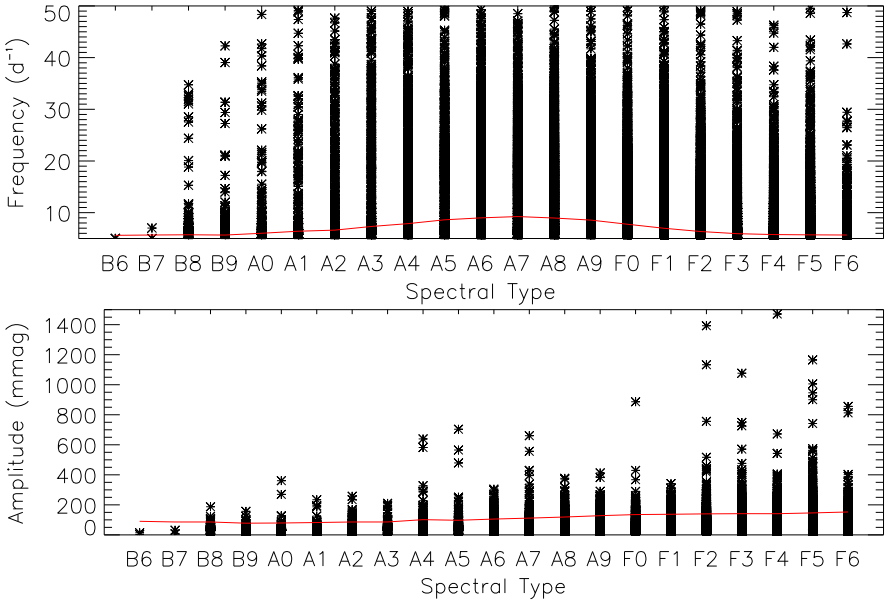

Figure 4.3: Frequency (top) and amplitude (bottom) distribution of the low-frequency pulsators with spectral type derived from $(J - H)$. The red line in the top plot shows the mean frequency for each spectral type. The red line in the bottom plot shows the mean amplitude multiplied by 10 for clarity.

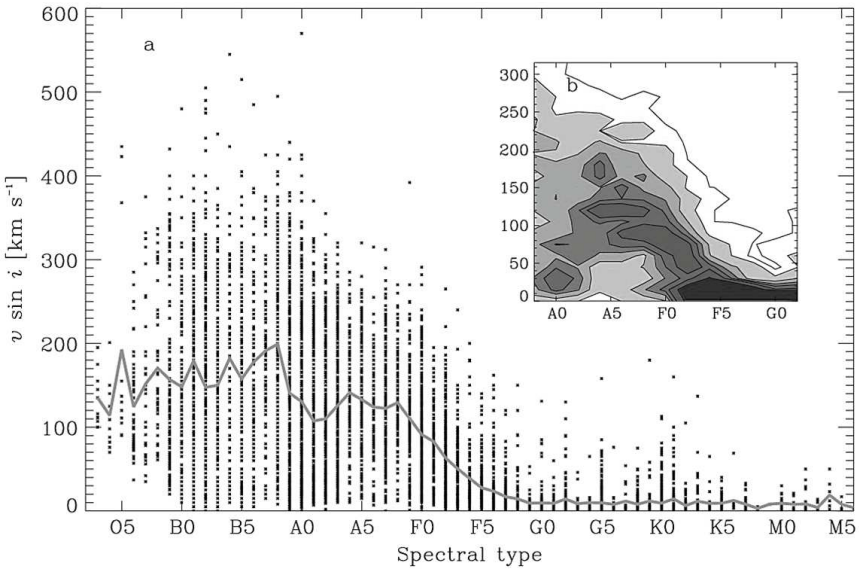

Figure 4.4: The projected rotation velocities, $v \sin i$, of stars in the HR diagram. The solid line in (a) is the average value per spectral type. The insert, (b), shows the density of the A- and F-type stars, where darker tones represent higher density. Figure from Royer (2009).

However, as this is neither a targeted study, nor are there accurate temperature diagnostics, the detection of peaks in the cooler stars in the sample must be regarded with caution. Such a large number of detections beyond the red boundary (Figure 4.2) leads to the suspicion that many of the detections are in fact false-positive. The frequencies of the detections in the cooler stars has begun to decrease, with more high-amplitude detections which are most probably due to the detection of binary harmonics. To investigate these targets further would require substantial effort as about 23 000 stars have spectral types cooler than F2.

With regards to the detections beyond the red-edge of the instability strip, it must also be noted that these stars may suffer significant reddening. The presence along the line-of-sight to the star of interstellar gas and dust may have shifted the assumed spectral types towards the cooler end of the scale presented here. It must also be realised that the local stellar environment may be home to extensive dust in circumstellar disks, such as is seen with the PMS stars. Most of the known pulsating PMS stars have $(J-H)$ colours greater than the cut-off applied to the sample, despite the young star being a hot A-type star (Zwintz 2008).

To provide an example of how the reddening affects the $(J-H)$ colour, and so the derived spectral type, the star J1403 (HD 122570 is considered; discussed in Chapter 6). The 2MASS J and H magnitudes for this star are 9.970 and 9.891, respectively, giving a $(J-H)$ colour of 0.079. Using the conversions of Tokunaga (2000) this implies a spectral type of A6. However, when taking into consideration the extinction along the line-of-sight (using data from Cardelli, Clayton & Mathis 1989; O'Donnell 1994; Schlegel, Finkbeiner & Davis 1998), the corrected colour is 0.051, placing this star at A4. Although still within the A-type stars, this demonstrates that the lack of reddening corrected colours can shift the determined spectral type to cooler stars.

4.3 The 50–300 d^{-1} Range

Of the 1.5 million F-, A- and B-type stars extracted from the WASP archive, 375 stars have been identified which show variations on the order of 30 min or less which are present in two or more seasons of observations. It is this region which the WASP project adds the most significant results to the study of the F-, A- and B-type stars, as its observing strategy fills a niche in the observations of these types of stars. The cadence of the WASP observations, coupled with the non-regular revisiting of observing fields provides data which can be used to search for high-frequency pulsators. Typically, such searches have been conducted on an one-by-one bases (e.g. Martinez, Kurtz & Kauffmann 1991) whereas the wide field-of-view afforded by WASP covers many more stars, making it a much more efficient tool for variability searches.

For these 375 objects, the periodograms were individually inspected, with the results of period searches presented in Table 4.1. The table shows two identifiers for each object (including the WASP ID which contains the J2000 coordinates), the $V-$band magnitude (Tycho-2; Høg et al. 1997), and a list of up to five detected frequencies and their corresponding amplitudes. Table 4.1 here shows an abridged version, with the full results shown in Appendix C.

As with the $< 50\,\mathrm{d}^{-1}$ results, the $(J-H)$ colour has been used to split the stars into the approximate spectral types to determine how the temperature of the star may effect the pulsations detected. However, with these stars the colours derived from a

Table 4.1: Abridged version of the photometric information for the 375 high-frequency pulsators. In the full table, Appendix C and available online[a], columns $6-15$ give the first five frequencies, if present, above $50\,\mathrm{d}^{-1}$.

WASP ID	Other ID	V	ν_1 (d^{-1})	A_1 (mmag)	...	ν_5 (d^{-1})	A_5 (mmag)
1SWASPJ000415.12-172529.6	HD 225186	9.05	60.08	3.40	...	–	–
1SWASPJ000537.79+313058.8	TYC 2259-818-1	11.70	52.92	1.47	...	–	–
1SWASPJ000830.50+042818.1	TYC 4-562-1	10.16	150.26	0.76	...	–	–
1SWASPJ000940.84+562218.9	TYC 3660-1935-1	10.34	66.37	3.15	...	–	–
1SWASPJ002436.35+165847.3	HD 2020	8.50	54.41	3.40	...	–	–

[a] http://vizier.u-strasbg.fr/viz-bin/VizieR-3?-source=J/MNRAS/439/2078/pulsetab

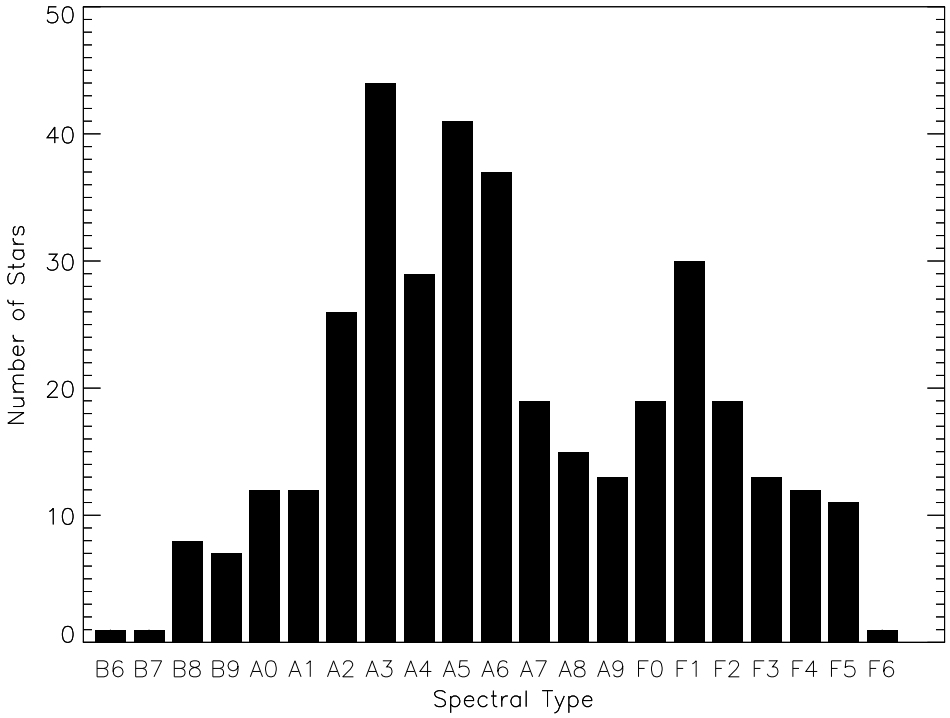

Figure 4.5: Distribution of the high-frequency pulsators with estimated spectral type.

simple colour index can lead to mis-classification, beyond the reasons stated above, and due to non-uniform chemical distributions at the surface of the star. Figure 4.5 shows the results of this procedure. It is clear from the figure that there are two peaks in the detections: in the early to mid-type A-type stars and the early F-type stars, with a significant number of the detections occurring in the A-type stars. This figure presents a contrasting result with the survey sample as a whole and the low-frequency detections (Figures 3.1 and 4.2) in that the A-type stars show a greater number of pulsators in this higher frequency regime when compared to the cooler stars in the same range.

The distribution of detected frequencies with spectral type, shown in Figure 4.6, shows no significant tendencies to a certain spectral type. There is a lack of high-frequencies towards the hotter end of the sample, however there are also fewer stars in this temperature range, so the small number of detections is expected. The highest

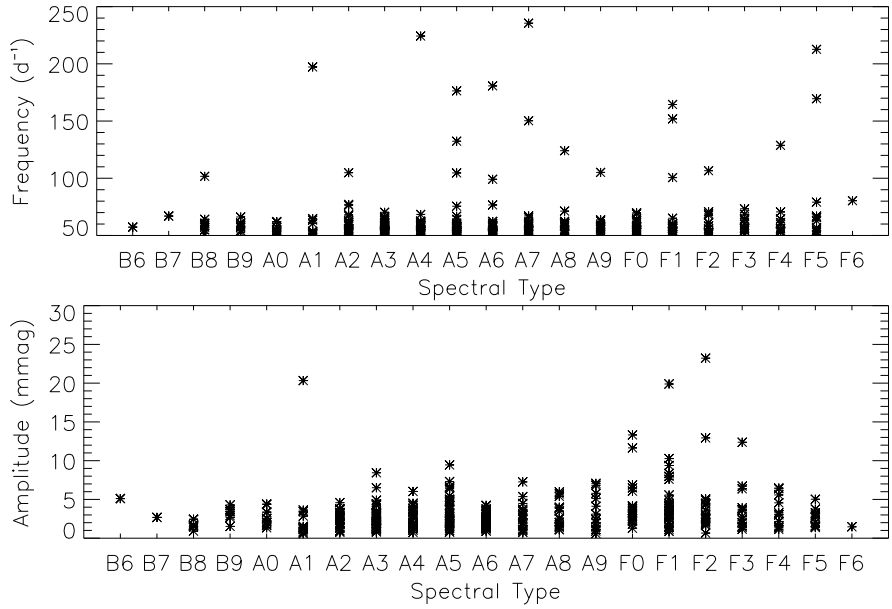

Figure 4.6: Frequency (top) and amplitude (bottom) distribution of the high-frequency pulsators with spectral type. Note, the data point for FO Aqr (F1 type, 104 mmag, 68 d^{-1}) has been excluded from the amplitude plot for clarity of the other data.

frequencies are detected in the roAp stars, with some high-frequency δ Sct and pulsating Am stars around 100 d^{-1} and the sdBV star(discussed in Chapter 6).

Figure 4.6 also shows the distribution of the detected amplitudes with spectral type. Unlike with the low-frequency range, all pulsations (expect FO Aqr, a well studied intermediate polar) have amplitudes below 25 mmag. Of course, in this frequency range there is no contamination from the harmonics of binary stars to accentuate the amplitude range. These amplitudes have also been confirmed through manual inspection of the light curves, and as such are confirmed to be due to pulsations. There has been no detection of the HADS stars in this frequency range, consistent with previous observations of this type of star.

The points in Figure 4.6 where the frequency is greater than about 100 d^{-1} represent the roAp stars, some high-frequency δ Sct stars, intermediate polars and sdBV stars. This is also the case for the amplitudes, except these are not due to any roAp star, due to their intrinsically low amplitudes.

Unlike the low-frequency results, the cooler F-type stars start to show a decline in pulsation detection later than F2 (Figure 4.5). This is an expected result, and is where the red-edge of the classical instability strip lies for the δ Sct stars, and there are many less stars in this range which can skew the results due to not accounting for reddening. The roAp stars are often found to be relatively cool amongst the A-type stars, which is why some of the highest frequency pulsations are found in the F-type stars in Figure 4.6 and, as previously stated, these stars show chemical spots on their surfaces, thus distorting the photometry. As these stars had their periodograms manually inspected, the results are more reliable than those in the low-frequency range. However, as the spectral types have been determined form the $(J - H)$ colour, caution must still be exercised as reddening factors have not been accounted for.

Included in the results of this frequency range are a number of already known pulsating stars (15 of the 375), in particular the sdBV pulsators. These stars have been highlighted in Table C.1. However, amongst these stars, there has been a detection of pulsations in a known sdB star, SB 815 (Graham & Slettebak 1973), which was previously determined not to vary (Østensen et al. 2010). This star is discussed in Chapter 6. The results of this survey highlight the power of continuous, long-term, photometric observations to detect low-amplitude variability.

4.4 The $> 300\,\mathrm{d}^{-1}$ Domain

The non-uniform sampling, coupled with the cadence of 30 s means the WASP data is not restricted by a Nyquist frequency. The exposure times, 30 s, would dictate the Nyquist frequency of $1\,440\,\mathrm{d}^{-1}$ but investigations can go beyond this 'limit' as the non-uniform revisiting of observing fields breaks the regularity. Given the possibility to probe to these very high frequencies, periodograms have been calculated up to $1\,440\,\mathrm{d}^{-1}$ for each of the WASP seasons for all of the targets in the survey. However, unlike with the lower frequency searches, the periodograms of this very high-frequency (VHF) search were not saved in their entirety due to the size of the files and the

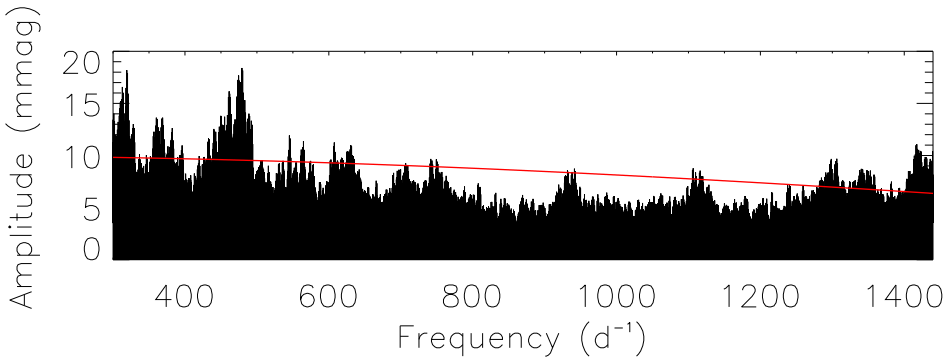

Figure 4.7: An example of the VHF periodograms where noise is identified as stellar variability. The red line represents the expected amplitude of a peak with an intrinsic amplitude of 10 mmag. The decrease in amplitude is a result of undersampling the pulsation.

storage available. Instead, on-the-fly peak identification and extraction was conducted, searching for the highest peak above $300\,\mathrm{d}^{-1}$ with a S/N value of greater than 3.0, with any identified peaks being saved to a file. Along with the principle peak, peaks with S/N > 3.0 in a range $\pm 5\,\mathrm{d}^{-1}$ were also extracted to check for aliases and any ambiguity between principle peaks for a given target.

The results show that there are many 'detections' in the data that occur just beyond $300\,\mathrm{d}^{-1}$ and around $400 - 500\,\mathrm{d}^{-1}$. Inspection of a small number of the periodograms show that in these frequency regions there are broad power excesses which have been identified as peaks. The source of these features is unclear, however they are presumed at this stage to be a result of noise, or effects from the $\sim$10 min field changes, i.e. cadence aliases. Figure 4.7 shows a high-frequency periodogram of a star which was identified to have VHF peaks, whereas upon visual inspection of the periodogram it becomes obvious that the peaks are not due to intrinsic variability. To date, one object has been identified as a new pulsator in the VHF regime and is discussed in Chapter 6.

To further complicate the detection of VHF peaks in WASP data, the amplitudes of pulsations in this domain will be diluted as a result of the exposure times. It is possible that a significant fraction of the pulsation is observed during the exposure,

thus no longer providing an 'instantaneous' measurement with regards to the pulsation period, as the ideal case would be. Coupled with this, the amplitude is decreased through under-sampling of the pulsation. An example of this is shown in Figure 4.7. The red line shows the decrease in amplitude of a 10 mmag pulsation at increasing frequencies. The dilution of the amplitude is described by a sinc function as the amplitude is an average of the cosine variations within the region bound by $\pm\nu_{sample}/2$. Mathematically the function is

$$\mathrm{f}(\nu) = \frac{2\sin\left(\frac{2\pi\nu/2}{\nu_{\mathrm{sample}}}\right)}{\frac{2\pi\nu}{\nu_{\mathrm{sample}}}}, \tag{4.1}$$

which can be simplified to

$$\mathrm{f}(\nu) = \mathrm{sinc}\left(\frac{\pi\nu}{\nu_{\mathrm{sample}}}\right), \tag{4.2}$$

where ν is the test frequency and ν_{sample} is the sampling frequency, which in the WASP case is 1/30s= 2880 d^{-1}.

To exploit this frequency domain to its full capacity, different detection methods need to be developed to distinguish between noise peaks and those due to intrinsic variability. And perhaps, as well as this, a different treatment of the raw WASP light curve with the aim of reducing the white noise level in this region of the periodogram.

4.5 Conclusions

This chapter has shown the diversity and quantity of pulsating A-type stars which can be found in the SuperWASP archive. Despite the low-frequency results being contaminated by many d^{-1} alias detections, there are still many thousands of potentially new discoveries of δ Sct stars. With closer inspection of these targets, coupled with future GAIA observations, accurate distances can be sought allowing these stars to be placed on the HR diagram. In doing so, the observational edges of the δ Sct instability strip can be better defined, thus allowing for the production of more accurate stellar models for these stars.

The spectral types of stars which have been found to show variability closely resembles the distribution of all the stars in the sample (cf. Figures 3.1 and 4.2). This is not a surprising result as it is in this spectral region that the instability strip crosses the main-sequence. Many A-type stars have been shown to have δ Sct pulsations in this frequency range (Rodríguez & Breger 2001; Balona & Dziembowski 2011), with similar correlations between the number of stars and the detected frequency and amplitude of the peaks.

The amplitudes found in the low-frequency range are consistent with the spectral types derived from the $(J-H)$ colour. The rotation velocity, $v \sin i$, decreases from the A- to F-type stars, allowing the pulsation amplitude to grow in the star (see Chapter 1). The rapid rotation seen in the A-type stars, with a peak at A5, causes deviation from the fundamental radial mode, splitting the mode into higher order, non-radial components. These higher order modes pulsate with lower amplitudes, and often show a more complex frequency spectrum. The results in the low-frequency range have been shown to follow this pattern.

In the high-frequency range, most of the detections occur in the A-type stars, with a secondary peak at F2. The amplitudes follow a similar pattern to the low-frequency detections, with respect to spectral type. However, in this range there are no detections of high-amplitude peaks. All detections in this range are below 25 mmag in amplitude (expect FO Aqr), this is consistent with the rapid rotation of the A-type stars. The exception to this is the slow rotation of the chemically peculiar Ap and Am stars that are known to pulsate in this range (Wolff 1983). However, these stars are intrinsically low-amplitude pulsators, with amplitudes up to about 10 mmag in $B-$band for the roAp stars (Kurtz et al. 2006) and about 5 mmag for the Am stars in SuperWASP photometry in this frequency range (Smalley et al. 2011).

There is much work to be done to exploit the full results of this survey, especially with regards to the low-frequency detections. Given the number of stars, and the variety of pulsation classes which occupy this frequency range, detailed follow-up observations are required to properly classify the results. The removal of false-positive detections due to alias peaks will provide a truer representation of the number of low-

frequency pulsators in the SuperWASP archive. The lower frequency stars represent the more evolved stars which are rarer to detect due to their relatively short life-time compared to the main-sequence stars (Rodríguez & Breger 2001).

The results of the VHF domain suggest a great deal of effort is required to exploit this frequency domain. It has become apparent, that while WASP has the capabilities to detect such high-frequency pulsations, a different method of peak identification, and even light curve reduction, is needed to overcome the issues with the high noise level in this domain. Further to this, as the amplitudes are reduced through under-sampling the pulsation and the length of the exposure times, the WASP observations are suitable for the detection of only the highest amplitude pulsators in this frequency domain.

5 Spectroscopy

5.1 Introduction

Before the results of the archive survey are presented, it is convenient, and useful, to discuss spectroscopy in general, and the spectral classification of the F-, A- and B-type stars.

There are several spectroscopic techniques that can be used to study the atmospheres of stars. From simple 'long-slit' spectroscopy, to the higher resolution 'echelle' spectroscopy, and the use of 'spectropolarimetry' to observe the magnetic field structure of a star. This Chapter will focus on the long-slit and echelle spectroscopic techniques as they have been employed for follow-up observations of the survey results.

5.2 Instrumentation

The equations in this section are from 'Astrophysical Techniques' by Kitchin (2003).

Many astronomical spectrographs make use of diffraction gratings which rely on constructive interference to form the desired spectrum. At its basics, a spectrograph consists of: a slit, a collimator, a dispersing element, a camera, and a detector. The slit provides the aperture for the instrumentation, the collimator then corrects the light from the slit to provide a parallel light beam for the dispersing elements which provides the main source of the resolution of the final spectrum. The element, either a prism, a grating, or a combination, split the light which is refocused by a camera onto the CCD detector.

As previously mentioned, the most common dispersion element is a diffraction grating. These consist of a reflective surface lined with parallel slits or groves. The diffraction grating is normally inclined to the path of the incident parallel light such

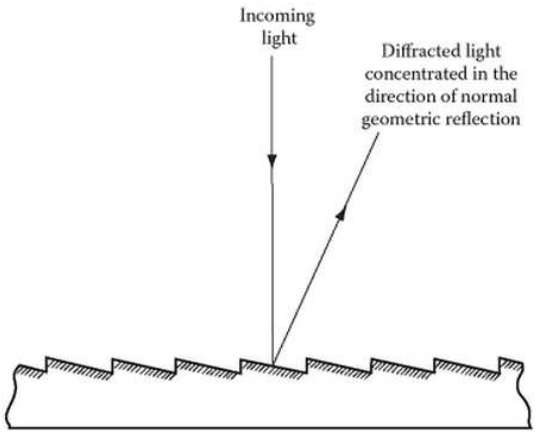

Figure 5.1: An enlarged section of a blazed grating. From Kitchin (2003).

that the grating equation is formed:

$$n\lambda = d(\sin\alpha \pm \sin\beta), \tag{5.1}$$

where n is the order, d is the spacing of the grating lines, and α and β are the angles that the incident and reflected light make with the normal, respectively. The disadvantage of this type of grating, however, is that each spectrum produced significantly decreases in intensity as the order increases. To combat this issue, the grating can be 'blazed'. This process changes the angles of the individual mirrors which make the grating (Figure 5.1). The angle that the blazed mirror surface makes to the parallel is called the 'Blaze Angle'. For the low-order observations of long-slit spectrographs, the angles are such that the light is concentrated on a specific order such that only a single spectrum is focused onto the CCD (others may be produced and seen in some spectrographs, or filtered out). In this case, the final image is of the slit with a bright 'streak' along the centre which represents the spectrum of the star. A visual representation of this is shown in Figure 5.2 with a slit image and 1D spectrum from the SALT/RSS.

The linear dispersion of a spectrum obtained, for a particular order, can be described by a relation between the focal length of the focusing camera, f_2, the wavelength

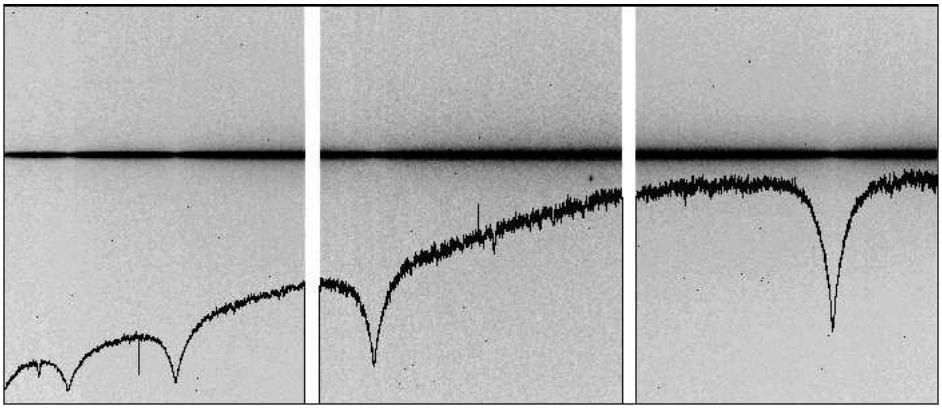

Figure 5.2: The image of a spectral slit and extracted spectrum from SALT/RSS. The dispersion direction is the x-axis, which is in CCD pixels. Evident are the breaks in the spectrum where the mosaic detectors are not present. The 1D spectrum has been extracted before any standard corrections or calibrations have been made.

λ and β, so that:

$$\frac{dx}{d\lambda} = f_2 \frac{d\beta}{d\lambda}. \tag{5.2}$$

This can be combined with the differential of the grating equation, equation (5.1), and assuming α to be constant, so that:

$$\frac{dx}{d\lambda} = \pm \frac{n f_2}{d \cos\beta}, \tag{5.3}$$

and given that β varies little over the given order, this effectively becomes:

$$\frac{dx}{d\lambda} \approx \text{constant}. \tag{5.4}$$

This is a useful results which differs from the strong wavelength dependence of spectrographs which use prisms. The wavelength calibrations that are conducted at the final stage of spectroscopic reduction remove the final variations in the wavelength.

The resolution of the spectrum obtained with a certain spectrograph is dependent on the order (n) of the spectrum as well as the number of lines on the grating (N), such that $R = Nn$. However, it can also be changed by the user by varying the width of the entrance slit. In increasing the slit width, the resolution is decreased, however the sensor is exposed to more light, thus ideal for fainter targets.

Optimum resolution occurs when

$$s = \frac{f_1 \lambda}{D}, \tag{5.5}$$

where s is the slit width, f_1 is the focal length of the collimator, and D is the width of the beam (and is equal to $L \cos \beta$, where L is the length of the grating). The dispersion of the spectrum can be written as

$$\frac{\lambda}{D} = \frac{\lambda}{Nn} \frac{d\beta}{d\lambda} \tag{5.6}$$

where N is the number of lines on the grating. Rearranging equations (5.5) and (5.2) and substituting into equation (5.6) and rearranging gives

$$s = \frac{\lambda}{Nn} \frac{f_1}{f_2} \frac{dx}{d\lambda}. \tag{5.7}$$

As f_1 and f_2 are constants, as is the differential, from equation (5.4), and $R = Nn$, the final dependence of the slit width on the resolving power is:

$$R \propto \frac{\lambda}{s}. \tag{5.8}$$

In this, the resolution is, for the long-slit spectrographs, limited by the the order n of the spectral observations, but can be varied with the slit width. However, it is possible to increase the resolution by either increasing N or n. This is the case for the 'echelle' spectrographs. Again, if the linear dispersion is considered, for an echelle grating this takes the form:

$$\frac{dx}{d\lambda} = \pm \frac{d \cos^3 \beta}{m f_2}, \tag{5.9}$$

as the blaze angle of the grating has been greatly increased (Figure 5.3). As the orders produced by these gratings are high, the resolution is much higher than in the long-slit version. Echelle spectrographs also require a second, low-order, cross-dispersing element before the CCD can be exposed to the spectrum as the orders overlap and are effectively stacked upon one-another. The final result of an echelle output is shown in Figure 5.4.

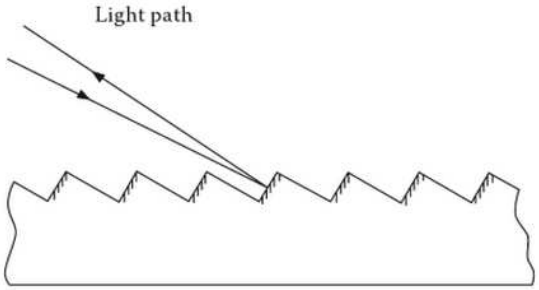

Figure 5.3: An enlarged section of a blazed echelle grating. The separation of the apertures is much smaller than for the normal grating. From Kitchin (2003).

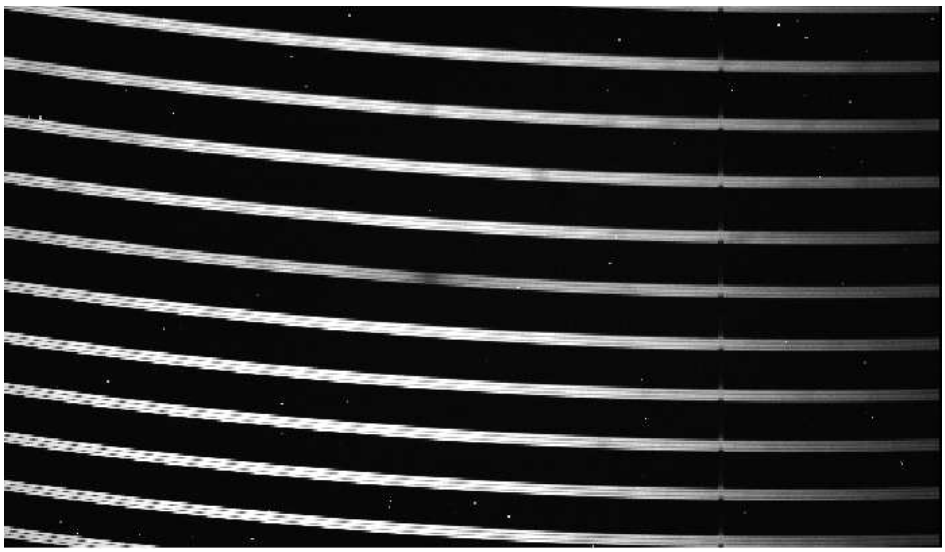

Figure 5.4: A section of the image of a dispersed spectrum from an echelle spectrograph (SALT/HRS). The many spectral orders have been separated with a 2^{nd} order cross-disperser. The spectral dispersion direction is the x-axis, and the order dispersion is in the y-axis. The spectrum has not been corrected for instrumental sensitivity.

5.2.1 Long-Slit Spectrographs

5.2.1.1 RSS

The Robert Stobie Spectrograph (RSS) is the primary instrument used on the 11 m Southern African Large Telescope (SALT) located at the Sutherland station of the South African Astronomical Observatory (SAAO; Burgh et al. 2003; Kobulnicky et al. 2003). It is a many-mode instrument, which is utilised here for its long-slit capabilities. It is sensitive in both the blue and red regions, with the user grating selection identifying where in its wavelength coverage the observations will be made. In this work, grating 'PG2300' is used, providing a wavelength coverage of $3800 - 5000$Å and a resolution of $R \sim 5600$ at the central wavelength. The slit width is set at $0.6''$, with no filers used to maximise throughput at all wavelengths.

The instrument's detection device is the SALT Imaging Camera (SALTICAM; O'Donoghue et al. 2003) which is a mosaic of three detectors leading to two breaks in the final spectrum where there is no detector (see Figure 5.2). In the instrument set-up that is used, these gaps fall at 4267Å and 4633Å and are 20Åwide. The throughput of the instrument configuration is very low. For an 11^{th} magnitude, typical A-type star, only 7 per cent of the stellar flux reaches the detector. As such, observations of about 500 s are needed to achieve a S/N of 100 for this type of star. Observations with RSS were made in service mode, utilising UK Science Consortium (UKSC) time.

5.2.1.2 ISIS

The Intermediate dispersion Spectrograph and Imaging System[1] (ISIS) is mounted on the 4.2 m William Herschel Telescope (WHT) located on La Palma, Spain. The instrument is capable of observing in both read and blue spectra simultaneously with the use of a dichroic filter. This work used both the blue and red arms of the spectrograph. To obtain the blue spectra, the R600B grating is used which provides a dispersion of

[1] `http://www.ing.iac.es/Astronomy/observing/manuals/ps/general/obs_guide.pdf`

33Å/mm covering 1825Å centred on 4500Å. The red arm observations are made with the R1200R grating centred on 6200Å covering 1055Å with 17Å/mm. The throughput of the ISIS set-up is much greater than the RSS, with the same 11^{th} magnitude star needing only 100 s observations to reach a S/N of 100 in the blue arm. The red arm S/N reaches about 65 for the same exposure time. Observations were made in service mode after proposal acceptance.

5.2.2 Echelle Spectrographs

5.2.2.1 HamSpec

The Hamiltonian Spectrograph (HamSpec; Vogt 1987) is mounted on the Shame 3 m telescope at Lick observatory, USA. The echelle grating has a blaze angle of 64.7° with 31.5 lines/mm. It is capable of observing 107 orders, between $57 \leq n \leq 163$, providing a wavelength coverage of $3500 - 10\,000$Å. The instrument has a peak throughput of about 7 per cent at around 6000Å. After light enters the slit, it first encounters the collimator, and after reflection from the echelle grating, passes through two cross-dispersion prisms which split the light perpendicular to the spectral dispersion. Finally the light is focused with a Schmidt camera onto the CCD.

Two stars in this work have been kindly observed with the HamSpec during John Southworth's (Keele University) allocated time by Kelsey I. Clubb (University of California, Berkeley). The reduction for these stars were conducted by Clubb using the automatic IDL reduction routines for HamSpec data. The code performs flat-field corrections, be-biases, cosmic ray cleaning and wavelength calibrations, but does not correct for the blaze function.

5.3 Data Reduction

There are several tools to produce a 1D spectrum from a FITS file of the slit image. Often, but not always, observatories produce their own pipelines to process the data.

This is very useful, and often a quick solution to data reduction. However, as the pipelines are produced for generic use, and all data are different, better results may be obtained with user step-by-step reductions. There are several packages which are capable of spectral data reduction, with observers quite often using IRAF packages. However, for the spectra presented in Chapter 6, packages available through the STARLINK project[2] have been used, with the main package being FIGARO (Shortridge et al. 2004).

To reduce spectral data, the observations need to be processed to remove artefacts introduced by the instrumentation, such as flat-field and bias effects, remove cosmic ray hits, and provide an accurate and precise wavelength calibration. The following are brief steps to the reduction process with the STARLINK software:

- Combine all bias frames into a master bias by running MEDSKY;
- Combine all flat-field frames into a master flat by running MEDSKY;
- Subtract the master bias frame from the target with ISUB;
- Divide the target by the master flat image with IDIV;
- Collapse the target spectrum to 1D using EXTRACT;
- Collapse the arc spectrum to 1D using EXTRACT;
- The code ARC can now be run which allows the user to match the arc spectrum to known wavelengths of emission;
- The wavelength solution is then copied to the target spectrum with XCOPY.

These steps leave the user with a 1D, wavelength calibrated spectrum, which can then be normalised and compared to standard stars to determine its spectral class.

[2]http://starlink.jach.hawaii.edu/starlink

5.4 Spectral Classification

This section is based on 'Stellar Spectral Classification' by Gray & Corbally (2009).

The fundamental purpose of spectroscopy if to group stars together (Gray 2014), as is the case with most other sciences. Beyond the overarching classes of F-, A- and B-type stars, subclasses exist to differentiate between phenomena observed in the spectra of stars.

The first stage of spectral analysis must be spectral classification. Approaching a spectrum without the knowledge of any spectral peculiarities will lead to confusion and quite probably the mis-identification of spectral features. Lists of standard stars exist for this sole purpose. Ideally, spectral standards should be observed at the same time as the target stars are observed to have comparable spectra from the instrument configuration and observing conditions. However, this is not always possible due to time constraints, and the proximity of standard stars to the target star. Usefully, however, there are many repositories online which have the normalised spectra of standard stars available to download. As such, the spectra for standard stars used in this Chapter are taken from the website of Richard O. Gray, `http://stellar.phys.appstate.edu/Standards/`, and are used in Gray & Corbally (2009), or from the VizieR catalogue of Gray et al. (2003). Spectral classification is conducted with low-resolution spectra of $R \sim 2000$, in the blue region from about $3800 - 4600$Å. The reason for this is historical and results from the wavelength dependence of old photographic plates.

As well as temperature classes, the MK classification system also considers the luminosity class of the star, which can be used as a proxy to estimate the surface gravity, $\log g$, of the star. Table 5.1 lists the class identifier and the type of star to which it refers.

Table 5.1: The luminosity classes of the MK classification system.

Class	Type of Star
Ia	Luminous supergiants
Ib	Less luminous supergiants
II	Bright Giants
III	Giants
IV	Subgiants
V	Main-sequence stars
VI, sd	Subdwarfs
D	White Dwarfs

5.4.1 The Normal Stars

The reference to 'normal' stars here is to differentiate those that show the expected spectral lines and those that do not. However, as was discussed in section 1.2, it is very difficult to determine what a normal A-type star is. Here it is assumed that normal refers to stars which follow the standard line rations between the Balmer, metal and Ca lines.

The normal early type stars have relatively simple spectra to classify. The presence of strong hydrogen lines, the growth of the Ca II K line and the development of the Mg II λ4481 all aid in the initial classification of a star. For the hottest stars studied here, the B-type stars, the spectrum is heavily populated with lines of He I, II and Si II, III, IV, as well as the Balmer lines. As the effective temperature of the stars decrease, the helium and silicon lines begin to weaken and the presence of Ca II and Mg II become the most dominant lines, other than the Balmer lines. At this point in the spectral sequence the B-type stars flow into the A-type stars. It is these stars which show the strongest Balmer lines, peaking at about A3, and the ever increasing Ca II K line. The Mg II λ4481 line is also becoming stronger in the A-type stars, with the slow development of other metal lines.

With the slow decrease in Blamer line strength from A3, and the increasing strength of the metal lines, the A-type stars merge into the F-type stars. These stars

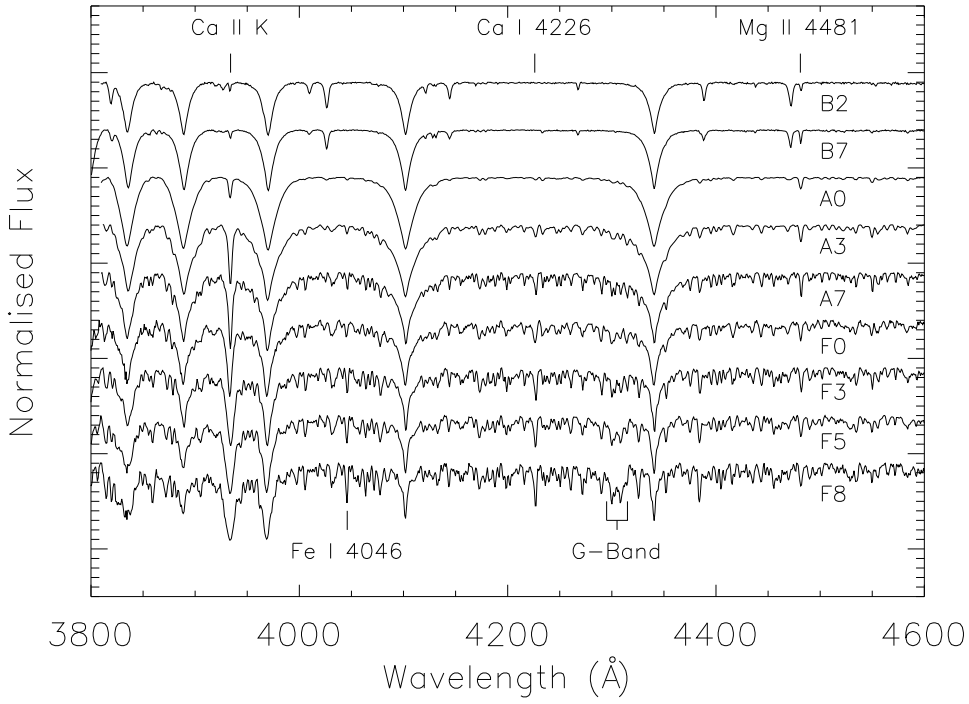

Figure 5.5: The spectral sequence of the early type stars. Many more lines start to form as the sequence decreases in temperature. The Balmer lines are strongest around A3, with the Ca II K line continually growing in strength. At about F3 the G-band feature around λ4300 starts to form due to the diatomic molecule CH. Recreated after Gray & Corbally (2009).

start to become dominated by many metal lines, and show a decreasing strength of and line blending in the Balmer line wings. The Ca I λ4226 line continues to grow, and the emergence of molecular lines occurs around F3 with the G-band formed due to the diatomic molecule CH at around λ4300. Figure 5.5 shows the change in the spectra from B2 through to F8. All stars are standard stars, or stars which match the standards very closely. The resolution of the spectra are 1.8Å.

A careful comparison must be first made between an observed target and the standard stars. Other than identifying peculiar lines in the spectrum, this process also

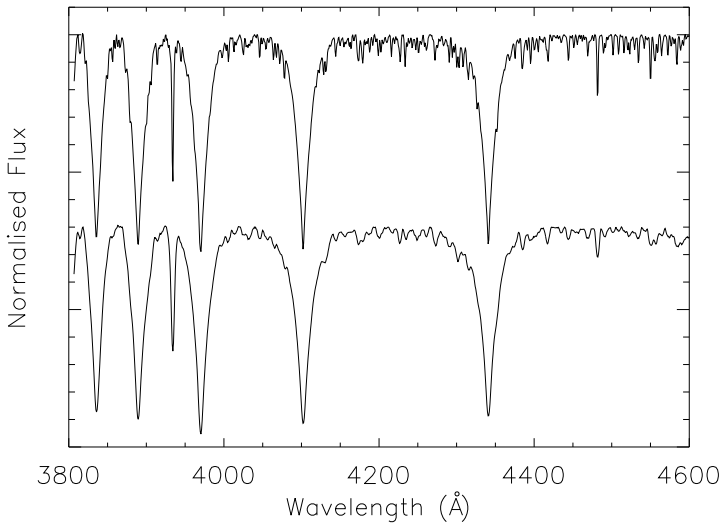

Figure 5.6: A comparison between a low and high $v \sin i$ spectrum of an A2 type star. The upper spectrum is of the slowly rotating star, with the lower being the rapidly rotating star. The $v \sin i$ is measured to be $180\,\mathrm{km\,s^{-1}}$. Despite the spectra being taken with the same resolution, it is clear that line definition is lost in the lower spectrum. Recreated after Gray & Corbally (2009).

enables an initial indication of the projected rotational velocity ($v \sin i$) of the star, as indicated in Figure 5.6. Here, a slowly rotating A2 star is compared with an A2 star with a $v \sin i = 180\,\mathrm{km\,s^{-1}}$. The rotation has the effect of reducing the spectral resolution, and as such, many of the lines are 'washed out' in the spectrum which may lead to an earlier classification that is incorrect.

As listed in Table 5.1, the luminosity classes also have an affect on the spectrum of a star. Figure 5.7 compares the spectra of six A5 stars with different luminosity classes. The classification of a star's luminosity provides an initial estimation of its surface gravity, $\log g$, for later spectral analysis. The luminosity has a dramatic effect on the appearance of a stellar spectrum. In the late B-type stars down to about A7 the main criterion for luminosity classification are the wings of the Balmer lines which narrow for increasing luminosity, however, after A7 to F2 this effect becomes very

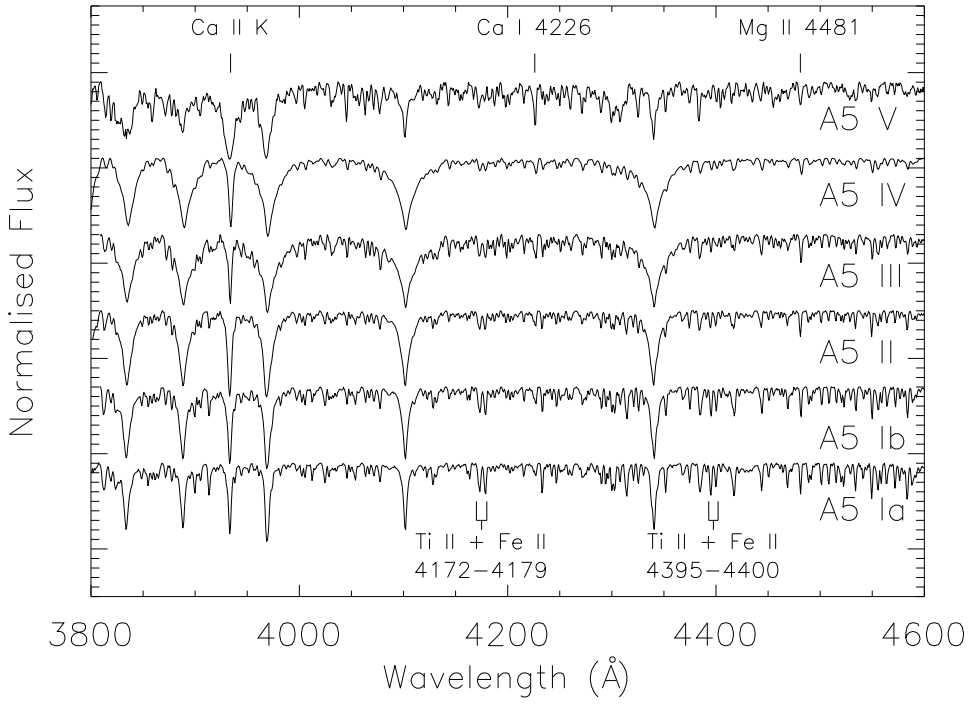

Figure 5.7: The luminosity effects at A5. The Ca II K line and the Mg II λ4481 lines are insensitive to luminosity, whereas the Balmer lines weaken with increasing luminosity and the blend of Fe II and Ti II at $\lambda\lambda 4172 - 4179$ and Fe II at λ4233 increase with luminosity. Recreated after Gray & Corbally (2009).

difficult to detect until it is not noticed after F2. When this is the case, the presence of ionised Fe and Ti lines must be used. The blended feature around $\lambda\lambda 4172 - 4179$ always increases in strength with luminosity in the late A- and F-type stars.

5.4.2 The Peculiar Stars

After comparison with the 'normal' stars, if it is found that the target star does not fit into the standard classification scheme the possibility that it is a peculiar star must be entertained. This will be apparent if the spectrum can be fit by several different spectral

types based on the Ca II K line, the Balmer lines and the metal lines, there are very strong lines that appear in the spectrum which are not expected for the temperature class, or if the metal lines are under-abundant based on the temperature derived from the Balmer lines.

There is a whole wealth of peculiarities in the late B- to mid F-type stars, and to discuss them all here in detail is unnecessary. The focus will be applied to the main classes of peculiar stars which show pulsations in their light curves. For a full discussion on the following classes of stars the reader is referred to the text *Stellar Spectral Classification* of Gray & Corbally (2009): the helium-strong and helium-weak B-type stars, the mercury-manganese (HgMn) B-type stars, and the barium dwarf F-type stars.

Below, the three main classes of pulsating peculiar stars have been selected for discussion. It is expected that these types of stars may be present in the results of the archive survey, and so more detail is presented on the classification of these stars.

5.4.2.1 The Am Stars

The non-magnetic, metallic-lined, Am stars are quite common among the A-type stars, with a predicted 50 per cent of A8 stars being classified as Am stars (Smith 1973). The first formal discussion of the Am stars was made by Titus & Morgan (1940) when they observed bright members of the Hyades Cluster. They noted six stars which were originally classified as Ap but were systematically less luminous than the rest of the sample. Analysis of the metallic lines suggested that they should be classed as F-type stars. However, the stars would then have unusually weak Ca II K lines for the F-type stars. As such, the authors choose to leave the classification as A-type stars due to two reasons: (1) they are A-type stars in the Henry Draper Catalogue, and (2) faint A-type stars observed with lower spectral resolution would not show the metallic line abnormalities and so would be classed as A-type stars based on the Ca K line. Formal identification for the Am stars was provided by Morgan, Keenan & Kellman (1943) who designated 63 Tau as the class prototype.

The Am stars are classified on the appearance of three features of the spectrum: the Ca K line, the Balmer lines, and the metallic lines. For a star to be classed as an Am star the Ca K line and the metallic lines must differ in spectral type by at least five subclasses, if the difference is less than this then they are classed as marginal Am stars, denoted 'Am:'. For an example, Figure 5.8 compares an A7m star to the three standard stars which match the three different features. The Am star plotted, HD 141795, has a Ca K line type the same as the A2 comparison, Blamer lines which match the A5 star, and metallic lines which are the same as the A9 star. To convey these differences in the spectral type of Am stars a special notation is used. For the example shown the spectral type is:

kA2hA5mA7

where the Ca K line, Hydrogen and metal lines are listed in order and denoted by the lower case letters k, h, and m, respectively. Further to this, Conti (1970) suggested that the Am phenomenon is present in stars with under-abundances of Ca and/or Sc and over-abundance of Fe group, and heavier, elements. More recently, detailed analysis of the typical abundance patterns in Am stars show under-abundances of C, N, O, Mg, Ca and Sc, and over abundances of Fe peak elements, Zr, Y and particularly Ba when compared to Solar abundances (Wolff 1983; Adelman et al. 1997; Fossati et al. 2007). These abundance patterns however result from detailed spectral analysis and not the initial classification of the star.

Finally, the spectra of Am stars normally are very sharp lined due to the intrinsically low $v \sin i$. Since the Ca K line used for classification is almost insensitive to rotation (see Figure 5.6) the lack of rapidly rotating Am stars is not a bias effect, and allows for a confident classification of Am status for a star. However, as the leading theory for the low $v \sin i$ in these stars is binarity, one must be very cautious when concluding that the Am phenomenon is present in a star, as binary contamination is a real possibility. Indications of a second star in the spectrum, such a double lines or the presence of lines commonly seen in cooler stars, must be carefully ruled out.

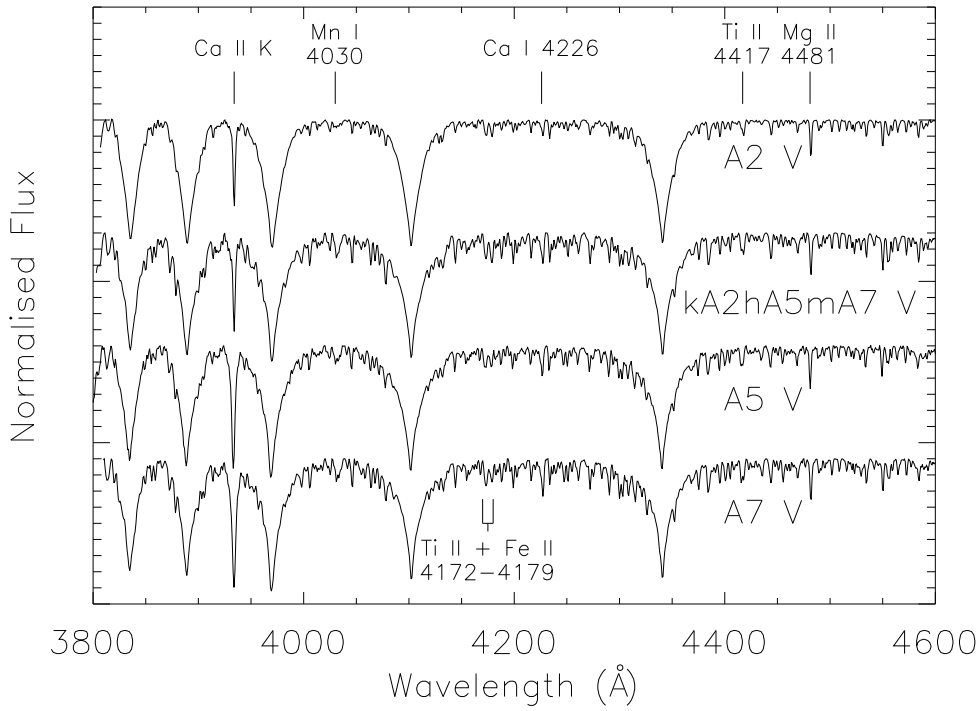

Figure 5.8: The spectrum of an Am star compared to the normal stars which constitute its classification. As can be seen, the Ca II K line agrees the the A2 star, the Balmer lines match the A5 star, and the metal lines have the same strength as the A7 star thus leading to the classification of kA2hA5mA7. Recreated after Gray & Corbally (2009).

The Am star classification is also applied to the ρ Puppis stars which are probably evolved versions of the Am stars. They show late F5 hydrogen lines and luminosities in the range II-III to Ib, suggesting that they are indeed evolved. There are some ρ Pup stars known to pulsate like δ Sct stars (Kurtz et al. 1995), which is why they are afforded a brief mention here. The presence of the pulsations in the ρ Pup stars suggests that convection has not yet fully set in, as the He II ionisation zone must still be intact, as well as this, Am abundance anomalies are still present in the atmosphere. The ρ Pup stars once belonged to a group called the δ Del stars (after δ Delphini, the group prototype), however this notation has been dropped due to conflicting descriptions on the characteristics of group members (Gray & Garrison 1989).

5.4.2.2 The Ap Stars

Rarer than the Am stars are the chemically peculiar Ap stars. Constituting only about 10 per cent of the A-type stars (Wolff 1968), the Ap stars have strong global magnetic fields and show over-abundances of the rare earth elements. They differ from the Am stars in that they only show enhancements of certain heavy elements, rather then nearly all.

The Ap stars have a long history, with Maury & Pickering (1897) identifying 12 stars having peculiar spectra between the F-, A-, and B-type stars. Work continued on the classification and grouping of the Ap stars throughout the early 20$^{\text{th}}$ Century with the creation of, and addition to, two groups based on either enhanced Si or Sr (Cannon & Pickering 1901; Cannon & Pickering 1912b; Cannon & Pickering 1912a). The beginnings of today's classification system however came from W.W. Morgan in a series of eight papers in the *Publications of the Yerkes Observatory* (1931-1933, also see Morgan 1933), in which he identified five groups of Ap stars, namely the: Mn II, λ4200, Eu II, Cr II, and Sr II stars. This was then built upon by Jaschek & Jaschek (1958) with the introduction of mixed element groups, and by Osawa (1965) who also considered the Ca II K line and Balmer lines, much in the same way as the Am stars are classified. Modern classification convention mainly uses the simple identification

of which elements are over-abundant, but in some cases the more detailed class is provided.

As is always the case with classification, the target star must first be assigned a 'normal' spectral type based, as previously mentioned, roughly on the Balmer lines in the spectrum. With the Ap stars, it is not wise to use the Ca II K line as a temperature indicator as this can be affected by the chemical peculiarities. For the early Ap stars the Balmer lines remain well structured and very similar to the 'normal' stars. However, with later Ap stars the structure of these lines can become very distorted and so it may only be possible to assign an estimate to the temperature or luminosity class. If this is the case, such classifications have the addition of a ':' (as with the marginal Am stars) to signify uncertainty. The hydrogen line profiles can also become very distorted when considering the rapidly oscillating Ap stars (Cowley et al. 2001), which is indeed one of the types of pulsators the survey will uncover.

Once the temperature and/or luminosity is established, one then concentrates on the lines which specify the type of peculiarity. The modern classification focuses on four elements that are prominent in the Ap stars: Si II, Cr II, Sr II, and Eu II. The specific lines which should be checked in the spectrum are shown in Table 5.2.

Figure 5.9 is a good example of a mixed-class Ap star, β CrB. Clearly present in the spectrum are most of the prominent lines listed in Table 5.2 apart from the Si II lines which only appear in the hotter Ap stars. The Cr II λ4111 is clearly visible in the wing of the H_δ line, the Sr II λ4077 line is stronger than the bracketing standard stars, and the Eu II λ4130 is very much enhanced with regards to the A7 and A9 stars. As can be seen, in the later type Ap stars some of the defining spectral lines can be hard to identify against the ever increasing strength of the metallic lines. However, careful comparisons can extract these lines from the spectrum.

Perhaps the most famous of the Ap stars, and worth a mention here, is Przybylski's star (Przybylski 1961). This star shows a most peculiar spectrum (Figure 5.10). Originally designated as a G0 star with unusual abundances by its discoverer, it is now considered as an Ap star who's strongest lines, other than the Blamer lines and Ca II H & K lines, are the ionised lanthanides with Fe under-abundant by about a factor of

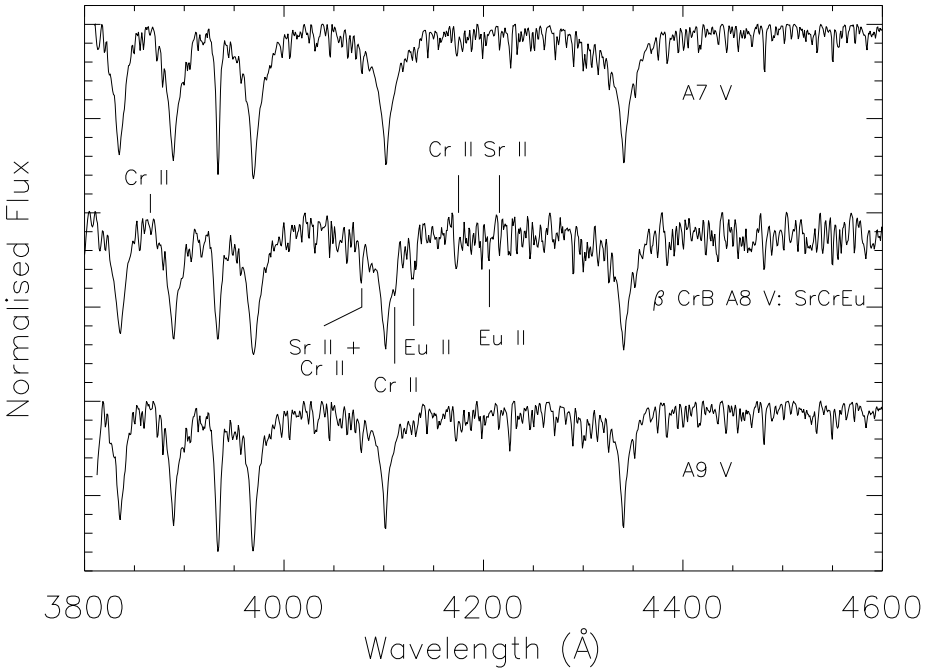

Figure 5.9: The spectrum of an Ap star, β CrB, compared to the normal stars which bracket its classification. There are lines which show significant over abundances compared to the normal stars. The presence of either Cr, Eu, Si or Sr, or a combination of them, lead to the classification of the star. Shown here is an A8p SrCrEu star. Recreated after Gray & Corbally (2009).

Table 5.2: The prominent lines used to classify Ap stars (from Gray & Corbally 2009).

Ion	λ (Å)	Comments
Si II	4128 & 4131	Form a close doublet in classification spectra; strongest lines of Si II
	4200	Appears in only the hotter Si II stars
	3856 & 3862	Use to confirm Si peculiarity
	4002, 4028 & 4076	Note 4076 coincides with Sr II λ4077
Cr II	4172	Generally strongest line of Cr II
	4111	Blended with H_δ; used to confirm Cr peculiarity
	3866	Use to confirm Cr peculiarity
	4077	Coincides with Sr II λ4077
Sr II	4077	Strongest line, but can be confused with Si II λ4076 & Cr II λ4077
	4216	Always confirm Sr peculiarity with this line
Eu II	4205	Generally least blended line of Eu II
	4130	Can combine with other lines and form a blend that appears similar to Si II $\lambda\lambda 4128 - 31$

10 below solar (Cowley & Mathys 1998; Bord et al. 1998; Cowley et al. 2000). Cowley et al. (2004) suggest there is evidence for two radioactive elements in the spectrum of Przybylski's star: promethium and technetium. However the presence of these two elements is quite controversial, especially Pm as its most stable isotope, ^{145}Pm, has a half life of just 17.7 yr thus requiring continual formation in the star's atmosphere. This star is quite an enigma among the Ap stars, and demonstrates the vast spectrum of peculiarity in stellar spectra and atmospheres.

Finally, one must also bear in mind the surface structure of the Ap stars. Due to their strong global magnetic fields, surface inhomogeneities occur in the form of spots. However, unlike spots on cooler stars, the spots on Ap stars result from the interaction between the magnetic fields and the peculiar elements in the atmosphere and are very stable, often lasting for tens of years. The spots form around the magnetic poles of the star. As the magnetic field axis and the rotational axis of the Ap stars are usually mis-aligned, as in the rigid rotator model of Stibbs (1950), the rotation of the star

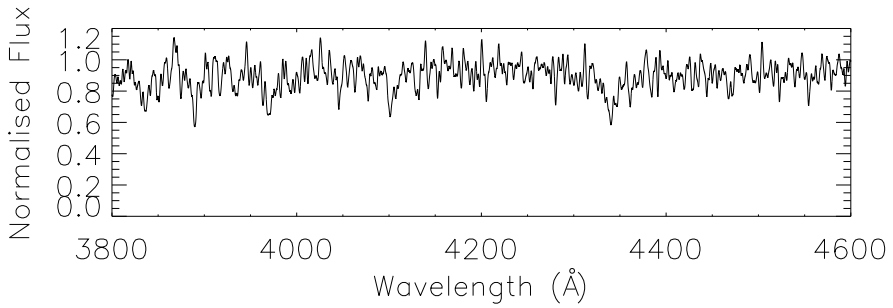

Figure 5.10: A spectrum of Przybylski's star. The spectrum was obtained with UVES, with the resolution reduced to that of classification resolution. There is significant weakening of the Balmer lines, leading to the original classification of G0, but also the presence of Sr, Eu and Cr lines. Data from the ESO archive, obtained by Cowley et al. (2004).

allows for different magnetic poles, and therefore spots to be viewed. As a result, the spectrum of an Ap star varies over its rotation period. This must be taken into account when performing abundance analysis, as with only a single spectrum lines of certain elements may not be present at that particular rotation phase.

The cool Ap stars also show a phenomenon in their Balmer lines called the core-wing anomaly which is most prevalent in the H_α profile. Figure 5.11 shows the effect with Przybylski's star and a synthetic spectrum computed with UCLSYN (Smalley, Smith & Dworetsky 2001) with a temperature of 6300 K and $\log g = 4.2$ (parameters from Kochukhov, Bagnulo & Barklem 2002). Only the H_α line has been synthesised for clarity. As can be seen, the core-wing anomaly consists of a transition between broad wings of the line and a unusually narrow core. The wings are generally indicative of temperatures in the range $7000 - 8000$ K, whereas the core is more representative of stars cooler than about 6000 K (Cowley et al. 2001). Kochukhov, Bagnulo & Barklem (2002) suggests that the core-wing anomaly is a temperature effect, with little influence from the chemical stratification seen in the Ap stars. Their computations show only a small increase in temperature, ≤ 500 K, is required in a hot Ap star to model the core-wing anomaly, whereas the cooler stars require an increase of up to 1000 K to model the phenomenon.

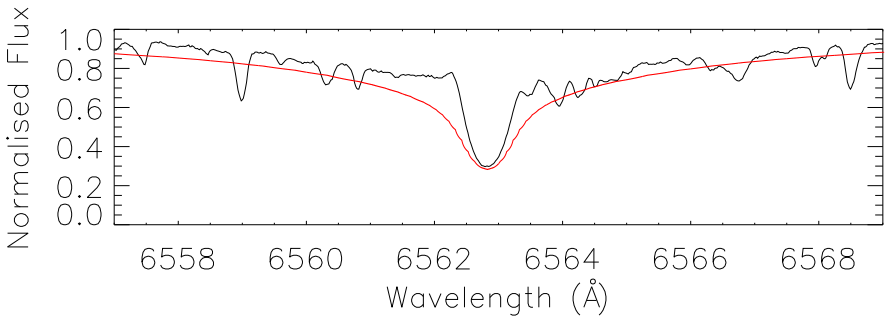

Figure 5.11: An example of the core-wing anomaly, using the UVES spectrum of Przybylski's star. The red synthesised spectrum has the parameters $T_{\rm eff} = 6300\,\mathrm{K}$ and $\log g = 4.2$ (Kochukhov, Bagnulo & Barklem 2002).

5.4.2.3 The λ Boötis Stars

The λ Boo stars are known to pulsate in the δ Sct frequency range, as well as two λ Boo stars being shown to pulsate in the lower frequency γ Dor regime (Zerbi et al. 1999; Gray & Kaye 1999; Paunzen et al. 2014). The frequencies in the stars are mostly below $50\,\mathrm{d}^{-1}$, however Mkrtichian et al. (2007) suggest there may be low-amplitude peaks up to $60\,\mathrm{d}^{-1}$ in 29 Cyg. Therefore there is a possibility that these stars will appear in the results of the survey, and hence are discussed here.

The λ Boo stars are rare, only constituting about 2 per cent of A-type stars (Gray & Corbally 2002), are metal-weak early A- to early F-type stars, and were first mentioned by Morgan, Keenan & Kellman (1943) when discussing λ Boo itself. This class of star have very few lines in their spectra beyond the Balmer lines and the Ca II K line, which itself is often weak when compared to the Balmer line type. The most commonly used indicator that a star is of this class in the strength of the Mg II λ4481 line compared to Fe I λ4383, which is significantly reduced when compared to the normal A-type stars. A full description of the optical characteristics of the λ Boo stars is given in Gray (1997).

Figure 5.12 shows the spectrum of λ Boo itself alongside a normal star of the same spectral type. Clearly, the spectrum of λ Boo is almost featureless, other than

the Balmer and Ca II K lines. The Mg II λ4481 is very much weakened, as are the other metals throughout the spectrum. Here, the A3 Va hydrogen lines of the MK standard, β Leo, best match the Balmer lines in λ Boo, leading to this being the primary classification. However, not unlike the Am stars, the λ Boo stars can have more specific spectral types based on their hydrogen, Ca K line and metallic lines. For λ Boo itself, the label is:

A3 Va kB9.5mB9.5 λ Boo,

where the hydrogen lines give rise to the 'A3 Va' class, the Ca K line the 'B9.5' class and the metallic lines the 'B9.5' class. The 'λ Boo' is also added to distinguish between other classifications of this style.

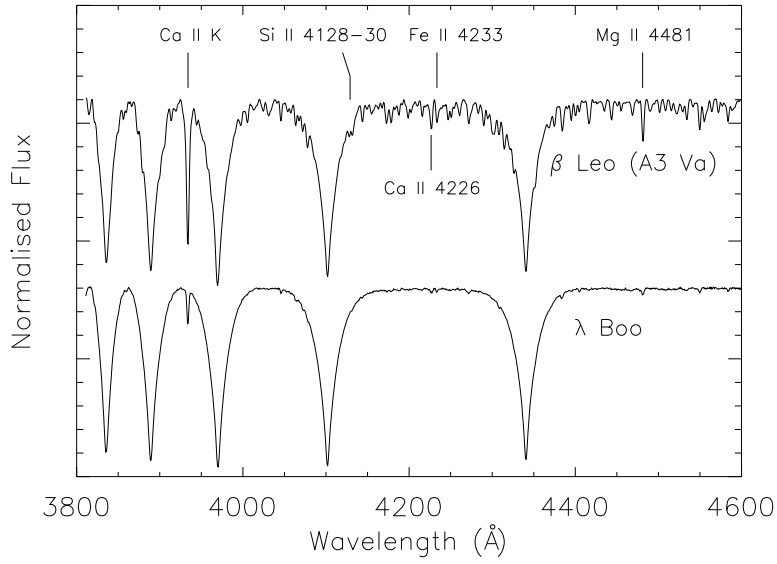

Figure 5.12: The spectrum of λ Boo compared to a normal star of the same temperature type. λ Boo shows very weak metal lines when compared to the normal star. The lack of metal lines suggests a spectral type of late B- or early A-type, however the Balmer lines are best fitted by an A3 star. Recreated after Gray & Corbally (2009).

5.5 Summary

This Chapter has introduced the spectroscopic techniques which will be employed in the following Chapter to further investigate the stars which have been discovered to pulsate in this survey. The concepts of the long-slit and echelle spectrographs have been given, alongside a description of the instruments used in this study. The data reduction techniques and procedures have also been given, making use of community software.

Details have been presented on the spectra of the A-type stars, with the procedure of spectral classification discussed, which relies on the comparison of an observed spectrum to that of a known MK standard spectrum. If a suitable match is not found, then one must consider the possibility that the star is a peculiar star, and careful consideration must be made to the specific signatures in the spectrum.

The main three types of chemically peculiar A-type stars presented are the metallic-lined Am stars, the magnetic Ap stars, and the under-abundant λ Boo stars. These particular stars are discussed in detail as they are known to be pulsationally variable in the frequency range tested in the survey. In summary, the Am stars show weak Ca K lines compared to their Balmer line profiles, and strong metallic lines when compared to the Balmer lines. The Ap stars show over-abundances of either Sr, Cr, Eu and Si, or a mixture of all. They also show strong lines of rare-earth elements in the red part of their spectra. The λ Boo stars show very plain spectra, with very weak metal lines reminiscent of a B-type star, whereas the Balmer lines are more akin to an A-type star.

The process of spectral classification is key in grouping and understand the different types of pulsating stars in the context of what is 'expected' from a certain group. Mis-classification can lead to false claims of new discoveries which are not predicted by current pulsation theory. As such, the methods described here have been meticulously applied to the spectroscopically observed stars in the WASP pulsation survey, presented in the next Chapter.

6 Discussion on Individual Targets

This work was partially published in Holdsworth et al. (2014b). Areas with significant contributions by co-authors have been highlighted.

Presented in this Chapter are the targets for which spectroscopic follow-up observations were obtained to further investigate and classify the stars. The focus was applied to the highest frequency pulsators discussed in Chapter 4. These objects are rarer than their lower frequency counterparts and provide the opportunity to push the current boundaries of both observations, in terms of the highest frequency pulsating Am and δ Sct stars, and the theory needed to explain these new observations.

As well as the high-frequency pulsators, spectra were obtained for targets which looked photometrically interesting, that is to say they show pulsation frequencies in a variety of ranges, i.e. in both the high- and low-overtone p mode regimes. It is not expected from current theory that p modes of both low- and high-frequency be found in the same star (Pamyatnykh 2000) (although at this stage binarity can not be ruled out). As such, the targets which exhibit such signatures may be of the utmost importance for the advancement of pulsation theory.

The discussion below presents the data for a selection of the pulsating δ Sct stars and pulsating Am stars, the full collection of new roAp stars and two sdBV pulsators. This selection does not represent the entire spectroscopically observed sample, but merely presents the most significant results. The photometric and spectroscopic observations that are not discussed here can be found in Appendix B.

Objects presented here were observed as some of their periodograms showed signatures that are reminiscent of the rare roAp stars, but towards the lower edge of the known frequency range. If found to be of the roAp class, they would provide interesting target for further observations as the lower frequency p modes are not expected to be excited in the roAp stars (Saio 2005). Other targets presented in the Appendix were chosen for their multi-periodic nature. These stars provide the ability to probe the star in greater detail as each of the frequencies probe different depths in the star.

The stars which are presented in this Chapter are those which have frequencies flagged in Chapter 4. As previously discussed, there is a chance that identified frequencies may be a result of white noise, or artefacts in the data. Candidates were therefore set aside for later analysis. This analysis consisted of analysing each of the seasons of a star with the Period04 program in the search for multiple detections of the same frequency. The search was conducted to a S/N level of 4.0. Stars which did not show multiple peaks in the $0.01\,\mathrm{d}^{-1}$ tolerance were rejected as false-positives. Extracted frequencies were fit with the least-squares sitting routine in Period04, with multiple frequencies, if present, fit simultaneously.

As many targets showed variability close to the 30 min ($50\,\mathrm{d}^{-1}$) lower cutoff, periodograms were calculated from $48\,\mathrm{d}^{-1}$ to avoid falsely claiming a detection which was in fact an alias of a lower frequency appearing above the $50\,\mathrm{d}^{-1}$ boundary.

6.1 The Spectroscopic Observations

Of the 375 targets which showed variability on the order of 30 min or less, spectroscopic follow-up was obtained for 40 stars. Included in this sample is a known roAp star, J0206 (HD 12932). This is the only known roAp star listed in the Renson & Manfroid (2009) catalogue that was detected in the WASP data (see section 3.5). It is included to provide both a photometric and spectroscopic comparison for the newly discovered roAp stars. Table 6.1 presents the photometric information on the subset of 40 stars.

6.1.1 Spectroscopy

As discussed in Chapter 5, the spectral observations were made with the Intermediate dispersion Spectrograph and Imaging System (ISIS) mounted on the 4.2 m William Herschel Telescope (WHT) in service mode for the northern targets, and the Robert Stobie Spectrograph (RSS) mounted on the 11 m Southern African Large Telescope (SALT) to observe the southern targets. As only low-resolution spectra are required

for spectral classification, the SALT/RSS spectra obtained $R \sim 5\,000$, and $R \sim 2\,000$ for WHT/ISIS observations. In addition, two objects were observed with the Hamilton Echelle Spectrograph (HamSpec; Vogt 1987) on the Shane 3 m telescope at Lick Observatory by K.I. Clubb, achieving a resolution of $R \sim 37\,000$. A final spectrum was obtained for a suspected sdBV star, J0209, using the Andalucia Faint Object Spectrograph and Camera, ALFOSC, instrument mounted on the Nordic Optical Telescope (NOT; obtained by R. Østensen).

Table 6.1: Photometric data for the 40 high-frequency WASP pulsators for which spectra were obtained. Column 8 is the number of WASP data points after cleaning, column 9 is the principal pulsation frequency, and column 10 is the WASP filter pulsational amplitude.

Abbreviated ID	Other ID	R.A. J2000	Dec J2000	V	$(J-H)$	N° of Seasons	npts	ν_{osc} (d^{-1})	Amp (mmag)
J0004	HD 225186	00:04:15.12	−17:25:29.6	9.05	0.152	4	13814	60.08	3.40
J0008	TYC 4-562-1	00:08:30.50	+04:28:18.2	10.16	0.087	3	23076	150.26	0.76
J0026[a]	TYC 2269-996-1	00:26:04.18	+34:47:32.9	10.04	0.232	3	13037	79.13	2.05
J0051	TYC 5270-1900-1	00:51:07.36	−11:08:31.9	11.52	0.059	3	21913	58.04	4.77
J0206[b]	HD 12932	02:06:15.80	−19:07:26.2	10.17	0.105	4	15269	124.10	1.38
J0353	HD 24355	03:53:23.09	+25:38:33.3	9.65	0.054	3	7951	224.31	1.65
J0410	HD 26400	04:10:45.78	+07:17:17.2	9.54	0.017	3	28629	68.22	2.70
J0429	HD 28548	04:29:27.24	−15:01:51.1	9.22	0.038	2	22195	65.65	4.41
J0629	HD 258048	06:29:56.85	+32:24:46.9	10.52	0.239	3	15343	169.54	1.49
J0651	TYC 8912-1407-1	06:51:42.17	−63:25:49.6	11.51	0.062	3	36597	132.38	0.79
J0855	TYC 2488-1241-1	08:55:22.22	+32:42:36.3	10.80	0.014	3	13203	197.27	1.40
J0902	TYC 4890-19-1	09:02:04.52	−07:20:47.6	12.43	0.219	3	35439	636.73	11.70
J1110	HD 97127	11:10:53.91	+17:03:47.5	9.43	0.172	3	11184	106.61	0.66
J1215	HD 106563	12:15:28.17	−11:24:41.3	10.55	−0.021	3	16354	65.46	1.48
J1250	TYC 297-328-1	12:50:56.15	+05:32:12.9	11.25	0.168	4	22902	68.99	4.30
J1403	HD 122570	14:03:41.51	−40:51:08.9	10.41	0.079	4	19613	99.12	1.27
J1430	TYC 2553-480-1	14:30:49.64	+31:47:55.1	11.56	0.094	3	21181	235.54	1.06
J1625	HD 147911	16:25:24.10	−21:41:18.6	9.17	0.186	5	21514	68.52	6.37
J1640	2MASS J16400299-0737293	16:40:02.99	−07:37:29.7	12.67	0.150	2	14511	151.93	3.52
J1648	TYC 2062-1188-1	16:48:36.99	+25:15:48.6	9.98	0.123	5	43024	105.12	0.60
J1757	TYC 2612-1843-1	17:57:26.48	+32:25:23.7	11.58	0.173	5	35794	63.71	2.46
J1758	2MASS J17584421+3458339	17:58:44.20	+34:58:33.9	12.93	0.11	5	74131	71.28	2.49
J1844	TYC 3130-2480-1	18:44:12.27	+43:17:51.9	11.25	0.072	5	39389	181.73	1.45
J1917	TYC 7926-99-1	19:17:33.42	−42:42:07.3	11.18	0.144	3	12120	164.47	1.85
J1921	TYC 3547-2692-1	19:21:28.84	+47:10:53.4	12.16	0.214	4	34224	128.76	1.99
J1938	2MASS J19383247+5609446	19:38:32.48	+56:09:44.6	13.17	−0.091	4	31556	231.62	5.05
J1940	2MASS J19400781-4420093	19:40:07.81	−44:20:09.2	11.30	0.066	5	25071	176.39	4.16
J1951	2MASS J19512756-6446247	19:51:27.55	−64:46:24.5	13.26	−0.010	4	28567	58.43	4.29
J2022	TYC 9311-73-1	20:22:36.50	−70:11:00.2	12.77	0.022	4	27249	62.54	3.30
J2026	TYC 5762-828-1	20:26:42.62	−11:52:45.1	11.80	0.232	4	15957	212.66	1.62
J2029	HD 195061	20:29:33.21	−18:13:12.2	9.81	0.072	6	24743	28.86	2.50
J2054	TYC 525-2319-1	20:54:19.84	+07:13:11.0	9.94	0.020	5	31892	104.86	1.10
J2155	2MASS J21553126+0849170	21:55:31.26	+08:49:17.0	12.83	0.214	4	29563	61.34	6.38
J2241	TYC 3218-888-2	22:41:54.21	+40:30:39.1	11.45	0.063	3	10389	75.54	3.32
J2254	TYC 569-353-1	22:54:34.21	+00:52:46.3	12.72	0.163	3	33997	52.59	5.06
J2255	TYC 6390-339-1	22:55:20.44	−18:36:35.3	11.95	−0.029	4	17232	66.96	2.68
J2305	TYC 9131-119-1	23:05:45.31	−67:19:03.0	11.43	−0.019	2	16265	92.75	1.61
J2313	TYC 577-322-1	23:13:26.32	+02:27:49.5	10.72	0.109	3	24001	60.42	5.97
J2345	2MASS J23455445-3932085	23:45:54.44	−39:32:08.2	13.60	0.006	2	11594	60.47	20.33

[a] See section 6.2 for details. [b] This is a known roAp star included for comparison.

All spectra have been flat-field corrected, de-biased, cleaned of cosmic-rays and have had wavelength calibrations applied. This was conducted in the manner described in Chapter 5, except for the HamSpec and ALFOSC spectra which were reduced by their respective observers using instrument optimised software: the HamSpec spectra are reduced using an IDL pipeline which performs that aforementioned procedures as well as order tracing and extraction. The ALFOSC spectrum was reduced using standard IRAF procedures. Normalisation was conducted using the UCLSYN spectral synthesis package (Smalley, Smith & Dworetsky 2001).

Stellar temperatures were derived in two ways. Initially the spectra were inspected using the UCLSYN code. Model atmospheres, from Castelli, Gratton & Kurucz (1997) with VALD 2014 atomic data (Kupka et al. 1999), with solar abundances and a constant $\log g = 4.0$, were synthesised and compared to the observed Balmer lines. The effective temperature ($T_{\rm eff}$) of the models were adjusted until a suitable fit to the cores and wings of the profiles was found. Due to the low-resolution classification spectra, the temperature was only attainable to within ± 200 K. Fixing the value of $\log g$ will introduce a bias in the resulting temperatures derived from the Balmer lines, this is also the case for assuming a solar abundance. Below about 8 000 K, there is little change in the line strength with $\log g$, it is only above 8 000 K that line strengths depend on both $T_{\rm eff}$ and $\log g$ (Gray & Corbally 2009). However, given the low-resolution spectra, and in some cases low S/N data, the differences between the measured effective temperature and the intrinsic temperature are accounted for in the large error bars.

Secondly, **B. Smalley** determined the effective temperatures from the stellar spectral energy distribution (SED). For the target stars these were constructed from literature photometry, using 2MASS (Skrutskie et al. 2006), DENIS (Fouqué et al. 2000), Tycho B and V magnitudes (Høg et al. 1997), USNO-B1 R magnitudes (Monet et al. 2003), TASS V and I magnitudes (Droege et al. 2006) CMC14 r' magnitudes (Evans, Irwin & Helmer 2002) as available. The stellar $T_{\rm eff}$ values were determined by fitting solar-composition (Kurucz 1993) model fluxes to the de-reddening SEDs. The model fluxes were convolved with photometric filter response functions. A weighted Levenberg-Marquardt non-linear least-squares fitting procedure was used to find the

solution that minimised the difference between the observed and model fluxes. Since $\log g$ is poorly constrained by the SEDs, $\log g$ was again fixed at 4.0 for all the fits. Stellar energy distributions can be significantly affected by interstellar reddening. However, in the absence of measured reddening values, it has been assumed that $E(B-V) = 0.02 \pm 0.02$ for the fitting. The uncertainties in $T_{\rm eff}$ includes the formal least-squares error and adopted uncertainties in $E(B-V)$ of ± 0.02 and $\log g$ of ± 0.5 added in quadrature.

The S/N for each spectrum was estimated using the DER_SNR code of Stoehr et al. (2008) built into the UCLSYN code. The spectral types were determined via comparison with MK Standard stars using the method of Gray & Corbally (2009), as described in Chapter 5. Information on the spectroscopic observations, and the results of the spectral classification and SED fitting are presented in Table 6.2.

Some targets show significant differences, beyond their errors, between the two different temperature measurement techniques. The most likely cause of this is an incorrect estimation of the reddening used in the SED fitting procedure. Fitting of the Balmer lines will provide the most reliable values as these are directly measured from the spectrum. However, there is some ambiguity when measuring Balmer line profiles either side of the Balmer maximum, at about A3. Here, comparison with the metal lines in the spectra must also be made to ensure a temperature the correct side of the maximum is chosen. This was standard procedure for all stars here though.

Table 6.2: Spectroscopic information on the 40 targets for which follow-up spectra were obtained. The standard error on the Balmer $T_{\rm eff}$ is $\pm 200\,$K.

ID	Telescope/ Instrument	Exposure (s)	Observation Date	S/N	Balmer $T_{\rm eff}$ (K)	SED $T_{\rm eff}$ (K)	Spectral Type
J0004	SALT/RSS	15	2012-05-31	180	7900	7518 ± 377	A5
J0008	SALT/RSS	99	2013-06-15	60	7300	7484 ± 336	A9p SrEu(Cr)
J0026S	WHT/ISIS	30	2011-11-22	100	6650	6100 ± 260	F4
J0026P	WHT/ISIS	30	2011-11-22	115	8100	7080 ± 320	A2m
J0051	SALT/RSS	200	2013-06-06	50	7850	8144 ± 479	A6
J0206	WHT/ISIS	30	2011-11-22	70	7600	7310 ± 318	A4p
J0353	WHT/ISIS	15	2012-10-24	50	8250	7417 ± 331	A5p SrEu
J0410	WHT/ISIS	20	2011-11-22	125	8150	7712 ± 346	A3m:
J0429	WHT/ISIS	15	2013-10-24	120	8200	8770 ± 334	A2m
J0629	WHT/ISIS	40	2012-10-24	40	6600	6211 ± 281	F4p EuCr(Sr)
J0651	SALT/RSS	1300	2012-09-11	70	7400	7843 ± 491	F0p SrEu(Cr)
J0855	WHT/ISIS	50	2011-11-22	80	7800	8287 ± 475	A6p SrEu
J0902	NOT/ALFOSC	300	2013-02-04	400	34558	10140 ± 1120	sdBV
J1110	WHT/ISIS	15	2012-12-25	55	6300	6707 ± 294	F3p SrEu(Cr)
J1215	WHT/ISIS	40	2012-12-25	70	8100	8437 ± 412	A3m:
J1250	WHT/ISIS	100	2012-12-25	100	8300	7099 ± 370	A4m
J1403	SALT/RSS	500	2012-05-08	140	7550	7500 ± 350	A9
J1430	WHT/ISIS	100	2012-12-25	85	7100	7479 ± 366	A9p SrEu
J1625	SALT/RSS	230	2012-05-08	235	8200	6147 ± 272	A1m
J1640	WHT/ISIS	1200	2013-02-01	95	7400	6282 ± 314	A8p SrEu
	SALT/RSS	600	2013-03-22	75	7400		A8p SrEu
J1648	WHT/ISIS	200	2013-02-01	80	7100	6939 ± 307	F0
J1757	WHT/ISIS	600	2013-02-01	105	7900	7425 ± 377	A7m:
J1758	WHT/ISIS	1200	2013-02-01	110	7700	7260 ± 480	A7m:
J1844	Shane/HamSpec	1800	2012-07-24	40	9700	8043 ± 435	A7p EuCr
J1917	SALT/RSS	249	2013-04-22	100	7800	6989 ± 293	A7m:
J1921	WHT/ISIS	500	2014-11-04	40	6200	6730 ± 480	F3p SrEuCr
J1938	WHT/ISIS	1000	2015-03-11	165	29240	17950± 3640	sdBV
J1940	SALT/RSS	759	2012-11-03	20	6900	7623 ± 411	F2p Eu
J1951	SALT/RSS	900	2013-04-25	75	8100	8076 ± 438	A5
J2022	SALT/RSS	500	2013-04-25	85	8200	7973 ± 507	A4m
J2026	WHT/ISIS	150	2013-04-25	60	6000	6528 ± 433	F8
J2029	SALT/RSS	25	2013-04-27	40	8000	7754 ± 339	A4m
J2054	Shane/HamSpec	1800	2012-07-24	60	7000	8372 ± 438	A3m:
J2155	SALT/RSS	800	2013-06-07	50	8100	6681 ± 555	A3
J2241	WHT/ISIS	100	2012-10-25	70	8100	7771 ± 391	A3m
J2254	SALT/RSS	600	2013-06-17	55	8150	7059 ± 450	A4
J2255	SALT/RSS	250	2013-05-13	50	8200	8564 ± 627	A3
J2305	SALT/RSS	139	2012-11-04	35	8050	8146 ± 374	A5m:
J2313	SALT/RSS	90	2013-06-19	65	8000	7794 ± 376	A5
J2345	SALT/RSS	1250	2013-06-07	75	9700	9772 ± 964	A3

6.2 The J0026 System

Multiperiodic photometric variability was detected in J0026 with a principle peak at $79.13\,\mathrm{d}^{-1}$ with an amplitude of 2.05 mmag in the WASP data (Figure 6.1). Table 6.3 shows all of the frequencies detected in the WASP photometry. Inspection of the photometric aperture revealed that this target is in fact a visual binary, with a separation of $22''$ (Figure 6.2 lower left), thus meaning that the source of the variability could be either of the two stars. The stars are distinguished in the Bonner Durchmusterung catalogue (Argelander 1903) with the suffixes S and P, the same notation is adopted here. Spectra have been obtained for each of the stars, leading to J0026S being classified as F4 and J0026P being classed as A2m.

It has been possible in this case to distinguish between which star is pulsating by using to outer-most photometric aperture of a star $65''$ from J0026P, namely J0025 (Figure 6.2 centre). Using the standard photometric aperture for J0025, it can be shown that this star is stable, however, when extending the aperture to include J0026P, variations of the same frequency seen in the J0026 system can be seen in the light

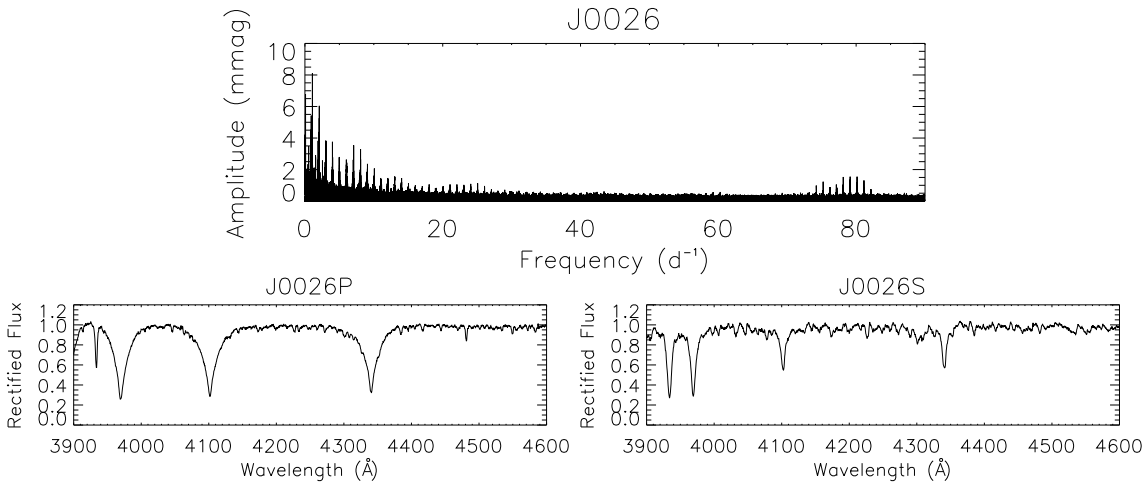

Figure 6.1: Periodogram and WHT/ISIS spectra for the J0026 system. The source of the pulsations is J0026P, classified as an A2m star. J0026S has been found to be a spectroscopic binary star, with a composite spectral type of F4.

Table 6.3: The frequencies extracted from the light curve of J0026.

Label	Low Frequency (d^{-1})	Amplitude (mmag)	Label	High Frequency (d^{-1})	Amplitude (mmag)
ν_1	1.0901	7.1160	ν_5	79.1327	1.9301
ν_2	8.0756	3.9455	ν_6	75.2151	1.8018
$\nu_1/2$	0.5451	3.2250	ν_7	75.2133	0.7238
$3\nu_1$	1.6468	1.6222	ν_8	78.1303	0.7021
ν_3	11.0317	0.5478	ν_9	78.0433	0.3761
ν_4	16.1510	0.5211	ν_{10}	71.9284	0.3299

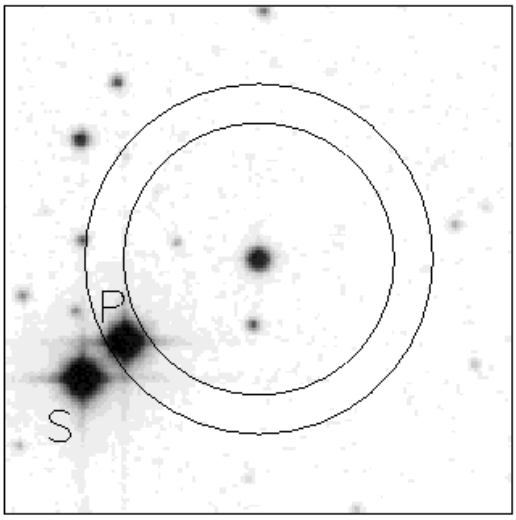

Figure 6.2: The photometric apertures of J0025 (centre) used to determine that the pulsations seen in the J0026 pair are originating on J0026P. The inner annulus is the standard aperture over which photometry is normally performed and shows J0025 to be constant, with the raw flux in the outer annulus showing pulsations.

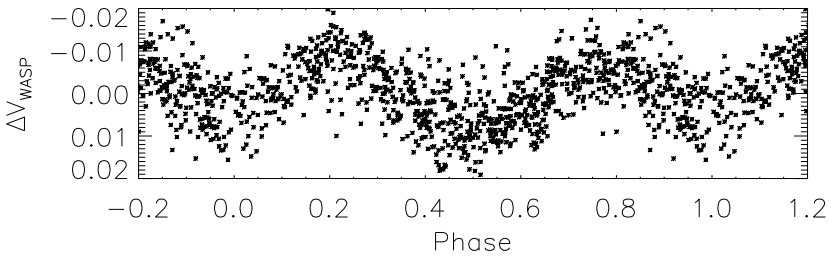

Figure 6.3: Phase folded light curve of J0026P, demonstrating the binarity of the star. The data are folded on a period of 1.83 d, and shown in phase bins of 0.001.

curve. Thus, this indicates that J0026P is the star hosting the pulsations. These are high-frequency pulsations in an Am star, superseding the previous maximum seen by Smalley et al. (2011) but, as shown below, not the highest known pulsations now seen in Am stars.

This technique was also used to determine the source of the low-frequency variations shown in Table 6.3. Not all frequencies have been recoverable, due to the lower quality data of the outer photometric annulus which is not processed to the full extent of the primary aperture. However, analysis of the largest photometric aperture in Figure 6.2 has shown that J0026P is the host ν_1 and $\nu_1/2$. The source of the low-frequency pulsations ν_2, ν_3 and ν_4 is undetermined. The presence of the low frequencies in J0026P suggest that it is a binary star. Figure 6.3 shows a phase folded light curve of J0026P, folded on $\nu_1/2$ or 1.83 d.

Further to the discussion on J0026P, the spectroscopic observations of J0026S show this star to be a spectroscopic binary star (Figure 6.4). The separation of the cores of the two H_α lines implies a radial velocity shift at that epoch of 172 ± 21 km s^{-1}. It is not only the H_α line which shows the separation, there are many lines which appear as pairs in the red-arm of the spectrum, but none are as noticeable as the H_α core. Therefore, it is concluded that there are at least four stars in this system.

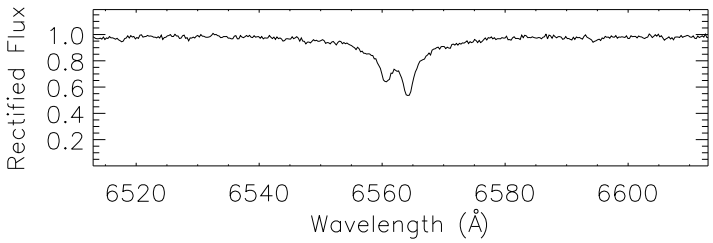

Figure 6.4: The H_α profile of J0026S showing the presence of two cores, indicating this star to be a spectroscopic binary. The radial velocity measured at this epoch is 172 ± 21 km s^{-1}.

6.3 The δ Scuti Stars

The spectral classification of the 40 observed stars led to the identification of 12 δ Scuti stars (30 per cent of the sample). These targets range from A3 to F8 in spectral type, covering a pulsation frequency range of $52 - 213\,\mathrm{d}^{-1}$. This upper limit is very high for δ Sct stars, and is greater than any other measured frequency (e.g. Balona et al. 2012a; Breger et al. 2012), however there may be a mis-interpretation of coherent noise in one of the periodograms, J2026, if so the upper frequency becomes $105\,\mathrm{d}^{-1}$. J2026 is the coolest star with spectroscopic follow-up, classified at F8. The peak in this star is detected with a S/N of about 7 using the method employed in the survey, and at a level of 4.7 when using the more robust method built into Period04, thus indicating that this is a real detection. When testing the selection criteria with pure noise in section 3.4.1, no peaks were identified with a S/N greater than 5.3, therefore reiterating that this is probably a real peak, however with a sample of 1 000 stars in the tests, such extreme cases of false-positive peaks may not have arisen. In the cooler stars, at the red-edge of the instability strip, the convective envelope extends further into the star, allowing for the flux blocking mechanism to be effective at driving the high-frequency p modes (Dupret et al. 2005). It is therefore feasible for J2026 to pulsate at this frequency, however dedicated follow-up of a few hours would be required to confirm the presence of the pulsation.

The spectra and periodograms of most of the observed δ Scuti stars are shown

in Appendix B.1, with J1648 and J2345 discussed here. This Chapter does not focus on the *normal* pulsating A-type stars as there are many excellent examples in the literature with higher quality data available (e.g. Breger et al. 2011; Southworth et al. 2011; Zwintz et al. 2011; Balona et al. 2012a; Balona et al. 2012b; Breger et al. 2012; Casey et al. 2013; Lehmann et al. 2013; Bowman & Kurtz 2014; Zwintz et al. 2014), however both J1648 and J2345 show multiperiodic light curves with either low or high amplitudes, respectively, and as such are worthy of discussion here.

J1648

There are 5 seasons of WASP data for J1648 covering a period from 2004 to 2011. The full light curve has over 52 600 data points. The periodogram, shown in Figure 6.5, shows low-frequency signatures below $14\,\mathrm{d}^{-1}$ as well as high-frequency peaks between 80 and $105\,\mathrm{d}^{-1}$.

The strongest signatures in the low-frequency domain are representative of ellipsoidal variability as $\nu_2 = {}^{\nu_1}/_2$, with what appear to be low-frequency pulsations between $7 - 11\,\mathrm{d}^{-1}$. The high-frequency pulsations consist of 9 frequencies in the amplitude range $0.22 - 0.72\,\mathrm{mmag}$. Although at very low-amplitude, the peaks have S/N values of 4 or greater after successive pre-whitening of the other detected frequencies. The frequencies and amplitudes are shown in Table 6.4. Two of the low-frequency peaks, ν_3 and ν_4, are close to day aliases, and so may be data artefacts rather than real peaks.

Due to the suspected ellipsoidal nature of the star (Figure 6.5), it is assumed that the low- and high-frequency pulsations are originating from two, or more, objects in the system. J1648 appears in the Washington Double Star catalogue (WDS; Mason et al. 2001) with three observations between 1970 and 2008, the average separation is $0.75''$. The two stars have magnitudes 10.2 and 12.4 in the $V-$band. However, there is a third star in close proximity to the pair, just $14''$ away ($V = 13.8$). This object falls within one pixel of the pair in the WASP data and as such is included in the photometric aperture. The $(J - H)$ colour of this third star suggests it is a G1 star, in

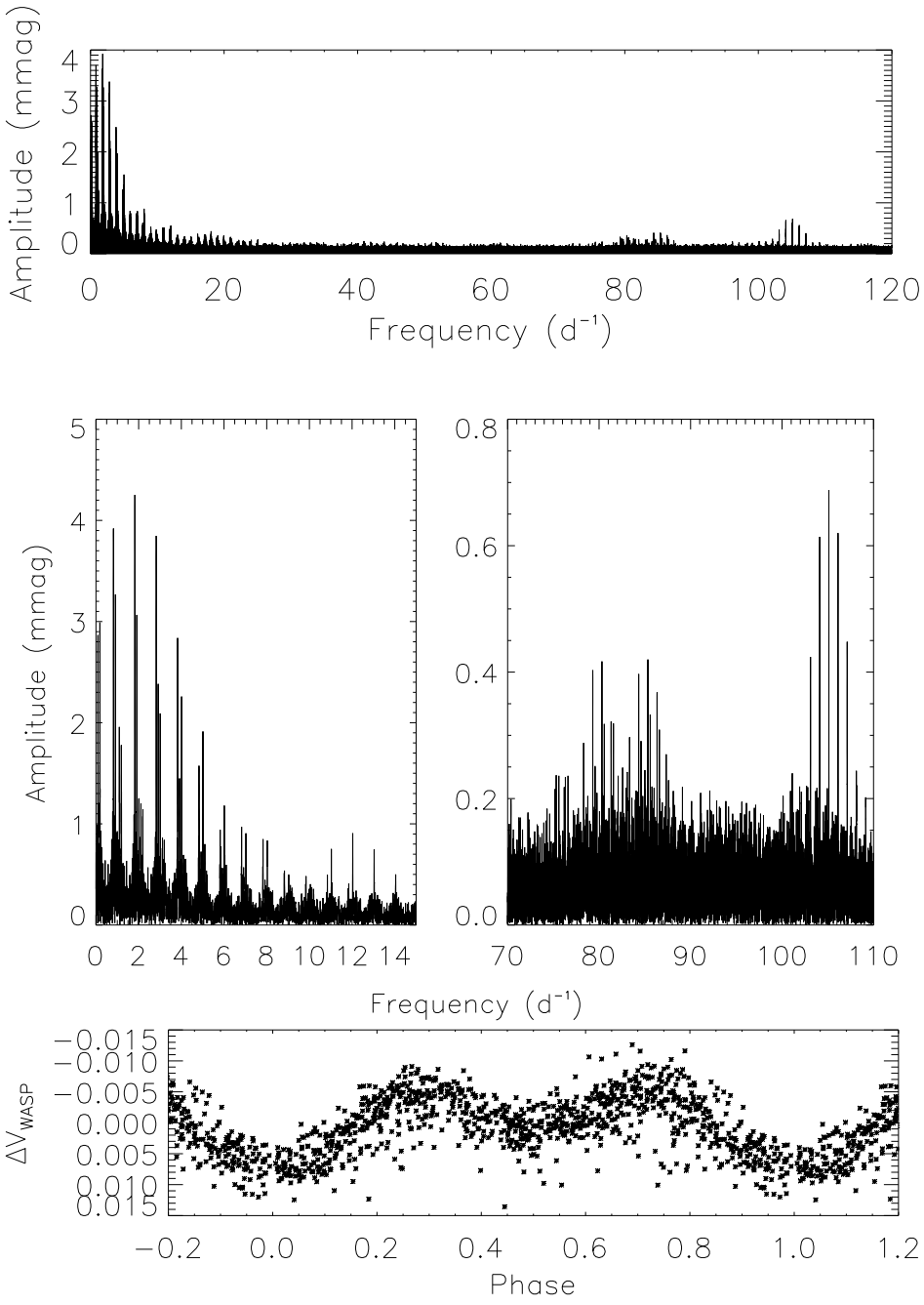

Figure 6.5: Full periodogram of the 2011 data of J1648, with higher resolution panels of the low- and high-frequency variability. Some of the low-frequency peaks are not recovered and as such are not astrophysical, but a result of light interaction from the other star in the aperture. The phase folded light curve in the bottom panel is folded on 1.1 d (ν_2), and shown in phase bins of 0.001.

which case it is not expected that any of the detected variability will originate here as the solar-like oscillations of G stars are much below the detection limits of the WASP instrument. However, a short period of dedicated photometric follow-up observations of the companion is required to defiantly rule out its contribution to the photometric variability of J1648, with further high-resolution spectroscopic monitoring of the binary pair suggested to try and disentangle the source of the variability.

An attempt has been made to apply the Phase Modulation (PM) method of Murphy et al. (2014) to determine whether the source of all pulsations is the same. The method was applied to the 2009, 2010 and 2011 data sets for J1648 as these were the most sampled seasons of data. The method was tested using frequencies ν_6, ν_7, ν_8, and ν_{10} from Table 6.4. The results for the high-frequency pulsations all show similar amplitudes of time delay (56.03 ± 9.77 s), with the low-frequency peak showing a much greater time delay (2907 ± 484 s). Unfortunately, due to the ground-based nature of the WASP data, it is not possible to split the data set into sections which will allow a reasonable frequency resolution for a definitive result, however this difference in time delay from the two frequency regions suggest the source of the pulsations is different. It must also be noted here that this method would work best on well-sampled, high-amplitude, pulsations, rather than the weak signals seen in this star. This method is also limited by its ability to detect short period binaries, especially when using sparsely sampled ground-based observations. The shortest period detectable is twice the time-

Table 6.4: The frequencies extracted from the light curve of J1648.

Label	Low Frequency (d^{-1})	Amplitude (mmag)	Label	High Frequency (d^{-1})	Amplitude (mmag)
ν_1	1.8206	4.1877	ν_7	105.1187	0.7179
ν_2	0.9103	3.5441	ν_8	85.3346	0.4521
ν_3	4.0109	2.0076	ν_9	85.5888	0.3642
ν_4	0.9967	1.3088	ν_{10}	80.3124	0.3454
ν_5	7.0221	0.7886	ν_{11}	80.5676	0.3057
ν_6	12.029	0.5788	ν_{12}	79.7680	0.2770
			ν_{13}	83.0874	0.2502
			ν_{14}	85.0086	0.2423
			ν_{15}	84.3794	0.2205

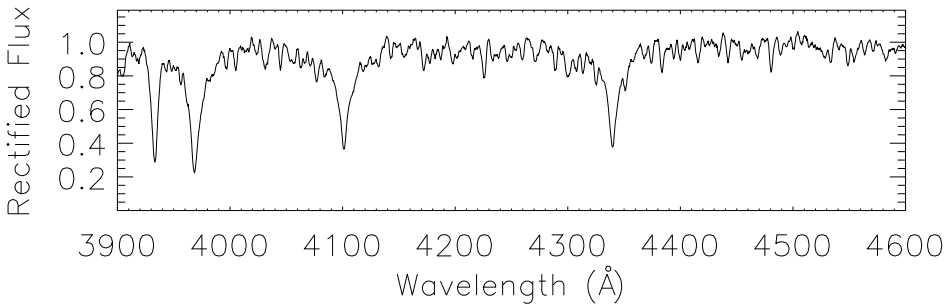

Figure 6.6: The WHT/ISIS spectrum of J1648. There is no indication that the spectrum is a composite or binary, however, at classification dispersion this is not possible to confirm. This star is classifies as F0.

base of the segments used. For example, here the data were split into 25 d segments as a result of the desired resolution, and so the shortest period detectable would be 50 d. The use of this method on many of the WASP pulsators is desirable, however their periods are often on the order of days making the application unfeasible.

The spectrum for J1648 was obtained using WHT/ISIS and achieved a S/N of about 80 (Figure 6.6). Spectral classification places it as an F0 star with an effective temperature of 7100 ± 200 K from the Balmer lines. There is no indication that the spectrum is composite, which could be expected with stars in close binaries. However, given the difference of about 2 magnitudes between the pair, a high S/N spectrum would be needed to investigate this further. The Ca II K line appears to perhaps be slightly weak for an F0 star, however the Ca I line at λ4226, the Hydrogen lines and the metal lines are consistent with an F0 star.

J2345

J2345 is the highest amplitude main-sequence pulsating star, above 50 d^{-1}, found in this survey. Frequency analysis shows 5 frequencies above 50 d^{-1}, and a single low-frequency peak corresponding to a period of 0.6770 d (Figure 6.7 and Table 6.5). Neither the light curve or a phased light curve are reminiscent of binarity – the data show a smooth sinusoidal variation, more akin to a g mode pulsation. Further to this, there are no

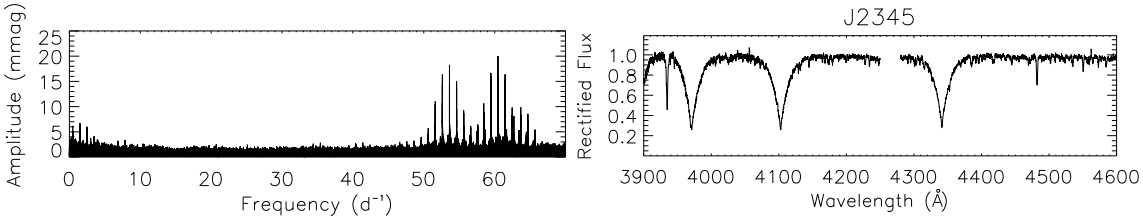

Figure 6.7: Periodogram and SALT/RSS spectrum of J2345. The low-frequency in the periodogram is a real signal. The spectrum is classed as a standard A3 type star.

Table 6.5: The frequencies extracted from the light curve of J2345 using all available data.

Label	Frequency (d^{-1})	Amplitude (mmag)	Label	Frequency (d^{-1})	Amplitude (mmag)
ν_1	1.4772	6.9103	ν_4	63.6886	8.8966
ν_2	60.4667	20.5221	ν_5	52.6233	3.2680
ν_3	53.6270	17.1626	ν_6	63.4363	2.8395

harmonics present in the low-frequency regime that are often found when binarity is present, nor a peak at $^{\nu_1}/_2$ seen in ellipsoidal variables.

The spectrum of J2345 is shown in Figure 6.7. It is classified as an A3 star and displays sharp lines, indicative of a low rotation velocity. There is no indication in the spectrum of a binary star, through line splitting or contamination of lines. Both the Balmer line fitting and the SED fitting derive an effective temperature of about 9700 K making this the hottest star with spectral observations, and also placing it well beyond the blue edge of the δ Sct instability strip.

J2345 is very similar to the A3V component of the Algol type binary system RZ Cas (HD 17138; Ohshima et al. 2001; Rodríguez et al. 2004). Both stars are classified with similar temperatures and both show pulsations at about 64 d^{-1} with $V-$band amplitudes of 20 mmag. RZ Cas also shows further, low-amplitude, peaks around the dominant peak, down to 0.59 mmag in the Strömgren b filter. This poses an interesting question as to whether J2345 is also in a binary system.

6.4 The Pulsating Am Stars

Of the spectroscopically observed targets, 14 stars (35 per cent) are classified as new pulsating Am or Am: stars, with a frequency range of $29 - 164\,\mathrm{d}^{-1}$, and temperature range of $7700 - 8300\,\mathrm{K}$. These results compliment those of Smalley et al. (2011) who used the WASP data to search for pulsations in known Am stars, as listed in the Renson & Manfroid (2009) catalogue. As this work takes a different approach to searching for pulsations, it is not unexpected that further pulsating Am stars are found.

Due to the ambiguity with stellar classification, it is possible that within this group of Am stars there are Ap stars which show multi-periodicity of the δ Sct type. Although it was not initially thought that Ap stars pulsate in the δ Sct range, Kurtz (2000) proposed a list of likely targets, with the first example of such a system being HD 21190 (Koen et al. 2001). *Kepler* observations have also detected this phenomenon in 5 of the 7 Ap stars that have been observed (e.g. Balona et al. 2011b). However, there are currently no known systems which exhibit both high-overtone roAp pulsations and low-overtone δ Sct pulsations.

Theoretical work by Saio (2005) suggests that both high- and low-overtone p modes cannot co-exist in magnetic Ap stars as δ Sct pulsations are suppressed by the presence of the magnetic field, whereas roAp pulsations can be enhanced. However, this survey has identified targets, such as J1917 (see section 6.6), which show both low- and high-overtone p modes in a single target. However, further observations are needed to eliminate any other explanations such as target blending and binary systems.

The pulsation frequencies detected by SuperWASP have pushed the high-frequency boundary of the pulsating Am stars. Previously the upper limit on the frequency was $70.76\,\mathrm{d}^{-1}$ found in a known Am star (HD 108452; Smalley et al. 2011), here that limit is pushed beyond $100\,\mathrm{d}^{-1}$ with observations of these frequencies in more than one object.

Below, two of the most interesting Am stars are discussed: J2054 which shows the highest amplitude pulsations in the observed Am stars, and J2305 which is a double mode pulsator with frequencies straddling $100\,\mathrm{d}^{-1}$. The observations for the remaining targets can be found in Appendix B.2.

J2054

J2054 shows two pulsations over $100\,\mathrm{d}^{-1}$. The strongest is at $104.86\,\mathrm{d}^{-1}$ with an amplitude of 1.1 mmag, the second is at $100.44\,\mathrm{d}^{-1}$ with an amplitude of 0.53 mmag (Figure 6.8). The Shane/HamSpec spectrum obtained for this target indicates that it is an A3m: star based on a weakened Ca K line and slightly enhanced Sr II (Figure 6.8). However there is no clear depletion of Sc II which is often the case with Am stars. A $v \sin i$ of ~ 50 km s^{-1} is estimated from the spectrum, a result consistent with the Am stars (see section 1.2.2).

Low-frequency variations are noted in the photometry, corresponding to a period of 1.3 d (Figure 6.8). When the data are folded on this period, the resulting phase diagram shows two maxima with unequal minima, suggesting an ellipsoidal variable. The light curve indicates a binary target, where the pulsations may originate in one or both components. However there is no evidence for this in the single spectrum that was obtained. Given the ellipsoidal nature of the light curve, the chemical abundance anomalies may be a result of contamination from the companion star, or stars. Fur-

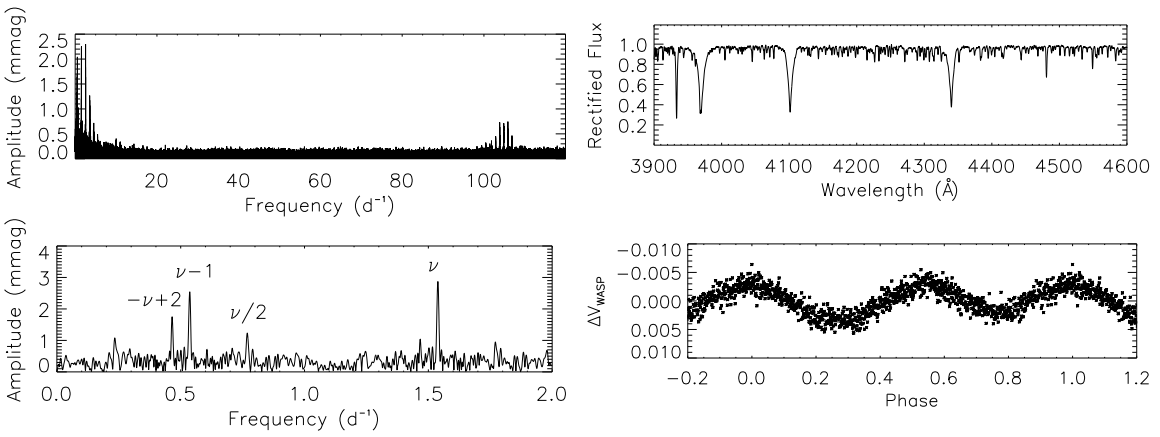

Figure 6.8: Top left: Periodogram of the WASP light curve for J2054. Top right: Shane/HamSpec spectrum showing the star to be A3m:. Bottom left: Low-frequency periodogram showing the true frequency (ν) and its sub-harmonic and their positive and negative aliases. Bottom right: Phase folded light curve of J2054. The data are folded on a period of 1.3 d and shown in phase bins of 0.001.

ther spectroscopic observations at various epochs are required to fully understand this system.

Based on the current observations, J2054 is the fastest Am star that has been found with SuperWASP, superseding the previous fastest, HD 108452 pulsating at $71\,\mathrm{d}^{-1}$ (Smalley et al. 2011). This result has therefore expanded the frequency range of the pulsating Am stars, encroaching farther into the domain of the roAp stars, further blurring the distinction between these two types of pulsator.

J2305

J2305 is a double-mode, high-frequency Am pulsating star similar in nature to J2054. It pulsates slightly slower than J2054 at 92.75 and $101.68\,\mathrm{d}^{-1}$ (Figure 6.9). This star is classified as an A5m: star (Figure 6.9), placing it just beyond the blue edge of the instability strip of Dupret et al. (2004).

No low-frequency variability is detected in the SuperWASP photometry, indicating that both pulsations are likely originating in J2305. Multiple periods have previously been observed in Am stars (e.g. Joshi et al. 2003; Balona et al. 2011d), however not at the frequencies or amplitudes presented here. This system presents a good case for further follow-up observations, both photometric and spectroscopic. The high-overtone p modes, coupled with the chemical peculiarities of the star may provide a further challenge to the theory on pulsations in Am stars, which, at one time, were not thought to pulsate (Wolff 1983).

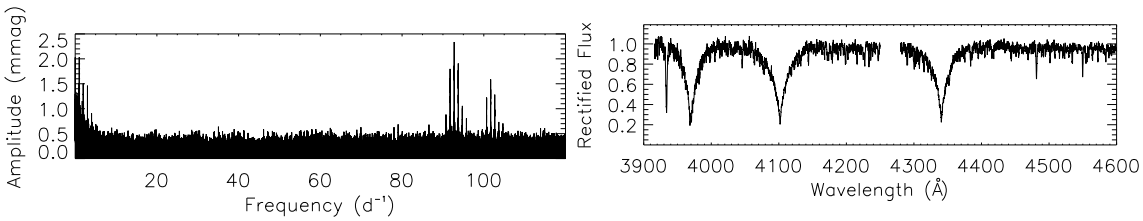

Figure 6.9: Periodogram and SALT/RSS spectrum of J2305. The low-frequency peaks are due to $1\,\mathrm{d}^{-1}$ aliases. Spectral classification places J2305 as an A5m: star.

6.5 The roAp Stars

This section presents the 11 new roAp stars (28 per cent of the sample) discovered in the SuperWASP archive. This represents the joint largest survey discovery of roAp stars, along with the 'Cape rapidly oscillating AP star survey' (Martinez, Kurtz & Kauffmann 1991; Martinez & Kurtz 1994). Some objects show a low-frequency signature in their periodogram which is attributed to rotational modulation. For these stars, both the low-frequency periodograms and the phase folded light curves are presented alongside a discussion of each object, with the details of the modulations shown in Table 6.6. The periodograms indicate the frequency (ν) on which the data are folded, as well as labels of other prominent peaks. In this frequency range the periodograms show the reflection of the $-1\,\mathrm{d}^{-1}$ aliases, labelled as $-\nu$, which must not be confused with the true peak. The solid line on each phase plot represents the harmonic fit. The false-alarm probability (FAP) is calculated using the method of Maxted et al. (2011).

Table 6.6: Rotationally modulated light curve data for the newly detected roAp stars.

ID	ν_{rot} (d^{-1})	Period (d)	Amp (mmag)	FAP
J0353	0.0717	13.95	6.37	<0.001
J0855	0.3234	3.09	2.55	0.096
J1640	0.2722	3.67	4.17	0.003
J1844	0.0495	20.20	7.65	0.000
J1940	0.1044	9.58	5.87	0.017

J0008

J0008 shows a roAp pulsation at $150.26\,\mathrm{d}^{-1}$ with an amplitude of 0.76 mmag (Figure 6.10). WASP has observed the target for three consecutive seasons with slight discrepancies in the pulsation frequency which is attributed to the $1\,\mathrm{d}^{-1}$ aliases. The spectrum obtained for this star (Figure 6.10) has been classified as A9p, with strong

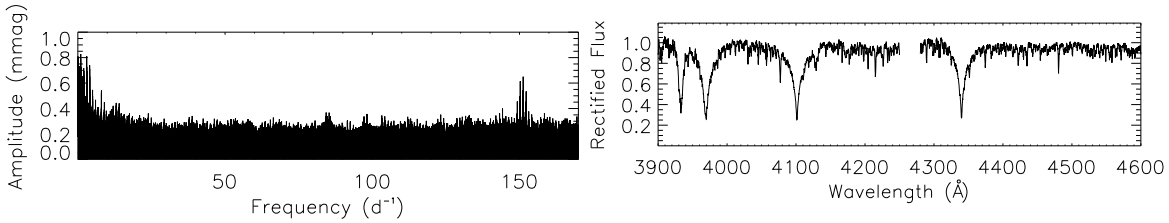

Figure 6.10: Periodogram and SALT/RSS spectrum of J0008. The low-frequency peaks in the periodogram are due to noise. The spectrum is classified as A9p.

enhancements of Sr II and Eu II. The spectrum confirms this to be a new roAp star. The sharp-lined nature of the spectrum indicates a low $v \sin i$.

The pulsations in J0008 are similar to those in HD 119027, which pulsates at $165.52\,\mathrm{d}^{-1}$ with a $B-$band amplitude of 2.0 mmag (Martinez, Kurtz & van Wyk 1994). HD 119027 is a hotter star, classified as A3p SrEu(Cr), and is also known to show amplitude modulation as a result of the beating of closely spaced frequencies.

J0353

J0353 displays a pulsation at $224.31\,\mathrm{d}^{-1}$ with an amplitude of 1.65 mmag as well as a low-frequency variation corresponding to 13.95 d (Figure 6.11). The spectrum of this star is classified as A5p with enhancements of Sr II and Eu II, confirming it as a new roAp star.

HR 1217 is a roAp star that shows a similar pulsation spectrum to J0353. Pulsating at about the same frequency ($232.26\,\mathrm{d}^{-1}$; Kurtz & Cropper 1981), HR 1217 is classified as an A9p SrEu(Cr) star. The rotation period of HR 1217 has been discussed at length in the literature; recently Rusomarov et al. (2013) presented a period of 12.45812 d derived from 81 longitudinal magnetic field data points spanning over 4 decades. Balona & Zima (2002) presented spectra of HR 1217 which show a core-wing anomaly in the H_α line, a feature which is also seen in the red spectrum of J0353.

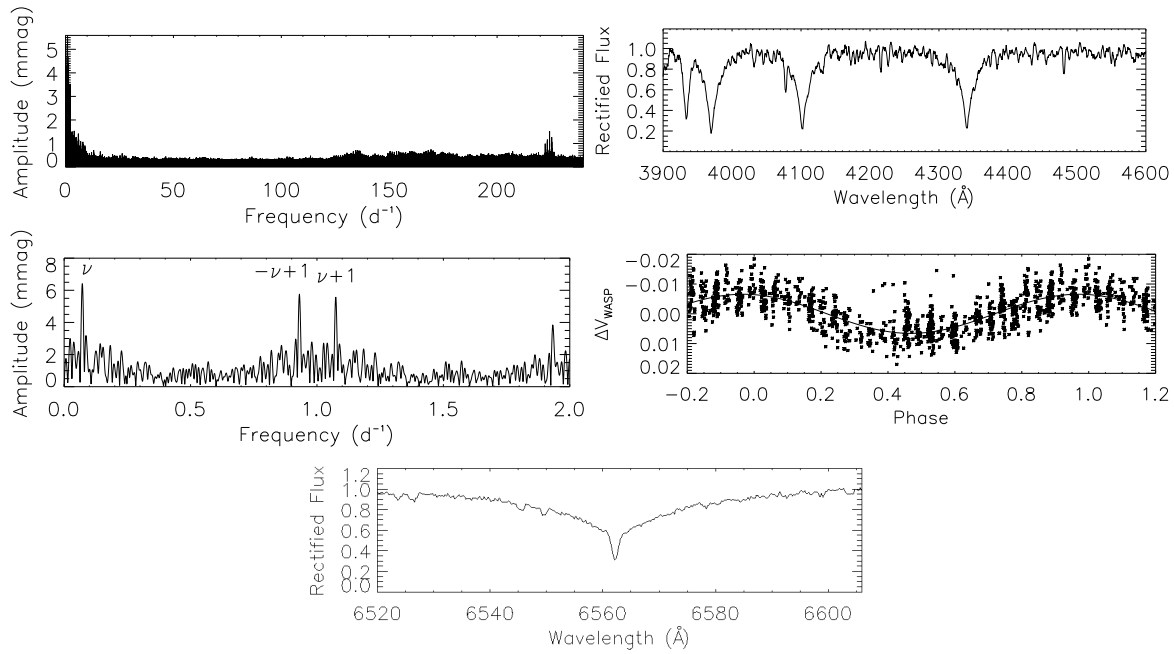

Figure 6.11: Top left: Periodogram of the WASP light curve for J0353. Top right: WHT/ISIS spectrum showing the star to be an A5p type. Middle left: Low-frequency periodogram of J0353 showing the rotation signature (ν) and its positive and negative aliases. Middle right: Phase folded WASP light curve for J0353. The data are folded on a period of 13.95 d, and shown in phase bins of 0.001. Bottom: The H_α profile showing the core wing anomaly.

J0629

J0629 pulsates at 169.54 d^{-1} with an amplitude of 1.49 mmag (Figure 6.12). The spectrum (Figure 6.12) shows strong over-abundances of Sr II, Cr II and Eu II. The photometric observations give no indication of rotational modulation. This star is classified as an F4p star.

Through both Balmer line analysis and SED fitting, J0629 is shown to be a very cool Ap star with a $T_{\rm eff}$ similar to the roAp star HD 213637 (6400 K; Kochukhov 2003), and thus placing J0629 amongst the coolest roAp stars.

Rapid oscillations in the Ap stars are systematically modelled to occur in the hotter, more luminous, members of the sub-class (Cunha 2002; Théado et al. 2009), however observations place them at much cooler temperatures. Kochukhov et al. (2013) presented nine Ap stars which they found with rapid oscillations, all of which were cool stars (7000 − 7850 K). J0629, and other roAp stars presented here, push further into the cool region, and away from the model expectations.

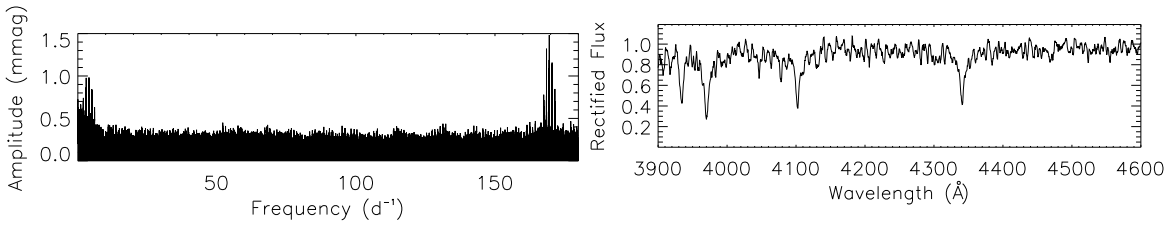

Figure 6.12: Periodogram and WHT/ISIS spectrum of J0629. The low-frequency peaks in the periodogram are due to 1 d^{-1} aliasing. The spectrum is classed as F4p.

J0651

J0651 is classified as an F0p star whose spectrum shows a strong over-abundance of Sr II at $\lambda\lambda$4077 & 4216 (Figure 6.13). Enhancements of Eu II features at $\lambda\lambda$4128 & 4205 and Cr II at λ4111 are also seen. The WASP photometry shows a pulsation at 132.38 d^{-1} (Figure 6.13), with no clear indication of rotational modulation.

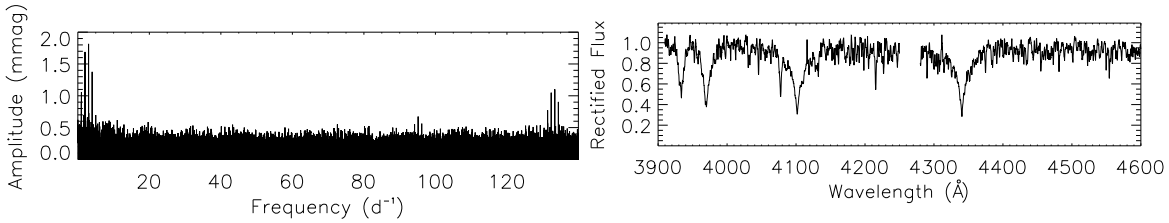

Figure 6.13: Periodogram and SALT/RSS spectrum of J0651. The low-frequency peaks in the periodogram are due to $1\,\mathrm{d}^{-1}$ aliasing. The spectrum is classified as F0p.

In the literature a very similar roAp star to J0651 can be found. Pulsating at a frequency of $137.17\,\mathrm{d}^{-1}$ with a $B-$band amplitude of 3.5 mmag, HD 9289 is an Ap SrEu star with a rotation period of 8.55 ± 0.08 d (Bidelman & MacConnell 1973; Kurtz & Martinez 1993; van Heerden, Martinez & Kilkenny 2012). Elkin, Kurtz & Mathys (2008) present photometric and spectroscopic T_{eff} values for HD 9289, deriving 7700 and 8000 K respectively, which are similar to those obtained for J0651 through Balmer line and SED fitting, 7400 ± 200 and 7800 ± 491 K, respectively.

J0855

J0855 shows a rapid pulsation at $197.27\,\mathrm{d}^{-1}$ with an amplitude of 1.4 mmag (Figure 6.14). Balmer line fitting gives a T_{eff} of 7800 K, and a spectral type of A6p when compared to MK standards. The spectrum also shows an over-abundance of Eu II at $\lambda\lambda$4205 & 4128, with weak Ca K and Ca I at λ4226 (Figure 6.14). As well as the high-frequency pulsation, the periodogram shows a low-frequency signature with a period of 3 d (Figure 6.14).

The temperatures derived for J0855 just agree within the errors, however the SED method is very poorly constrained as indicated by the error bar. Assuming a T_{eff} of that derived through Balmer line fitting, J0855 is almost identical to the known roAp star HD 190290 (Martinez & Kauffmann 1990). The pulsations of the two are at the same frequency, with J0855 showing a larger estimated $B-$band amplitude. The ISIS red-arm spectrum shows a core-wing anomaly in the H_α line, as HD 190290 does.

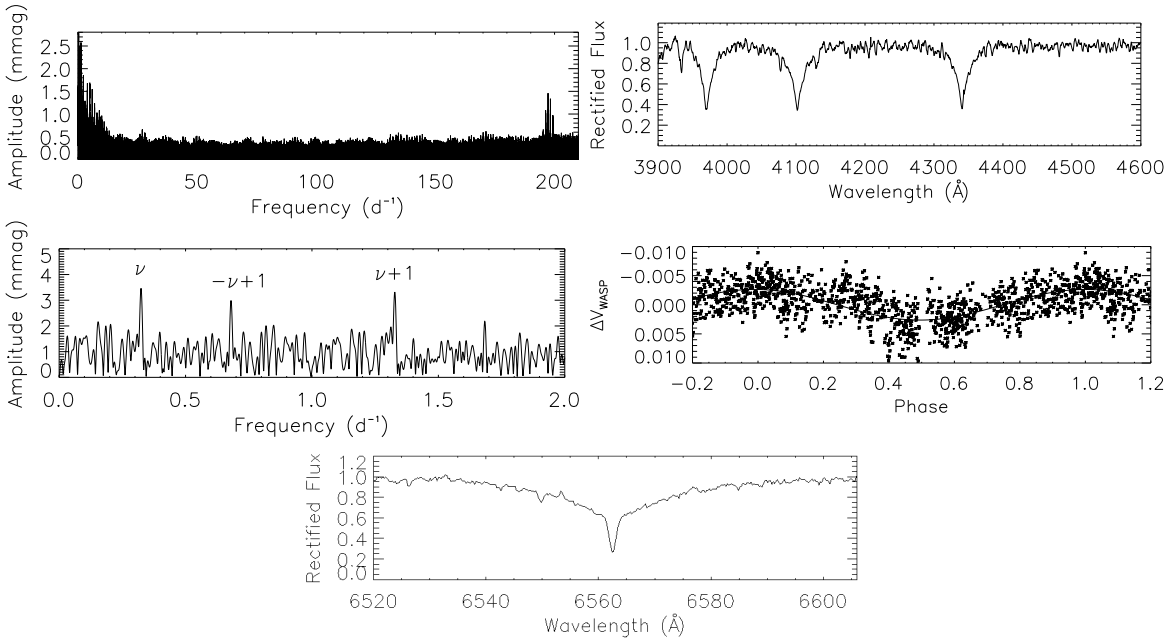

Figure 6.14: Top left: Periodogram of J0855. Top right: WHT/ISIS spectrum showing J0855 to be an A6p star. Middle left: Low-frequency periodogram with the true rotation peak labelled (ν) with the positive and negative aliases. Middle right: Phase folded light curve, folded on a period of 3.09 d and shown in phase bins of 0.001. Bottom: The H_α profile showing the core-wing anomaly.

J1110

J1110 exhibits a low-amplitude pulsation at 106.61 d^{-1} (Figure 6.15). The WHT/ISIS spectrum places the star as a cool F3p with a $T_{\rm eff}$ measured from the Balmer lines of 6500 K. The spectrum shows a slight over-abundance of Eu II at $\lambda\lambda$4128 & 4205, and a marginal over-abundance of Sr II (Figure 6.15). Also noted is the weak Ca K and Ca I at λ4226 line which may be due to stratification in the atmosphere. These features are also suggestive of an Am star, however there is no clear evident of an increase in metallic line strength, as is seen in the Am stars. On the other hand, from classification dispersion spectra it can be hard to distinguish between the Ap and Am stars.

J1110 has the lowest pulsation frequency of the WASP roAp stars and is the second coolest, as derived from the Balmer lines. J1110 is similar in amplitude and

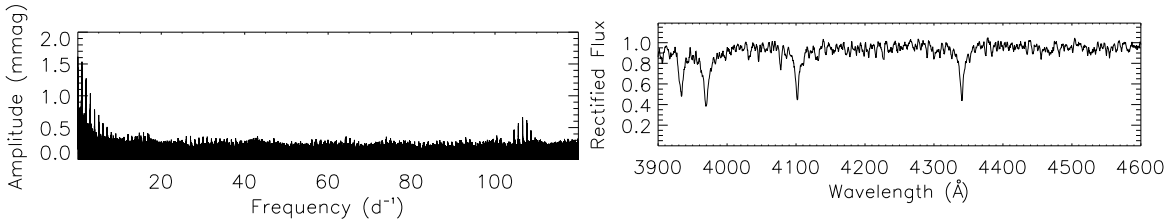

Figure 6.15: Periodogram and WHT/ISIS spectrum for J1110. The low-frequency peaks in the periodogram are due to $1\,\mathrm{d}^{-1}$ aliasing. The spectrum is classed as F3p.

frequency to HD 193756. However, HD 193756 is classified as A9 with a temperature of 7500 K derived from its H_α profile (Elkin, Kurtz & Mathys 2008).

The pulsation seen in J1110 is just $1\,\mathrm{d}^{-1}$ higher than that seen in the Am pulsator, J2054. This shows that, photometrically, the boundary between the roAp stars and the classically lower frequency pulsators is becoming more ambiguous, and that spectroscopic observations are a must before a star can labelled as a specific type of pulsator. These observations will also allow for the determination whether a magnetic field is present in the star, provided the spectroscopic resolution is high enough. Further to this, modelling of this system, as an Ap star, will provide an indication of the frequency ranges in which pulsations can be expected to be found – results which do not match the observations will allow this star to provide further modelling constraints.

J1430

Pulsating at a frequency of $235.5\,\mathrm{d}^{-1}$ with an amplitude of 1.06 mmag (Figure 6.16), J1430 is classified as an A9p star with an effective temperature of 7100 K derived from the Balmer lines. The spectrum shows an over-abundance of Eu II (Figure 6.16). J1430 is the fastest roAp star found in the WASP archive, and is third fastest of all the roAp stars.

HD 86181 is similar to J1430 in both pulsations and temperature. HD 86181 has a T_{eff} of 7900 K (Balmforth et al. 2001), but is classified as only having an over-abundance of Sr. The H_α line profile of J1430 indicates the presence of a core-wing anomaly.

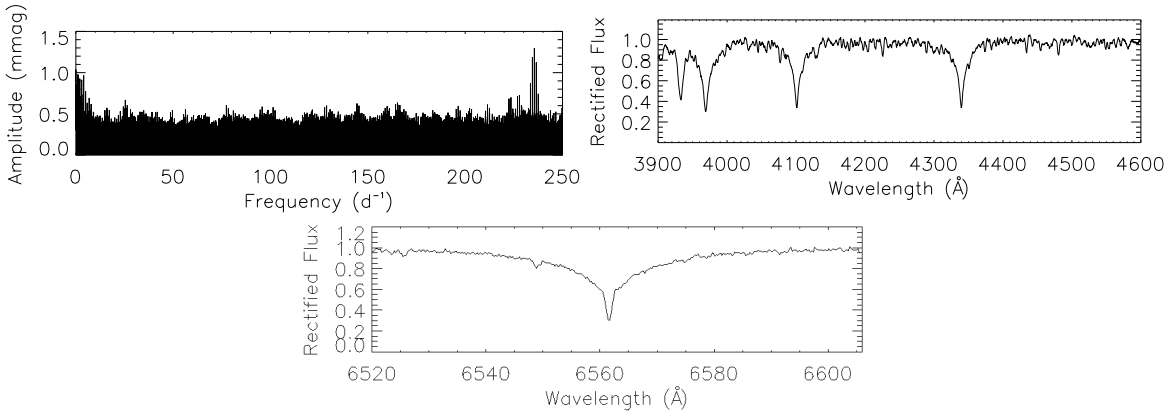

Figure 6.16: Periodogram and WHT/ISIS spectrum of J1430. The low-frequency peaks in the periodogram are due to noise. The spectrum is classified as A9p. The bottom panel shows the core-wing anomaly.

J1640

WASP photometry shows J1640 to pulsate at 151.93 d^{-1} with an amplitude of about 3.5 mmag (Figure 6.17). The classification spectrum shows over-abundances of both Sr II and Eu II allowing for the star to be classified as A8p (Figure 6.17). A low-frequency signature with a period of 3.67 d is also detected in the photometry due to the rotation of the star (Figure 6.17).

Two spectra were obtained of this target using two different instruments. The separate analysis of both spectra resulted in the same classification and T_{eff}. There are no known roAp stars which exhibit a similar pulsation spectrum as J1640, in the sense that J1640 is exhibits pulsations of 3.52 mmag in the broad-band photometry, making it one of the highest amplitude pulsators. Despite the spectra being obtained at different rotation phases, there is no noticeable difference in line strength at the resolution obtained, after the SALT/RSS spectrum has be reduced to the same resolution as the WHT/ISIS observation.

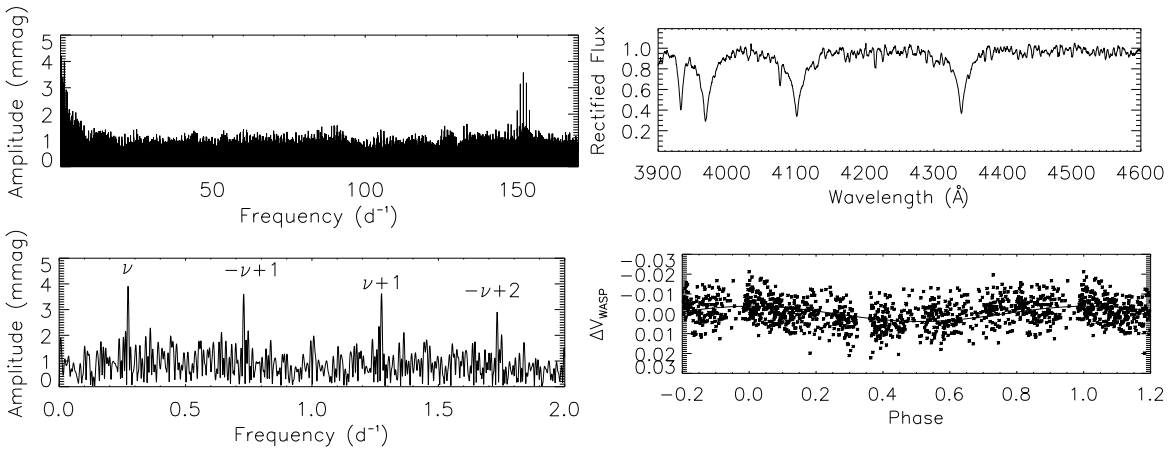

Figure 6.17: Top left: Periodogram of the WASP light curve of J1640. Top right: WHT/ISIS spectrum showing the star to be of A8p type. Bottom left: Low-frequency periodogram with the rotation signature (ν) labelled with the positive and negative aliases. Bottom right: Phase folded light curve of J1640. The data are folded on a period of 3.67 d and are shown in phase bins of 0.001.

J1844

J1844 shows a low-amplitude pulsation at 181.73 d^{-1} (Figure 6.18). This star is classified as A7p with a T_{eff} from SED fitting of 8670 ± 450 K. Balmer line determination of the effective temperature is not reliable for this star as it is difficult to rectify the orders of the echelle spectra correctly when such a broad feature is present. The spectra for this target were obtained using the Hamilton Echelle Spectrometer mounted on the Shane 3 m telescope at Lick observatory (Figure 6.18). J1844 was also observed photometrically by the *Kepler* telescope. Identified as KIC 7582608, the target has been observed in Long Cadence mode for the duration of the mission. Analysis of the *Kepler* data is published in Holdsworth et al. (2014c) and presented in Chapter 7.

J1844 is observed to have to have a rotationally modulated light curve with a period of 20 d (Figure 6.18), a signature which is also present in the *Kepler* data. This is the longest rotation period detected in a roAp star from the WASP survey. The monoperiodic pulsation is similar to HD 12098 which pulsates at 189.22 d^{-1} with a $B-$band amplitude of 3 mmag (Martinez et al. 2000).

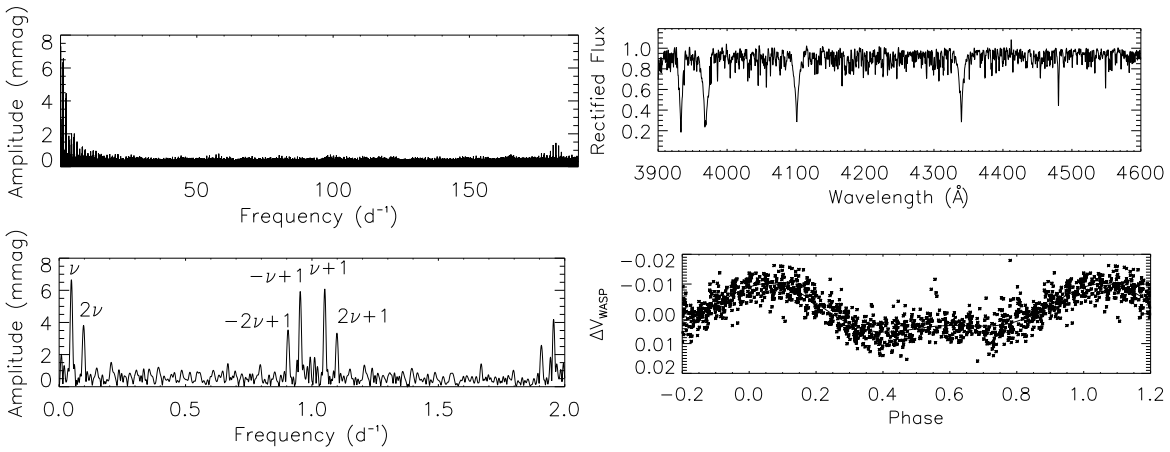

Figure 6.18: Top left: Periodogram of the WASP light curve for J1844. Top right: Shane/HamSpec spectrum. Bottom left: Low-frequency periodogram showing the rotation signature (ν), its harmonic (2ν) and their aliases. Bottom right: Phase folded light curve of J1844. The data are folded on a period of 20.2 d, and are shown in phase bins of 0.001.

Distinguishing between the rotation period and its harmonic in the periodogram can be difficult. With the roAp stars it is possible to use the pulsations to determine the rotation period by applying the oblique pulsator model. However for other stars this is not possible. Phase folding the light curve can help to identify the correct period, as well as comparison with a $v \sin i$ measured from spectroscopy.

J1921

The pulsation in J1921 occurs at 128.76 d^{-1} with an amplitude of 1.99 mmag (Figure 6.19). The frequency in J1921 is close to that of HD 122970, at 129.73 d^{-1}, but the amplitude of the WASP roAp star is estimated to be about twice the amplitude of HD 122970. The WHT/ISIS spectrum is shown in Figure 6.19, and indicates a temperature of 6 200 K, in agreement with the SED fitting also performed. These place the star cooler than HD 122970, and as the coolest in the WASP data.

J1921 is a difficult star to classify. The characteristic features of a hot Ap star are present, such as Si II at $\lambda\lambda$3856 & 3862 as well as the doublet at $\lambda\lambda$4128, 4132. Eu II is

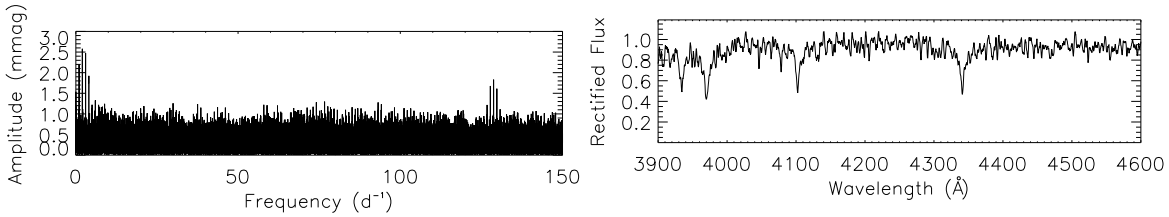

Figure 6.19: Periodogram and WHT/ISIS spectrum of J1921. The low-frequency peaks in the periodogram are due to noise. The star is classified as F3p.

also present at λ4205 as is Sr II at λ4077 (Figure 6.19). It is possible though, that the Sr II feature is in fact Si II at λ4076, but it is not expected that the Si be such a strong line here. The other common line of Sr II at λ4216 does not appear to be enhanced. Signatures on the wing of H_δ may be due to Cr II at λ4111 (the other most likely ions are Fe I or Fe II), but Cr II is not detected at the other wavelengths used to confirm the Cr peculiarity. The Ca I at λ4226 is weak, as well as Mg II at λ4481. These detections, or lack of, suggest that J1921 may be a hot Bp star, however there are no lines of He I detected, as would be expected, and the spectrum shows many metal lines which are not present in the spectra of B-type stars.

Fitting of the Balmer lines in J1921 suggest it is an F8 type star, with a $T_{\rm eff}$ of 6 200 K. At this temperature, the G-band feature at λ4300 should be almost as strong as the H_γ line, which is clearly not the case. Further to this, the Ca K line is weak for this type, being comparable to that of an A7 star. With this difference between the Ca K and Balmer lines, it could be expected that this is in fact an Am star, with a third classification for the metal lines. As previously noted, the Am stars show an under-abundance of Sc II, as is the case here with lines at $\lambda\lambda$4400 and 4417. However, the peculiarity found in the spectrum with regards to the metal lines makes it impossible to match them to MK standards. The presence of many lines which are not apparent in other classification dispersion spectra make it difficult to label this star.

The red-arm ISIS spectrum of J1921 provides inconclusive evidence of the class of the star. There are features where lines of Nd III and La II are expected for roAp stars, however at classification dispersion their presence cannot be guaranteed. The H_α

profile shows the common core-wing anomaly of the Ap stars, but this alone cannot be used to class the star. Interestingly, there is no evidence of the Na D doublet at λ5893, indicating that the reddening for this object is very small, and in agreement with that used in the SED fitting.

The spectrum of J1921 is, in many respects, similar to that of J1110 presented above. Both stars show low temperatures from both methods (J1110: $T_{\rm eff_H} = 6\,300\,{\rm K}$, $T_{\rm eff_{SED}} = 6\,707\,{\rm K}$; J1921 $T_{\rm eff_H} = 6\,200\,{\rm K}$, $T_{\rm eff_{SED}} = 6\,730\,{\rm K}$) and the line profiles of the Balmer and Ca K lines are almost identical. However, the metals line profiles of J1110 are consistent with a normal A-type star, whereas J1921 show much stronger features. When compared to the Ap stars, J1921 is peculiar even in this class.

J1940

J1940 shows a pulsation at $176.39\,{\rm d}^{-1}$, and is the highest amplitude roAp star discovered by SuperWASP at 4.2 mmag (Figure 6.20). Given the effects of amplitude reduction of pulsations in the WASP data, J1940 may be the highest amplitude roAp star known, with a predicted amplitude of about 13 mmag in the $B-$band based on the conversion of Medupe & Kurtz (1998). The SALT/RSS classification spectrum was obtained at a low S/N due to the faintness of the target. After smoothing the spectrum (by convolving it with a Gaussian profile), it is deduced that J1940 is an F2p star with enhancements of Eu II (Figure 6.20). A low-frequency signal is also detected in the photometry with a period of 9.58 d (Figure 6.20).

J1940 is a prime example of the large pixel sizes of the WASP cameras, and the possible blending that this introduces. Figure 6.21 left shows a DSS image of the target star (centre) and surrounding objects. The over-plotted circle represents the photometric aperture of WASP (with a radius of 48″, 3.5 WASP pixels). To confirm the source of the high-frequency pulsation, the TRAPPIST telescope (Jehin et al. 2011) was used to observe the target for 3 h (obtained and reduced by M. Gillon). TRAPPIST is a 0.6 m robotic telescope situated at the ESO La Silla Observatory. Backed by a CCD camera of 2048×2048 pixels, the instrument achieves a plate scale of 0.6″ per

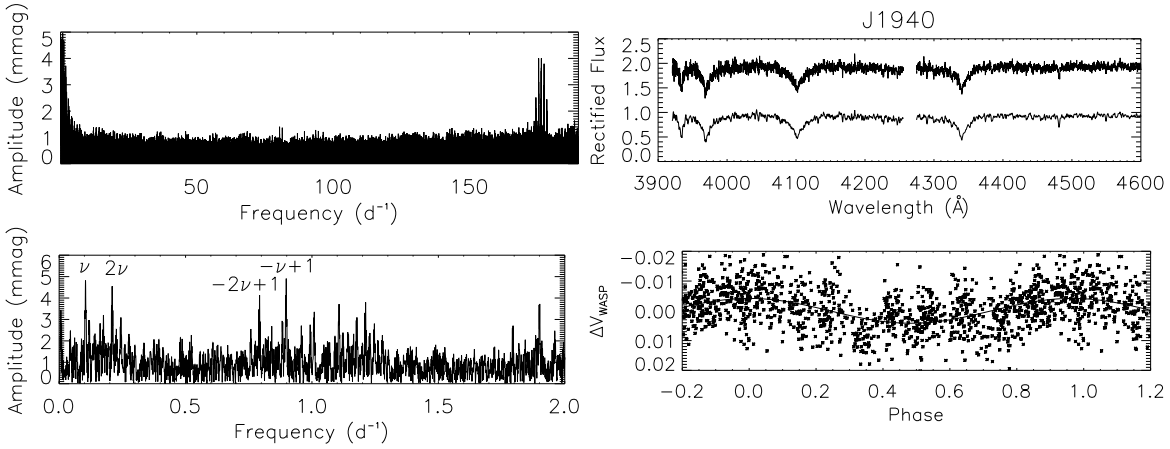

Figure 6.20: Top left: Periodogram of the WASP light curve of J1940. Top right: SALT/RSS spectrum of J1940. The upper spectrum is the raw data, while the lower one is the smoothed spectrum. Bottom left: Low-frequency periodogram of the light curve with the rotation signature labelled (ν) and its harmonic and their positive and negative aliases. Bottom right: Phase folded light curve of J1940. The data are folded on a period of 9.58 d and shown in phase bins of 0.001.

pixel. This vastly superior plate scale compared to WASP, enabled the confirmation that J1940 is the source of the pulsation (Figure 6.21 right). However, due to the short data set it is not possible to confirm the origin of the low-frequency signature which could still originate from one of the other objects in the WASP aperture.

Further observations have been made of J1940 using the 1.9 and 1.0 m telescopes at the Sutherland Station of the SAAO. These data will be discussed in Chapter 8.

6.6 Hybrid Pulsators

Presented below are two further stars which show pulsations above $80\,\mathrm{d}^{-1}$ for which spectra have been obtained. Both show pulsations in two distinct frequency ranges, something that current theory did not predict for the A-type stars (Pamyatnykh 2000).

Balona et al. (2012a) conducted simulations of a *Kepler* δ Sct star (KIC 4840675) which shows both low- and high-frequency pulsations. They found that when convec-

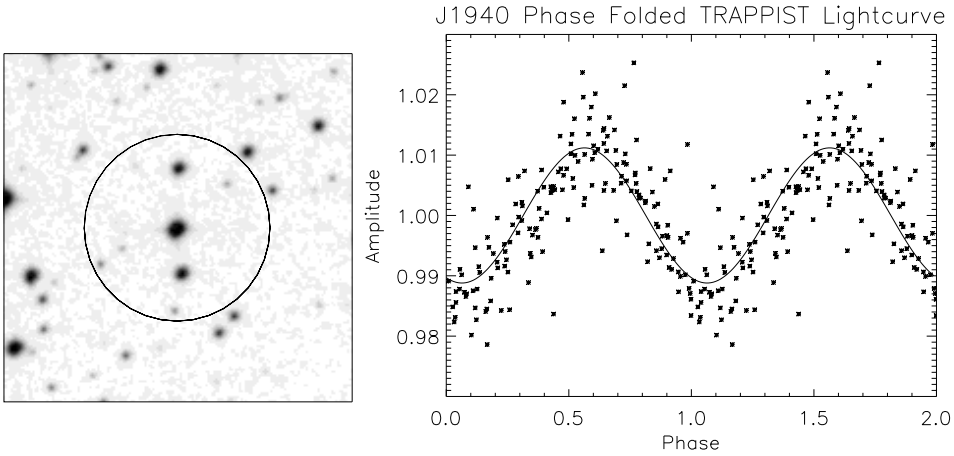

Figure 6.21: Left: Photometric aperture (dark circle) for J1940 (central star) showing how multiple stars may fall into the aperture. Image from DSS. Right: Phase folded TRAPPIST light curve for J1940. Obtained to confirm the origin of the variability seen in the WASP data. Data are folded on the principal frequency of $176.39\,\mathrm{d}^{-1}$.

tion is suppressed, both high- and low-order p modes were excited in the H ionisation zone. However they discount the possibility of convection suppression in their star due to the large $v \sin i$ they measured and a lack of resemblance to roAp stars which show frequencies in a similar range to KIC 48404675. Similarly, Antoci et al. (2011) proposed that a small convection layer near the surface of the star can excite solar-like oscillations in the A-type stars, however conclusive evidence has yet to be found. Therefore, to identify more targets which show this hybrid pulsation pattern is key to test these theories.

Of the two targets discussed, J1403 is classified as a normal A-type star, whereas J1917 is classed as an Am: star.

J1403

J1403 is an interesting target as WASP observations show it to pulsate in two distinct frequency ranges (Figure 6.22). Nine pulsational frequencies are detected between 25 and $34\,\mathrm{d}^{-1}$ and four between 87 and $100\,\mathrm{d}^{-1}$. The star is classified as A9 from the

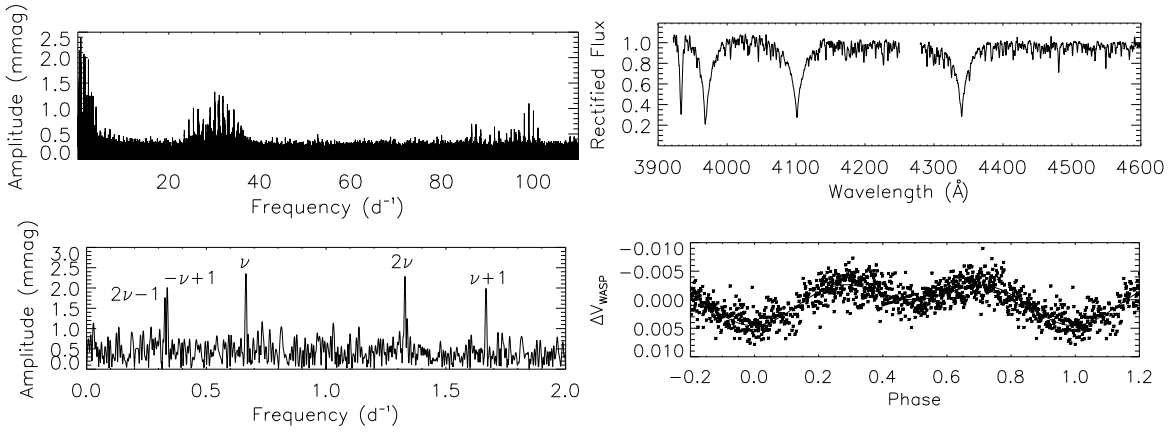

Figure 6.22: Top left: Periodogram of the WASP light curve of J1403. Top right: SALT/RSS spectrum suggesting a normal A9 type star. Bottom left: Low-frequency periodogram showing the ellipsoidal signature (ν) and its harmonic and their positive and negative aliases. Bottom right: Phase folded light curve of J1403. The data are folded on a period of 1.5053 d and shown in phase bins of 0.001.

SALT/RSS spectrum (Figure 6.22), however it is noted that different classifications are recorded in the literature (e.g. A3/5III, Houk 1978; F0V, Pickles & Depagne 2010; F8 (HD)). Low-frequency variations are also detected in J1403 at a period of 1.5053 d (detected with a FAP of 0.0). The phase folded plot (Figure 6.22) shows that this target is most likely an ellipsoidal variable. In such a case, it is possible that the pulsations in the difference frequency ranges originate from two separate stars. Time-resolved high-resolution spectra would be required to solve this issue, or high-precision and high-cadence photometry may allow for the PM method of Murphy et al. (2014) to be applied, as long as the rotation period is much greater than the pulsation period. With the WASP observations this is not a viable method as the rotation period is short and therefore under sampled in the WASP data. Any attempt at photometric PM observations would require a high-duty cycle over many orbital periods, with cadences in the second or sub-second regime to increase the likelihood of detecting phase modulation. At $V = 10.4$, this is possible for this star.

J1917

J1917 shows strong pulsations in two separate regions. There are multiple pulsations in the δ Sct range (41.3, 45.5, 53.1 & 61.0 d^{-1}) and a single peak in the higher frequency domain (164 d^{-1}). A classification dispersion spectrum was obtained with SALT/RSS, revealing the star to be Am: in nature (Figure 6.23) due to the weak Ca K line.

Due to the large pixel size of the WASP instrument, there is a blending issue with J1917, with multiple objects in the photometric aperture (Figure 6.24). Therefore, to determine if all of the detected signals are from the target star, dedicated photometry was performed with the TRAPPIST telescope (by M. Gillon). Figure 6.23 shows the light curve and periodogram (bottom row) of the TRAPPIST observations. It is clear that both the low- and high-frequency pulsations originate from J1917.

Further to this, the star is listed in the WDS catalogue (Mason et al. 2001) with a separation of 1.3″ based on two observations in the 1930s. A distance to J1917 is

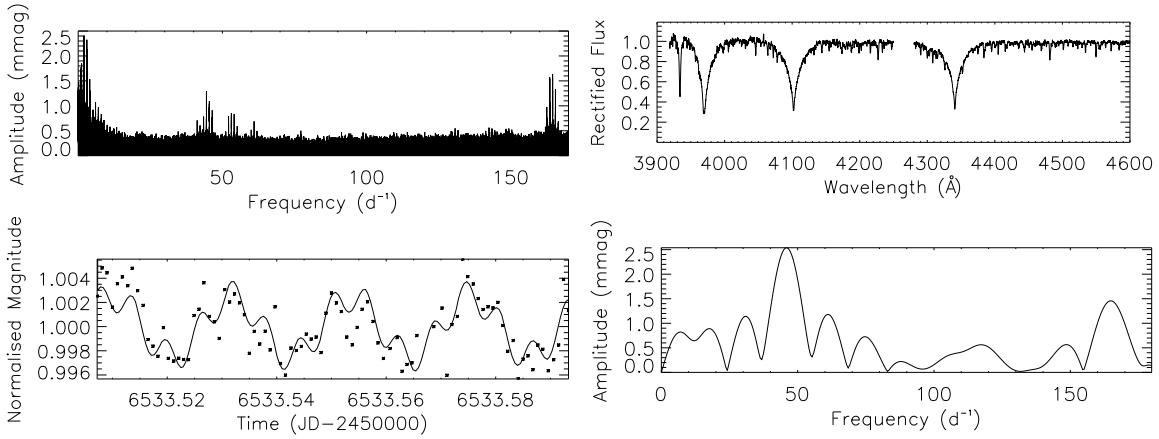

Figure 6.23: Top left: The WASP periodogram of J1917. Top right: SALT/RSS spectrum of J1917 showing it to be an A7m: star. Bottom left: Two hours of TRAPPIST follow-up observations confirm the pulsations originate on J1917 (the data have been binned on 1 min intervals). Bottom right: Periodogram of the TRAPPIST data. The peak at 45 d^{-1} is stronger than in the WASP periodogram as there are many pulsations contributing power that are not resolved in just 2 h. The high-frequency peak is at about the same amplitude as the WASP data.

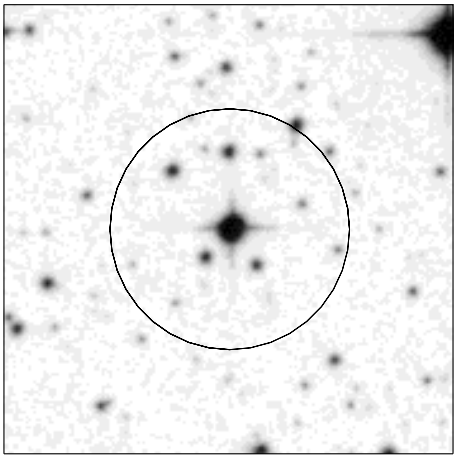

Figure 6.24: Photometric aperture (dark circle) for J1917 showing multiple stars in the WASP aperture. Follow-up observations using the TRAPPIST telescope confirm the pulsations are originating from the central object. Image from DSS.

estimated, based on the V magnitude and M_V from Gray (1992), to be about 400 pc, which suggests a binary separation of at least 500 au. The two components of the visual binary system have magnitudes of 10.8 and 14.0 in the V-band (Mason et al. 2001). If the companion is a main-sequence star, given the spectral type of the primary, it is estimated to be a G-type star. None of the pulsations, given their amplitudes, are expected to originate from a G star. Therefore, it is proposed that either both sets of pulsations originate on the Am star, or that there is an unresolved binary system with two pulsating components. Further observations of this target have been obtained with the VLT/UVES instrument and consist of two hours of time-resolved high-resolution spectra. These are discussed in Chapter 8.

6.7 The sdBV Stars

As mentioned in Chapter 4, there were three sdBV stars which were found to pulsate in the WASP data. One star, J2344, had previously been observed by Østensen et al. (2010) using the NOT, who found no pulsations down to their detection limit. This

star was found in the $50 - 300\,\mathrm{d}^{-1}$ frequency range as part of the main-stream survey. The other two stars, J0902 and J1938, are new sdBV pulsating stars. One, J1938, was found in the $50 - 300\,\mathrm{d}^{-1}$ range, while the other was found in the archive during an investigative foray into the VHF frequency domain. These stars show the power of the WASP instrument to find pulsating stars away from the main-sequence, through both long-term monitoring of the sky, and the observing strategy employed by the project.

J1938

J1938 is a newly identified sdBV star which pulsates at a frequency of $231.62\,\mathrm{d}^{-1}$ with an average amplitude of 5.05 mmag (Figure 6.25). Over the period of WASP observations, the amplitude has decreased from about 5 mmag to 3.4 mmag. This variation is shown in Figure 6.26 where it can also be seen that the frequency splits into two well resolved peaks with the amplitude being 'shared' between them.

J1938 is similar to the well studied sdBV star Balloon 090100001 (Baran, Pigulski & O'Toole 2008; Telting et al. 2008; Baran et al. 2009). This star also shows amplitude variations in photometric and spectroscopic data. However, in Balloon 090100001 there are many pulsation frequencies present which are both p and g modes which the energy can be transferred between. The amplitude variations seen in J1938 may be a result of the beating of the two peaks, or energy transfer between odd and even modes.

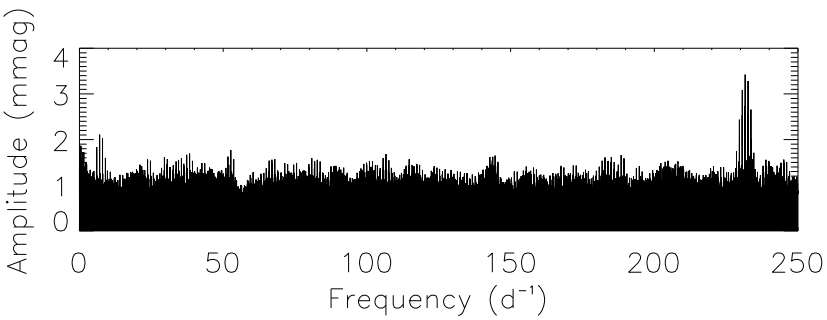

Figure 6.25: Periodogram of J1938 showing the pulsation at $231\,\mathrm{d}^{-1}$. The low-frequency peaks are due to d^{-1} aliases.

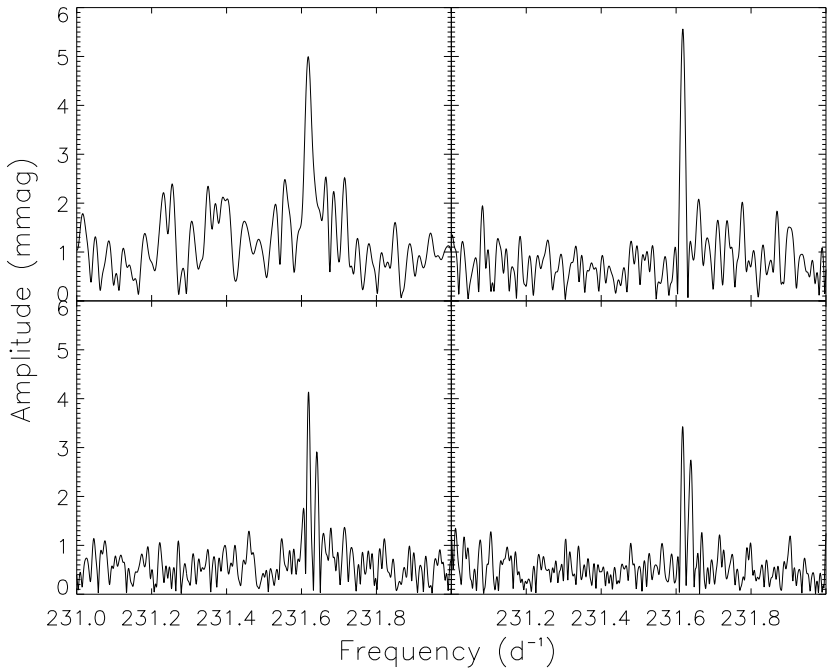

Figure 6.26: Periodogram of the separate seasons for J1938 showing the amplitude variation of the peak, and the splitting of the mode into two well resolved frequencies.

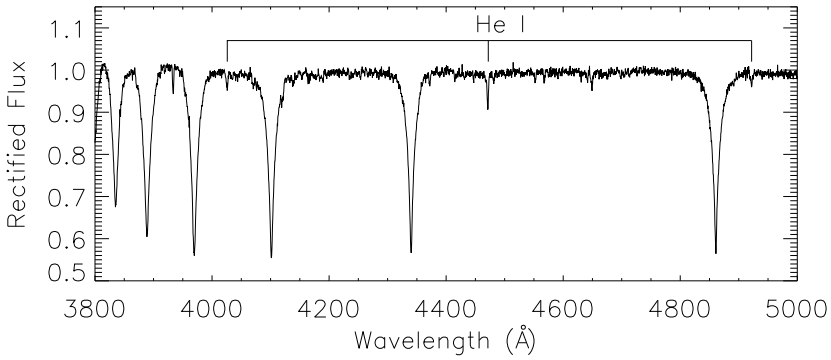

Figure 6.27: WHT/ISIS spectrum of J1938 showing it to be an sdB star. Lines of He I are labelled.

The spectrum of J1938 was obtained with WHT/ISIS and shows the star to be an sdBV type. The spectrum id quite bare, with the Balmer lines and He I lines present (Figure 6.27). Spectral fitting by **R. Østensen** determined a temperature of $29\,240 \pm 87$ K and a $\log g$ of 5.35 ± 0.01 (cgs).

J2344

As previously mentioned, this star (HIP 117100; with a parallax of 4.56 ± 1.72 mas; van Leeuwen 2007) has been observed by Østensen et al. (2010) during their search for variable sdB stars using the NOT. From their observations, they defined the star as '*not observed to vary*', rather than non-variable due to their high detection limits. The light curve which they obtained consisted of just 84 data points with a cadence of 10 s. Their observing strategy was aimed at identifying high-amplitude high-frequency pulsations in the sdB stars.

The WASP observations of J2344 cover four seasons, with a total of 30 658 data points. The pulsation, at $216\,\mathrm{d}^{-1}$, is detected in all seasons of the data with an average amplitude of 1.64 mmag (Figure 6.28). As well as the sdBV pulsation, there are further pulsation frequencies at $8.68\,\mathrm{d}^{-1}$ and $22.31\,\mathrm{d}^{-1}$ with amplitudes of 1.29 and 1.16 mmag, respectively. These low-frequency pulsations may originate from a main-sequence companion, as most sdBV stars are found in binaries, or they may be g modes in the same star, as is observed with the DW Lyn sdBV stars (Schuh et al. 2006).

The binary solution to the low-frequency peaks seems unlikely in this case. Of the know sdB binary systems, the amplitudes of peaks caused by binary motion are much larger than those observed here. HW Vir was the fist system to be observed as an sdB and M-dwarf companion, and showed an amplitude of about 0.26 mag (Kiss et al. 2000), with later discoveries pushing this down to 83 mmag (Maxted et al. 2002). These large amplitudes are explained by the reflection effect; when the sdB star and the companion are sufficiently close, a bright hot spot is produced on the companion by the hotter sdB star. The brightening varies sinusoidally with the binary period as the hotter hemisphere of the companion comes in and out of the observers view. The amplitudes observed here are much below this limit. There is no indication in the light curve of J2344 that this star is a binary, however the periodograms suffer greatly from low-frequency noise, and as such binarity can not be entirely ruled out. However, Geier & Heber (2012) analyses a VLT/FEROS spectrum of this star and found no contamination from a main-sequence companion.

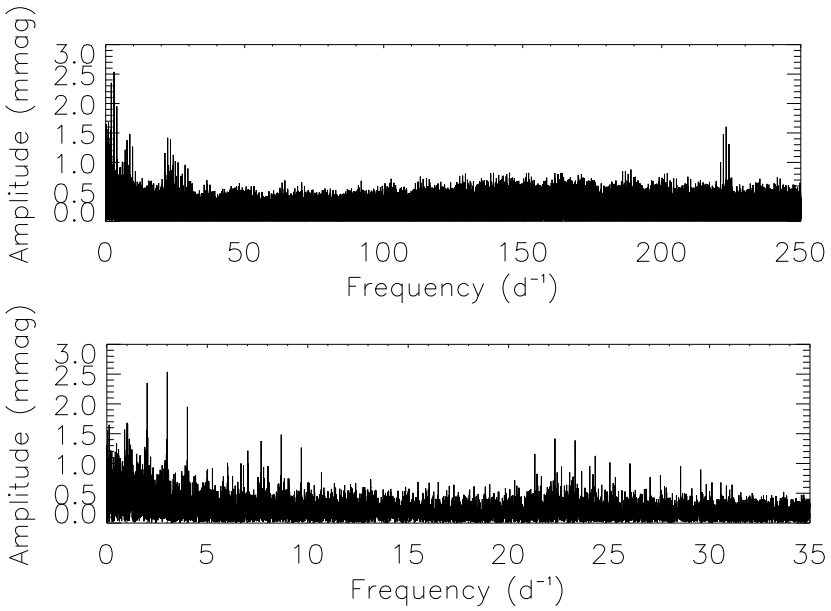

Figure 6.28: Periodogram of the WASP light curve of J2344. The low-frequency range is shown in more detail due to the multiple frequencies present. The principle peak at $3\,\mathrm{d}^{-1}$ is an alias.

The presence of g modes in the frequency range $18 - 48\,\mathrm{d}^{-1}$ for sdBV stars were first detected by Green & Stephenson (2003), however in a different temperature range from the p mode pulsators of the same frequency. Jeffery & Saio (2006) were later able to extend the instability strips of the sdBV stars, so that the p and g mode regions overlapped, by including nickel opacities in their calculations. All of the sdBV with pulsation periods in the range $216 - 288\,\mathrm{d}^{-1}$ are DW Lyn stars, except one (KL UMa; O'Toole, Heber & Benjamin 2004). This is further support that J2344 is of the DW Lyn hybrid type. There is also only one star which pulsates in this range that is known to be a binary (again KL UMa), suggesting J2344 is probably a single star.

There are conflicting temperatures for J2344 presented in the literature. McDonald, Zijlstra & Boyer (2012) suggest J2344 has an effective temperature of 37 448 K with an error of 4.4 per cent. This value is derived through SED fitting and does not take into account interstellar reddening and assumes a solar metallicity for the fits, an assumption which is inaccurate for the sdB stars. A more accurate result is presented

by Geier et al. (2013) who use their FEROS spectrum to derive a $T_{\rm eff}$ of $27\,000 \pm 500$ K. Further to this, Heber et al. (1984) found a value of $28\,800 \pm 1\,500$ K, and Németh, Kawka & Vennes (2012) find a $T_{\rm eff}$ of $28\,390 \pm 265$ K. These values from spectral fitting provide a more reliable temperature estimate than that of McDonald, Zijlstra & Boyer (2012), so it is taken that the $T_{\rm eff}$ of this star is $28\,000 \pm 1570$, placing it in the DW Lyn temperature range.

An attempt has been made to fit the SED of J2344 using the same method as above, but with $\log g$ set to 4.5, as this is a known sdB star which have high surface gravities. However, the star is too hot, causing none of the model atmospheres to be fit to the photometric values. There is therefore no temperature determination for J2344 in this work. If the low-frequency peaks are indeed caused by g mode pulsations, the lower temperature is expected. The instability strips of the short-period, p mode, sdBV stars and the longer period, g mode, pulsators overlap at a temperature of about $T_{\rm eff} \sim 29\,000$ K, about the temperature of J2344.

Previous to *Kepler*, these hybrid pulsators were seen to have amplitudes much larger than their non-hybrid counterparts. However, Reed et al. (2010) found pulsations in *Kepler* targets which are below ground-based detection limits. *Kepler* observations have also shown g modes to be of higher amplitude than the p modes in the same star, unlike previously observed hybrid sdBV stars, as well as J2344 here.

The presence of both p and g modes in a single star is key to understanding the stellar structure, as the different excitation mechanisms probe different depths in the star. Further observations of J2344 are required to confirm the presence of the g modes, excluding the possibility of a pulsating binary companion. Well determined $T_{\rm eff}$ and $\log g$ values are required to place the star in a $\log g - T_{\rm eff}$ diagram to determine whether it lies in the same location as the known hybrid pulsators.

J0902

The results from an investigation into the VHF domain, above $300\,{\rm d}^{-1}$, showed a clear detection in one object: J0902. In the SuperWASP archive, this star has $V = 12.4$ and

a $(J-H)$ value of 0.219, suggesting a spectral type of about F6. The target appears in the SIMBAD database as TYC 4890-19-1 and gives $B = 11.9$. There are no references to this target in published works.

The SuperWASP photometry shows a pulsation at $636.73\,\mathrm{d}^{-1}$ with an amplitude of 11.70 mmag, and a second peak at $615.33\,\mathrm{d}^{-1}$ with an amplitude of 2.44 mmag (Figure 6.29). These frequencies are much higher than those expected in the A- and F-type main-sequence pulsators, indicating that this star is a compact pulsator. Expanding on the SED fitting presented in Table 6.2, where the $\log g$ was set to 4.0 (resulting in $T_{\mathrm{eff}} = 10\,140 \pm 1\,120\,\mathrm{K}$), the $\log g$ was increased to 4.5, the maximum of the Kurucz flux models (Kurucz 1993), resulting in $T_{\mathrm{eff}} = 10\,260 \pm 1\,140\,\mathrm{K}$. However, visual inspection of the fitted spectrum, Figure 6.30, shows a significant under-fitting an available GALEX near-UV flux, indicating that this target is much hotter. The reddening along the line-of-sight to this object is $E(B-V) = 0.03 \pm 0.01$ from the dust maps of Schlegel, Finkbeiner & Davis (1998), which is in agreement with the parameters used for the SED fitting (namely $E(B-V) = 0.02 \pm 0.02$).

A spectrum of J0902 was obtained with the Andalucia Faint Object Spectrograph and Camera, ALFOSC, instrument mounted on the Nordic Optical Telescope (by R. Østensen) on 04/02/2013 (Figure 6.31). As can be seen, there are many helium

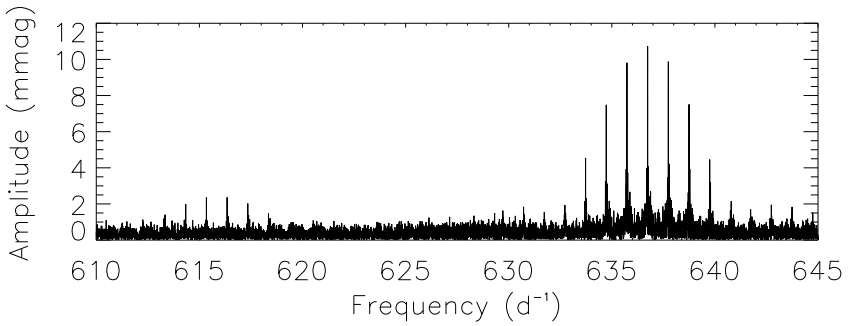

Figure 6.29: Periodogram of the WASP light curve of J0902 showing two pulsation periods.

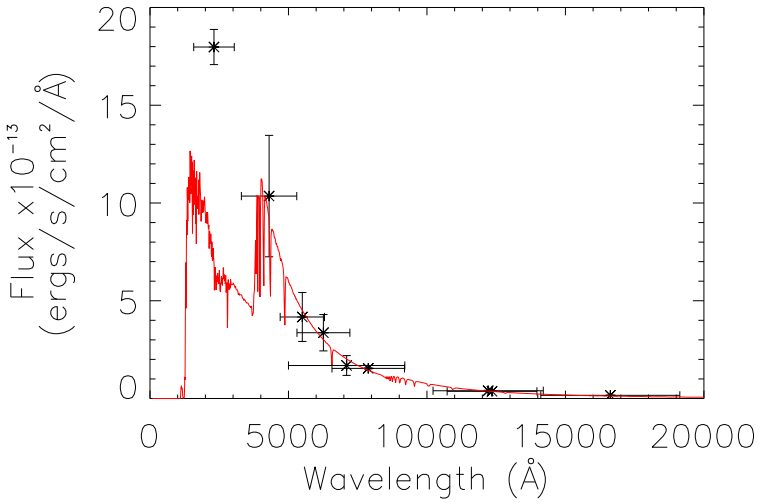

Figure 6.30: The fitted SED of J0902, showing an under-fitted GALAX near-UV flux. The red line represents the fit of parameters: $T_{\rm eff} = 10\,250\,\mathrm{K}$, $\log g = 4.5$ and solar-metallicity.

lines present in the spectrum, and other than the Balmer lines, the spectrum is quite featureless. A spectral fit performed by Østensen gives an effective temperature of $34\,558 \pm 153\,\mathrm{K}$ and a $\log g = 5.82 \pm 0.03$. This star is therefore classed as a pulsating subdwarf B star. This temperature explains the discrepancy between the SED fitted spectrum and the available GALEX flux.

The pulsations in J0902 are typical of those found in sdBV stars, with the short period, 136 s, indicating that the variations are due to p mode pulsations driven by the iron opacity bump (Østensen 2010). This is so far the only new compact pulsator extracted from the WASP archive which has pulsations above $300\,\mathrm{d}^{-1}$. Further investigations are needed in this frequency range to fully exploit the potential of the WASP data, and to expand the number of this type of pulsating star. However, as previously discussed, the procedures used to explore the lower frequency domains, coupled with the amplitude dilution effects, lead to the conclusion that to successfully extract peaks in the VHF domain, significant work is required, work beyond the scope of this thesis.

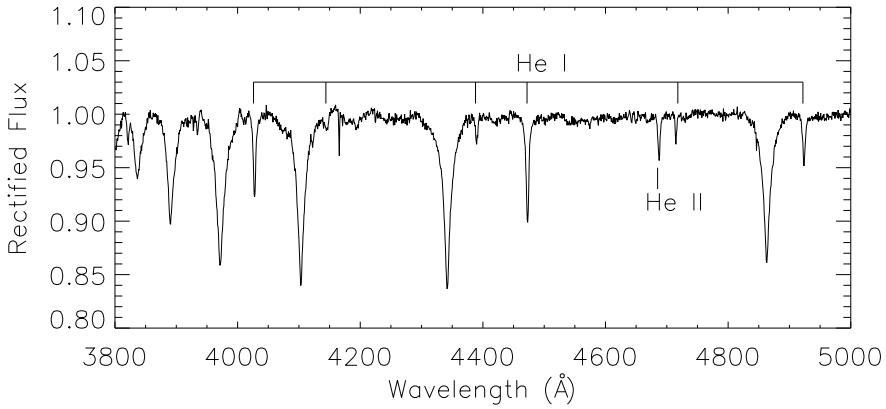

Figure 6.31: NOT/ALFOSC spectrum of the sdBV star J0902. The He is slightly over abundant for this type of star.

6.8 Conclusions

This Chapter has presented and discussed a selection of the 375 high-frequency pulsating systems that have been found in the SuperWASP data. Follow-up spectroscopic observations have been obtained for these objects to be able to properly classify them in terms of spectral type and so pulsation class. This relatively small number of detailed observations show a selection of what the SuperWASP data can offer the A-star community. Further classification of the 375 high-frequency stars may provide a selection of both chemically peculiar and chemically normal stars to test the frequency limits of pulsation theory in the A-type stars.

The discovery of 11 new roAp stars means this work has contributed about 22 per cent of the know roAp stars to date, the joint largest single addition to this class of pulsating star. Within this class, the coolest roAp stars to date have been identified, pushing further into the F-type stars. This shows that more work is needed to model the roAp stars at cooler temperatures. Theory has failed to predict the existence of roAp stars with temperatures lower than about 7400 K (Balmforth et al. 2001; Cunha 2002; Théado, Vauclair & Cunha 2005; Théado & Cunha 2006; Dupret, Théado &

Noels 2008), however observations show their existence down to about 6300 K. There is also an indication that the largest amplitude roAp star known has been discovered in the SuperWASP archive, again pushing the current limits of theses stars, and providing further observational constrains for theoretical modelling. Beyond the roAp stars, many new pulsating δ Sct stars have been presented, along with the rarer pulsating Am stars.

The frequencies discovered in the Am and δ Sct stars have extended the known frequency ranges of these class of pulsator, further blurring the distinction between pulsation classes. Further to this, the temperatures derived for some of the stars suggest they are much hotter than the current theoretical blue-edge of the instability strip. Further spectroscopic observations are required to clarify this, and to probe the individual stars further.

Due to the blind nature of the survey, unexpected results have also been found, such as the multi-periodic systems like J1403 and J1917 where further observations are required to deduce the nature of the systems. Much more work is needed to continue to expand and build upon the results presented here, both photometrically and spectroscopically.

With the results of the GAIA mission, much more accurate distances, and hence luminosities, will enable these stars to be precisely placed in the HR diagram, testing the edges of the currently understood pulsational instability strip of each pulsator class.

It is becoming ever more evident that rigid classification of the pulsating A-type stars from photometric observations alone is not viable. The continued discovery from both ground- and space-based instruments are providing results which no longer conform to the original groupings.

7 KIC 7582608 - a roAp Star in the *Kepler* FoV

This work was published in Holdsworth et al. (2014c). Areas with significant contributions by co-authors have been included for completeness, but are highlighted as such.

One of the new roAp stars presented in Chapter 6 is in the original *Kepler* field. Designated J1844 in the WASP archive, this star is designated KIC 7582608 in the *Kepler* database. After discovery in the WASP data, a Guest Observer proposal was submitted to the Guest Observer Office for Short Cadence observations of this star for one Quarter (Q19). The proposal was a collaboration between the author (PI), B. Smalley (Co-I), D.W. Kurtz and M.S. Cunha. The proposal was accepted by the panel and awarded the observing time. Unfortunately, shortly after this, the second reaction wheel on the *Kepler* satellite failed, ending the *Kepler* mission. As such, the work presented in this Chapter makes use of the available long cadence *Kepler* data.

7.1 Introduction

To date, the *Kepler* mission has enabled the discovery of four roAp stars, all which have pulsation amplitudes much below the detection limits of ground-based photometry. The first to be found in the *Kepler* data was KIC 8677585 (Balona et al. 2011b), a known A5p star observed during the 10 d commissioning run with the 1 min Short Cadence (SC) mode. This roAp star pulsates at multiple frequencies in the range $125 - 145\,\mathrm{d}^{-1}$ with amplitudes in the range of $8.4 - 32.9\,\mu$mag. This star also shows a low frequency variation at about $3\,\mathrm{d}^{-1}$ which Balona et al. (2011b) suggest is a g-mode γ Doradus pulsation, after consideration of other possibilities.

The second roAp star in the *Kepler* data is KIC 10483436 (Balona et al. 2011a) pulsating at two frequencies, each mode showing a quintuplet separated by the well

determined rotation period. Again, the amplitudes of pulsation are much below the ground-based detection limits, namely in the range $5 - 69\,\mu$mag.

KIC 10195926 is the third identified roAp star in *Kepler* data (Kurtz et al. 2011). As with KIC 10483436, KIC 10195926 pulsates in two independent modes with amplitudes less than $170\,\mu$mag. Both modes show rotational splitting. The precision of the *Kepler* data has allowed the authors to claim KIC 10195926 has two pulsational axes, the first evidence of such a phenomenon in roAp stars.

The forth *Kepler* roAp is KIC 4768731 (Niemczura et al. 2014). Discovered to be an Ap star through spectral classification, KIC 4768731 is the second slowest roAp pulsator, varying with a frequency of $61.45\,\mathrm{d}^{-1}$ at an amplitude of $62.6\,\mu$mag (Smalley et al. 2015).

KIC 7582608, presented here, represents the fifth roAp star in the *Kepler* field. The star shows a single pulsation at $181.7324\,\mathrm{d}^{-1}$ with an amplitude of 1.45 mmag in the WASP broad-band filter. It was observed by the *Kepler* satellite for the full duration of the mission in the 30 min Long Cadence (LC) mode. As a result, the true pulsation frequency is above the Nyquist frequency of the *Kepler* LC data. Although this results in a reduction of the observed pulsation amplitude, it has been shown that frequencies higher than the Nyquist can be reliably extracted from LC data (Murphy, Shibahashi & Kurtz 2013).

7.2 Spectroscopic Observations

Two epochs of spectra for KIC 7582608 have been obtained using the Hamilton Echelle Spectrograph (HamSpec) mounted on the 3.0 m Shane telescope at Lick Observatory (Vogt 1987). The observations were taken on 2012 July 24 and 2013 June 28 (by K. I. Clubb) and have a resolution of $R \sim 37\,000$ and a signal-to-noise ratio (S/N) of about 40. The spectra were reduced in IDL with instrument specific software that performs flat-field corrections, de-biases, cosmic-ray cleaning, and wavelength calibrations. The data were reduced by K. I. Clubb. Three spectra from 2012 and two from 2013

Table 7.1: Details of spectroscopic observations taken with HamSpec on the Shane 3.0-m telescope. The rotational phase has been calculated as shown in the text.

BJD-245 0000.0 Co-added	BJD-245 0000.0 Single	Exposure time (s)	Rotational phase
6132.83304	6132.81003	1800	0.88
	6132.83394	1800	0.88
	6132.85516	1800	0.88
6471.80976	6471.79915	1800	0.47
	6471.82036	1800	0.47

have been co-added to produce two single spectra. Table 7.1 gives the spectral details, including the rotation phase at which the spectra were taken (see section 7.3.1).

The two spectra show velocity shifts away from rest wavelengths for each epoch. These shifts are calculated by comparison with strong, unblended lines of Mg II λ4481, Ca II λ4226, and the Na D lines using cross-correlation, resulting in shifts of 45.8 ± 2.8 and $50.5 \pm 2.8\,\mathrm{km\,s^{-1}}$ for 2012 and 2013, respectively.

Figure 7.1 gives examples of spectral lines of elements found in the atmospheres of Ap stars extracted from the spectra. Note the variation of line strengths between the two different epochs and thus rotational phase, indicative of surface chemical abundance anomalies in the form of spots. Close to maximum optical light, at phase 0.88 in 2012 (the upper black lines in Figure 7.1), stronger lines of the rare earth elements are seen compared to the second epoch at phase 0.47 (red lower lines in Figure 7.1) where the opposite hemisphere is observed. The ephemeris for the phase (ϕ) calculations are calculated for the first light maximum (BJD) in the WASP data such that

$$\phi(E) = 245\,3151.8797 + 20^{\mathrm{d}}.4339 \times E \tag{7.1}$$

where E is the number of cycles elapsed since the initial epoch.

The spectra show sharp lines indicative of low $v \sin i$. An accurate $v \sin i$ value cannot be determined from these spectra as they are limited by the spectral resolution, but is estimated at $v \sin i \leq 4\ \mathrm{km\,s^{-1}}$. Higher resolution spectra are required to constrain this value.

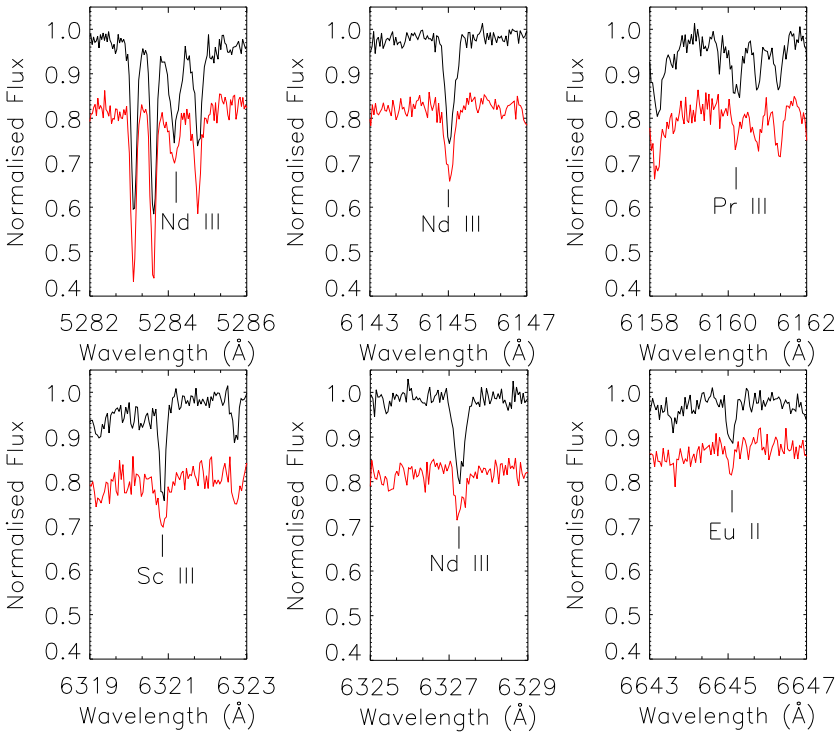

Figure 7.1: A selection of spectral lines which demonstrate the Ap nature of KIC 7582608. The upper black line shows the 2012 spectrum, with the lower red line showing the 2013 spectrum offset by 0.15 for clarity. There is clear variability in the strength of the peculiar lines due to the rotational phase difference. Both spectra have had velocity shifts removed to align the spectral lines with their rest wavelengths.

The spectral lines typically used to determine the mean magnetic field modulus in Ap stars, $\langle B \rangle$, such as Cr II λ6147.1 and Fe II $\lambda\lambda$6147.7 & 6149.2 (Mathys 1990), show no sign of Zeeman splitting; however this can be attributed to a lack of resolution in the spectra. Instead the method of Mathys & Lanz (1992) is used to estimate this value by comparing the relative intensities of Fe II $\lambda\lambda$6147.7 & 6149.2. There is a change of relative strengths between the two spectra, however the λ6147.7 line remains the stronger of the two. From this comparison it is found that $\langle B \rangle = 3.13 \pm 0.32$ kG and 2.97 ± 0.32 kG for the 2012 and 2013 spectra, respectively. It is noted by Mathys & Lanz (1992) that for their stars with no resolvable magnetically split lines, this method of comparing Fe II $\lambda\lambda$6147.7 & 6149.2 produces systematically lower values of the mean magnetic field modulus. Therefore it is suggested that the values derived here for KIC 7582608 are representative of a lower limit on $\langle B \rangle$.

To determine the $\log g$ and $T_{\rm eff}$, UCLSYN (Smith & Dworetsky 1988; Smith 1992; Smalley, Smith & Dworetsky 2001) was used to perform an abundance analysis by measuring the equivalent widths of 77 Fe I lines and 57 Fe II lines (e.g. Gonzalez 1998; Santos, Israelian & Mayor 2000; Fulbright 2000; Johnson 2002; Bruntt, De Cat & Aerts 2008; Doyle et al. 2013). The effective temperature was found to be $T_{\rm eff} = 8700 \pm 100$ K by requiring no dependence of abundance with excitation potential (EP); the abundance of Fe I increases with increasing $T_{\rm eff}$, and has a greater effect on the lines with low EP. Therefore, requiring no trend between Fe abundance and EP yields the temperature of the star. For Fe II lines, the effect is reversed i.e. the high EP lines are most sensitive to temperature. For the $\log g$ determination, the ionisation balance between Fe I and Fe II was tested; as only Fe II abundances are sensitive to the surface gravity, agreement between the two abundances provide a measure of $\log g$. This gave a $\log g$ of 4.3 ± 0.4 (cgs) for KIC 7582608. The photometrically derived value presented in the *Kepler* Input Catalogue (KIC) of 4.1 agrees with this calculation.

The Fe abundance measured from the extracted lines is $\log {\rm A(Fe)} = 8.4 \pm 0.2$, indicating an over-abundance relative to solar of [Fe/H] = +0.9 dex based on the solar chemical composition presented by Asplund et al. (2009).

B. Smalley also determined the $T_{\rm eff}$ of KIC 7582608 using stellar spectral en-

ergy distribution (SED) fitting. This process used literature photometry from 2MASS (Skrutskie et al. 2006), U, B and V magnitudes from Everett, Howell & Kinemuchi (2012), g', r' and i' from Greiss et al. (2012), the TASS I magnitude (Droege et al. 2006), and GALEX fluxes (Martin et al. 2005) to reconstruct the SED. To determine the reddening of the star, the Na D lines from the spectra were measured and applied to the relation of Munari & Zwitter (1997) to derive an $E(B-V) = 0.04 \pm 0.02$.

The stellar $T_{\rm eff}$ value was determined by fitting a [M/H] = 0.0 Kurucz (1993) model to the de-reddened SED. The model fluxes were convolved with photometric filter response functions. A weighted Levenberg-Marquardt non-linear least-squares fitting procedure was used to find the solution that minimised the difference between the observed and model fluxes. The $\log g$ value used was that derived above, 4.3 $\pm$ 0.4, for the fit. The uncertainty in $T_{\rm eff}$ includes the formal least-squares error and adopted uncertainties in $E(B-V)$ of $\pm$0.02, $\log g$ of $\pm$0.4 and [M/H] of $\pm$0.5 added in quadrature. As a result of the SED fitting, a temperature of 8670 ± 450 K for KIC 7582608 is derived. Assuming a standard error of 200 K for the KIC temperature, their quoted value of 8149 ± 200 K agrees with these measurements.

7.3 SuperWASP Discovery Data

Presented here is a more in depth analysis of the data which led to the identification of KIC 7582608 as a roAp star, than was presented in Chapter 6.

KIC 7582608 was initially observed by WASP in 2004, and subsequently in the 2007, 2008, 2009 and 2010 seasons. During 2007, there were two observing fields which collected data on KIC 7582608, these are distinguished using 'a' and 'b'. The details for each season are presented in Table 7.2. Observations were taken in a variety of conditions which results in significant errors and night to night fluctuations in the final data. The final column in Table 7.2 represents the weighted reduced-χ^2 (Bevington 1969) previously used in Chapter 3 (equation 3.3).

As can be seen from Table 7.2, the 2004 and, especially the 2008 seasons of data

Table 7.2: Details of WASP observations of KIC 7582608. BJD is given as BJD−254 0000.0

WASP season	BJD start	Length (d)	Number of data points	χ^2/n
2004a	3139.67092	138.69311	1967	3.47
2004b	3139.66262	116.82519	1586	4.15
2004*	3139.66262	138.70141	3553	3.78
2007a	4230.56374	66.10058	3381	0.84
2007b	4297.39089	38.08300	1660	1.16
2007*	4230.56374	104.91015	5041	0.94
2008	4577.59791	112.95654	7585	10.04
2009	4941.57840	125.93750	10917	1.08
2010	5307.57254	124.95556	12293	1.00

*Combined data sets a and b.

have a χ^2/n value deviating from 1.00 indicating that these seasons will result in less reliable results.

7.3.1 The Rotation Signature

The WASP light curve for KIC 7582608 shows the strong modulation which is typical of Ap stars. A Lomb-Scargle periodogram was calculated using the Fortran code FASPER (Press & Rybicki 1989; Press et al. 1992) in the frequency range $0-2\,\mathrm{d}^{-1}$. Only the best quality data were used for the calculation, spanning 1201.9644 d, to best constrain the period, i.e. the 2007, 2009 and 2010 seasons. Using PERIOD04 (Lenz & Breger 2005), a rotation frequency of $\nu_{\mathrm{rot}} = 0.0489\,382 \pm 0.0000\,004\,\mathrm{d}^{-1}$ was found, which corresponds to a rotation period of $P_{\mathrm{rot}} = 20.4339 \pm 0.0017\,\mathrm{d}$. The errors are the analytical errors taken from PERIOD04 (Montgomery & Odonoghue 1999). A more realistic error for the rotation period would be the Rayleigh criterion for the data set i.e. an error on the period of 0.3474 d. Figure 7.2 shows a labelled periodogram and phase folded light curve of just the 2010 season for clarity. As well as the rotation frequency, a second weaker signature is detected at $2\nu_{\mathrm{rot}}$, which can be seen in the right panel of Figure 7.2 as a small bump at phase 0.5. This signature can be explained with another spot on the opposite hemisphere of the star which appears smaller, most likely due to projection

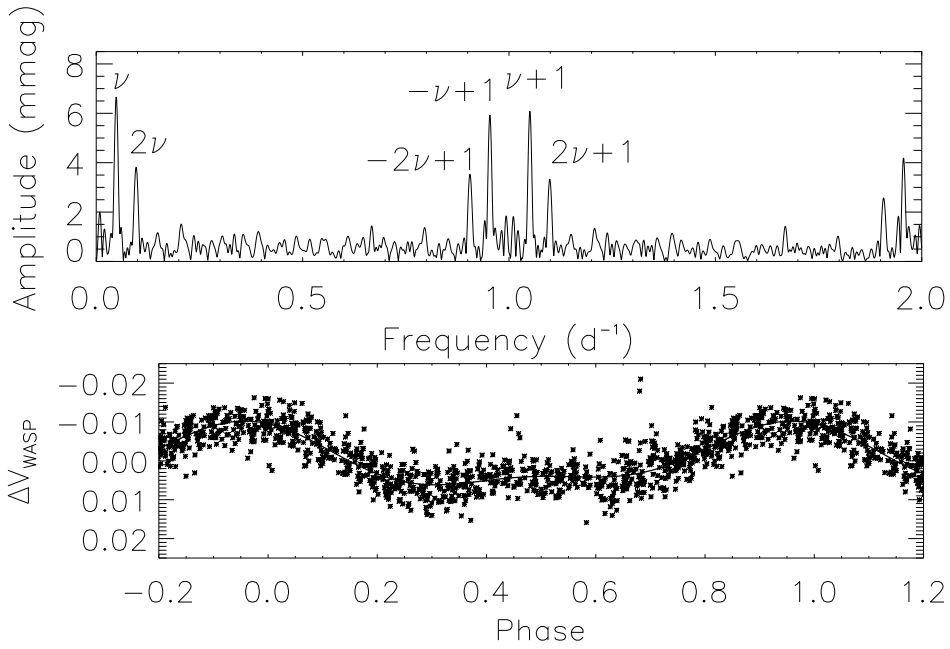

Figure 7.2: Top panel: labelled periodogram of the 2010 season of WASP data, where ν is the rotation frequency. Bottom panel: the phase folded light curve of the 2010 WASP data. The data are folded on the period derived from combining the 2007, 2009 and 2010 seasons, i.e. 20.4339 d and are binned 10 : 1.

effects. However, the smaller spot may also be formed from a different element which is less abundant in the stellar atmosphere (e.g. Lüftinger et al. 2010).

7.3.2 The Pulsation Signature

To best analyse the pulsation in the WASP data, the data are pre-whitened to $10\,\mathrm{d}^{-1}$ by fitting a series of sinusoids to a limit of the approximate noise level, the top of the Fourier grass, at high-frequency for each data set individually. The noise level varied greatly between seasons, with pre-whitening occurring between 0.7 and 2.5 mmag for the flattest and most noisy data sets, respectively. In this way the rotational variability is removed from the light curve, and any further systematic effects, especially the dominant 'red' noise (Smith et al. 2006) remaining after the data have passed

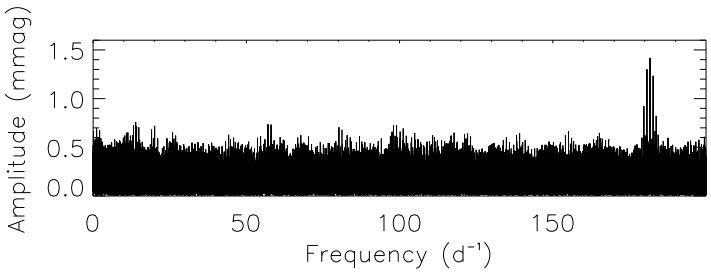

Figure 7.3: Periodogram of the 2010 season WASP data after pre-whitening has been performed. The pulsation is clearly seen at $181.7324\,\mathrm{d}^{-1}$ at an amplitude of about 1.45 mmag.

Table 7.3: Frequencies, amplitudes and phases of the pulsation extracted from the WASP data using a non-linear least-squares fit. The zero-point for the phases is BJD 245 3151.6245.

Season	Frequency (d^{-1})	Amplitude (mmag)	Phase (rad)
2004a	181.7247 ± 0.0011	1.429 ± 0.337	1.644 ± 0.238
2004b	181.7243 ± 0.0017	1.444 ± 0.435	1.865 ± 0.307
2004	181.7241 ± 0.0013	1.274 ± 0.316	1.827 ± 0.252
2007a	181.7339 ± 0.0008	1.452 ± 0.222	-1.386 ± 0.152
2007b	181.7353 ± 0.0009	1.638 ± 0.373	1.577 ± 0.228
2007	181.7347 ± 0.0006	1.549 ± 0.195	-0.769 ± 0.125
2008	181.7334 ± 0.0011	1.597 ± 0.349	1.465 ± 0.220
2009	181.7387 ± 0.0004	1.460 ± 0.154	0.724 ± 0.105
2010	181.7276 ± 0.0005	1.436 ± 0.158	2.067 ± 0.109

through the WASP pipeline. The resulting periodogram for the 2010 season is shown in Figure 7.3. The results of a non-linear least-squares fit is shown for each season in Table 7.3.

Other than extracting the correct pulsational frequency and amplitude (in the WASP photometric passband), there is no further information that can be gleaned from the WASP data. The noise characteristics of the WASP data do not allow for a reliable extraction of rotational sidelobes as both the sidelobes and the Fourier noise occur at approximately the same amplitude. As the pulsation frequency is above the Nyquist frequency of *Kepler* LC data, some confusion may be had in disentangling the

true peak from the many other aliases if the data do not have a large enough time span, a scenario which the WASP data allows to be disregard. Finally, however, it is noticed that the extracted frequencies from the WASP data from the different seasons vary beyond their errors, an observation that shall be revisit in section 7.4.3.

7.4 *Kepler* Observations

KIC 7582608 has been observed by the *Kepler* satellite for the full duration of the mission, a little over 4 yr. The data were collected in the LC mode with a cadence of 30 min. There are no SC data for this target.

7.4.1 The Rotation Signature

Figure 7.4 shows Q10 of the data. It is clear that the star has a well defined rotation period, mapped out by surface brightness anomalies in two hemispheres. This is typical behaviour of an Ap star which has a strong global magnetic field. To determine the rotation period of the star, all quarters of data were combined, removing any obvious outlying data points and quarter-to-quarter zero-points, resulting in a light curve varying about zero magnitude. A periodogram was then calculated which showed two frequencies, the rotation frequency and the harmonic. The principal peak has a frequency of $\nu_{\rm rot} = 0.0488\,920 \pm 0.0000\,003\,{\rm d}^{-1}$, which corresponds to a rotation period of $P_{\rm rot} = 20.4532 \pm 0.0001\,{\rm d}$. As with the WASP data, the rotational frequency was calculated with Period04, and the errors are the analytical errors. This value is close to that derived from the WASP light curve in section 7.3.1, but deviates by $\sim 28\,{\rm min}$. The *Kepler* data have a much higher duty cycle than that of the WASP observations, as such it is suggested that the daily and seasonal gaps in the WASP data have led to the discrepancies between the two derived rotation periods. Combining the two data sets provides a time string covering 3285 d from which a rotation period of $P_{\rm rot} = 20.4401 \pm 0.0005\,{\rm d}$ is calculated.

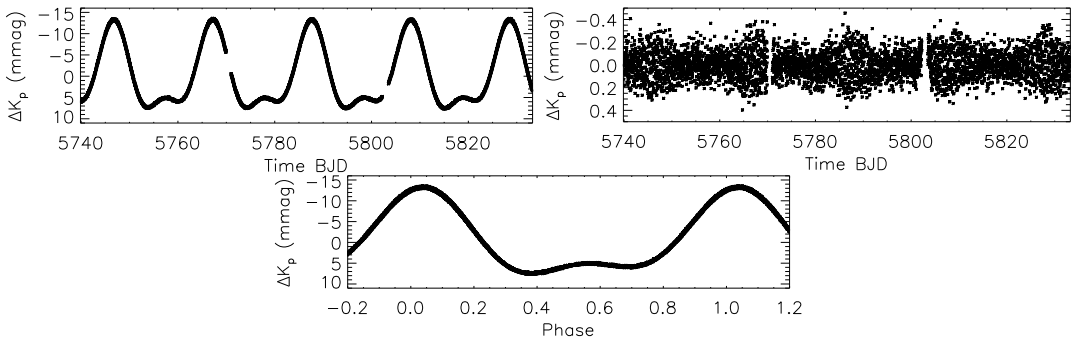

Figure 7.4: Top left: The LC data of KIC 7582608 from Q10. The ordinate is BJD-245 0000. Top right: Q10 LC data after pre-whitening (described in section 7.4.2) has removed the rotational modulation signature leaving only the pulsation variation. Only the pulsation envelope is seen here due to the scale. Note that the pulsation maxima coincide with the rotational maxima. Bottom: The phase folded light curve showing the stability of the spots over the quarter.

7.4.2 The Pulsation Signature

Due to the barycentric corrections applied to the time stamps of the *Kepler* observations, the regular sampling of the data has been broken. Murphy, Shibahashi & Kurtz (2013) have shown that it is possible to directly analyse the true pulsation frequency even if it occurs above the nominal Nyquist frequency of the LC data, rather than analysing a low-frequency alias. This is the case of the pulsation in KIC 7582608.

To analyse the high-frequency signature, each quarter of data is pre-whitened to the approximate noise level at higher frequencies, thus removing all peaks with amplitudes greater than 5 μmag below 1 d^{-1}. This procedure removes both instrumental variations at very low-frequency, such as loss of fine pointing, stars moving across the CCD, reaction wheel zero-crossings and breaks in observations for data downloads (Murphy 2012), and the rotational spot variations. As these are well-separated in frequency from the 181 d^{-1} pulsation frequency, the filtering has no effect on the analysis, except to make the noise close to white noise so that the light curve can be examined by eye and so that the least-squares error estimates are realistic (i.e. are not influenced by the low-frequency variations). Initially, the pre-whitened data are combined

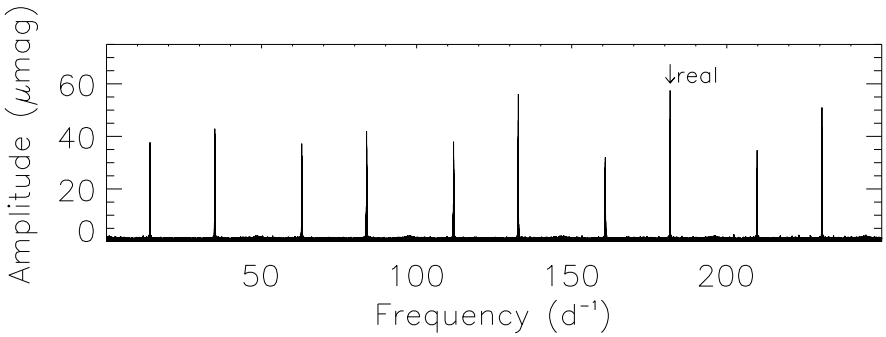

Figure 7.5: Periodogram of the individually pre-whitened Q00−Q17 *Kepler* data. The real peak can be identified as the strongest signal at $181.7\,\mathrm{d}^{-1}$.

and a full periodogram is calculated to show the true pulsation in the LC data. Figure 7.5 presents the result, with the highest amplitude peak at $181.7324\,\mathrm{d}^{-1}$, which agrees with that found from the WASP data in section 7.3.2. Note that the amplitude is much lower than that seen in the WASP data as a result of the multiple Nyquist crosses. The observed amplitude, A, is related to the true amplitude, A_0, by

$$A = \mathrm{sinc}\left(\frac{\pi}{n}\right) A_0\,, \tag{7.2}$$

where n is the number of points per cycle (Murphy 2014).

Taking the full data set and extracting just the pulsation range shows, in Figure 7.6, a 'ragged' multiplet split by the rotation frequency of the star. The central peak is the true pulsation frequency, as confirmed with the WASP data, with the rotationally split side lobes describing the variations in phase and amplitude with the varying aspect over the rotation cycle. A closer look at the principal peak, Figure 7.6 (right), highlights the complex and unstable nature of the pulsation frequency, an observation discussed in section 7.4.3.

Each quarter of data have been analysed individually, with the periodograms shown in Figure 7.7 and the results of a linear least-squares fit shown in Table D.1. To produce the data in Table D.1, the highest amplitude peak in the $181 - 182\,\mathrm{d}^{-1}$ was found and removed with a linear least-squares fit. The residuals were then searched for the next strongest signature, which was removed in the same way. When all pulsation

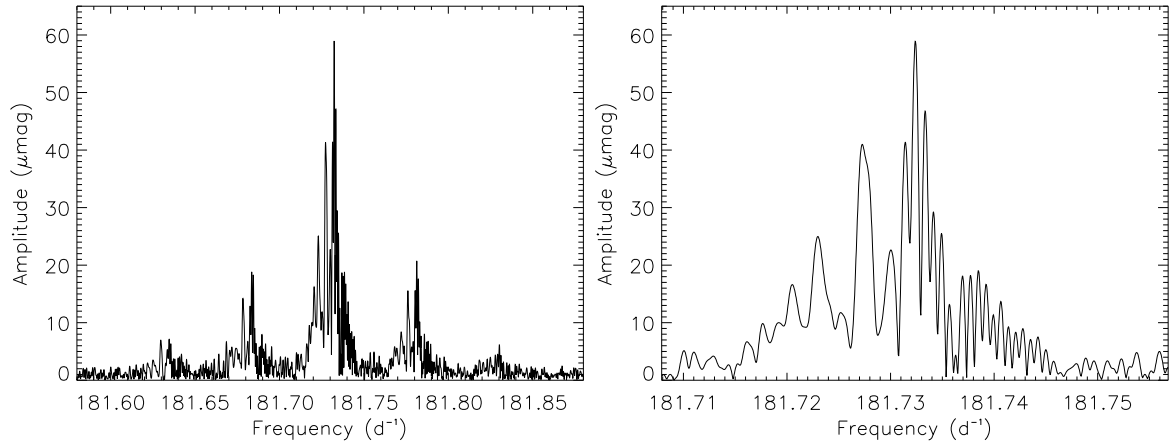

Figure 7.6: The roAp pulsation frequency seen in the *Kepler* Q00−Q17 LC data. Left: An amplitude spectrum showing the multiplicity of closely spaced peak around each of the frequency quintuplet components of the obliquely pulsating mode. Right: a higher resolution look at the central peak of the quintuplet. Each of the rotational sidelobes has a similar structure, as expected for oblique pulsation.

signatures had been removed from the light curve, the sidelobes were forced to be separated by exactly the rotation frequency to test the phase relations of the sidelobes in the original data. The results show that $\phi_{-1} = \phi_{+1} \neq \phi_0$ suggesting that the mode is a distorted mode. Pulsation modes are distorted in roAp stars as a result of their magnetic field: the magnetic field distorts the pulsation such at a single spherical harmonic can no longer full describe the mode (e.g. Kurtz & Martinez 1993; Takata & Shibahashi 1995). Distorted dipoles arise when there is also a component of the quadrupole magnetic field in the star.

To test this result, a basic geometry of a pure dipole mode with sidelobes resulting from distortion and rotation alone is assumed. In this case, $l = 1$ and $m = 0$. The relationship of Kurtz, Shibahashi & Goode (1990) between the amplitude of the central peak and the first sidelobes is used, such that

$$\tan i \tan \beta = \frac{A_{+1} + A_{-1}}{A_0}, \tag{7.3}$$

where i is the rotational inclination of the star, β is the obliquity of the pulsation axis to the rotation axis (cf. Figure 1.5), and A_0 and $A_{\pm 1}$ are the amplitudes of the central and

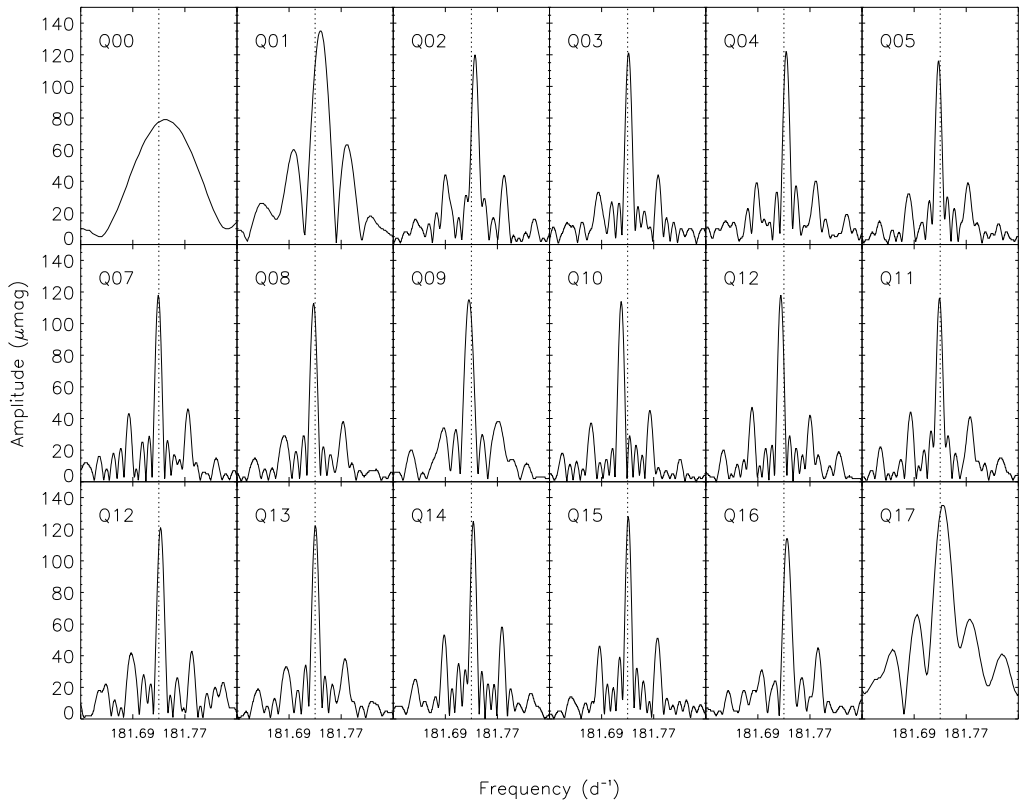

Figure 7.7: Periodograms of each quarter of *Kepler* data centred on the pulsation frequency. The vertical dashed line at $181.73\,\mathrm{d}^{-1}$ is to guide the eye when noting the frequency variability from quarter-to-quarter, as discussed in section 7.4.3. The values of the pulsation frequency are shown in Table D.1.

first sidelobes, respectively. Using an average value for the amplitudes calculated for each quarter of data (Table D.1), $\tan i \tan \beta = 0.67 \pm 0.03$ is calculated. This provides a relation between i and β, but not the values individually. For this a measure of the $v \sin i$ of the star is required as well as an estimate of the stellar radius. As the $v \sin i$ was not able to be determined in section 7.2, an upper of $4\,\mathrm{km\,s^{-1}}$ was estimated. Using this upper limit, the radius derived from Torres, Andersen & Giménez (2010) relationships of $1.77 \pm 0.92\,\mathrm{R_\odot}$, and the rotation period of 20.4339 d, an estimate an upper limit on i of 66° and a lower limit on β of 17° is made. From the double wave nature of the light curve shown in Figure 7.4, it is apparent that $i + \beta > 90°$ so that both magnetic poles are seen, a criterion that the calculated values do not fulfil. In fact, no values of i and β sum to $> 90°$ and satisfy $\tan i \tan \beta = 0.67$. Therefore, $\tan i \tan \beta$ is calculated using the assumption that the pulsation is a quadrupole mode such that $l = 2$ and $m = 0$. Again, from Kurtz, Shibahashi & Goode (1990), the relationship between the combined relative amplitudes of the first and second sidelobes which can be used to describe the geometry of the pulsation such that

$$\tan i \tan \beta = 4 \times \frac{A^{(2)}_{+2} + A^{(2)}_{-2}}{A^{(2)}_{+1} + A^{(2)}_{-1}}, \tag{7.4}$$

where i and β are as before, and $A^{(2)}_{\pm 1}$ and $A^{(2)}_{\pm 2}$ are the amplitudes of the first and second sidelobes of the quadrupole mode, respectively. Using an average value for the the amplitudes calculated for each quarter of data (Table D.1), a value of $\tan i \tan \beta = 1.44 \pm 0.14$ is calculated. Taking the value of i as before, β is calculated to be $\sim 33°$ resulting in $i + \beta > 90°$ as expected from the light curve. The satisfaction of this equation, coupled with the double wave nature of the light curve suggests that KIC 7582608 is a quadrupole pulsator. It must be noted that given the error on the radius, if a value much below that of $1.77\,\mathrm{R_\odot}$ is used, i would be unconstrained. However, given the observations of the quadrupole components of the pulsation (cf. Figure 7.7), this conclusion is justified.

7.4.3 Pulsation Variability

The analysis presented in this section, and sub-sections, was contributed to by D. W. Kurtz, until section 7.4.3.3.

As discussed in section 1.4.3, some roAp stars show highly stable pulsational frequencies, amplitudes and phases over time spans of years whereas others show variability. Kurtz et al. (1994) and Kurtz et al. (1997) discussed frequency variability for the roAp star HR 3831 with ground-based data spanning 16 yr which led them to claim that the frequency variability could be cyclic, however later work did not supported this. Similar frequency variability was reported for another roAp star; Martinez, Kurtz & van Wyk (1994) discuss HD 12932 and identify seven further roAp stars for which frequency variability was known at that time.

An issue with ground-based studies is the low duty-cycle. The data are sparse, and the frequency variability time scales can be of order years, hence alias ambiguities plague the analyses. However with the *Kepler* data this issue has been overcome. For example, Balona (2013b) studied the *Kepler* roAp star KIC 10483436, and showed what appears to be non-periodic frequency variability over a time span of 1250 d.

The question arises as to what causes frequency variability in roAp stars. Is it a change in the pulsation cavity, either because of structural changes in the star, or changes in the magnetic field? Is it externally caused by orbital perturbations of a companion, or companions? Is it some combination of these?

Balona (2013b) shows an amplitude spectrum for KIC 10483436 where the largest amplitude pulsation mode has a frequency quintuplet, split by the rotation frequency ($P_{\rm rot} = 4.3$ d), caused by oblique pulsation. For the entire *Kepler* data set the amplitude spectrum can be described as 'ragged'. This is similar in nature to Figure 7.6. While this is typical for stochastically excited pulsators, such as solar-like stars and red giant stars, stochastic excitation is not likely for roAp stars as there is no substantial convection zone near the surface of the star in which the modes can be excited to the amplitudes seen in the roAp stars. Thus the multiplicity of closely spaced peaks that make up each component of the oblique pulsator quintuplet must arise because of

frequency, amplitude and/or phase variations over the time span of the data set.

Given the history of non-periodic frequency modulation seen in some roAp stars, it this therefore necessary to study the time dependence of both the frequency and amplitude of the pulsation mode in KIC 7582608. To do this, the same data set in section 7.4.2 is used, but is split into sections with a length of 100 pulsations cycles, or about 0.55 d. These were then fitted with the frequency $\nu_1 = 181.7324\,\mathrm{d}^{-1}$, which is the highest peak in Figure 7.6, by linear least-squares to each section of the data, giving 2487 measurements. The function fitted was

$$\Delta m = A\cos(\nu(t - t_0) + \phi)\,, \tag{7.5}$$

with t_0 taken to be the first occurrence of maximum light in the WASP data (BJD 2453151.8797). If the pulsation mode is stable, then the amplitude and phase modulation would only occur with the rotation frequency $0.0489\,382\,\mathrm{d}^{-1}$ determined in section 7.3.1 as expected in the oblique pulsator model.

7.4.3.1 Amplitude Modulation

Figure 7.8 shows the pulsation amplitude as a function of rotational phase for the entire 1460 d data set phase folded on the rotation period. The measurements have been averaged in groups of 20 within narrow phase bins to smooth the curve. It can be seen that there is no change in pulsation amplitude over the entire 1460 d time span of the data. The only variation seen is the amplitude modulation with rotation caused by the oblique pulsation mode.

This variation is similar to that of another *Kepler* roAp star, KIC 10195926. Figure 10 of Kurtz et al. (2011) shows the double wave nature of the amplitude variation with rotation phase, caused by the geometry of the mode and differing aspects of the view. This is also the case here in KIC 7582608 seen in Figure 7.4 which suggests that both poles may be seen in this star, although with low visibility for the second pole (the small bump seen in Figure 7.4 at rotation phase 0.5). This is in agreement with the values of i and β derived in section 7.4.2.

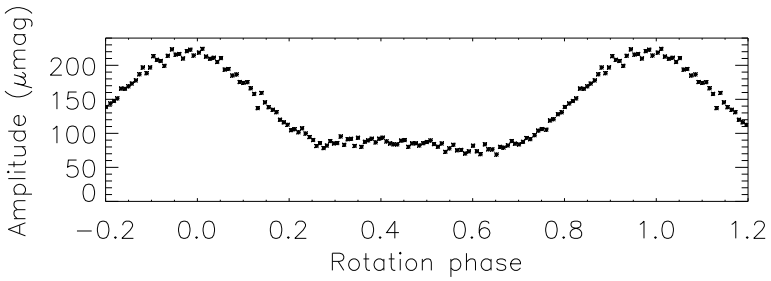

Figure 7.8: Pulsation amplitude as a function of the 20.4339 d rotation phase, calculated with all quarters of data. The zero point in time, t_0 = BJD 2453151.8797, was selected to be the time of maximum rotational brightness of KIC 7582608, hence the maximum pulsation amplitude coincides with the rotational light extremum.

7.4.3.2 Phase and Frequency Variability

Unlike the amplitude, the phase varies dramatically over the 4 yr time span. Figure 7.9 shows the pulsation phase over the entire 1460 d data set from the same data used for the amplitudes. This is very different from the example of KIC 10195926 where the pulsation phase is stable over the entire observation period, and shows π-rad phase reversal at quadrature (figure 10 of Kurtz et al. 2011). Selecting a shorter data range of 200 d, it is possible to see in Figure 7.10 that the pulsation phase varies with rotation phase, as is expected from the oblique pulsator model.

To examine the rotational variation of the pulsation phase, the longer term curvature has been removed from Figure 7.10 and the data phased with the rotation period as seen in Figure 7.11. The pulsation phase varies by nearly 1 rad over the rotation cycle. This is similar to what is seen in other roAp stars that have been studied in enough detail. The best cases to refer to are those of KIC 10195926 (Kurtz et al. 2011), HR 3831 (Kurtz et al. 1997) and HD 6532 (Kurtz et al. 1996). For those three stars both pulsation poles are seen, the principal pulsation modes are primarily dipolar, and there is an obvious phase reversal at quadrature. However, outside of that phase reversal, there is smooth pulsation phase variation over the rotation period with an amplitude

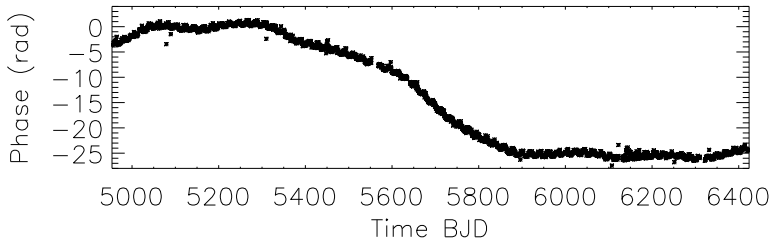

Figure 7.9: The phase variation over the entire observation period. A constant pulsation frequency would led to a straight line in the plot, the variation seen suggests there is a better frequency fit to the data. To form a continuous plot, 2π rad has been added or subtracted to the phase where appropriate.

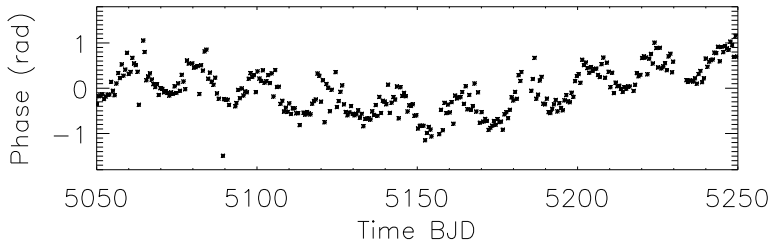

Figure 7.10: This plot shows the phases determined for a section of the 0.55 d long (100 pulsation cycles) in the time span BJD 2455050 − 2455250.

of order of 1 rad, as in KIC 7582608. Therefore, the only difference for KIC 7582608 is that the other pulsation pole does not come into sight. This variation of pulsation phase with rotation is a consequence of magnetic and rotational effects on the light curve, along with the geometry of the mode and aspect of our view (Bigot & Kurtz 2011).

In equation (7.5) it can be seen that phase and frequency are coupled; a change in one could be interpreted as a change in the other. If it is assumed that the phase is constant and only the frequency is variable, then the light variations may be written as

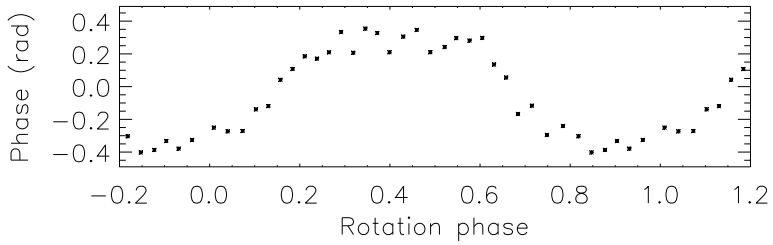

Figure 7.11: This plot shows the phases determined for a section of the 0.55 d long (100 pulsation cycles) in the time span JD 2455050 − 2455250. The points are 10-point averages of the 0.55 d phases in narrow rotational phase bins for smoothing.

$$\Delta m = A\cos(\nu(t)(t - t_0) + \phi_0)\,, \tag{7.6}$$

where

$$\nu(t) = \nu_0 + \delta\nu(t)\,, \tag{7.7}$$

and ν_0 is constant. It is then possible to re-group the terms to give

$$\Delta m = A\cos(\nu_0(t - t_0) + \phi(t))\,, \tag{7.8}$$

where

$$\phi(t) = \phi_0 + \delta\nu(t)\,(t - t_0)\,. \tag{7.9}$$

Hence, frequency and phase variability are inextricably intertwined. Therefore the phase variations are interpreted to be the result of frequency variability.

Figure 7.9 is the equivalent of a traditional $O - C$ diagram. With a correct constant frequency it is expected that the phases would follow a straight line in the plot, any linear trend with a slope can mean that another frequency is a better fit. Equations (7.6−7.9) allow for the conversion between phase and frequency. Anywhere in Figure 7.9 where the trend is non-linear, frequency variations are present.

From the deviations of linearity in Figure 7.9, it is possible to see that the pulsation frequency of KIC 7582608 is strongly variable over the 1460 d data set. That is the reason for the 'raggedness' in the amplitude spectrum seen in Figure 7.6.

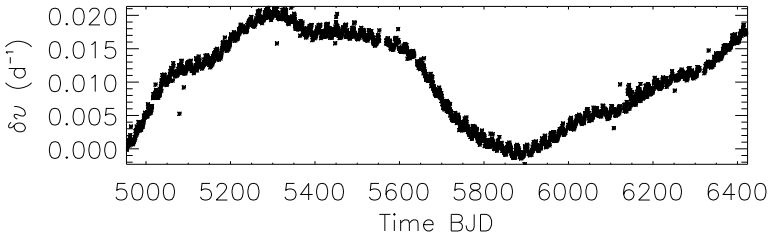

Figure 7.12: The frequency variability, $\delta\nu(t)$, over the 1460 d data set calculated from Fig. 7.9 with a linear trend removed and the application of equation (7.9).

To examine the frequency variability further, a linear trend was removed from the phases in Figure 7.9 – which is equivalent to fitting a different starting frequency initially – and converted the phases to frequency changes using equation (7.9). The result is shown in Figure 7.12. It can be seen that there is frequency variability on many time scales. Whether the largest variation seen on the length of the data set is a consequence of a binary companion or is intrinsic is uncertain. This analysis does show why the amplitude spectrum is 'ragged', although the origin of the frequency variability is not clear.

7.4.3.3 Binary Interpretation of Frequency Variation

One potential cause of frequency variability is external. If the pulsating star is a member of a binary, or multiple system, then the orbital motion causes frequency variability as a result of Doppler shifts. This is a periodic phenomenon and has been described in detail by Shibahashi & Kurtz (2012), who show that the orbital motion results in each pulsation frequency peak being split into a multiplet separated by the orbital frequency. They call their technique for studying binary motion FM, for frequency modulation. The number of components to the multiplet is a function of a parameter α, which itself is dependant on the mass of the companion, the orbital period, the pulsation period and the eccentricity; in general, for low eccentricity and low α only

a triplet is expected. Figure 7.6 is not reminiscent of such a simple pattern. Periodic amplitude modulation also produces frequency multiplets in the amplitude spectrum; oblique pulsation is a good example of this. However, this is also not seen in Figure 7.6.

It is evident that in KIC 7582608 there are frequency variations occurring over many different time scales. As such, Figure 7.6 does not fit the expected FM pattern. However, due to the possibility that the large scale frequency variations are due to binary interaction, it is important to investigate this further as, if confirmed, this is an important result for roAp binary systems. To pursue this line of enquiry, the pre-whitened Q00−Q17 data are split into sections of $P_{\rm rot}$ in length, giving 72 individual data sets to analyse. This aims to reduce the effects of the shorter time-scale frequency variations which have been shown to be present. This provides good temporal coverage of a binary orbit without sacrificing frequency resolution. A periodogram for each rotation cycle was then calculated and fitted with a non-linear least-squares routine to extract the pulsation frequency and corresponding error. In doing this, the pure frequency variations are extracted, allowing the phase to be a free parameter in the fitting procedure. Each individual data set is analysed independently, such that the phases extracted are not of use here. This, therefore, is a different analysis to that presented in Figures 7.9 and 7.12, where concentration was on phase rather then frequency variations. The results of this analysis are presented in Figure 7.13 and Table D.2. It is clear that there are long-term frequency variations on approximately the same time period as the observations. The extent of the frequency variations is about $0.02\,\mathrm{d}^{-1}$ ($0.25\,\mu$Hz). To test if this variation was intrinsic to the star, or an instrumental effect, another *Kepler* roAp star was analysed in the same way, namely KIC 10195926. The results showed that the pulsation in that star was stable over the total *Kepler* observations. This implies that the variations seen in KIC 7582608 are indeed intrinsic to the star.

Assuming that the frequency variability is due to an external factor, i.e. due to orbital motion, it is possible to extract orbital parameters from the frequency variations. Taking the frequency shifts to be caused by Doppler shifts, the frequencies can be

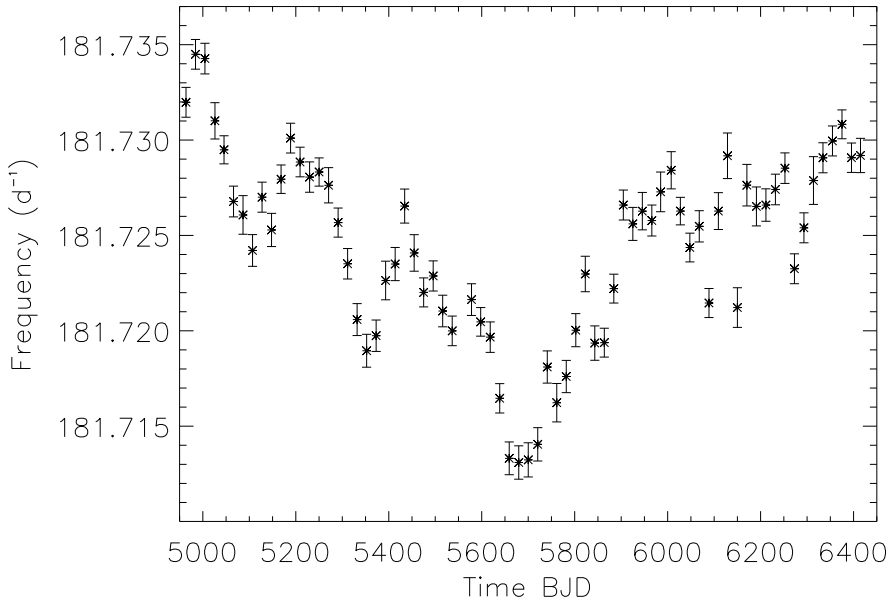

Figure 7.13: Frequencies calculated for each rotation period using a non-linear least-squares routine. The data values are presented in Table D.3.

converted into radial velocities (RVs) using:

$$V_{\rm rad} = c\left(\frac{\nu_i - \nu_{\rm ref}}{\nu_{\rm ref}}\right), \tag{7.10}$$

where c is the speed of light, ν_i is a given frequency and $\nu_{\rm ref}$ is a reference frequency. As the intrinsic pulsation frequency is not known, $\nu_{\rm ref}$ is taken to be the mean of ν, resulting in relative, rather than absolute, radial velocities. In addition to the *Kepler* data, the frequencies of each WASP season of data from Table 7.3 have been included, adding a further nine data points, now totalling 81 (Table D.3).

To determine the orbital parameters, **J. Southworth** used JKTEBOP (Southworth 2013) to analyse the measured RVs, testing both circular and eccentric orbits. The best fit the code produced is that of an eccentric system, with an eccentricity of $e = 0.39$ and a period of $P_{\rm orb} = 1203 \pm 34$ d. The data have been folded on the given period and plotted with the resultant fit, as shown in Figure 7.14. The full parameters are shown in Table 7.4. To determine the absolute values for the RVs, two spectroscopically determined RVs (blue dots in Figure 7.14) from the Lick spectra reported in

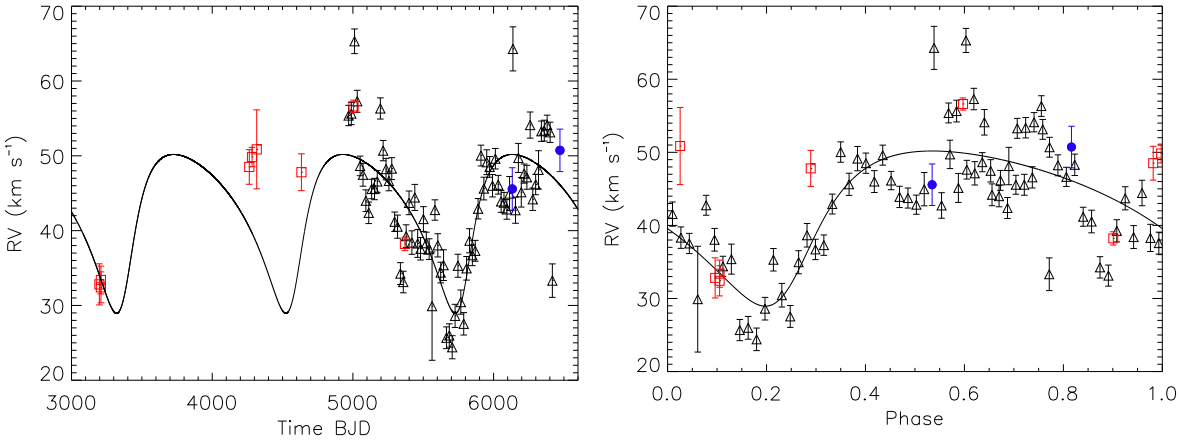

Figure 7.14: The phase folded eccentric radial velocity curve derived for KIC 7582608 from photometric data. The black triangles are *Kepler* data, the red squares represent WASP data, and the blue dots are derived from the spectra. The line represents the fit from JKTEBOP. The spectroscopic RVs were not used to determine the fit, but used to determine the absolute value. The fit parameters are shown in Table 7.4.

Table 7.4: Radial velocity fit parameters for KIC 7582608. The mass function was calculated assuming a value of m_1 of 1.8 $M_\odot$.

Parameter	Value
$e \cos \omega$	-0.301 ± 0.089
$e \sin \omega$	-0.247 ± 0.088
e	0.390 ± 0.055
ω (°)	219.3 ± 20.5
$P_{\rm orb}$ (d)	1203 ± 34
K_1 (km s^{-1})	10.62 ± 1.13
$f(m_1, m_2, \sin i)$ ($M_\odot$)	0.149 ± 0.016

section 7.2 have been included. It must be noted that the spectroscopic RVs are not used in determining the fit, just the absolute values.

The fit is in good agreement with most of the *Kepler* and WASP observations. The 2007 and 2008 seasons of the WASP data (between BJD 4200 and 4700 in Figure 7.14 left) are perhaps the worst fitting data. The 2008 data are of low quality (see Table 7.2) which may explain the discrepancy. However, the mis-fitting 2007 data,

Table 7.5: Calculated secondary masses for a given value of the binary inclination

Inclination i (°)	Secondary mass ($M_\odot$)
90	1.07
80	1.09
70	1.16
60	1.30
50	1.55
40	2.00

which are of good quality, cannot be explained. The 2009 and 2010 data are in good agreement with the simultaneous *Kepler* observations.

Using the mass function presented in Table 7.4, a set of solutions are calculated for the secondary mass given a range of binary inclination angles. The results are presented in Table 7.5. It is likely that the inclination is close to 90° as no signature from a secondary star is detected, at a ~ 5 per cent level, in the spectra presented in section 7.2, implying a magnitude difference of at least 3 mag. As such, this would imply a companion of G-type or later. It is clear that KIC 7582608 is in need of long-term follow-up spectroscopic observations to further monitor the potential RV shifts.

7.5 Modelling

Stellar modelling was conducted by M.S. Cunha.

The detection of even a single pulsation frequency in KIC 7582608 may provide additional constraints to the star's global properties. To investigate this possibility linear, non-adiabatic stability analysis was conducted with a grid of models covering the theoretical instability strip for roAp stars (Cunha 2002), restricting the effective temperature to values larger than 7650 K, taken in intervals of 50 K. The grid comprises stellar masses between 1.7 and 2.2 $M_\odot$, varying in intervals of 0.05 $M_\odot$. The starting point for the grid is a set of evolutionary tracks computed with the code MESA (Paxton

et al. 2011; Paxton et al. 2013), with an initial mass fraction of hydrogen and helium of $X = 0.70$ and $Y = 0.28$, respectively. The effective temperature and luminosities taken from these evolutionary tracks are then used to generate the equilibrium models necessary for the non-adiabatic computations. The analysis follows closely that first presented by Balmforth et al. (2001) and, with some additions, by Cunha et al. (2013). The models are comprised of two programs (Balmforth 1992; Houdek 1996) and are run sequentially. An important aspect of the models is that they are composed of two different regions, namely, the equatorial region, where convection proceeds normally, and the polar region, where convection is assumed to be suppressed by the magnetic field. The first program computes the equilibrium model based on input parameters of mass, luminosity and effective temperature. The atmospheric temperature and surface pressure are then determined using an isothermal atmosphere. Two spherically symmetric models are produced, one to represent the equatorial region and one for the polar region. The models are built from the surface to an internal reference depth as required. As such the two models have different structures due to the magnetic field which is corrected for by forcing the temperature, pressure and helium abundance at the base of the two models to be the same. When this is done, the luminosity and radius of the polar model are varied to compensate. The difference in luminosity of the two models is discussed by Balmforth et al. (2001), but is disregarded as the errors introduced in the luminosity by line blanketing in Ap stars would have a greater effect.

The second program introduces the pulsation into the model. The pulsation equations for linear adiabatic radial oscillations are solved which provide a trial solution which is iterated in the linearised non-adiabatic pulsation equations.

The boundary condition of the pulsations in roAp stars can also be investigated within these modelling codes. There has been much discussion in the literature regarding this topic; in many roAp stars, the observed frequencies are above the acoustic cut-off frequency, that is to say the frequency above which the wave will propagate away into the atmosphere and dissipate. However, as the theoretical cut-off frequencies do not account for the magnetic field (Cunha 1998) it is not possible to say if these cut-off frequencies are correct. In the modelling conducted here, the transmissive

Table 7.6: Modelling parameters for the cases illustrated in Fig. 7.15, all computed with $M = 1.8\,\mathrm{M}_{\odot}$, $T_{\mathrm{eff}} = 8000\,\mathrm{K}$, and $\log g = 4.18$.

Case	Model	Y_{surf}	τ_{min}	Boundary condition
A	Equatorial	0.01	3.5×10^{-5}	Reflective
A	Polar	0.01	3.5×10^{-5}	Reflective
B	Polar	0.01	3.5×10^{-5}	Transmissive
C	Polar	0.1	3.5×10^{-5}	Reflective
D	Polar	0.01	3.5×10^{-4}	Reflective

boundary condition is where the wave is free to propagate away. The second condition to be considered is the reflective boundary. In this case, the wave is fully reflected even if physically this may not be the case.

The minimal optical depth, τ_{min} where τ is given by $d\tau = -\kappa\rho\, ds$ and κ is the opacity, ρ is the gas density and s is the distance along a photon's path, is also tested in the model by using two different values. Thermal stratification on a stellar atmosphere is derived from a temperature-optical depth relation ($\mathrm{T} - \tau$) fitted to a Kurucz model atmosphere (Shibahashi & Saio 1985). As the pulsations in the roAp stars are of high-frequency pulsations below the photosphere depend heavily upon the overlaying atmosphere. Therefore, the different values of τ_{min} are used to test the dependence of the atmosphere on the pulsations.

Following Cunha et al. (2013), for each set of mass, effective temperature, and luminosity, four different cases are considered, which together cover the main uncertainties in the modelling. The first of these constitutes the standard case, in which the equilibrium model is characterised by the surface helium abundance $Y_{\mathrm{sur}} = 0.01$ and the minimum optical depth $\tau_{\mathrm{min}} = 3.5 \times 10^{-5}$, and the pulsation analysis applies a fully reflective boundary condition at the surface. The other four cases are obtained by swapping these properties, one at the time to: $Y_{\mathrm{sur}} = 0.1$, $\tau_{\mathrm{min}} = 3.5 \times 10^{-4}$, and a transmissive boundary condition. The cases are shown in Table 7.6.

The model assumes that the pulsations have a time dependence of $\mathrm{e}^{-\mathbf{i}\omega t}$, where $\omega = \omega_r + \mathbf{i}\,\eta$ and ω is the angular frequency, ω_r is the real part of the angular frequency

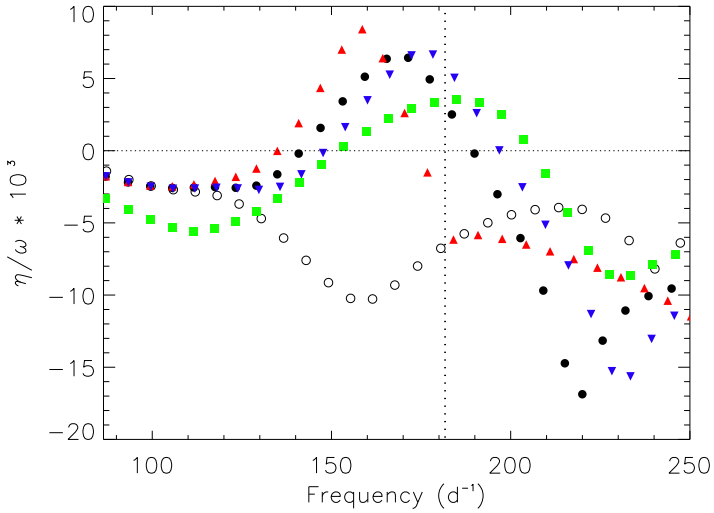

Figure 7.15: The relative growth rates for the four cases presented in Table 7.6. The black open circles are for the standard equatorial region (case A, equatorial) and the black filled circles for the standard polar region (case A, polar). The other three cases correspond to modifications to the standard polar region as described in Table 7.6: upwards red triangles for case B, down facing blue triangles for case C, and green squares for case D. The vertical dotted line represents the pulsation frequency. The oscillations are stable if the ratio between the imaginary, η, and the real, ω, parts of the eigenfrequencies is below zero.

and η is the growth rate. Pulsations are unstable if η is greater than zero, indicating that variability may be observed in those frequency ranges.

Figure 7.15 shows an example of the results obtained from the stability analysis for a fixed mass, effective temperature and luminosity. All four cases are shown for the polar region. For the equatorial region, the results of the different cases are very similar and, thus, only the standard case is presented. Clearly, the growth rates are negative for all high radial order modes in the equatorial region, indicating pulsation stability when convection takes place normally. In contrast, when convection is suppressed modes at the observed frequency become unstable in three out of the four cases studied for this set of mass, effective temperature and luminosity.

The results of the stability analysis performed on the grid are presented on the HR diagram in Figure 7.16. The enclosed region corresponds to the models that show

unstable modes at the observed frequency in the polar region of at least one of the four cases studied. Despite the rather weak constraints that exist on the effective temperature and luminosity of KIC 7582608, there is a clear indication that the results of the stability analysis are consistent with the KIC values, as well as with the effective temperature determinations performed in this work. Thus, KIC 7582608 seems to be an additional example of the group of stars whose pulsational instability is well explained by the opacity mechanism acting on the hydrogen ionisation region. It is noted that this is in contrast with a number of cases discussed by Cunha et al. (2013), in which clear evidence exists for a disagreement between the observed frequency range and the region of frequencies predicted to be excited by this mechanism, and which led the authors to suggest that an alternative excitation mechanism, possibly connected the perturbation to the turbulent pressure, must be in place for a subset of roAp stars.

Under the assumption that the opacity mechanism acting in the hydrogen ionisation region is indeed responsible for driving the observed frequency, the results of the stability analysis further constrain the possible values of the luminosity of KIC 7582608 as a function of its effective temperature. An improvement in the determination of the effective temperature and $\log g$ of this star in the future will, thus, lead to a stronger constraint on its luminosity, via the results of the stability analysis. This is because the region of excited modes depends strongly on the radius of the star.

7.6 Position in the HR Diagram

To place KIC 7582608 in a theoretical HR diagram, both the calculated values from the spectra and the values from the KIC are used. From the KIC, the values are $R = 1.82\,\mathrm{R}_\odot$, $T_{\rm eff} = 8149\,\mathrm{K}$, and $\log g = 4.10$. From these the star's luminosity, L, is calculated to be $\log L/L_\odot = 1.12$.

Using the values derived from the spectra, namely $T_{\rm eff} = 8700 \pm 100\,\mathrm{K}$, $\log g = 4.3 \pm 0.4$ and [Fe/H]$= 0.9 \pm 0.5$, and the calibrations from Torres, Andersen & Giménez (2010), the derived mass, radius and luminosity of KIC 7582608 are: $M = 2.37 \pm$

$0.43\,\mathrm{M}_\odot$, $R = 1.77 \pm 0.92\,\mathrm{R}_\odot$ and $\log L/L_\odot = 1.21 \pm 0.45$.

The positions of KIC 7582608 are shown in Figure 7.16 along with other roAp stars and non-oscillating Ap (noAp) stars for which temperatures and luminosities are available in the literature (Balona, priv. commun.). The position of the open square is determined from the KIC values, whilst the filled square is from the spectral values. In both cases, KIC 7582608 appears to be close to the zero-age main-sequence, and is amongst the hotter, if not the hottest, known roAp stars. Further spectral observations are required to improve the effective temperature and luminosity measurements.

It is important to note here that both positions fall within the area bound by the solid lines. It is in this region that modelling has shown unstable pulsation modes of the same frequency as that observed in KIC 7582608.

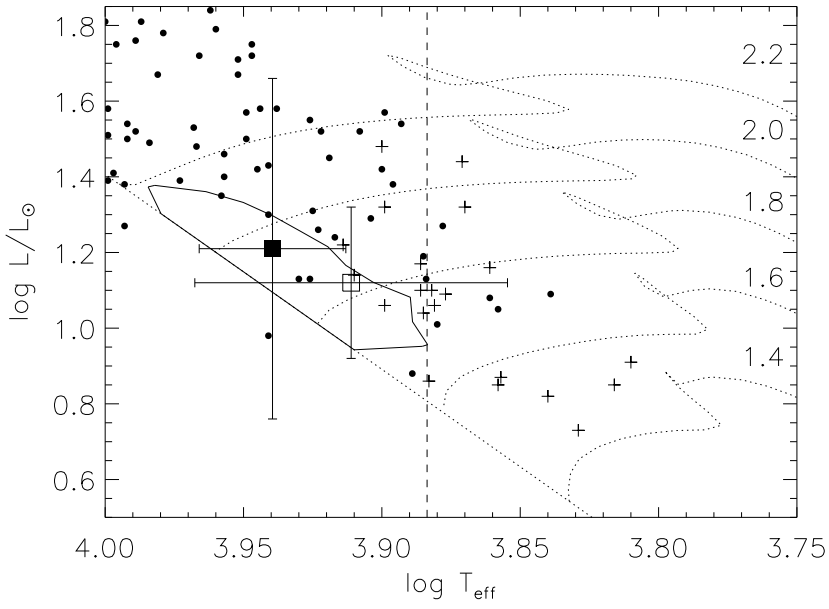

Figure 7.16: The position of KIC 7582608 in the theoretical HR diagram. The filled square is calculated with the spectroscopic temperature and derived radius, while the open square is calculated from the KIC values. The other roAp stars (crosses) and noAp stars (dots) are shown for context. The vertical dashed line indicates the lower temperature tested for the models, the area enclosed by the solid line represents the region where unstable modes are modelled (see section 7.5 for further details). The zero-age main-sequence and evolutionary tracks are from Bertelli et al. (2008).

7.7 Conclusion

Two sources of photometric data for the fifth roAp star found in the *Kepler* satellite field-of-view have been analysed. The multi-season WASP data allow for the direct extraction of the pulsation frequency and amplitude of the star. However, this data set is not of high enough precision to perform an in depth analysis of the pulsation variability. For that, the LC *Kepler* data were utilised. Although the pulsations are above the Nyquist frequency of the LC data, the pulsational multiplet frequencies have been reliably extracted, albeit at greatly diluted amplitudes.

Analysis of the pulsation frequencies has shown that the pulsation mode amplitude is stable over the 4 yr of observations. The amplitude varies on the shorter 20 d rotation period which is expected for roAp stars from the oblique pulsator model. The frequency, however, shows a 'ragged' multiplet when analysing the full *Kepler* data set together. This 'raggedness' is a result of frequency variability over the observation period. The reason for this frequency variability is not apparent though. One possibility for this instability is intrinsic variations in the pulsation cavity of the star, leading to slight variations in the frequency over many years. The phase variations over time are not similar to other roAp stars observed by *Kepler*, as they show phase reversal by π rad at quadrature. Here, the phase variations vary with the rotation period, as expected, but it also varies over the observation period.

An explanation for this long-term phase, or frequency, variation is the notion that KIC 7582608 may be a binary star. The long-term frequency variations have been interpreted to be a result of Doppler shifts due to binary motion. By converting these shifts to radial velocities and applying a binary fitting code, it is concluded that if the star is indeed in a binary, the orbit must be eccentric, with $e = 0.39$, and have a period of about 1200 d. This result may contradict the suggestion by Schöller et al. (2012) that magnetic Ap stars become roAp stars if they are not born in close binaries. Of course, the potential secondary object to KIC 7582608 may have been captured by the Ap star after formation. However, proof of this may be difficult to obtain; stars formed in different locations will show difference abundances, however given the Ap nature of

KIC 7582608 a direct comparison would not provide accurate results. Alternatively, age determination from high S/N spectra of the two stars may provide an indication as to whether they formed at the same time, through analysis the line profiles sensitive to surface gravity. Further observations are planned for this star to increase the number of spectroscopic RVs to which a binary model can be fit. If confirmed to be a binary star, KIC 7582608 would be the first known roAp star in a relatively close binary orbit.

Modelling of the pulsation frequency suggests that the pulsation in KIC 7582608 is driven by the κ-mechanism acting in the hydrogen ionisation zone, as is the case with most other roAp stars. Linear non-adiabatic modelling shows that the pulsations are driven in the polar regions where the convention is suppressed by the magnetic field. The mode stability analysis produces results that are consistent with the effective temperature and luminosity of KIC 7582608.

Spectroscopic observations show the variations in the surface abundance of rare earth elements which are over-abundant in Ap stars, when compared to the Sun. An estimation of the $v \sin i$ is made at $4\,\mathrm{km\,s^{-1}}$, but is limited by the resolution of the spectra. The resolution also restricts the measurement of the magnetic field of the star through Zeeman splitting, but using the method of Mathys (1990), an lower limit of $\langle B \rangle = 3.05 \pm 0.23$ kG is estimated. The echelle spectra, coupled with the abnormal line profiles, make temperature and $\log g$ determinations from the Hydrogen lines particularly difficult. Therefore, the equivalent widths of Fe I & Fe II are used to determine these parameters. Further spectroscopic observations at higher resolution will provide the ability to improve the estimations of temperature, luminosity and $\log g$, as well as providing additional RV measurements.

8 Conclusions and Further Work

A survey of the SuperWASP archive has yielded many results with regards to the detection of pulsations in A-type stars. In total, over 50 000 stars have been identified to vary with frequencies between 5 and 300 d^{-1}. The majority of theses results were found in the low-frequency range, between 5 and 50 d^{-1}, with 375 stars showing variations in the rage $50 - 300\,\mathrm{d}^{-1}$.

8.1 Summary

The WASP project, the leading ground-based discoverer of exoplanets, has collected photometric data of over 31 million stars, and reaches a precision of 1 per cent for the brightest stars (Pollacco et al. 2006). This precision, with the high-cadence observations (30 s between exposures), provides the ideal database to search for pulsations in the A-type stars.

The A-type stars, as a whole, are rapid rotators (with $v \sin i > 120\ \mathrm{km\,s^{-1}}$; Adelman 2004) which serves to broaden their spectral lines, making abundance analysis difficult. Observations have claimed weak, tangled magnetic fields (Böhm-Vitense 2006) in the normal A-type stars which is not expected due to their shallow convective zone. Therefore, the normal A-type stars are not expected to show surface spots or flares which have recently been reported (Balona 2011; Balona 2012; Pedersen 2013).

Contrary to the normal A-type stars, the chemically peculiar sub-classes of the Am and Ap stars show much lower projected rotational velocities than the normal A-type stars, theorised to be a result of binary synchronisation for the Am stars, and magnetic breaking for the Ap stars. The Am stars are defined by their weak Ca K line and strong metal lines when compared to the profile of the Balmer lines. The slow rotation in these stars allows for chemical diffusion to occur in the absence of meridional circulation. Recent observation by the *Kepler* telescope have also lead to the hypothesis that the Am stars show spots on their surface (Balona et al. 2015),

which would indicate a magnetic field similar to the weak disordered ones of the normal A-type stars.

On the other hand, the Ap stars show very strong dipole magnetic fields, which allow for magnetic levitation, coupled with gravitational settling, to produce significant spots of rare earth elements on the surfaces of these stars. These spots can be stable over many years, to decades, thus enabling accurate rotation periods to be derived. The Ap stars are rarely found in binary systems, with none confirmed to be in close systems. The binarity rate of this sub-class is much lower than the normal A-type stars.

The A-type stars have long been known to show pulsational variability (Eggen 1956; Kurtz 1982; Cousins, Caldwell & Menzies 1989). The pulsating A-type stars cover a broad frequency range, from about $0.5\,\mathrm{d}^{-1}$ for the γ Dor stars (e.g. Balona, Krisciunas & Cousins 1994; Kaye et al. 1999; Uytterhoeven et al. 2011), through the δ Sct stars (e.g. Breger 2000; Samadi, Goupil & Houdek 2002; Bradley et al. 2015), to the highest frequency roAp star at $257\,\mathrm{d}^{-1}$ (e.g. Kurtz et al. 2006; Elkin et al. 2011; Holdsworth et al. 2014b).

To detect pulsations in the light curves of the A-type stars in the SuperWASP archive, the Lomb-Scargle periodogram, as implemented in the FASPER code of Press et al. (1992), was identified to provide the best results. This was selected over methods such as Fourier Transforms, least-squares fitting, the string length method and phase-dispersion minimisation as it is computationally fast, deals well with unevenly sampled data, and has been shown to be effective in previous variability studies (e.g. Durán-Rojas et al. 2009; Smalley et al. 2011; Barclay et al. 2011).

Chapter 2 proceeds to work with the WASP data to determine the optimal limits in which to detect pulsations in A-type stars. To obtain the best results from a light curve, it was found that further clipping, beyond that performed by the custom pipeline, of outlying data points was required. As such, a resistant mean algorithm was coded, following Huber (1981), and incorporated into the light curve extraction algorithm. With this implemented, 13 060 unique *Kepler* targets were selected from the results of a variability study of the *Kepler* data by Debosscher et al. (2011), based on a

$(J - H)$ colour of 0.4 or less, thus targeting the F-type and hotter stars. These stars constituted a wide range of variability types, from low-frequency rotationally variable stars to the δ Sct pulsators. To increase the speed of periodogram computation of the corresponding WASP targets, a simplified calculation of the periodogram noise was presented, and as such, a lower S/N detection limit of 2.5 was implemented, over the widely used value of 4.0 (Breger et al. 1993; Koen 2010).

In determining whether WASP had detected the same variation in a star that the *Kepler* data showed, two detection methods were implemented. One method, Method A, only constrained the frequency, whereas the second, Method B, also constrained the amplitude. It was clear that Method B gave more physically meaningful results, particularly when considering the low-amplitude and low-frequency variations. The WASP data clearly demonstrated that it was not possible to detect very low-amplitude variations (below 0.5 mmag), as would be expected from a comparison between ground- and space-based photometry. The low-frequency range, using the presented periodogram calculation method, is dominated by noise and alias effects, thus affecting the detection ability.

A detailed discussion and analysis of the results was conducted. The peaks which were not detected in the WASP data were explained with the consideration of the noise characteristics of the WASP data, as well as the stellar magnitude, detection S/N, alias confusion and target dilution due to other objects in the photometric aperture. Non-detections also resulted from inaccuracies in the *Kepler* catalogue data, or in the pipeline data that were used to compile the comparison catalogue. Finally, variable variables were considered, as is the case for KIC 7106206 which shows a decrease in amplitude of the (originally) principle peak in the data (Bowman & Kurtz 2014), and is eventually not seen in the WASP data (Bowman, Holdsworth & Kurtz 2015).

The final conclusions from this study are that: the minimum amplitude detectable in WASP data is 0.5 mmag, the lowest reliable frequency is 0.5 d^{-1}, the lowest S/N limit is 2.5, stellar magnitudes must be within $7 \leq r \leq 14$, false alarm probabilities should be below 0.8, light curves require more than 1 000 data points, and the sky count is required to be less than 5 000.

Chapter 3 then introduced the survey of the archive. The stars which formed the survey were selected using the above magnitude range and required number of data points, as well as a $(J - H)$ colour of 0.25 or less. Data were processed with a combination of BASH scripts controlling the underlying FORTRAN codes which read the light curve and discard data that did not fit the aforementioned criteria, applied a modified version of the FASPER code (a decrease in the oversampling factor showed no difference in results but decrease the computation time by 2 s per light curve), and identified peaks in the resulting periodogram. The codes were applied to the Ap stars in the Renson & Manfroid (2009) catalogue to test their viability. The aim of this was to identify the known roAp stars, with the possibility of detecting pulsations in other Ap stars. The search only detected one known roAp star, and no new pulsators. The main reason for this is the colour response of the WASP instrument ($4000 - 7000$Å; Pollacco et al. 2006) compared to the wavelength at which the roAp stars show the highest amplitude ($B-$band; Medupe & Kurtz 1998). This test did however show that the codes are capable of detecting 1.0 mmag pulsations in a blind study.

The results of the full archive search were then presented in Chapter 4. Over 202 500 targets have been found to vary with frequencies in the range $5 - 300\,\mathrm{d}^{-1}$. To split the results into more manageable frequency ranges, two frequency ranges were selected and analysed separately: $5-50\,\mathrm{d}^{-1}$ and $50-300\,\mathrm{d}^{-1}$. The low-frequency range is where most of the δ Sct stars are found, however this region also suffers greatly from alias effects. In trying to account for the alias effects, it is estimated that of the 202 281 stars detected to vary in this range, only about 43 000 are due to astrophysical variability. The distribution of spectral types of the detected peaks follows closely the distribution of the total survey sample, with many cooler stars beyond the edge of the instability strip being found to vary. These stars maybe reddened objects (as the reddening was not accounted for in the calculation of the spectral type), or those with false detections of the day aliases.

In the high-frequency range, 375 stars are found to be variable. These stars constitute younger δ Sct stars, roAp stars and sdBV stars. Due to the relatively small number of these stars, each had their light curves manually inspected to confirm the

detections. The frequencies of the detected peaks suggest that most of the detections are of δ Sct type, with a few detections in the roAp and sdBV range.

The very high-frequency (VHF) range, $> 300\,\mathrm{d}^{-1}$, was also explored with the same detection codes used for the lower frequency ranges. Only one new object was detected. The data and periodogram characteristics in this regime are different from those in the the lower frequency ranges, thus implying that a much more detailed analysis is required in this range, with the development of specific codes for this range (see section 8.3.1).

Chapter 5 presented the spectroscopic techniques employed in later chapters of the thesis. The long-slit spectrographs used in this work, RSS on the SALT and ISIS on the WHT, achieve spectral resolutions of about 5 000 and 2 000, respectively, which is what is required for spectral classification. The spectra obtained by these instruments are reduced with STARLINK software packages, primarily FIGARO (Shortridge et al. 2004). Spectra are flat-field corrected, be-biased, clean of cosmic rays, and wavelength calibrated. Normalisation of the 1D spectrum is conducted with the UCLSYN package (Smalley, Smith & Dworetsky 2001).

Further to the discussion on the A-type stars in Chapter 1, a detailed discussion of their spectral characteristics was given. The normal A-type stars show very plain spectra, dominated by the Balmer lines. Metal lines start to appear in the cooler stars in the sequence, and the Ca K line strengthens. The chemically peculiar stars show discrepancies between their Ca K line and metal lines, when compared to the Balmer lines, in the Am stars, whereas the Ap stars show strong over-abundances of Cr, Sr, Eu or Si, or a mixture, in classification spectra.

Chapter 6 then proceeds to present a more detailed analysis of a selection of the high-frequency pulsators found in the WASP archive (Holdsworth et al. 2014b). These stars represent a sub-set of the spectroscopically observed sample. Two 'normal' δ Sct stars are discussed as they represent the highest frequency ($105\,\mathrm{d}^{-1}$), thus possibly the youngest star, and highest amplitude (20.5 mmag) 'normal' A-type stars found by the survey. Both stars appear to be in binary or multiple systems where more than one component may pulsate. These systems are prime targets to apply the FM

(Shibahashi & Kurtz 2012) and PM (Murphy et al. 2014) techniques to determine the binary parameters.

Two of the chemically peculiar Am stars are discussed in detail as these stars were once thought not to pulsate (Breger 1970; Wolff 1983), but the findings of this work show pulsations greater than 6 mmag, and amplitudes up to 73 mmag detected by Smalley et al. (2011). One of the targets discuss, J2054, shows ellipsoidal variation in its light curve, thus agreeing with the hypothesis that Am stars are in binaries, whereas the other star, J2305, does not show this feature, neither is there indication of binarity in its spectrum.

All of the confirmed rapidly oscillating Ap stars are presented as these new detections constitute an increase of the known roAp stars by 22 per cent. They are spectroscopically classified and compared to the known systems from the literature. Within the results are both the hottest (J1844) the coolest (J1921) roAp stars, and the highest amplitude roAp star (J1940; see section 8.2.1). Following the roAp stars, the stars which show hybrid pulsations are discussed. These stars shows pulsations in two distinct frequency ranges, making them prime targets for which to conduct follow-up observations to determine if they are single or multiple systems (see section 8.2.2). If found to be single stars, they will provide contrary evidence to the theoretical models (e.g. Pamyatnykh 2000; Saio 2005) which do not predict high- and low-overtone modes in the same star.

Finally, the Chapter presents three sdBV stars found in the survey. One star had previously been determined to be a non-pulsating sdB star, while two others are entirely new discoveries. J2344 shows pulsation in the high- and low-frequency ranges suggesting this is a rare hybrid sdBV star of the DW Lyn type (Schuh et al. 2006). These stars provide the opportunity to study both the core and surface structures due to the different depths the pulsations probe. These results show the power of such a survey – with the availability of long time-base observations reanalysis of stars can reveal previously undetected variability, or those stars which show variable amplitudes over time.

The final chapter, Chapter 7, a detailed analysis is given of a roAp star found in

the *Kepler* field-of-view, KIC 7582608 (Holdsworth et al. 2014c). The star was observed by the *Kepler* telescope for the duration of the primary mission in LC mode. Although the pulsation frequency ($181\,\mathrm{d}^{-1}$) was well above the Nyquist frequency of the LC data ($24\,\mathrm{d}^{-1}$), a detailed analysis of the pulsation mode was conducted in the super-Nyquist regime (Murphy, Shibahashi & Kurtz 2013). The analysis of the data showed that this star is a quadrupole pulsator due to its rotationally split quintuplet.

The frequency of the pulsation in KIC 7582608 was also observed to vary over the 4 yr of *Kepler* observations, as well as in the WASP data. The source of this variability could not be determined, but such variations have also been discussed for other roAp stars in the literature. One theory is that the variability is due to binary motion. The combination of the WASP and *Kepler* data were used to determine possible binary parameters of the star. Further to this, it is suggested that KIC 7582608 is in a multiple system, with the roAp star in a synchronous 24.4 d orbit, with this binary pair orbiting the triplet centre-of-mass with a period of 1 200 d (Shibahashi, priv. comm.). However long-term follow-up is required to confirm, or otherwise, these hypotheses.

8.2 Current and Planned Observations

The extension of the work presented in this thesis has begun with the observations of several of the stars presented in Chapter 6. Most of the follow-up observations have been photometry of the roAp stars, but with time-resolved spectroscopy obtained for a hybrid candidate. This section details the observations already obtained, and those planned for future proposal rounds.

8.2.1 The roAp Stars

SAAO Observations

A three week observing run at the SAAO was awarded to perform follow-up photometric observations of three roAp stars found in the SuperWASP archive. The stars were

observed with the Sutherland High-speed Optical Cameras (SHOC) mounted on the 1.0 and 1.9 m telescopes in 2014 November. The proposal team consisted of: Holdsworth (PI; Keele University, UK), Smalley (Keele University, UK), Medupe (North West University, SA), Nhlapo (North West University, SA), and Kurtz (University of Central Lancashire, UK). All observations were taken through a Bessell $B-$band filter, with variable exposure times and image binning, based on the seeing conditions and target magnitude. The data were reduced at the telescope with the SHOC pipeline developed by Marissa Kotze[1].

The three stars observed were: J0008, J0651 and J1940. The observations confirmed the pulsation period detected in the WASP data and provide a higher precision periodogram of the variations. An interesting result has arisen from these observations concerning the pulsation amplitude of J1940 (which is seen in the WASP data at a frequency of 176.39 $d^{-1}$and an amplitude of 4.16 mmag). This star was observed for a few hours over 12 nights. The pulsation amplitude was observed to vary over the course of the observations (Figure 8.1). Amplitude variations of this magnitude have not been previously observed in roAp stars which show only a single pulsation period. This has been observed in multiperiodic roAp stars where the amplitude variations are though to be caused by beating effects of close periods. The WASP data of this star do not show any further pulsation periods. A further two week observing run has been proposed for J1940 using the same instrument at SAAO. The observations will increase the frequency resolution aiding the determination of whether mode beating is producing the significant increase in amplitude.

APT Fairborn Observations

Follow-up observations have also been made with the 0.75 m APT at Fairborn Observatory, Arizona, with a Johnson $B-$band filter (Paunzen et al. 2013a). The observations were scheduled and extracted by Gerald Handler. The observations, shown in Fig-

[1] `http://www.saao.ac.za/~marissa/SHOCpipeline/SHOCpipeline.pdf`

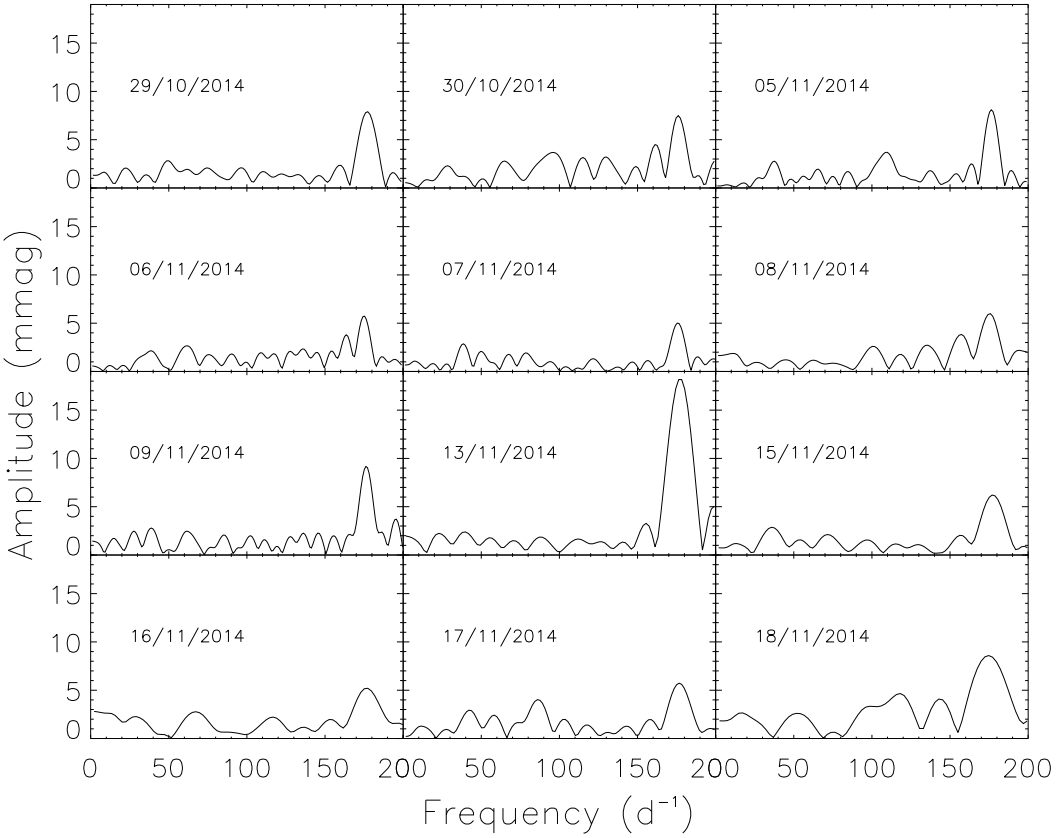

Figure 8.1: Observations of J1940 showing the amplitude variation over the observing period.

ure 8.2, have confirmed the pulsation frequency seen in the WASP data, and with a higher photometric precision. This higher precision has allowed for the detection of a harmonic of the principle frequency in one star, J0353.

As well as the APT observations, J0353 has been awarded K2 SC time during Campaign 4. The star will be observed for about 80 d at μmag precision. This will be the first time that a roAp star discovered from ground-based photometry will be observed by the *Kepler* telescope in SC. The aim of the observations is to determine if further pulsation modes exist below the ground-based detection limits. As the APT ob-

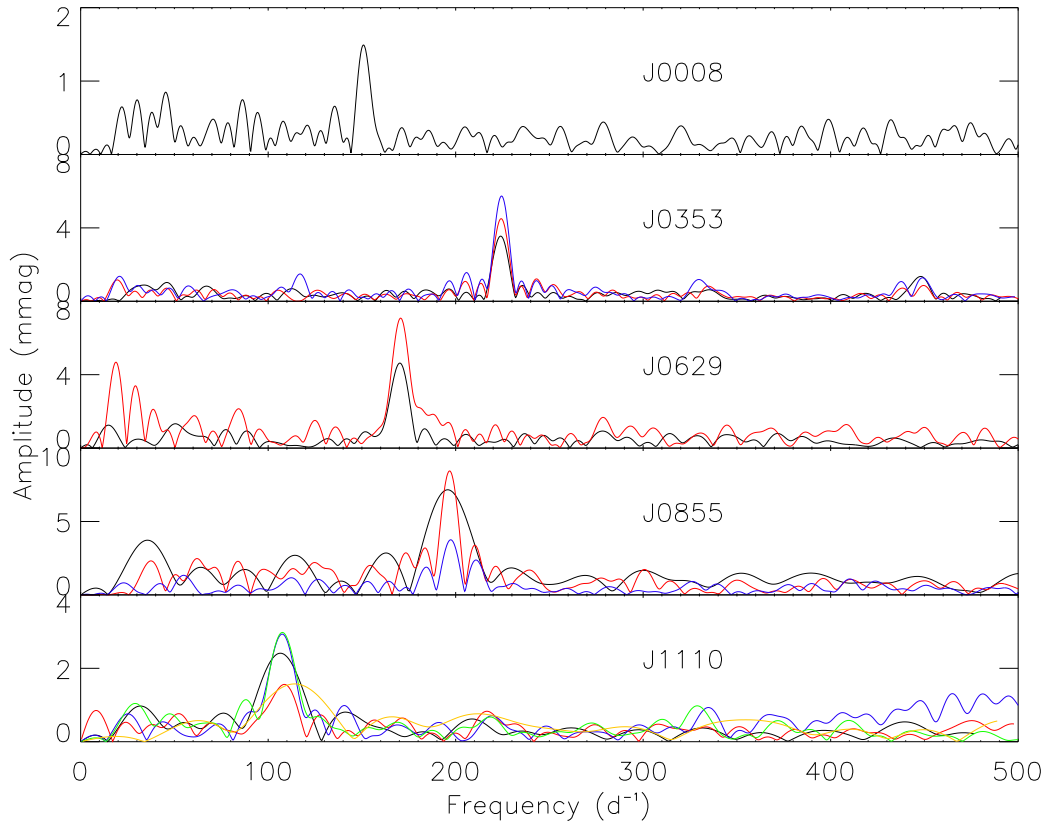

Figure 8.2: Observations of 5 roAp stars discovered in the survey. These results form the basis of further follow-up observations. Different colours represent different nights for each object, with the order of observation being: black, red, blue, green, orange.

servations show amplitude variation over the three nights of observations, it is thought that further modes are present to cause a beating effect. These observations will also confirm the rotational signal detected in the WASP data, through light curve variation and mode splitting.

8.2.2 A Hybrid Candidate

High-resolution, time-resolved spectra have been obtained for J1917, a hybrid candidate star, with UVES on the VLT/UT2 telescope. Two hours of data were collected in service mode for the proposal 093.D-0907 (Holdsworth, Smalley, Antoci, Maxted) to determine the source of the pulsations detected in the SuperWASP photometry. As discussed in section 6.6, the star is a visual binary, but it is unlikely that either of the sets of pulsation originate from a companion to the spectroscopically classified Am star. Therefore it is proposed that the system may have another companion, and unresolved sdBV star. The aim of the UVES observations is to determine if a third member is present, through the observation of He lines in the spectrum, and to find the source of the pulsations.

An in depth analysis of this data will form a separate publication to this thesis, however a initial preview of the data has been made. Tracing the Mg II λ4481 line over the duration of the observations gives an indication that two objects are present in the slit (Figure 8.3). This implies that the star is not a hybrid, but a multiple system with at least two pulsating components. A detailed analysis of the spectra will search for the presence of He lines, and the source of the pulsations.

8.2.3 *STEREO/HI* Observations of Low-Frequency Pulsators

To investigate further the low-frequency detections in the WASP archive, data from the Solar TErrestrial RElations Observatory (*STEREO*; Kaiser et al. 2008) Heliospheric Imagers (HIs; Eyles et al. 2009) are to be searched for coincident observations. The instruments consist of two cameras: HI-1 with a FOV of $20^\circ \times 20^\circ$, pixels of $70''$ and

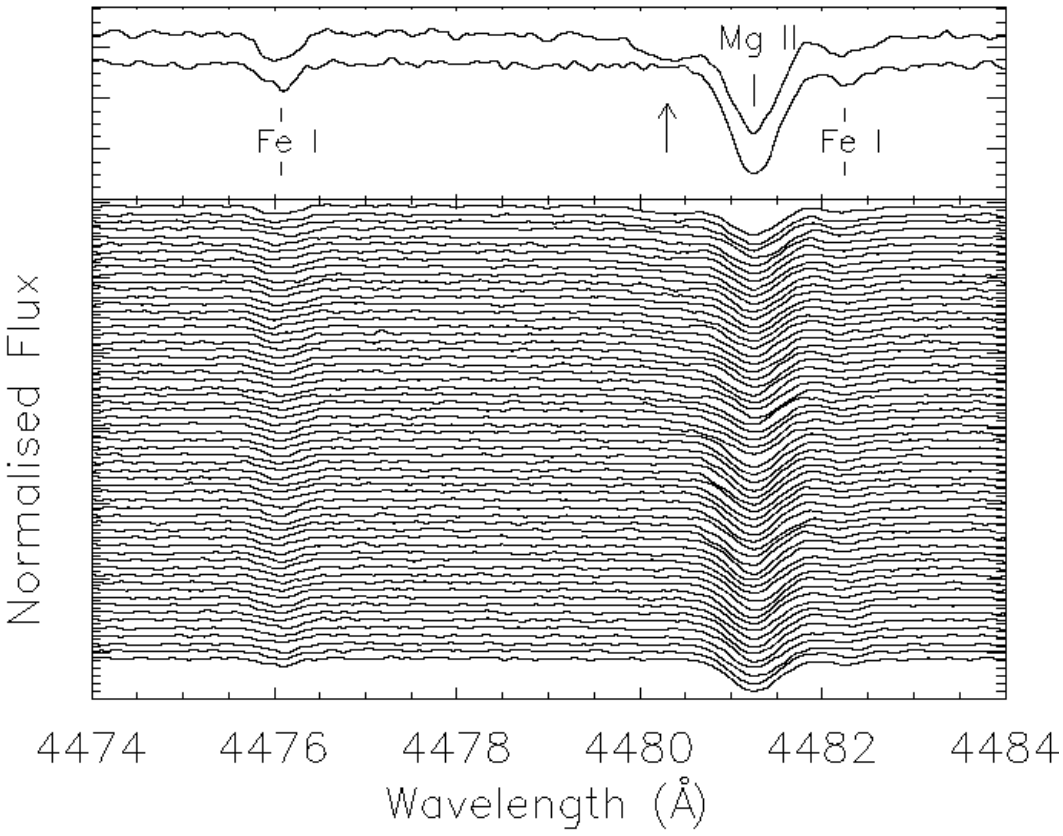

Figure 8.3: The Mg II λ4481 line of J1917 over two hours of VLT/UVES observations, with time progressing with upwards vertical position. A second line, on the blue edge of the Mg II line appears in the later spectra of the series, and is marked by the arrow. It is thought to be from a second object on the slit, suggesting this to be a multiple system. The top panel shows the first (bottom) and last (top) spectra of the series to highlight the effect. Each spectrum is offset by 0.1 flux units.

a cadence of 40 min, and HI-2 with a FOV of 70°×70°, pixels of 4′ and a cadence of 120 min. Both cameras observe stars in the range $4 \leq R \leq 12$. Despite having large pixels, these instruments have previously been successfully used to study different types of stellar variability (e.g. Wraight et al. 2012b; Wraight et al. 2012a; Paunzen et al. 2013b; Holdsworth et al. 2014a). The space-based nature of the observations will allow for the removal of alias ambiguities of the ground-based WASP observations. Due to the cadences, the observations will only be able to check variability up to $18\,\mathrm{d}^{-1}$ in the best cases, and $6\,\mathrm{d}^{-1}$ in the worst. However, this is adequate to test the low-frequency detections, with the possibility of combining the two data sets to investigate the $0 - 5\,\mathrm{d}^{-1}$ frequency range.

8.3 Future Work

There are many different ways in which the results and methods presented in this thesis can be extended in to future projects. It has been shown that the SuperWASP archive contains a wealth of pulsating stars, with other systems still to be identified. Below are two further uses of the archive to exploit the data to its full potential.

8.3.1 Extension into the Very High-Frequency Region

To extend the study of the A-type pulsators in the sample already selected, a concerted effort to characterise the very high-frequency regime would provide the potential to discover more pulsating sdBV and white dwarf stars then those presented here. A deeper understanding of the sources of the VHF noise must be sought, with the aim of eliminating, or at least reducing, the effects on the calculated periodogram.

To determine the optimal data quality and selection criteria, a study similar to that presented in Chapter 2 would be required to be conducted on known sdBV and white dwarf pulsators. This would provide an indication of the potential discovery rate of these compact pulsators, and the capabilities of the data. Similar tests to those

presented in section 3.5 could be used to characterise the data sets used to quantify any non-detections of known stars. Further to this, considering the dilution which the VHF peaks suffer, due to the sampling of their light curves, a more rigorous resistant mean algorithm may be implemented to further remove the out-lying points from the light curve with the aim of minimising the noise in the periodogram so to detect even the lowest amplitude peaks.

8.3.2 Whole Archive Search

With the increase in computing power and data storage facilities since work on the A-type survey began, it would now be possible to perform a survey on the entire SuperWASP archive. In doing so, no selection biases exist at all for any class of pulsator, only post analysis of pseudo stellar parameters will give an indication of the stellar type. This will remove the affects of reddening on the $(J-H)$ colour cuts used in the survey presented here, thus including further A-type stars such as the PMS objects.

Consideration of the low-frequency properties of some type of stars would be required however, particularly when searching for pulsations in stars which are surrounded by disks or proto-stellar clouds, such as the PMS stars. The low-frequency variability in these objects can produce extremely 'noisy' light curves. As such, the resistant mean cutting routine may destroy the high-frequency signals, if present, in these stars. An investigation into low-frequency noise filtering would be required to optimise the detection rates.

The criteria developed here would be used in the selection of targets with useful data sets i.e. the number of data points, background limits and magnitude limits. In addition to this, the χ^2/n measure of the quality, used in section 3.5, of a light curve should also be implemented. This would reduce the the number of light curves for which a low-quality periodogram would be calculated, thus saving computation time and disk space.

In addition, on-the-fly peak detection is also suggested to reduce the I/O processes

which increase the computation time. A less stringent detection algorithm would need to be developed for this type of survey due to the different amplitudes and frequencies which would be present in the periodograms. The development of carefully considered automatic classification software would be required to manage the number of variable objects discovered. As of 2015 February, there are over 31 million unique objects in the WASP archive, suggesting the management of the 1.5 million targets in this thesis would need to be adapted to cope with such an increase in targets; further segregation of targets by R.A. and Dec. minutes rather than just hours would reduce the number of stars per directory, and consequently the data access time would be shorter.

The work presented in this thesis has shown that the SuperWASP data are capable of providing an extensive database of variability in the A-type stars. Due to their different complexities, both the low-frequency range and the very high-frequency range require individual studies to be conducted, but it has been shown that different types of variability are detectable in these regions. The central frequency range had been fully explored and exploited, allowing for a large number of new detections of pulsations in A-type stars to be made. Clearly the SuperWASP archive has much more to offer the A star community, as well as other fields of variable stars across the HR diagram.

The methodologies developed here can be applied to other archives, such as the OGLE (Udalski et al. 1992), ASAS (Pojmanski 1997) and HATnet (Bakos et al. 2004), in similar searches for high-frequency stellar variability. Although these surveys may not have as high a cadence as the WASP project, it will still be possible to search for a variety of variable stars.

8.3.3 85 mm Lens Data

In summer 2012 the 200 mm lenses of the SuperWASP-South instrument were changed for 85 mm lenses. This change has allowed for brighter stars to be observed without saturating the CCDs. A survey of the new data for the brighter stars should be conducted for variability, using the pre-existing codes and methodologies presented in this thesis. The detection of variability in these brighter stars will provide greater oppor-

tunity to perform higher resolution and S/N spectroscopic follow-up of the targets, with the possibility of time-resolved spectroscopic observations to determine whether different spectral lines, which probe different depths of the stellar atmosphere, vary with different frequencies. Currently, observations of this type are often not possible to perform with the targets found in this survey due to their relative faintness, and thus the need for increased exposure times which would under-sample the pulsation.

Final Remarks

This work has shown the diversity of the SuperWASP survey, and the potential that the archive holds for all-sky stellar variability studies. Particularly, the observing strategy of the instruments provide a unique opportunity to investigate an otherwise often understudied frequency domain. The photometric precision that the WASP data achieves has enabled the discovery of thousands of variable A-type stars, from the lowest frequency δ Sct stars, to the rapidly oscillating Ap stars, and the compact subdwarf B stars. The approach taken by this study, in that no prior knowledge of the type of star in known, removes selection biases when targeting specific types of pulsator. This approach enables the detection of pulsations in stars which would otherwise not be targeted.

Results will soon be available from the GAIA mission which will enable the results of this survey to be placed on the HR diagram, thus allowing for more accurate modelling of theses stars, and providing better constrains on the instability strip. With the ongoing observations with the *Kepler* telescope, and future space-based missions such as TESS and Plato, the ability to provide targets which will yield significant science results is key; the results of this thesis, and future work with the WASP archive, can, and is, providing these targets in the hope that *"in the not too distant future we shall be competent to understand so simple a thing as a star"*.

A The Known roAp Stars

Table A.1: Known roAp stars from the literature. The photometric amplitudes are in mmag. Frequencies marked witn an '*' indicate a multiperiodic pulsator.

HD	Other ID	V	Spectral Type	Principle Frequency (d^{-1})	Amplitude	Reference
			Photometric Targets			
					(ΔB)	
6532	Ap Scl	8.45	Ap SrCrEu	202.82*	5	1
9289	BW Cet	9.38	Ap SrEu	137.14*	3.5	2
12098	V988 Cas	8.07	F0 (HD)	189.22*	3	3
12932	BN Cet	10.25	Ap SrEuCr	124.14	4	4,5
19918	BT Hyi	9.34	Ap SrEuCr	99.31*	2	6
24712	HR 1217	6.00	Ap SrEu(Cr)	232.26*	10	7
42659	UV Lep	6.77	Ap SrCrEu	148.45	0.8	8
60435	V409 Car	8.89	Ap Sr(Eu)	114.59*	16	9
75425[a]		9.58	Ap Sr(EuCr)	48.32	2.1	10
80316	LX Hya	7.78	Ap Sr(Eu)	194.59*	2	11
83368	HR 3831	6.17	Ap SrEuCr	124.14*	10	12
84041	AI Ant	9.33	Ap SrEuCr	96.00*	6	13
86181	V437 Car	9.32	Ap Sr	232.26	4.6	14
99563	XY Crt	8.16	F0(HD)	134.58*	10	15
101065	Przbylski's Star	7.99	Controversial	119.01	13	12
119027	LZ Hya	10.02	Ap SrEu(Cr)	165.52*	2	16
122970	PP Vir	8.31	–	129.73*	2	17
128898	α Cir	3.20	Ap SrEu(Cr)	211.76*	5	18
134214	HI Lib	7.46	Ap SrEu(Cr)	257.14*	7	19
137949	33 Lib	6.67	Ap SrEuCr	173.49*	3	12
150562	V835 Ara	9.82	A/F(p Eu)	133.33	0.8	20
161459	V834 Ara	10.33	Ap EuSrCr	120.00	1.3	21
166473	V694 CrA	7.92	Ap SrEuCr	163.64*	2	22
176232	10 Aql	5.89	F0p SrEu	124.14*	0.6	23
185256	V4347 Sgr	9.94	Ap Sr(EuCr)	141.18	3	24
190290	CK Oct	9.91	Ap EuSr	197.26*	2	25
193756	QR Tel	9.2	Ap SrCrEu	110.77	1.5	26
196470	AW Cap	9.72	Ap SrEu(Cr)	133.33	0.7	27
201601	γ Equ	4.68	F0p	116.13*	3	28
203932	BI Mic	8.82	Ap SrEu	244.07*	2	9
213637	MM Aqr	9.61	A(p EuSrCr)	125.22*	1.5	29
217522	BP Gru	7.53	Ap (Si)Cr	103.60*	4	30
218495	CN Tuc	9.36	Ap EuSr	194.59	1	26

Continued on next page...

Table A.1: *Continued*

HD	Other ID	V	Spectral Type	Principle Frequency (d^{-1})	Amplitude	Reference
			SuperWASP Discoveries			
					($\Delta V_{\rm WASP}$)	
24355	J0353	9.65	Ap SrEu	224.31	1.65	31
97127	J1110	9.43	Ap SrEu(Cr)	106.61	0.66	31
258048	J0629	10.52	Ap EuCr(Sr)	169.54	1.49	31
	J0008	10.16	Ap SrEu(Cr)	150.26	0.61	31
	J0651	11.51	Ap SrEu(Cr)	132.38	0.79	31
	J0855	10.8	Ap EuSr	197.27	1.4	31
	J1430	11.56	Ap EuSr	235.54	1.06	31
	J1640	12.67	Ap SrEu	151.93	3.52	31
	KIC 7582608	11.25	Ap Cr	181.73	1.85	31
	J1921	12.16	Ap SrEuCr	128.76	1.99	This work
	J1940	13.0	A/F(p Cr)	176.39	4.16	31
			Kepler Targets			
					($\Delta V_{\rm KPLR}$)	
225914	KIC 4768731	9.17	Ap	61.45*	0.063	32,33
	KIC 8677585	10.19	A5p	143.42*	0.033	34
	KIC 10195926	10.66	Ap	84.21*	0.079	35
	KIC 10483436	11.38	Ap	116.90*	0.068	36
	KIC 7582608	11.25	Ap CrEu	181.73	1.85	31,37

Continued on next page...

Table A.1: *Continued*

HD	Other ID	V	Spectral Type	Principle Frequency (d^{-1})	Amplitude	Reference
			Spectroscopic Targets			
					($m\,s^{-1}$)	
69013		9.56	Ap	126.14	80-210	38
75445		7.12	Ap SrEu	159.84	20-30	39
92499		8.88	Ap	138.46	28-86	40
96237	TX Crt	9.45	Ap	105.88	100	38
115226		8.50	Ap	132.60	1250	42
116114		7.02	Ap	67.61	125	41
132205		8.72	A2 EuSrCr	201.68	37-97	43
137909	β CrB	3.68	F0p	88.89*	30	44
143487		9.43	Ap	144.00	25-66	40
148593		9.15	A2 Sr	134.71	20-50	43
151860		9.01	A2 SrEu	117.04	25-84	43
154708		8.76	Ap	180.00	60	45
177765		9.15	A5 SrEuCr	61.02	7-150	46
218994		8.56	Ap	101.41	900	47

[a]Controversial

References: 1 Kurtz & Kreidl (1985); 2 Kurtz & Martinez (1993); 3 Martinez et al. (2000); 4 Kreidl (1990); 5 Schneider & Weiss (1990); 6 Martinez & Kurtz (1991a); 7 Kurtz (1981); 8 Martinez, Kurtz & Ashley (1993); 9 Kurtz (1984); 10 Martinez (1996); 11 Kurtz, Shibahashi & Goode (1990); 12 Kurtz (1982); 13 Martinez (1991); 14 Kurtz et al. (1994); 15 Dorokhova & Dorokhov (1998); 16 Martinez & Kurtz (1991b); 17 Handler & Paunzen (1999); 18 Kurtz & Cropper (1981); 19 Kreidl (1985); 20 Martinez & Kurtz (1992); 21 Martinez & Kauffmann (1990); 22 Kurtz & Martinez (1987); 23 Heller & Kramer (1988); 24 Kurtz & Martinez (1995); 25 Martinez & Kurtz (1990b); 26 Martinez & Kurtz (1990a); 27 Martinez et al. (1990); 28 Kurtz (1983a); 29 Martinez, Meintjes & Ratcliff (1997); 30 Kurtz (1983b); 31 Holdsworth et al. (2014b); 32 Niemczura et al. (2014); 33 Smalley et al. (2015); 34 Balona et al. (2011b); 35 Kurtz et al. (2011); 36 Balona et al. (2011a); 37 Holdsworth et al. (2014c); 38 Elkin et al. (2011); 39 Kochukhov et al. (2009); 40 Kochukhov et al. (2013); 41 Elkin et al. (2005); 42 Kochukhov et al. (2008); 43 Elkin et al. (2010a); 44 Hatzes & Mkrtichian (2004); 45 Kurtz et al. (2006); 46 Alentiev et al. (2012); 47 González et al. (2008).

B Spectra and Periodograms from Chapter 6

Below are presented the remaining periodograms and spectra which were not shown in Chapter 6. They are separated into the different classes discussed in the text.

B.1 The δ Scuti Stars

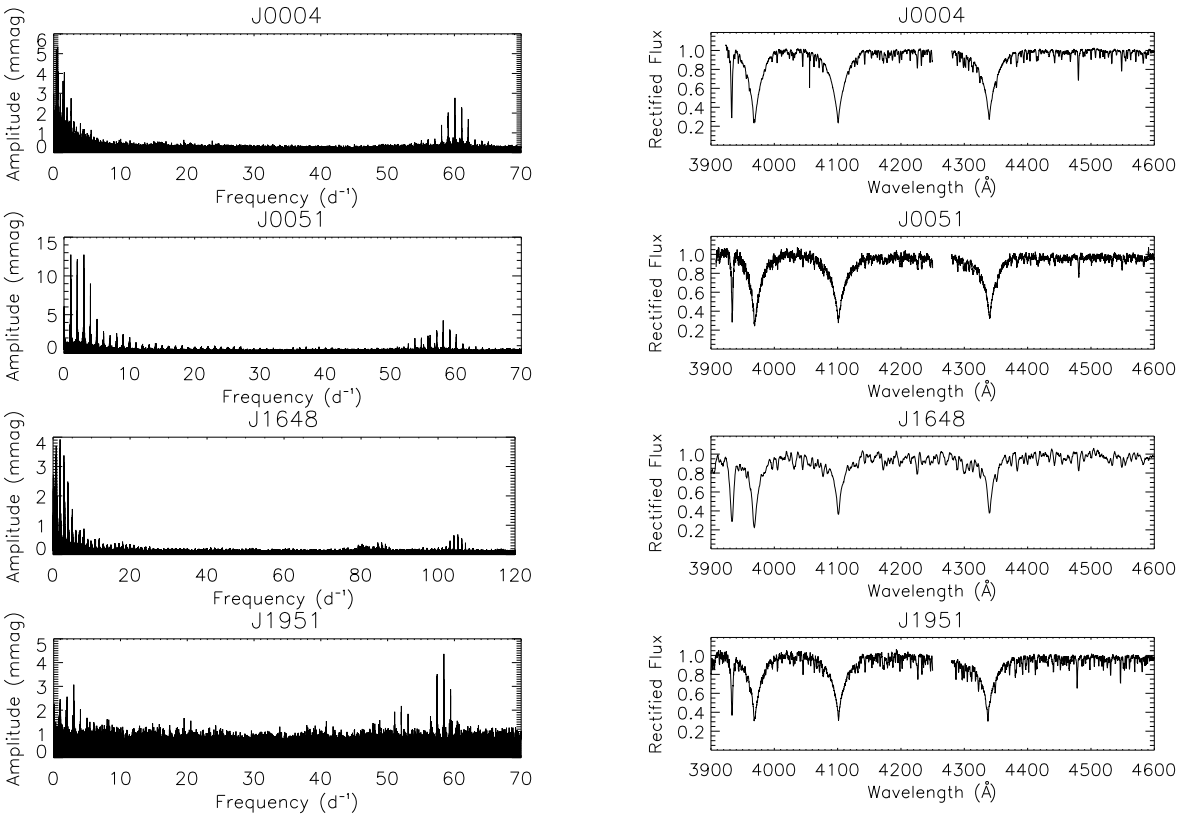

Figure B.1: Periodograms and spectra of the δ Scuti targets.

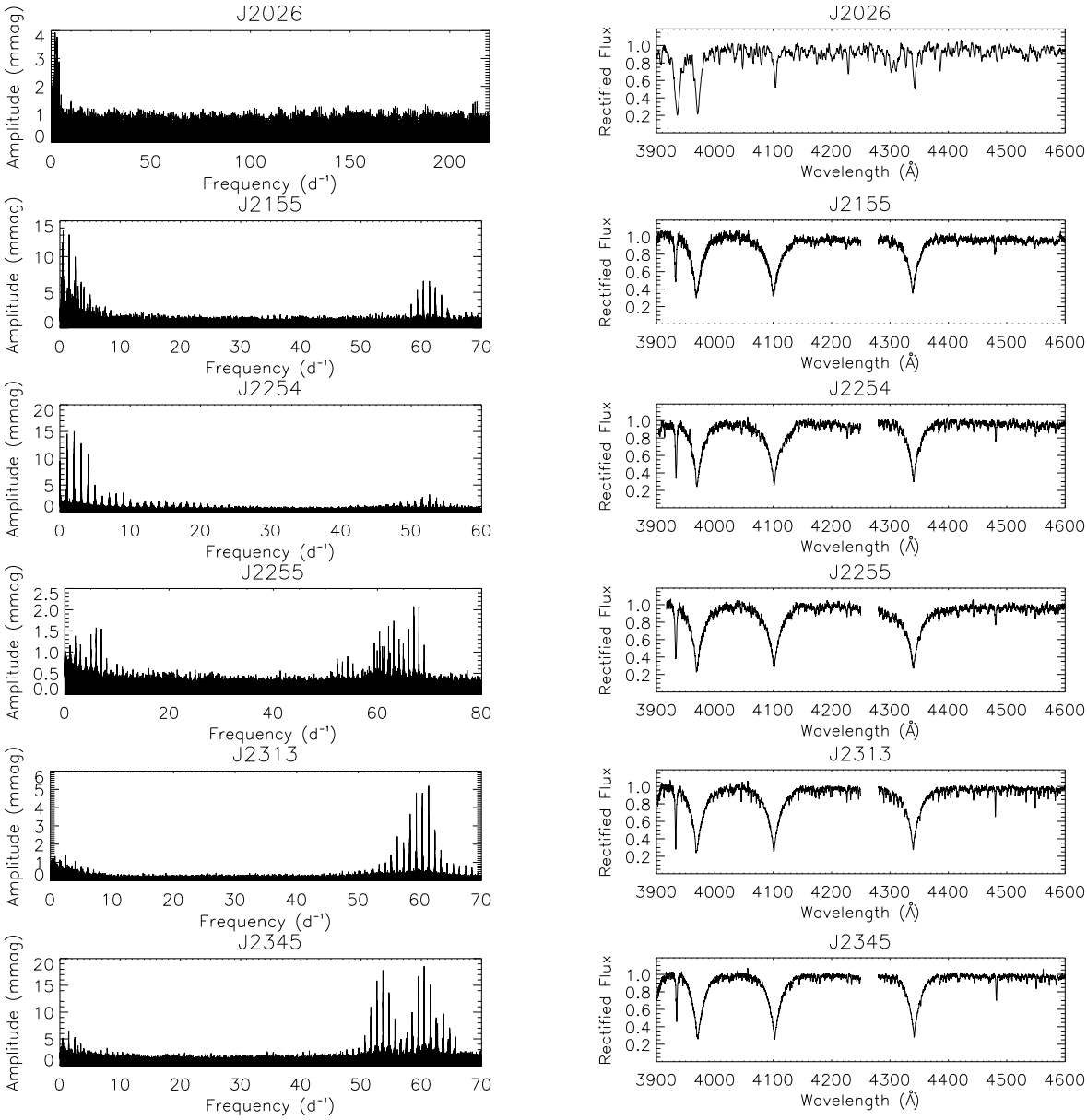

Figure B.1: *Continued.*

B.2 The Am Stars

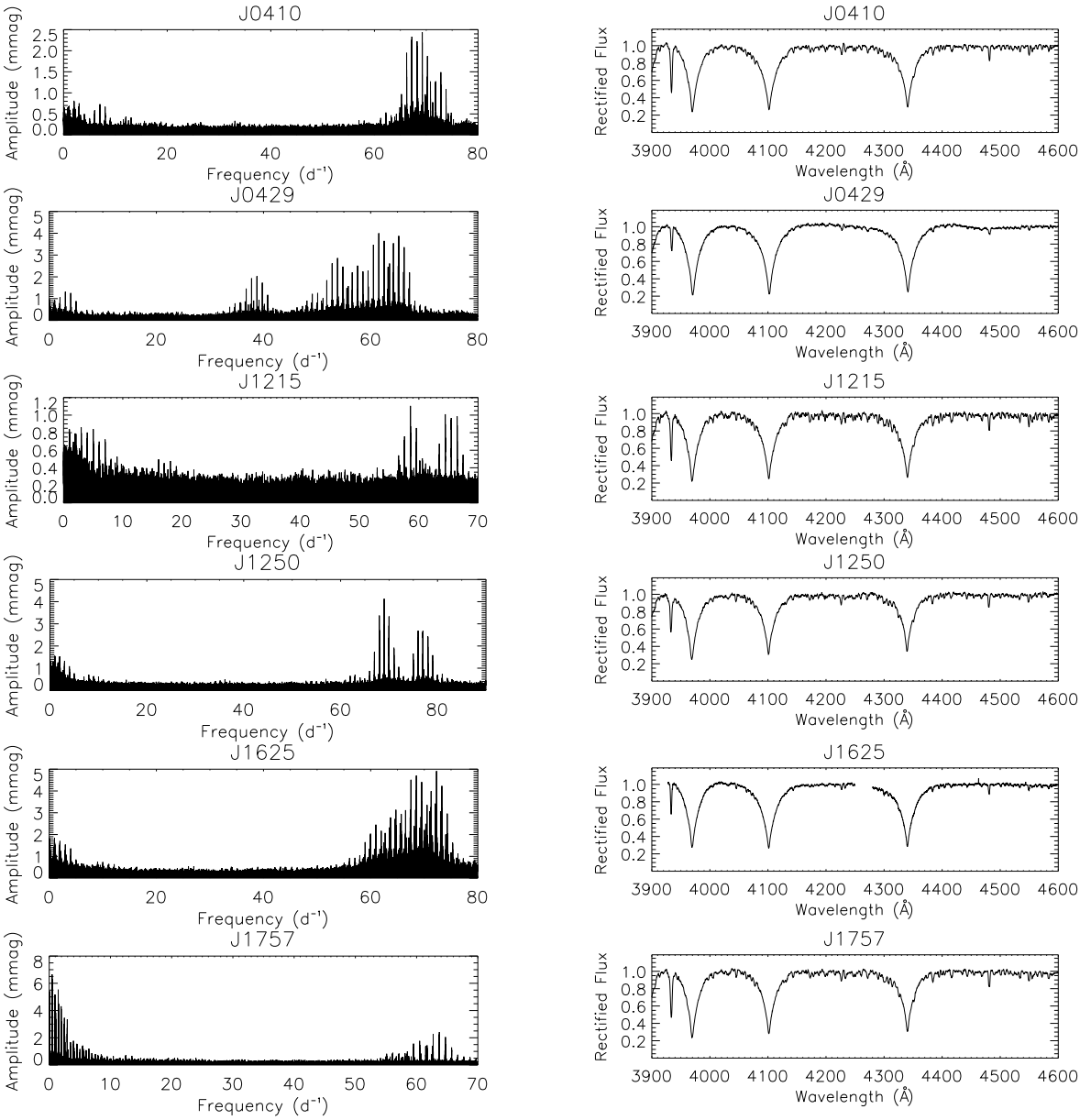

Figure B.2: Periodograms and spectra of the Am and Am: targets.

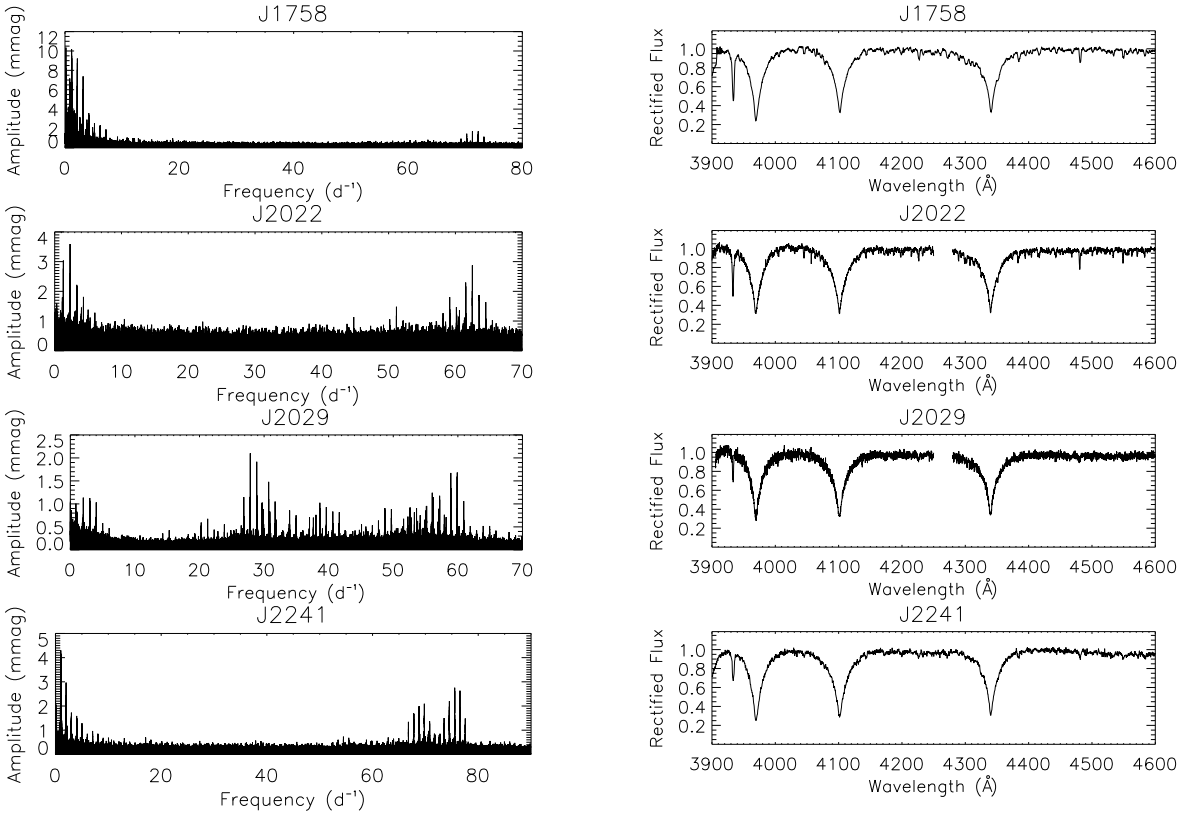

Figure B.2: *Continued.*

C Full version of Table 4.1

Table C.1: Photometric information for all pulsators. Columns 6 – 15 give the first five frequencies (in d^{-1}) and amplitudes (in mmag), if present, above $50\,d^{-1}$.

WASP ID	Other ID	V	ν_1 (d^{-1})	A_1 (mmag)	ν_2 (d^{-1})	A_2 (mmag)	ν_3 (d^{-1})	A_3 (mmag)	ν_4 (d^{-1})	A_4 (mmag)	ν_5 (d^{-1})	A_5 (mmag)
1SWASPJ000415.12-172529.6	HD 225186	9.05	60.08	3.40	–	–	–	–	–	–	–	–
1SWASPJ000537.79+313058.8	TYC 2259-818-1	11.70	52.92	1.47	–	–	–	–	–	–	–	–
1SWASPJ000830.50+042818.1	TYC 4-562-1	10.16	150.26	0.76	–	–	–	–	–	–	–	–
1SWASPJ000940.84+562218.9	TYC 3660-1935-1	10.34	66.37	3.15	–	–	–	–	–	–	–	–
1SWASPJ002436.35+165847.3	HD 2020	8.50	54.41	3.40	52.84	1.83	50.97	1.41	–	–	–	–
1SWASPJ002602.95+344745.8	TYC 2269-(996-1/906-1)	9.87	79.13	2.05	75.21	1.44	–	–	–	–	–	–
1SWASPJ002743.71+491053.5	TYC 3256-2380-1	11.84	51.36	1.31	–	–	–	–	–	–	–	–
1SWASPJ003241.25+314626.6	TYC 2262-285-1	11.91	65.05	4.49	–	–	–	–	–	–	–	–
1SWASPJ003346.25+052202.2	2MASS J00334627+0522021	13.73	52.95	6.83	–	–	–	–	–	–	–	–
1SWASPJ003557.24+073632.9	HD 3284	8.43	53.41	1.12	50.16	0.69	–	–	–	–	–	–
1SWASPJ005107.36-110831.9	TYC 5270-1900-1	11.52	58.04	4.77	54.71	2.63	–	–	–	–	–	–
1SWASPJ010204.03+513159.1	TYC 3275-688-1	11.38	57.40	4.12	53.23	3.97	57.81	2.05	52.40	1.77	50.36	1.52
1SWASPJ011658.14+432457.6	2MASS J01165815+4324573	12.32	62.83	4.58	–	–	–	–	–	–	–	–
1SWASPJ012051.94+482923.1	TYC 3269-202-1	12.62	60.43	3.59	64.32	3.37	53.03	3.22	–	–	–	–
1SWASPJ012558.93+553738.4	TYC 3674-899-1	11.99	58.81	2.84	55.58	2.76	53.94	2.06	58.75	1.43	–	–
1SWASPJ013036.65+550528.6	TYC 3674-1670-1	10.42	52.35	0.91	–	–	–	–	–	–	–	–
1SWASPJ013157.95+211032.4	TYC 1204-323-1	11.45	58.53	3.63	55.58	1.58	57.49	1.40	–	–	–	–
1SWASPJ013513.35+563156.8	TYC 3679-1751-1	12.01	70.26	8.44	74.06	6.44	70.13	2.99	–	–	–	–
1SWASPJ013953.56-243032.3	2MASS J01395356-2430328	13.10	56.38	5.79	–	–	–	–	–	–	–	–
1SWASPJ014746.41+435450.3	TYC 2827-457-1	9.83	54.31	2.12	58.38	1.67	54.56	0.97	55.83	0.97	–	–
1SWASPJ014942.68-073117.4	TYC 5278-7-1	10.62	58.48	4.23	53.48	4.17	54.47	2.18	–	–	–	–
1SWASPJ020615.80-190726.2	HD 12932	10.17	124.10	1.38	–	–	–	–	–	–	–	–
1SWASPJ023008.13+531202.5	TYC 3687-1348-1	10.32	53.41	2.12	–	–	–	–	–	–	–	–
1SWASPJ023158.62+443818.8	TYC 2844-873-1	10.48	59.19	3.79	62.65	3.11	59.10	2.50	54.25	1.00	–	–
1SWASPJ023211.85+124113.3	HD 15747	8.51	64.33	3.91	–	–	–	–	–	–	–	–
1SWASPJ023710.30+500103.3	TYC 3303-1639-1	12.26	51.99	3.83	–	–	–	–	–	–	–	–
1SWASPJ024400.57+420342.3	TYC 2853-1458-1	10.62	53.43	1.98	–	–	–	–	–	–	–	–
1SWASPJ024637.11-251233.4	HD 17392	10.40	66.16	2.90	–	–	–	–	–	–	–	–
1SWASPJ025243.52+104924.5	TYC 643-614-1	12.93	80.39	3.19	79.24	1.63	76.29	1.46	76.62	1.44	79.04	1.23
1SWASPJ025535.67-180743.0	TYC 5867-257-1	12.17	51.19	2.56	–	–	–	–	–	–	–	–
1SWASPJ030026.62+382522.9	TYC 2847-973-1	10.70	50.56	1.51	51.42	1.29	57.59	1.07	–	–	–	–
1SWASPJ031455.69+041800.6	HD 20203	8.85	52.24	2.41	–	–	–	–	–	–	–	–
1SWASPJ032009.58+385202.1	HD 275214	10.92	53.46	1.81	–	–	–	–	–	–	–	–
1SWASPJ032301.25-121919.8	HD 20999	10.74	50.45	2.47	–	–	–	–	–	–	–	–
1SWASPJ033214.24+010413.7	TYC 64-99-1	11.69	53.11	3.06	–	–	–	–	–	–	–	–
1SWASPJ033254.50+075355.8	TYC 650-1437-1	10.47	56.75	2.67	56.75	2.62	53.44	2.12	56.53	2.06	53.22	1.30
1SWASPJ035323.09+253833.3	HD 24355	9.65	224.31	1.65	–	–	–	–	–	–	–	–
1SWASPJ035429.77+342018.1	TYC 2365-1415-1	12.39	57.73	4.48	54.27	4.20	57.07	2.96	–	–	–	–
1SWASPJ035457.70+125422.0	HD 24572	9.47	58.76	2.57	55.14	1.17	54.61	1.03	55.14	1.03	51.29	0.87
1SWASPJ040401.81-114454.1	HD 25674	8.69	66.09	3.14	62.86	1.85	–	–	–	–	–	–
1SWASPJ040602.47+263308.2	HD 25748	9.27	55.74	5.58	59.16	3.55	–	–	–	–	–	–
1SWASPJ040855.77-093726.5	HD 26271	9.88	54.69	2.00	–	–	–	–	–	–	–	–
1SWASPJ040915.06-045737.4	HD 26278	9.93	55.72	0.95	–	–	–	–	–	–	–	–
1SWASPJ041025.61+315150.8	HD 281664	10.76	56.41	1.42	51.91	1.01	–	–	–	–	–	–

Table C.1: *Continued*

WASP ID	Other ID	V	ν_1 (d^{-1})	A_1 (mmag)	ν_2 (d^{-1})	A_2 (mmag)	ν_3 (d^{-1})	A_3 (mmag)	ν_4 (d^{-1})	A_4 (mmag)	ν_5 (d^{-1})	A_5 (mmag)
1SWASPJ041028.28+371831.3	TYC 2370-514-1	11.55	60.09	4.19	–	–	–	–	–	–	–	–
1SWASPJ041045.78+071717.1	HD 26400	9.54	68.22	2.70	71.82	1.53	65.92	0.86	68.37	0.63	–	–
1SWASPJ041109.15+352547.0	HD 279523	10.46	52.28	1.74	–	–	–	–	–	–	–	–
1SWASPJ041612.00-414659.0	TYC 7581-1192-1	12.59	61.66	2.57	58.15	1.85	–	–	–	–	–	–
1SWASPJ041803.94+311959.5	2MASS J04180395+3119596	12.26	50.88	2.53	–	–	–	–	–	–	–	–
1SWASPJ042033.85+125932.3	2MASS J04203388+1259322	13.24	56.57	7.98	–	–	–	–	–	–	–	–
1SWASPJ042306.60-080635.1	HD 27811	9.54	50.26	2.79	53.74	2.08	–	–	–	–	–	–
1SWASPJ042652.63-035505.3	2MASS J04265263-0355048	12.40	50.89	5.71	–	–	–	–	–	–	–	–
1SWASPJ042737.30+425905.6	HD 276325	10.57	52.11	4.24	–	–	–	–	–	–	–	–
1SWASPJ042816.49+075038.9	TYC 669-1481-1	11.77	64.69	3.60	–	–	–	–	–	–	–	–
1SWASPJ042927.24-150151.1	HD 28548	9.22	65.25	4.41	57.55	4.23	61.52	3.47	53.81	2.59	65.14	2.22
1SWASPJ043027.32+302314.6	HD 282262	10.93	52.48	2.29	–	–	–	–	–	–	–	–
1SWASPJ043129.98-261828.1	TYC 6467-2422-1	11.47	64.39	4.05	63.10	2.18	53.49	2.09	64.41	2.08	–	–
1SWASPJ043225.87+153252.9	HD 285874	11.80	62.94	2.98	66.09	2.82	69.68	2.26	–	–	–	–
1SWASPJ044335.20-424033.0	HD 30204	10.23	60.66	5.37	55.57	2.10	57.43	1.84	57.16	1.73	55.30	1.58
1SWASPJ044340.95-204001.4	TYC 5898-82-1	10.98	76.65	3.35	72.28	2.04	61.57	1.86	67.58	1.37	–	–
1SWASPJ044622.28+062943.9	HD 30266	8.78	52.54	3.51	54.12	1.83	51.11	1.07	–	–	–	–
1SWASPJ045012.48+132144.1	TYC 695-1324-1	10.63	56.64	1.16	53.54	0.88	53.02	0.82	50.60	0.72	53.17	0.68
1SWASPJ045336.98+092702.1	HD 287243	10.87	54.73	0.80	52.48	0.71	–	–	–	–	–	–
1SWASPJ045405.95-165937.3	HD 31322	9.28	50.40	4.78	–	–	–	–	–	–	–	–
1SWASPJ045516.70+152710.3	HD 31316	9.82	55.15	1.99	58.98	1.61	51.63	1.34	–	–	–	–
1SWASPJ045845.10+245259.7	HD 284021	11.17	53.00	1.96	–	–	–	–	–	–	–	–
1SWASPJ050016.18-144456.0	HD 32119	10.43	52.00	23.22	55.55	2.53	–	–	–	–	–	–
1SWASPJ050157.21+125555.2	HD 287370	10.18	58.62	3.84	58.62	2.19	54.28	1.54	54.28	1.17	51.93	0.97
1SWASPJ050226.71-433024.7	HD 32626	9.65	54.88	1.70	61.17	1.20	–	–	–	–	–	–
1SWASPJ050358.83+143221.2	HD 32463	10.57	59.95	1.10	–	–	–	–	–	–	–	–
1SWASPJ050404.10+025721.7	HD 32541	9.56	60.61	0.91	54.53	0.69	57.35	0.63	57.22	0.55	53.04	0.48
1SWASPJ050428.08-080048.6	TYC 5323-493-1	10.03	52.93	1.96	57.30	1.80	53.86	1.55	60.70	1.51	–	–
1SWASPJ050602.87+122759.2	TYC 693-218-1	9.98	53.38	1.85	–	–	–	–	–	–	–	–
1SWASPJ050824.58+025329.9	2MASS J05082457+0253300	11.97	56.23	3.11	–	–	–	–	–	–	–	–
1SWASPJ051007.80-040955.6	HD 293856	9.79	51.62	1.38	54.78	0.90	–	–	–	–	–	–
1SWASPJ051023.20-071019.8	TYC 4763-851-1	10.08	62.25	1.70	58.76	1.42	–	–	–	–	–	–
1SWASPJ051235.14-050909.9	TYC 4759-318-1	9.87	51.82	3.26	–	–	–	–	–	–	–	–
1SWASPJ051630.19+330946.1	HD 34113	9.24	57.06	6.51	53.69	5.25	–	–	–	–	–	–
1SWASPJ051708.85-012446.6	HD 290169	10.22	67.07	3.73	66.96	2.25	63.53	1.77	63.73	1.29	63.25	1.23
1SWASPJ051755.70+123300.2	TYC 707-841-1	11.84	61.43	1.09	–	–	–	–	–	–	–	–
1SWASPJ051828.87-010430.8	HD 290235	10.03	54.28	3.20	57.49	1.59	52.93	1.11	53.13	0.89	–	–
1SWASPJ051945.60+274347.3	TYC 1855-226-1	10.71	69.86	3.60	73.67	2.81	65.93	2.62	73.49	1.46	69.75	1.38
1SWASPJ052000.76+043120.2	HD 242761	10.33	54.70	1.59	61.16	1.50	61.23	1.19	55.71	1.10	57.79	1.07
1SWASPJ052202.09-023614.9	HD 294001	10.02	58.67	1.28	57.44	1.00	–	–	–	–	–	–
1SWASPJ052247.21-045612.4	HD 294038	10.22	53.25	1.35	50.48	0.95	–	–	–	–	–	–
1SWASPJ052303.43-041550.8	HD 35221	10.24	57.72	4.59	53.98	2.47	–	–	–	–	–	–
1SWASPJ052511.65+013329.7	HD 287847	9.96	61.08	1.81	58.37	1.12	55.19	0.92	–	–	–	–
1SWASPJ052516.13+023141.2	HD 287819	10.09	58.42	1.77	–	–	–	–	–	–	–	–
1SWASPJ052531.12+025300.2	HD 287808	10.12	56.09	1.88	52.88	1.05	–	–	–	–	–	–
1SWASPJ052550.20-030041.6	HD 294060	10.08	52.99	1.84	–	–	–	–	–	–	–	–
1SWASPJ052553.84+154309.9	HD 243582	10.59	62.22	3.05	55.66	1.48	62.28	1.22	59.16	1.09	–	–
1SWASPJ052639.96-084536.1	TYC 5332-1721-1	10.31	53.65	1.25	–	–	–	–	–	–	–	–
1SWASPJ052650.32+000506.9	TYC 101-2278-1	11.87	52.40	2.53	–	–	–	–	–	–	–	–
1SWASPJ052712.15+000737.0	HD 290413	10.25	61.92	1.63	61.85	1.49	58.36	1.20	58.26	1.12	58.38	0.56
1SWASPJ052738.61-015801.8	HD 290469	9.87	56.04	2.94	53.77	1.12	–	–	–	–	–	–
1SWASPJ052741.57+035743.0	TYC 109-527-1	10.14	54.15	1.31	–	–	–	–	–	–	–	–
1SWASPJ052912.81+292705.3	TYC 1860-325-1	10.52	54.27	1.54	50.70	1.29	–	–	–	–	–	–
1SWASPJ052950.26-010208.9	HD 290521	10.16	53.47	0.88	–	–	–	–	–	–	–	–
1SWASPJ053117.83-485852.2	HD 274959	13.00	52.86	3.76	–	–	–	–	–	–	–	–
1SWASPJ053213.57+024240.7	HD 288005	9.92	53.13	2.85	–	–	–	–	–	–	–	–
1SWASPJ054539.66-305435.0	HD 38597	8.65	63.40	3.63	66.78	2.30	56.16	2.22	–	–	–	–
1SWASPJ054552.49-290531.7	HD 38629	8.92	57.11	2.66	53.09	2.55	–	–	–	–	–	–

Table C.1: *Continued*

WASP ID	Other ID	V	ν_1 (d^{-1})	A_1 (mmag)	ν_2 (d^{-1})	A_2 (mmag)	ν_3 (d^{-1})	A_3 (mmag)	ν_4 (d^{-1})	A_4 (mmag)	ν_5 (d^{-1})	A_5 (mmag)
1SWASPJ054618.89-291613.0	TYC 6502-907-1	11.59	51.62	0.93	53.67	0.79	51.62	0.77	–	–	–	–
1SWASPJ054658.22-290130.8	TYC 6502-788-1	11.10	54.42	2.49	51.24	2.20	–	–	–	–	–	–
1SWASPJ054910.64-240244.5	HD 39072	9.86	51.46	2.14	54.79	2.05	51.09	1.25	–	–	–	–
1SWASPJ055517.88-223230.9	TYC 6491-766-1	11.11	64.16	2.45	59.08	1.87	62.06	1.58	–	–	–	–
1SWASPJ055659.14-265008.7	TYC 6499-13-1	11.84	58.30	2.65	51.52	2.21	59.30	1.76	55.00	1.56	58.36	1.15
1SWASPJ060741.55-165222.9	HD 42005	9.54	50.73	1.27	–	–	–	–	–	–	–	–
1SWASPJ060828.93-431437.9	TYC 7623-1062-1	10.87	59.01	0.92	55.25	0.88	–	–	–	–	–	–
1SWASPJ060847.33+272024.7	TYC 1885-970-1	11.28	51.53	3.09	–	–	–	–	–	–	–	–
1SWASPJ060935.45-172651.2	HD 42370	9.49	54.10	7.26	–	–	–	–	–	–	–	–
1SWASPJ061025.71-273106.7	HD 42608	9.85	53.77	1.67	50.37	1.38	–	–	–	–	–	–
1SWASPJ061122.55-582124.7	TYC 8533-329-1	10.69	53.46	1.04	–	–	–	–	–	–	–	–
1SWASPJ061204.18-205439.0	TYC 5945-497-1	9.69	60.71	2.23	56.73	1.83	55.73	1.07	60.71	1.05	56.88	1.02
1SWASPJ061232.28-212953.7	HD 42915	9.03	59.58	0.79	51.10	0.74	57.18	0.67	57.48	0.63	52.26	0.52
1SWASPJ061341.56-232056.9	HD 43137	8.44	61.37	1.71	70.08	1.14	–	–	–	–	–	–
1SWASPJ061626.40-401229.1	TYC 7616-1344-1	11.46	62.84	2.86	59.26	2.17	62.84	1.00	59.54	0.81	57.60	0.69
1SWASPJ061837.06+302856.6	2MASS J06183700+3028566	12.86	61.04	12.94	56.28	11.24	56.28	4.65	52.47	4.38	–	–
1SWASPJ061849.25-630039.4	HD 44726	10.38	55.80	1.00	52.28	0.96	–	–	–	–	–	–
1SWASPJ061849.66-630038.8	HD 44726	10.38	55.80	0.99	52.28	0.95	–	–	–	–	–	–
1SWASPJ062039.55-471443.2	TYC 8106-1344-1	10.75	56.94	2.00	53.40	1.22	52.52	0.56	–	–	–	–
1SWASPJ062244.07+265226.6	TYC 1886-473-1	11.64	57.62	4.20	–	–	–	–	–	–	–	–
1SWASPJ062723.78-441012.2	HD 45795	8.52	52.58	1.13	–	–	–	–	–	–	–	–
1SWASPJ062733.49-490700.3	TYC 8111-2005-1	10.48	52.91	3.53	57.06	1.95	–	–	–	–	–	–
1SWASPJ062739.73-270214.5	TYC 6515-7-1	9.73	52.59	2.16	–	–	–	–	–	–	–	–
1SWASPJ062956.85+322446.9	HD 258048	10.52	169.54	1.49	–	–	–	–	–	–	–	–
1SWASPJ063122.24-680242.0	2MASS J06312224-6802417	12.87	54.17	2.88	–	–	–	–	–	–	–	–
1SWASPJ063210.76-473822.5	TYC 8107-1152-1	10.61	54.47	1.92	50.83	0.97	–	–	–	–	–	–
1SWASPJ063300.37-464211.7	TYC 8103-179-1	12.37	52.91	4.43	53.24	1.25	–	–	–	–	–	–
1SWASPJ063337.32-260937.5	TYC 6512-855-1	10.66	53.24	1.23	–	–	–	–	–	–	–	–
1SWASPJ063403.10+293906.6	TYC 1892-250-1	11.67	56.40	2.96	–	–	–	–	–	–	–	–
1SWASPJ063404.74-313821.8	TYC 7074-439-1	10.39	55.94	2.54	52.31	1.20	52.46	0.89	50.52	0.77	–	–
1SWASPJ063408.86-500732.8	TYC 8112-1557-1	10.45	53.05	0.97	–	–	–	–	–	–	–	–
1SWASPJ063502.56-272928.2	TYC 6516-300-1	12.69	53.48	1.47	52.26	1.45	–	–	–	–	–	–
1SWASPJ063809.50-422414.6	TYC 7622-559-1	11.25	53.39	1.01	–	–	–	–	–	–	–	–
1SWASPJ063859.75-170552.1	TYC 5952-2099-1	11.07	58.05	2.41	–	–	–	–	–	–	–	–
1SWASPJ064038.43-272729.1	TYC 6516-594-1	11.17	51.80	1.64	–	–	–	–	–	–	–	–
1SWASPJ064102.54+303941.8	TYC 2435-1127-1	10.64	60.48	1.36	–	–	–	–	–	–	–	–
1SWASPJ064113.79+370607.7	TYC 2447-217-1	9.78	52.05	2.31	–	–	–	–	–	–	–	–
1SWASPJ064141.75-363805.6	TYC 7099-1113-1	11.61	67.15	3.70	62.96	1.84	59.84	1.37	55.67	1.19	59.44	1.17
1SWASPJ064414.04-350739.3	TYC 7095-2233-1	12.13	55.41	2.39	54.06	2.14	53.00	1.91	51.49	1.82	50.64	1.72
1SWASPJ064416.60-210102.2	TYC 5961-1874-1	10.52	62.03	1.54	58.62	1.09	61.02	1.06	–	–	–	–
1SWASPJ064436.95-543845.6	2MASS J06443693-5438454	10.84	52.91	1.52	–	–	–	–	–	–	–	–
1SWASPJ064638.23-460154.7	TYC 8117-517-1	11.87	55.24	1.28	–	–	–	–	–	–	–	–
1SWASPJ064814.27-392832.2	HD 49776	10.16	51.62	1.88	55.11	1.81	55.31	1.11	52.47	0.66	55.76	0.50
1SWASPJ064920.15-313307.8	HD 49896	9.48	53.75	1.69	57.71	1.27	51.53	0.96	53.94	0.69	57.71	0.50
1SWASPJ065030.82-304523.3	TYC 7088-1747-1	11.83	54.25	1.68	57.33	1.12	–	–	–	–	–	–
1SWASPJ065142.17-632549.6	TYC 8912-1407-1	11.51	132.38	0.79	–	–	–	–	–	–	–	–
1SWASPJ065354.22-484249.0	TYC 8121-2354-1	11.24	53.67	1.18	50.26	0.68	–	–	–	–	–	–
1SWASPJ065430.75+153025.3	TYC 1331-1828-1	10.99	58.53	2.27	55.12	1.70	55.20	1.43	55.08	1.14	58.00	1.00
1SWASPJ065520.94-551542.4	TYC 8541-495-1	10.78	61.02	2.77	64.83	2.39	72.10	1.82	64.41	1.74	60.57	1.62
1SWASPJ065604.16+200817.3	HD 50929	9.50	50.89	0.56	–	–	–	–	–	–	–	–
1SWASPJ065616.29+201327.7	TYC 1352-337-1	11.22	53.12	1.40	–	–	–	–	–	–	–	–
1SWASPJ065912.27+123529.7	2MASS J06591227+1235297	11.94	64.34	2.65	64.51	2.09	60.54	1.80	68.32	1.76	64.46	1.65
1SWASPJ070056.34-510658.2	HD 53072	8.91	57.11	4.41	–	–	–	–	–	–	–	–
1SWASPJ070220.88+290657.1	HD 268031J	11.30	52.75	4.76	–	–	–	–	–	–	–	–
1SWASPJ070317.15+191937.8	TYC 1352-1496-1	10.30	52.21	0.83	51.18	0.62	–	–	–	–	–	–
1SWASPJ070354.65-423246.8	HD 53679	9.64	57.61	1.68	51.12	1.57	57.61	1.22	54.18	1.18	54.48	0.70
1SWASPJ071034.11+232149.6	TYC 1896-1611-1	9.74	59.17	2.00	55.81	1.27	–	–	–	–	–	–

Table C.1: *Continued*

WASP ID	Other ID	V	ν_1 (d^{-1})	A_1 (mmag)	ν_2 (d^{-1})	A_2 (mmag)	ν_3 (d^{-1})	A_3 (mmag)	ν_4 (d^{-1})	A_4 (mmag)	ν_5 (d^{-1})	A_5 (mmag)
1SWASPJ071221.10-532053.2	TYC 8550-1022-1	10.88	62.56	4.51	55.23	3.54	58.50	2.54	61.95	2.28	67.04	1.42
1SWASPJ071350.08+222135.0	TYC 1358-621-1	10.78	53.44	6.64	–	–	–	–	–	–	–	–
1SWASPJ071647.75+261319.6	2MASS J07164776+2613195	12.77	59.86	3.69	–	–	–	–	–	–	–	–
1SWASPJ071927.03+293639.2	TYC 1921-1403-1	10.03	54.73	3.25	–	–	–	–	–	–	–	–
1SWASPJ073716.10+015113.8	TYC 178-184-1	10.26	61.03	3.17	57.59	1.53	–	–	–	–	–	–
1SWASPJ074731.84+002001.8	TYC 180-956-1	9.64	59.48	3.56	52.22	2.48	55.50	2.47	62.99	1.43	55.07	1.20
1SWASPJ074803.78+002231.5	TYC 180-424-1	10.99	51.66	1.91	54.72	1.90	–	–	–	–	–	–
1SWASPJ075821.74+484948.2	TYC 3410-1564-1	11.05	54.48	2.97	52.19	1.78	–	–	–	–	–	–
1SWASPJ081944.97-072329.6	TYC 4860-524-1	11.80	51.61	2.46	51.81	1.67	–	–	–	–	–	–
1SWASPJ082137.35+273747.6	TYC 1936-940-1	11.45	51.58	1.86	–	–	–	–	–	–	–	–
1SWASPJ082147.91+114251.4	TYC 803-675-1	11.07	52.23	1.48	–	–	–	–	–	–	–	–
1SWASPJ082242.62+144506.9	2MASS J08224261+1445071	12.91	52.80	8.36	–	–	–	–	–	–	–	–
1SWASPJ082744.02+124142.8	TYC 804-1258-1	10.34	51.71	0.83	–	–	–	–	–	–	–	–
1SWASPJ082850.62+534738.7	HD 233534	8.74	65.54	3.75	61.86	1.76	51.07	1.52	54.38	1.23	–	–
1SWASPJ084407.29+155550.5	HD 74362	8.57	52.42	1.72	55.49	1.57	51.92	1.50	54.53	1.47	–	–
1SWASPJ085512.48-135413.7	TYC 5455-1367-1	12.07	52.64	3.35	–	–	–	–	–	–	–	–
1SWASPJ085522.22+324236.3	TYC 2488-1241-1	10.80	197.27	1.40	–	–	–	–	–	–	–	–
1SWASPJ090331.25-031457.6	2MASS J09033124-0314575	13.14	65.96	5.02	–	–	–	–	–	–	–	–
1SWASPJ090415.23-463259.5	HD 78022	10.22	60.47	1.28	54.06	1.02	–	–	–	–	–	–
1SWASPJ091025.79-034640.6	HD 78871	8.76	51.22	2.56	–	–	–	–	–	–	–	–
1SWASPJ091504.69-224324.8	2MASS J09150468-2243247	12.29	52.40	2.58	–	–	–	–	–	–	–	–
1SWASPJ091553.89-431053.7	2MASS J09155388-4310535	12.31	59.01	4.30	62.71	2.65	53.38	1.33	50.88	1.33	55.78	0.97
1SWASPJ092006.60-434608.6	TYC 7703-1083-1	10.98	55.44	2.50	51.74	1.67	53.13	1.01	–	–	–	–
1SWASPJ092108.28-161423.7	HD 80750	8.77	60.15	3.40	56.49	3.33	–	–	–	–	–	–
1SWASPJ093539.76-364421.7	TYC 7166-1251-1	11.71	58.92	2.28	61.59	2.14	56.04	1.32	64.84	1.18	–	–
1SWASPJ094120.24-282900.7	TYC 6614-168-1	11.21	52.32	3.62	–	–	–	–	–	–	–	–
1SWASPJ094216.53-204551.7	TYC 6055-79-1	11.25	57.36	4.18	56.27	1.30	54.23	1.30	51.10	1.21	51.34	1.07
1SWASPJ095807.27-430143.8	TYC 7702-793-1	11.77	54.52	3.40	61.78	2.13	–	–	–	–	–	–
1SWASPJ100012.21-401742.6	TYC 7711-2858-1	12.13	56.71	6.39	53.51	4.73	–	–	–	–	–	–
1SWASPJ100131.56-183222.3	HD 86929	8.67	54.76	1.56	–	–	–	–	–	–	–	–
1SWASPJ100817.98-363045.2	2MASS J10081797-3630453	13.56	51.36	5.40	–	–	–	–	–	–	–	–
1SWASPJ101326.10-431022.4	TYC 7720-75-1	12.18	58.31	4.00	55.07	2.80	–	–	–	–	–	–
1SWASPJ101534.28+071338.7	2MASS J10153426+0713385	12.37	54.34	3.65	60.97	2.39	57.53	2.31	54.28	1.65	–	–
1SWASPJ101638.30-023959.4	TYC 4907-995-1	10.81	57.14	3.09	57.06	2.32	57.14	2.02	53.76	1.68	53.88	1.37
1SWASPJ102214.40-405957.1	TYC 7713-1400-1	11.10	57.68	4.23	53.44	1.66	50.64	1.37	–	–	–	–
1SWASPJ102822.51-341738.4	HD 90780	9.22	60.23	3.49	60.23	2.73	56.40	1.32	60.43	0.80	56.70	0.66
1SWASPJ104007.53-443936.4	2MASS J10400748-4439363	13.00	61.28	4.91	–	–	–	–	–	–	–	–
1SWASPJ104916.57+055225.5	TYC 260-590-1	11.49	53.74	2.61	57.27	2.43	–	–	–	–	–	–
1SWASPJ105255.33-405130.3	TYC 7728-1009-1	10.71	50.46	1.28	–	–	–	–	–	–	–	–
1SWASPJ111053.91+170347.5	HD 97127	9.43	106.61	0.66	–	–	–	–	–	–	–	–
1SWASPJ112648.94-074731.1	HD 99506	8.38	50.05	2.11	–	–	–	–	–	–	–	–
1SWASPJ112825.74-394347.2	TYC 7743-154-1	12.02	50.53	1.37	–	–	–	–	–	–	–	–
1SWASPJ113630.35+151505.1	TYC 1438-815-1	9.94	51.89	1.14	–	–	–	–	–	–	–	–
1SWASPJ115253.12-381230.2	TYC 7742-1061-1	10.84	67.79	2.62	–	–	–	–	–	–	–	–
1SWASPJ120030.77+360856.7	TYC 2529-200-1	11.39	51.72	3.01	–	–	–	–	–	–	–	–
1SWASPJ120107.88+305842.6	HD 104366	9.28	57.41	1.31	–	–	–	–	–	–	–	–
1SWASPJ120225.12-364411.5	TYC 7243-1187-1	10.61	55.90	2.06	56.94	1.51	55.90	1.14	53.68	1.12	50.80	1.06
1SWASPJ121528.17-112441.3	HD 106563	10.55	58.58	1.48	65.46	1.29	–	–	–	–	–	–
1SWASPJ122400.98-491917.1	HD 107873	10.12	55.27	4.90	51.79	3.09	52.01	2.09	55.29	1.92	58.56	1.77
1SWASPJ122554.30-291922.2	TYC 6694-288-1	11.20	61.86	1.50	55.43	1.27	58.35	1.21	58.46	1.06	52.46	1.01
1SWASPJ122732.77+111648.6	HD 108452	10.80	70.76	4.50	–	–	–	–	–	–	–	–
1SWASPJ124642.89+000728.9	TYC 290-976-1	10.93	52.23	2.76	55.44	1.96	55.65	1.12	–	–	–	–
1SWASPJ125056.15+053212.9	TYC 297-328-1	11.25	68.99	4.30	76.99	3.62	–	–	–	–	–	–
1SWASPJ125300.39-102014.3	TYC 5538-287-1	10.60	51.63	1.39	–	–	–	–	–	–	–	–
1SWASPJ131559.92-360604.6	TYC 7275-591-1	12.58	49.98	5.21	–	–	–	–	–	–	–	–
1SWASPJ133636.96-413248.6	TYC 7796-1693-1	12.02	56.59	3.39	56.75	2.56	55.00	2.25	–	–	–	–
1SWASPJ133638.85-443948.6	TYC 7800-811-1	11.09	52.77	2.15	–	–	–	–	–	–	–	–

Table C.1: *Continued*

WASP ID	Other ID	V	ν_1 (d^{-1})	A_1 (mmag)	ν_2 (d^{-1})	A_2 (mmag)	ν_3 (d^{-1})	A_3 (mmag)	ν_4 (d^{-1})	A_4 (mmag)	ν_5 (d^{-1})	A_5 (mmag)
1SWASPJ134540.12-382652.7	TYC 7789-1580-1	11.51	50.85	1.46	–	–	–	–	–	–	–	–
1SWASPJ140011.39-325611.1	HD 122056	10.25	61.52	2.73	50.84	1.65	58.56	1.45	60.13	1.44	57.15	1.38
1SWASPJ140057.83-153409.0	2MASS J14005780-1534088	12.31	51.62	6.03	–	–	–	–	–	–	–	–
1SWASPJ140341.51-405108.9	HD 122570	10.41	99.12	1.27	87.53	1.19	91.56	0.79	95.23	0.57	–	–
1SWASPJ141738.71-354648.9	TYC 7294-1010-1	10.40	59.72	3.05	–	–	–	–	–	–	–	–
1SWASPJ142301.56+271218.8	TYC 2011-370-1	10.32	50.61	1.34	–	–	–	–	–	–	–	–
1SWASPJ142736.57+264440.8	TYC 2011-269-1	10.11	54.44	2.16	51.02	1.44	–	–	–	–	–	–
1SWASPJ143049.64+314755.1	TYC 2553-480-1	11.56	235.54	1.06	–	–	–	–	–	–	–	–
1SWASPJ143533.94-442659.1	HD 127954	9.43	51.26	1.53	–	–	–	–	–	–	–	–
1SWASPJ143828.85-222444.4	TYC 6165-1005-1	11.87	55.78	4.91	–	–	–	–	–	–	–	–
1SWASPJ144252.26-281517.6	HD 129361	10.66	54.64	6.72	51.66	2.74	54.73	2.32	52.74	2.21	50.77	1.56
1SWASPJ144435.98-212827.4	HD 129702	10.58	57.08	2.43	53.66	1.76	56.49	1.52	56.51	1.22	–	–
1SWASPJ144902.32+065829.1	TYC 332-1080-1	11.48	63.45	1.52	58.69	1.42	60.15	1.22	56.09	1.20	51.34	0.87
1SWASPJ145752.81-342118.0	TYC 7306-712-1	11.74	53.78	5.57	–	–	–	–	–	–	–	–
1SWASPJ150614.44-205836.6	TYC 6181-423-1	11.52	52.52	3.60	–	–	–	–	–	–	–	–
1SWASPJ150658.93-313838.9	HD 133729	9.17	88.97	6.39	88.93	1.86	89.02	1.83	–	–	–	–
1SWASPJ151036.10+064309.1	HD 134609	9.97	60.27	3.89	53.27	3.07	60.29	1.67	60.31	1.20	63.79	1.16
1SWASPJ151415.78-250133.2	TYC 6766-1620-1	10.92	63.41	4.40	–	–	–	–	–	–	–	–
1SWASPJ151906.66-183048.6	2MASS J15190666-1830483	12.23	51.90	3.50	–	–	–	–	–	–	–	–
1SWASPJ152012.80+250418.9	2MASS J15201277+2504190	12.17	54.20	2.77	51.75	1.65	54.47	1.62	–	–	–	–
1SWASPJ153633.39+271029.2	HD 139325	9.810	54.87	6.88	–	–	–	–	–	–	–	–
1SWASPJ154132.21-375216.8	2MASS J15413220-3752172	11.96	50.76	1.64	–	–	–	–	–	–	–	–
1SWASPJ154403.57+304555.9	TYC 2571-1615-1	11.43	54.62	2.52	51.40	1.71	57.67	1.24	–	–	–	–
1SWASPJ154953.44-225041.6	TYC 6778-95-2	11.91	62.60	7.08	57.01	3.13	59.49	2.49	59.37	1.41	–	–
1SWASPJ155259.17+062022.8	TYC 365-1205-1	11.55	52.63	3.15	52.23	1.77	52.64	1.29	–	–	–	–
1SWASPJ160259.11-231004.6	HD 143746	10.42	53.28	1.50	52.86	1.43	–	–	–	–	–	–
1SWASPJ160409.89-095705.5	TYC 5615-441-1	10.33	50.87	1.15	–	–	–	–	–	–	–	–
1SWASPJ160439.18-135423.9	2MASS J16043916-1354237	13.39	52.11	11.65	68.14	8.71	55.88	5.61	51.11	5.02	85.18	4.78
1SWASPJ160803.69+070428.9	V338 Ser[a]	12.84	179.35	44.94	181.65	12.39	236.99	11.97	181.72	9.13	237.99	8.46
1SWASPJ161601.73-330505.2	TYC 7347-1324-1	10.86	61.60	2.95	62.01	1.88	65.70	1.81	–	–	–	–
1SWASPJ161658.12-242307.1	TYC 6797-669-1	11.47	66.96	2.78	67.32	1.73	–	–	–	–	–	–
1SWASPJ162524.10-214118.6	HD 147911	9.17	68.52	6.37	72.29	3.54	64.71	2.58	60.97	2.42	64.49	2.33
1SWASPJ163145.35-154857.9	2MASS J16314535-1548582	11.56	54.17	1.16	–	–	–	–	–	–	–	–
1SWASPJ163810.08+510350.3	TYC 3505-1909-1	11.93	59.15	3.00	59.15	2.05	55.76	1.57	–	–	–	–
1SWASPJ164002.99-073729.7	2MASS J16400299-0737293	12.67	151.93	3.52	–	–	–	–	–	–	–	–
1SWASPJ164551.30+254413.2	TYC 2062-209-1	11.28	53.70	2.16	50.48	1.04	–	–	–	–	–	–
1SWASPJ164836.99+251548.6	TYC 2062-1188-1	9.98	105.12	0.60	–	–	–	–	–	–	–	–
1SWASPJ165956.36+371011.9	TYC 2602-589-1	12.77	55.83	3.06	52.59	2.52	–	–	–	–	–	–
1SWASPJ171158.90+394011.2	TYC 3077-1500-1	12.76	55.96	1.79	53.46	1.24	–	–	–	–	–	–
1SWASPJ171303.98+355842.9	HIP 84233	11.48	54.50	7.60	56.78	7.54	59.05	6.98	61.32	5.57	52.23	5.50
1SWASPJ173235.45+100200.2	TYC 996-1340-1	10.46	66.86	4.94	66.83	3.52	69.41	2.34	63.00	1.98	68.32	1.80
1SWASPJ175133.94+434030.6	HD 162935	9.09	52.22	2.44	–	–	–	–	–	–	–	–
1SWASPJ175726.48+322523.7	TYC 2612-1843-1	11.58	63.71	2.46	60.50	1.87	62.64	1.65	57.12	1.04	56.04	0.87
1SWASPJ175844.20+345833.9	2MASS J17584421+3458339	12.74	71.28	2.49	–	–	–	–	–	–	–	–
1SWASPJ175848.89+411507.3	TYC 3097-914-1	11.75	52.54	3.26	–	–	–	–	–	–	–	–
1SWASPJ180158.09+304716.6	TYC 2621-2108-1	11.16	55.91	2.00	52.76	1.14	55.70	0.93	54.00	0.92	56.08	0.79
1SWASPJ180158.16+304714.8	TYC 2621-2108-2	11.57	55.91	1.99	52.76	1.28	54.00	0.99	55.70	0.98	56.08	0.62
1SWASPJ180842.96+390351.8	HD 166410	8.41	54.85	2.06	54.85	1.96	52.39	1.23	50.39	0.52	55.07	0.51
1SWASPJ181101.73+193146.9	HD 348025	9.94	52.66	1.29	–	–	–	–	–	–	–	–
1SWASPJ181947.42+421038.2	TYC 3111-438-1	11.67	55.79	2.42	–	–	–	–	–	–	–	–
1SWASPJ183230.78+503702.3	TYC 3534-2362-1	9.97	70.62	4.56	63.19	2.35	66.84	2.10	66.99	1.50	55.90	1.40
1SWASPJ183432.98+404426.9	TYC 3109-497-1	11.67	55.57	3.06	52.08	2.19	–	–	–	–	–	–
1SWASPJ184412.27+431751.9	TYC 3130-2480-1	11.25	180.73	0.93	–	–	–	–	–	–	–	–
1SWASPJ185011.33+485122.8	2MASS J18501133+4851229	13.17	64.44	3.27	–	–	–	–	–	–	–	–
1SWASPJ190150.41-363952.7	HD 176423	9.05	60.20	3.49	56.31	2.23	–	–	–	–	–	–
1SWASPJ190206.79-362141.8	HD 176497	8.35	55.79	2.51	52.55	1.68	–	–	–	–	–	–
1SWASPJ190858.19+430538.9	HD 179010	9.29	52.25	1.45	–	–	–	–	–	–	–	–

Table C.1: *Continued*

WASP ID	Other ID	V	ν_1 (d^{-1})	A_1 (mmag)	ν_2 (d^{-1})	A_2 (mmag)	ν_3 (d^{-1})	A_3 (mmag)	ν_4 (d^{-1})	A_4 (mmag)	ν_5 (d^{-1})	A_5 (mmag)
1SWASPJ191109.74+551220.8	HD 179836	8.96	60.22	1.80	62.06	1.74	58.71	1.59	58.74	1.14	62.11	1.08
1SWASPJ191733.41-424207.2	TYC 7926-99-1	11.18	164.48	1.85	53.13	0.81	–	–	–	–	–	–
1SWASPJ192128.83+471053.4	TYC 3547-2692-1	12.16	128.76	1.53	–	–	–	–	–	–	–	–
1SWASPJ192152.96-310843.7	TYC 7424-1424-1	10.77	55.31	2.01	51.73	1.70	–	–	–	–	–	–
1SWASPJ192355.82+394636.8	TYC 3138-1852-1	11.16	51.90	1.42	–	–	–	–	–	–	–	–
1SWASPJ192403.18-350929.7	TYC 7432-1684-1	11.26	57.72	1.62	–	–	–	–	–	–	–	–
1SWASPJ192616.74+620507.8	2MASS J19261675+6205078	12.17	56.15	3.01	58.16	2.76	–	–	–	–	–	–
1SWASPJ193137.99+482633.0	HD 184333	8.76	59.97	1.73	59.97	1.22	56.86	1.11	60.13	0.84	53.12	0.63
1SWASPJ193152.60-323453.8	TYC 7429-489-1	11.19	55.35	2.44	51.86	1.63	–	–	–	–	–	–
1SWASPJ193832.48+560944.6	2MASS J19383247+5609446	13.17	231.62	3.88	–	–	–	–	–	–	–	–
1SWASPJ194007.81-442009.2	2MASS J19400781-4420093	13.02	176.39	4.16	–	–	–	–	–	–	–	–
1SWASPJ194030.54-422807.7	HD 185370	9.49	53.16	1.56	–	–	–	–	–	–	–	–
1SWASPJ194233.80+591846.9	2MASS J19423382+5918468	12.99	59.89	3.19	–	–	–	–	–	–	–	–
1SWASPJ195127.55-644624.5	2MASS J19512756-6446247	13.18	58.43	4.29	–	–	–	–	–	–	–	–
1SWASPJ195738.44-213015.3	TYC 6325-1797-1	12.26	53.19	6.47	–	–	–	–	–	–	–	–
1SWASPJ195912.66+504548.6	TYC 3570-437-1	12.77	57.81	3.22	–	–	–	–	–	–	–	–
1SWASPJ200006.72+460730.4	TYC 3558-1238-1	10.90	52.13	1.79	–	–	–	–	–	–	–	–
1SWASPJ201051.13+615608.4	TYC 4236-114-1	10.06	52.14	1.18	–	–	–	–	–	–	–	–
1SWASPJ201124.78+461727.5	HD 192119	10.03	52.64	7.31	52.39	3.52	52.67	0.93	–	–	–	–
1SWASPJ201246.78-362024.3	HD 191714	9.57	52.03	3.27	52.09	2.22	–	–	–	–	–	–
1SWASPJ202236.50-701100.2	TYC 9311-73-1	12.77	62.54	3.30	59.15	2.11	–	–	–	–	–	–
1SWASPJ202409.06-543235.0	HD 193677	7.60	53.85	6.07	50.58	5.46	–	–	–	–	–	–
1SWASPJ202642.62-115245.1	TYC 5762-828-1	11.80	212.66	1.62	–	–	–	–	–	–	–	–
1SWASPJ202933.21-181312.2	HD 195061	9.91	59.91	2.20	56.17	1.85	56.04	1.19	52.60	1.18	56.13	1.14
1SWASPJ203649.57+052925.8	TYC 518-927-1	11.14	51.70	1.46	–	–	–	–	–	–	–	–
1SWASPJ203842.13+421502.5	TYC 3161-804-1	10.14	57.59	2.15	51.71	1.95	54.66	1.60	–	–	–	–
1SWASPJ204038.40-174858.1	TYC 6335-1015-1	11.41	51.91	1.95	–	–	–	–	–	–	–	–
1SWASPJ204129.07-470809.3	TYC 8411-485-1	11.30	50.80	2.14	–	–	–	–	–	–	–	–
1SWASPJ204239.56-024839.1	TYC 5181-584-1	10.80	61.03	3.68	57.58	3.39	53.83	2.79	61.02	2.58	57.58	2.57
1SWASPJ204931.81+083109.4	HD 198368	9.15	52.96	2.31	58.70	2.10	55.22	2.09	57.84	1.74	58.38	1.40
1SWASPJ204945.42+523705.9	TYC 3951-423-1	9.96	57.22	5.46	53.53	2.29	53.69	0.97	–	–	–	–
1SWASPJ205140.83+052908.4	TYC 520-29-1	10.78	53.31	4.04	–	–	–	–	–	–	–	–
1SWASPJ205156.68+155137.8	TYC 1647-1944-1	10.35	77.12	1.32	76.26	1.31	73.21	1.22	73.08	1.15	68.50	0.89
1SWASPJ205235.68+194358.7	HD 353161	11.21	64.75	3.45	61.07	2.60	64.70	1.54	61.59	1.40	58.02	1.35
1SWASPJ205237.54-060917.3	TYC 5191-864-1	12.43	53.79	2.01	–	–	–	–	–	–	–	–
1SWASPJ205419.83+071311.0	TYC 525-2319-1	9.94	104.86	0.80	100.44	0.34	–	–	–	–	–	–
1SWASPJ205746.10-480332.4	HD 199247	9.73	53.67	1.26	50.24	1.07	51.46	0.75	58.26	0.59	52.72	0.42
1SWASPJ205955.23+164644.0	HD 199958	9.97	52.66	0.75	–	–	–	–	–	–	–	–
1SWASPJ210222.85+131242.7	TYC 1115-1317-1	12.07	57.86	3.11	53.32	3.02	57.14	2.05	55.87	1.82	50.93	1.58
1SWASPJ210239.86-081834.6	HD 200257	10.06	54.55	1.54	52.06	1.16	51.36	0.98	51.24	0.78	54.67	0.74
1SWASPJ210301.76+555957.2	HD 239551	9.90	52.60	2.38	–	–	–	–	–	–	–	–
1SWASPJ210704.81-355211.3	HD 200835	8.39	54.40	3.36	55.34	3.04	58.54	2.51	50.90	2.09	51.85	1.53
1SWASPJ210829.78-043934.9	TYC 5201-1009-1	10.40	51.71	1.36	57.72	0.35	–	–	–	–	–	–
1SWASPJ211116.86+163609.9	HD 201763	9.32	52.45	0.69	60.37	0.30	–	–	–	–	–	–
1SWASPJ211719.93+372244.9	TYC 2714-142-1	11.92	64.07	3.84	60.44	3.78	–	–	–	–	–	–
1SWASPJ212101.11+505359.7	TYC 3601-63-1	11.13	56.91	2.06	–	–	–	–	–	–	–	–
1SWASPJ212126.52-540434.2	2MASS J21212652-5404346	13.70	58.24	6.49	51.77	6.39	64.71	6.38	71.18	5.42	77.66	3.48
1SWASPJ212527.65+513209.4	TYC 3602-357-1	9.61	52.46	1.87	–	–	–	–	–	–	–	–
1SWASPJ212719.56+502017.0	TYC 3598-552-1	10.53	57.57	1.60	57.56	1.44	53.85	1.40	–	–	–	–
1SWASPJ213432.52-174847.9	HD 205263	9.86	52.27	0.82	–	–	–	–	–	–	–	–
1SWASPJ213704.68+333103.1	TYC 2721-1209-1	10.54	50.92	1.11	53.33	1.08	–	–	–	–	–	–
1SWASPJ213734.11+060505.9	2MASS J21373410+0605056	13.99	54.39	9.38	59.73	6.97	–	–	–	–	–	–
1SWASPJ214007.55+500921.4	TYC 3599-700-1	10.23	51.88	2.52	–	–	–	–	–	–	–	–
1SWASPJ214304.74-214046.5	HD 206516	11.05	53.73	2.22	51.36	1.37	50.51	1.19	53.73	1.17	50.68	0.80
1SWASPJ214305.66+103003.8	HD 206619	9.40	53.64	1.45	53.81	1.03	–	–	–	–	–	–
1SWASPJ214345.18+502055.9	TYC 3599-373-1	9.97	61.35	2.95	57.96	1.80	54.01	1.37	57.70	1.33	54.42	1.26
1SWASPJ214516.98+203420.9	TYC 1674-319-1	11.44	52.98	2.85	–	–	–	–	–	–	–	–
1SWASPJ215531.26+084917.0	2MASS J21553126+0849170	13.53	61.34	6.38	–	–	–	–	–	–	–	–

Table C.1: *Continued*

WASP ID	Other ID	V	ν_1 (d^{-1})	A_1 (mmag)	ν_2 (d^{-1})	A_2 (mmag)	ν_3 (d^{-1})	A_3 (mmag)	ν_4 (d^{-1})	A_4 (mmag)	ν_5 (d^{-1})	A_5 (mmag)
1SWASPJ215936.17-612527.3	2MASS J21593617-6125274	13.98	54.91	6.58	53.12	6.43	–	–	–	–	–	–
1SWASPJ220002.90-053445.5	TYC 5230-895-1	10.40	50.86	1.23	–	–	–	–	–	–	–	–
1SWASPJ220055.19+362926.7	TYC 2731-2421-1	9.44	54.82	1.00	51.63	0.97	–	–	–	–	–	–
1SWASPJ220500.06+211923.4	TYC 1692-471-1	11.79	51.83	2.37	–	–	–	–	–	–	–	–
1SWASPJ221421.53-043352.0	TYC 5228-565-1	10.41	51.09	0.78	–	–	–	–	–	–	–	–
1SWASPJ221702.86+241636.9	2MASS J22170288+2416368	12.96	61.33	3.82	–	–	–	–	–	–	–	–
1SWASPJ221755.37-082103.7	FO Aqr	12.70	68.88	104.78	58.98	35.87	63.93	28.21	68.88	19.76	73.83	15.57
1SWASPJ222014.72+275412.2	TYC 2226-2039-1	12.16	65.60	1.94	–	–	–	–	–	–	–	–
1SWASPJ222030.83+050516.5	TYC 566-1496-1	11.51	57.77	13.32	54.40	9.85	52.13	2.82	–	–	–	–
1SWASPJ222145.75+291823.6	TYC 2230-451-1	11.03	53.19	1.14	–	–	–	–	–	–	–	–
1SWASPJ222614.22+422701.5	TYC 3208-705-1	10.78	60.54	1.52	59.82	1.51	64.26	1.45	52.97	1.25	56.00	1.24
1SWASPJ222839.47-404202.8	HD 212954	10.18	53.44	1.38	53.44	0.89	52.98	0.73	–	–	–	–
1SWASPJ223248.22+384350.8	HIP 111298	10.80	53.31	1.35	63.17	1.14	56.43	0.85	63.22	0.79	60.00	0.79
1SWASPJ223445.16+375006.1	TYC 3201-1333-1	10.82	68.39	1.08	60.98	1.01	65.65	0.82	64.39	0.60	59.47	0.60
1SWASPJ223649.70+383714.3	TYC 3201-922-1	10.69	58.45	1.64	51.44	1.13	–	–	–	–	–	–
1SWASPJ224154.21+403039.1	TYC 3218-888-2	11.45	75.54	3.32	68.80	2.61	–	–	–	–	–	–
1SWASPJ225434.21+005246.3	TYC 569-353-1	12.74	52.59	5.06	–	–	–	–	–	–	–	–
1SWASPJ225451.98+204752.4	TYC 1710-406-1	10.76	56.19	3.78	–	–	–	–	–	–	–	–
1SWASPJ225517.99-031039.6	AO Psc[b]	13.20	100.62	19.89	107.31	13.60	93.94	9.06	106.11	4.18	107.07	4.12
1SWASPJ225520.44-183635.3	TYC 6390-339-1	11.95	66.96	2.68	63.14	1.90	60.40	1.55	63.19	1.32	59.95	1.32
1SWASPJ225817.77+374758.3	2MASS J22581778+3747582	12.86	50.68	3.77	–	–	–	–	–	–	–	–
1SWASPJ230545.31-671903.0	TYC 9131-119-1	11.43	101.68	1.67	92.75	1.61	–	–	–	–	–	–
1SWASPJ230751.90+500653.3	TYC 3631-579-1	10.51	59.07	1.85	–	–	–	–	–	–	–	–
1SWASPJ231326.32+022749.5	TYC 577-322-1	10.72	60.42	5.97	57.34	2.75	–	–	–	–	–	–
1SWASPJ231521.48+290501.4	TYC 2248-1751-1[a]	12.30	242.57	37.64	242.57	12.54	243.93	12.20	243.93	11.66	244.07	10.63
1SWASPJ231824.68+125440.8	TYC 1167-1562-1	10.43	73.36	2.77	–	–	–	–	–	–	–	–
1SWASPJ231833.49+430514.4	2MASS J23183349+4305144	13.42	50.60	4.25	–	–	–	–	–	–	–	–
1SWASPJ231848.87+330427.9	TYC 2756-79-1	11.64	59.78	5.03	55.95	3.07	52.36	1.92	–	–	–	–
1SWASPJ232313.78+515429.5	TYC 3648-524-1	9.94	54.28	3.43	57.44	1.76	–	–	–	–	–	–
1SWASPJ232340.64+511432.0	TYC 3648-1915-1	10.60	76.36	2.89	73.52	2.03	72.44	1.95	72.33	1.27	76.06	1.27
1SWASPJ232623.51-320300.4	TYC 7514-113-1	10.88	57.13	1.67	–	–	–	–	–	–	–	–
1SWASPJ232819.07+384549.0	HD 221025	8.73	57.81	2.62	–	–	–	–	–	–	–	–
1SWASPJ232847.63+051454.3	ZZ Psc[a]	13.03	104.65	9.45	104.63	8.47	96.05	7.55	96.03	7.45	95.99	6.72
1SWASPJ232850.88+444559.5	TYC 3242-1028-1	10.03	52.24	4.18	–	–	–	–	–	–	–	–
1SWASPJ232935.93+102209.3	2MASS J23293590+1022092	12.00	62.38	2.59	–	–	–	–	–	–	–	–
1SWASPJ233023.01-233425.8	2MASS J23302304-2334260	11.74	57.66	4.25	54.71	2.54	57.72	1.73	51.75	1.37	50.81	1.17
1SWASPJ233650.22+475142.5	TYC 3641-62-1	9.62	54.06	2.20	–	–	–	–	–	–	–	–
1SWASPJ233722.45+233540.5	HD 222066	8.96	62.15	4.35	58.13	2.77	54.41	2.29	65.89	1.92	65.93	1.60
1SWASPJ234057.11+511909.0	TYC 3650-1404-1	10.20	54.86	3.38	51.48	1.52	–	–	–	–	–	–
1SWASPJ234341.76+435459.5	TYC 3244-980-1	11.89	56.97	12.38	53.74	3.08	–	–	–	–	–	–
1SWASPJ234354.44-281834.1	2MASS J23435445-2818344	13.56	53.44	10.27	80.16	3.70	–	–	–	–	–	–
1SWASPJ234422.01-342700.3	HIP 117100[c]	11.00	223.16	1.42	–	–	–	–	–	–	–	–
1SWASPJ234554.44-393208.2	2MASS J23455445-3932085	13.60	60.47	20.33	53.63	18.28	63.69	9.72	–	–	–	–
1SWASPJ235451.54-155922.0	2MASS J23545155-1559218	12.10	57.25	5.11	53.72	2.67	–	–	–	–	–	–

[a] Known sdBV pulsators
[b] Known intermediate polar
[c] Known sdBV star, not known to vary

D Tables from Chapter 7

Table D.1: A linear least-squares fit of the quintuplet. For each Quarter, t_0 has been chosen to force the first sidelobes to have equal phase.

Quarter	ID	Frequency (d^{-1})	Amplitude (μmag)	Phase (rad)	Quarter	ID	Frequency (d^{-1})	Amplitude (μmag)	Phase (rad)
	$\nu - 2\nu_{\rm rot}$	181.6431	19.741 ± 2.485	1.659 ± 0.126		$\nu - 2\nu_{\rm rot}$	181.6312	14.139 ± 1.607	-2.986 ± 0.114
	$\nu - \nu_{\rm rot}$	181.6910	40.390 ± 2.537	-1.269 ± 0.063		$\nu - \nu_{\rm rot}$	181.6792	37.914 ± 1.616	-2.887 ± 0.043
Q01	ν	181.7390	123.843 ± 2.544	2.259 ± 0.021	Q05	ν	181.7272	117.505 ± 1.612	-2.419 ± 0.014
	$\nu + \nu_{\rm rot}$	181.7870	36.489 ± 2.538	-1.342 ± 0.069		$\nu + \nu_{\rm rot}$	181.7752	36.364 ± 1.615	-2.907 ± 0.044
	$\nu + 2\nu_{\rm rot}$	181.8349	11.999 ± 2.487	2.168 ± 0.207		$\nu + 2\nu_{\rm rot}$	181.8231	13.575 ± 1.607	-2.596 ± 0.119
	$\nu - 2\nu_{\rm rot}$	181.6377	12.892 ± 1.812	-1.570 ± 0.141		$\nu - 2\nu_{\rm rot}$	181.6312	9.305 ± 1.850	-3.064 ± 0.199
	$\nu - \nu_{\rm rot}$	181.6868	36.330 ± 1.818	-1.688 ± 0.050		$\nu - \nu_{\rm rot}$	181.6802	36.056 ± 1.854	-2.765 ± 0.051
Q02	ν	181.7358	117.870 ± 1.817	-1.040 ± 0.015	Q06	ν	181.7292	113.495 ± 1.854	-2.212 ± 0.016
	$\nu + \nu_{\rm rot}$	181.7849	44.590 ± 1.818	-1.666 ± 0.041		$\nu + \nu_{\rm rot}$	181.7782	41.683 ± 1.854	-2.762 ± 0.044
	$\nu + 2\nu_{\rm rot}$	181.8339	14.600 ± 1.812	-1.425 ± 0.124		$\nu + 2\nu_{\rm rot}$	181.8272	11.886 ± 1.850	-2.326 ± 0.157
	$\nu - 2\nu_{\rm rot}$	181.6337	14.135 ± 1.520	2.753 ± 0.108		$\nu - 2\nu_{\rm rot}$	181.6301	14.240 ± 1.695	-0.707 ± 0.119
	$\nu - \nu_{\rm rot}$	181.6826	38.813 ± 1.519	-0.438 ± 0.039		$\nu - \nu_{\rm rot}$	181.6788	38.421 ± 1.697	-0.800 ± 0.044
Q03	ν	181.7316	122.950 ± 1.524	-3.075 ± 0.012	Q07	ν	181.7276	113.775 ± 1.699	-0.224 ± 0.015
	$\nu + \nu_{\rm rot}$	181.7805	43.710 ± 1.523	-0.432 ± 0.035		$\nu + \nu_{\rm rot}$	181.7763	38.983 ± 1.697	-0.804 ± 0.044
	$\nu + 2\nu_{\rm rot}$	181.8295	15.899 ± 1.520	2.878 ± 0.096		$\nu + 2\nu_{\rm rot}$	181.8251	10.953 ± 1.696	-0.516 ± 0.155
	$\nu - 2\nu_{\rm rot}$	181.6353	15.271 ± 1.533	-2.772 ± 0.100		$\nu - 2\nu_{\rm rot}$	181.6291	14.525 ± 1.796	0.428 ± 0.124
	$\nu - \nu_{\rm rot}$	181.6846	39.188 ± 1.536	0.172 ± 0.039		$\nu - \nu_{\rm rot}$	181.6777	34.324 ± 1.797	0.455 ± 0.053
Q04	ν	181.7339	123.790 ± 1.534	-2.447 ± 0.012	Q08	ν	181.7263	116.102 ± 1.803	0.998 ± 0.016
	$\nu + \nu_{\rm rot}$	181.7832	45.875 ± 1.537	0.180 ± 0.033		$\nu + \nu_{\rm rot}$	181.7749	37.724 ± 1.799	0.459 ± 0.048
	$\nu + 2\nu_{\rm rot}$	181.8324	17.410 ± 1.532	-2.740 ± 0.088		$\nu + 2\nu_{\rm rot}$	181.8235	13.191 ± 1.797	0.657 ± 0.136

Table D.1: *Continued.*

Quarter	ID	Frequency (d^{-1})	Amplitude (μmag)	Phase (rad)	Quarter	ID	Frequency (d^{-1})	Amplitude (μmag)	Phase (rad)
	$\nu - 2\nu_{\rm rot}$	181.6230	12.911 ± 1.581	1.770 ± 0.123		$\nu - 2\nu_{\rm rot}$	181.6369	17.362 ± 2.279	-0.798 ± 0.131
	$\nu - \nu_{\rm rot}$	181.6711	36.045 ± 1.588	1.652 ± 0.044		$\nu - \nu_{\rm rot}$	181.6850	41.355 ± 2.298	-0.933 ± 0.056
Q09	ν	181.7191	112.235 ± 1.585	2.196 ± 0.014	Q14	ν	181.7331	115.532 ± 2.306	-0.366 ± 0.020
	$\nu + \nu_{\rm rot}$	181.7672	40.729 ± 1.587	1.635 ± 0.039		$\nu + \nu_{\rm rot}$	181.7812	41.746 ± 2.297	-0.940 ± 0.055
	$\nu + 2\nu_{\rm rot}$	181.8153	11.504 ± 1.586	1.822 ± 0.137		$\nu + 2\nu_{\rm rot}$	181.8292	15.442 ± 2.279	-1.038 ± 0.148
	$\nu - 2\nu_{\rm rot}$	181.6268	14.607 ± 1.669	0.685 ± 0.114		$\nu - 2\nu_{\rm rot}$	181.6331	16.573 ± 1.595	-1.985 ± 0.096
	$\nu - \nu_{\rm rot}$	181.6758	38.438 ± 1.672	0.520 ± 0.044		$\nu - \nu_{\rm rot}$	181.6821	35.849 ± 1.601	-2.145 ± 0.045
Q10	ν	181.7247	113.928 ± 1.672	1.055 ± 0.015	Q15	ν	181.7311	123.619 ± 1.604	-1.627 ± 0.013
	$\nu + \nu_{\rm rot}$	181.7737	35.002 ± 1.672	0.534 ± 0.048		$\nu + \nu_{\rm rot}$	181.7802	43.531 ± 1.600	-2.152 ± 0.037
	$\nu + 2\nu_{\rm rot}$	181.8226	15.010 ± 1.669	0.674 ± 0.111		$\nu + 2\nu_{\rm rot}$	181.8292	13.050 ± 1.594	-1.965 ± 0.122
	$\nu - 2\nu_{\rm rot}$	181.6310	16.549 ± 1.558	2.799 ± 0.094		$\nu - 2\nu_{\rm rot}$	181.6383	18.673 ± 1.696	-2.639 ± 0.091
	$\nu - \nu_{\rm rot}$	181.6800	42.547 ± 1.559	-0.515 ± 0.037		$\nu - \nu_{\rm rot}$	181.6871	40.539 ± 1.717	0.308 ± 0.042
Q11	ν	181.7290	115.728 ± 1.561	-3.072 ± 0.014	Q16	ν	181.7359	121.373 ± 1.713	-2.267 ± 0.014
	$\nu + \nu_{\rm rot}$	181.7781	40.892 ± 1.560	-0.497 ± 0.038		$\nu + \nu_{\rm rot}$	181.7846	42.846 ± 1.716	0.309 ± 0.040
	$\nu + 2\nu_{\rm rot}$	181.8271	9.240 ± 1.559	2.828 ± 0.169		$\nu + 2\nu_{\rm rot}$	181.8334	11.927 ± 1.697	-2.482 ± 0.142
	$\nu - 2\nu_{\rm rot}$	181.6344	15.754 ± 1.747	-1.083 ± 0.111		$\nu - 2\nu_{\rm rot}$	181.6403	15.675 ± 2.683	1.605 ± 0.171
	$\nu - \nu_{\rm rot}$	181.6838	40.520 ± 1.746	-0.949 ± 0.043		$\nu - \nu_{\rm rot}$	181.6880	40.562 ± 2.694	-1.123 ± 0.067
Q12	ν	181.7332	121.494 ± 1.748	-0.416 ± 0.014	Q17	ν	181.7357	126.786 ± 2.709	2.686 ± 0.021
	$\nu + \nu_{\rm rot}$	181.7826	43.475 ± 1.745	-0.917 ± 0.040		$\nu + \nu_{\rm rot}$	181.7835	42.579 ± 2.699	-1.102 ± 0.063
	$\nu + 2\nu_{\rm rot}$	181.8319	13.826 ± 1.745	-0.673 ± 0.126		$\nu + 2\nu_{\rm rot}$	181.8312	14.389 ± 2.685	2.481 ± 0.186
	$\nu - 2\nu_{\rm rot}$	181.6329	17.911 ± 1.550	2.217 ± 0.087					
	$\nu - \nu_{\rm rot}$	181.6817	41.099 ± 1.554	-0.946 ± 0.038					
Q13	ν	181.7306	125.120 ± 1.553	2.776 ± 0.012					
	$\nu + \nu_{\rm rot}$	181.7794	39.683 ± 1.553	-0.952 ± 0.039					
	$\nu + 2\nu_{\rm rot}$	181.8282	11.574 ± 1.551	2.600 ± 0.134					

Table D.2: Frequencies used to produce Fig. 7.13. The errors are calculated from a non-linear least-squares fit.

Time BJD	Frequency (d^{-1})	Time BJD	Frequency (d^{-1})
4963.7671	181.7320 ± 0.0008	5802.3528	181.7200 ± 0.0009
4984.2117	181.7345 ± 0.0008	5822.8063	181.7230 ± 0.0009
5168.2941	181.7279 ± 0.0007	5843.2594	181.7194 ± 0.0009
5188.7478	181.7301 ± 0.0008	5863.7128	181.7194 ± 0.0008
5209.2016	181.7288 ± 0.0008	5884.1660	181.7222 ± 0.0008
5229.6560	181.7281 ± 0.0008	5904.6193	181.7266 ± 0.0008
5250.1101	181.7283 ± 0.0007	5925.0727	181.7256 ± 0.0009
5270.5649	181.7276 ± 0.0009	5945.5263	181.7263 ± 0.0010
5291.0198	181.7257 ± 0.0008	5965.9804	181.7258 ± 0.0008
5311.4745	181.7235 ± 0.0008	5066.0280	181.7268 ± 0.0008
5331.9294	181.7206 ± 0.0008	5984.8715	181.7273 ± 0.0010
5352.3840	181.7190 ± 0.0009	6007.5842	181.7284 ± 0.0010
5004.4821	181.7343 ± 0.0008	6027.3340	181.7263 ± 0.0007
5372.8283	181.7197 ± 0.0008	6047.7788	181.7244 ± 0.0008
5393.2929	181.7226 ± 0.0010	6067.9677	181.7255 ± 0.0008
5413.7468	181.7235 ± 0.0009	6088.8822	181.7215 ± 0.0008
5434.2004	181.7265 ± 0.0009	6109.1427	181.7263 ± 0.0010
5454.6438	181.7241 ± 0.0010	6128.6775	181.7292 ± 0.0012
5475.0869	181.7220 ± 0.0008	6150.0715	181.7212 ± 0.0010
5495.5400	181.7229 ± 0.0008	6170.5048	181.7276 ± 0.0011
5516.0033	181.7210 ± 0.0008	5086.4811	181.7261 ± 0.0010
5536.4567	181.7200 ± 0.0008	6190.9585	181.7265 ± 0.0010
5549.6156	181.7340 ± 0.0063	6211.4119	181.7266 ± 0.0009
5026.0295	181.7310 ± 0.0010	6231.8650	181.7274 ± 0.0008
5577.9772	181.7216 ± 0.0008	6252.3183	181.7285 ± 0.0008
5597.8081	181.7205 ± 0.0007	6272.7716	181.7233 ± 0.0008
5618.2624	181.7197 ± 0.0008	6293.2248	181.7254 ± 0.0008
5638.7170	181.7165 ± 0.0008	6313.6787	181.7279 ± 0.0013
5659.1718	181.7133 ± 0.0009	6334.1328	181.7291 ± 0.0008
5679.6264	181.7131 ± 0.0009	6354.5869	181.7300 ± 0.0008
5700.0815	181.7132 ± 0.0009	6375.0414	181.7308 ± 0.0008
5720.5361	181.7140 ± 0.0009	5106.9345	181.7242 ± 0.0008
5740.9905	181.7181 ± 0.0008	6395.4963	181.7291 ± 0.0008
5761.4448	181.7162 ± 0.0010	6414.8678	181.7292 ± 0.0009
5045.5742	181.7295 ± 0.0007	5127.3876	181.7270 ± 0.0008
5781.8989	181.7176 ± 0.0008	5147.8410	181.7253 ± 0.0009

Table D.3: Radial velocity measurements used to produce Fig. 7.14.

Time BJD	RV ($\mathrm{km\,s^{-1}}$)	Orbital Phase	Time BJD	RV ($\mathrm{km\,s^{-1}}$)	Orbital Phase
		WASP Measurements			
3198.0752	33.8740 ± 2.7464	0.0961	4316.4324	51.9240 ± 5.2791	0.0254
3209.0133	33.4756 ± 2.0667	0.1052	4634.0762	48.8651 ± 2.4607	0.2893
3209.0175	34.4544 ± 1.8562	0.1052	5004.5471	57.6739 ± 0.8293	0.5972
4263.6140	49.5729 ± 2.3153	0.9815	5370.0503	39.2848 ± 0.9058	0.9009
4283.0188	50.9015 ± 1.2920	0.9976			
		Kepler Measurements			
4969.5193	56.4493 ± 1.3612	0.5681	5705.8440	25.4675 ± 1.5437	0.1799
4988.8706	56.7084 ± 1.4855	0.5842	5726.2986	29.6631 ± 1.5466	0.1969
5011.7055	66.3719 ± 1.6475	0.6031	5746.7529	36.3605 ± 1.5402	0.2139
5030.8823	58.3534 ± 1.4691	0.6191	5767.2070	31.5044 ± 1.6158	0.2309
5051.3364	49.7120 ± 1.3093	0.6361	5787.6611	28.6040 ± 1.4977	0.2479
5071.7897	48.5287 ± 1.5284	0.6531	5808.1150	36.0218 ± 1.5763	0.2649
5092.2434	45.0591 ± 1.4496	0.6701	5828.5684	39.7112 ± 1.6092	0.2819
5112.6968	43.4423 ± 1.4387	0.6871	5849.0217	37.7732 ± 1.3943	0.2989
5133.1499	46.6247 ± 1.2990	0.7040	5869.4748	38.3586 ± 1.3958	0.3159
5153.6030	46.6250 ± 1.4314	0.7210	5889.9282	43.9849 ± 1.3632	0.3329
5173.1674	47.6350 ± 1.4521	0.7373	5910.3813	51.0960 ± 1.3936	0.3499
5195.0516	57.3907 ± 1.4170	0.7555	5930.8350	46.6841 ± 1.5171	0.3669
5214.9639	51.7571 ± 1.3571	0.7720	5951.2888	50.2033 ± 1.6614	0.3839
5235.4182	49.2860 ± 1.4313	0.7890	5971.7429	49.5742 ± 1.3861	0.4009
5255.8728	47.7015 ± 1.3118	0.8060	5992.1973	47.0606 ± 1.4947	0.4179
5276.3273	49.3531 ± 1.4662	0.8230	6012.6519	50.6747 ± 1.3699	0.4349
5296.7822	42.2438 ± 1.3001	0.8400	6033.1067	47.1976 ± 1.2533	0.4519
5317.2370	41.5897 ± 1.5476	0.8570	6053.5615	44.9607 ± 1.4562	0.4689
5337.6919	35.3159 ± 1.4623	0.8740	6074.0163	44.8032 ± 1.3711	0.4858
5358.1467	34.1897 ± 1.4421	0.8910	6094.4709	43.8970 ± 1.3106	0.5028
5378.6008	40.3191 ± 1.5196	0.9080	6113.5872	46.0190 ± 2.2752	0.5187
5399.0552	44.7721 ± 1.5833	0.9250	6137.5049	65.3551 ± 2.9457	0.5386
5419.4988	39.4650 ± 1.5712	0.9420	6155.8340	43.7882 ± 1.7461	0.5538
5439.9524	45.4938 ± 1.7445	0.9590	6176.2873	50.7768 ± 1.9439	0.5708
5460.4160	39.3453 ± 1.8627	0.9760	6196.7410	46.1893 ± 1.9796	0.5878
5480.8693	38.6341 ± 1.5015	0.9930	6217.1943	48.6851 ± 1.2788	0.6048
5501.3225	42.6083 ± 1.6560	0.0100	6236.6157	48.1910 ± 1.5989	0.6210
5521.7657	39.3860 ± 1.4660	0.0270	6259.9195	55.1713 ± 1.7476	0.6403
5542.2293	38.5864 ± 1.3828	0.0440	6278.5542	45.2504 ± 1.4912	0.6558
5562.6829	30.9665 ± 7.2416	0.0610	6299.0076	47.2231 ± 1.3649	0.6728
5583.1367	43.8159 ± 1.3629	0.0780	6319.4614	49.1835 ± 2.5602	0.6898
5603.5908	39.0943 ± 1.5518	0.0950	6339.9153	54.3449 ± 1.3614	0.7068
5624.0349	35.4591 ± 1.3780	0.1119	6360.3699	54.4262 ± 1.3964	0.7238
5644.4795	36.4433 ± 2.0544	0.1289	6380.7837	55.1782 ± 1.3183	0.7408
5664.9344	26.7362 ± 1.4514	0.1459	6401.8716	54.2052 ± 1.3573	0.7583
5685.3892	27.0453 ± 1.5588	0.1629	6417.7593	34.3778 ± 2.2375	0.7715
		Spectroscopic Measurements			
6132.8340	45.5689 ± 2.8384	0.5347	6471.7993	50.7300 ± 2.8384	0.8164

Publications

Proceedings

- Holdsworth D. L., Smalley B., 2014, IAUS 301, 423
- Holdsworth D. L., Smalley B., 2014, Putting A Stars into Context: Evolution, Environment, and Related Stars, 301

Refereed

- Paunzen, E., Skarka, M., Walczak, P., Holdsworth, D.L., Smalley, B., West, R.G., Janik, J., 2015, MNRAS, 453, 1241
- Smalley, B., Niemczura, E., Murphy, S. J., Lehmann, H., Kurtz, D. W., Holdsworth, D. L., Cunha, M. S., Balona, L. A., Briquet, M., Bruntt, H., De Cat, P., Lampens, P., Thygesen, A. O., Uytterhoeven, K., 2015, MNRAS, 452, 3334
- Bowman, D. M., Holdsworth, D. L., Kurtz, D. W., 2015, MNRAS, 449, 1004
- Holdsworth D.L., Smalley B., Kurtz D. W., Southworth J., Cunha M. S., Clubb K. I., 2014, MNRAS, 443, 2049
- Paunzen E., Skarka M., Holdsworth D. L., Smalley B., West R. G., 2014, MNRAS, 440, 1020
- Smalley B., Southworth J., Pintado O. I., Gillon M., Holdsworth D. L., Anderson D. R., Barros S. C. C., Collier Cameron A., Delrez L., Faedi F., Haswell C. A., Hellier C., Horne K., Jehin E., Maxted P. F. L., Norton A. J., Pollacco D., Skillen I., Smith A. M. S., West R. G., Wheatley P. J., 2014, A&A, 564, A69
- Holdsworth D. L., Smalley B., Gillon M., Clubb K. I., Southworth J., Maxted P. F. L., Anderson D. R., Barros S. C. C., Cameron A. C., Delrez L., Faedi F., Haswell C. A., Hellier C., Horne K., Jehin E., Norton A. J., Pollacco D., Skillen I., Smith A. M. S., West R. G., Wheatley P. J., 2014, MNRAS, 439, 2078
- Holdsworth D. L., Rushton M. T., Bewsher D., Walter F. M., Eyres S. P. S., Hounsell R., Darnley M. J., 2014, MNRAS, 438, 3483

Object Index

Bibliography

Abt H. A., Morrell N. I., 1995, ApJS, 99, 135

Abt H. A., Moyd K. I., 1973, ApJ, 182, 809

Abt H. A., 1961, ApJS, 6, 37

Adelman S. J., 2004, in Zverko J., Ziznovsky J., Adelman S. J., Weiss W. W., eds, The A-Star Puzzle, IAU Symposium Vol. 224, p. 1

Adelman S. J., Caliskan H., Kocer D., Bolcal C., 1997, MNRAS, 288, 470

Aerts C., Christensen-Dalsgaard J., Kurtz D. W., 2010, Asteroseismology, Springer

Aguirre V. S., Casagrande L., Miglio A., 2014, in Feltzing S., Zhao G., Walton N. A., Whitelock P., eds, Setting the scene for Gaia and LAMOST, IAU Symposium Vol. 298, p. 375

Alentiev D., Kochukhov O., Ryabchikova T., Cunha M., Tsymbal V., Weiss W., 2012, MNRAS, 421, L82

Antoci V., 2014, in Guzik J. A., Chaplin W. J., Handler G., Pigulski A., eds, Precision Asteroseismology, IAU Symposium Vol. 301, p. 333

Antoci V., Handler G., Campante T. L., Thygesen A. O., Moya A., Kallinger T., Stello D., Grigahcène A., Kjeldsen H., Bedding T. R., Lüftinger T., Christensen-Dalsgaard J., Catanzaro G., Frasca A., De Cat P., Uytterhoeven K., Bruntt H., Houdek G., Kurtz D. W., Lenz P., Kaiser A., van Cleve J., Allen C., Clarke B. D., 2011, Nature, 477, 570

Antoci V., Handler G., Grundahl F., Carrier F., Brugamyer E. J., Robertson P., Kjeldsen H., Kok Y., Ireland M., Matthews J. M., 2013, MNRAS, 435, 1563

Antoci V., Cunha M., Houdek G., Kjeldsen H., Trampedach R., Handler G., Lüftinger T., Arentoft T., Murphy S., 2014, ApJ, 796, 118

Argelander F. W. A., 1903, Eds Marcus and Weber's Verlag, Bonn (1903)

Asplund M., Grevesse N., Sauval A. J., Scott P., 2009, Annu. Rev. Astron. Astrophys., 47, 481

Aurière M., Silvester J., Wade G. A., Bagnulo S., Donati J.-F., Johnson N., Lignières F., Landstreet J. D., Lüftinger T., Mouillet D., Paletou F., Petit P., Strasser S., 2004, in Zverko J., Ziznovsky J., Adelman S. J., Weiss W. W., eds, The A-Star Puzzle, IAU Symposium Vol. 224, p. 633

Aurière M., Wade G. A., Lignières F., Hui-Bon-Hoa A., Landstreet J. D., Iliev I. K., Donati J.-F., Petit P., Roudier T., Théado S., 2010, A&A, 523, A40

Babcock H. W., 1960, ApJ, 132, 521

Bagnulo S., Landstreet J. D., Lo Curto G., Szeifert T., Wade G. A., 2003, A&A, 403, 645

Bagnulo S., Hensberge H., Landstreet J. D., Szeifert T., Wade G. A., 2004, A&A, 416, 1149

Bagnulo S., Landstreet J. D., Mason E., Andretta V., Silaj J., Wade G. A., 2006, A&A, 450, 777

Bakos G., Noyes R. W., Kovács G., Stanek K. Z., Sasselov D. D., Domsa I., 2004, PASP, 116, 266

Balmforth N. J., 1992, MNRAS, 255, 603

Balmforth N. J., Cunha M. S., Dolez N., Gough D. O., Vauclair S., 2001, MNRAS, 323, 362

Balona L. A., Dziembowski W. A., 2011, MNRAS, 417, 591

Balona L. A., Zima W., 2002, MNRAS, 336, 873

Balona L. A., 2011, MNRAS, 415, 1691

Balona L. A., 2012, MNRAS, 423, 3420

Balona L. A., 2013a, MNRAS, 431, 2240

Balona L. A., 2013b, MNRAS, 436, 1415

Balona L. A., 2014a, MNRAS, 437, 1476

Balona L. A., 2014b, MNRAS, 441, 3543

Balona L. A., 2015, MNRAS, 447, 2714

Balona L. A., Cunha M. S., Gruberbauer M., Kurtz D. W., Saio H., White T. R., Christensen-Dalsgaard J., Kjeldsen H., Christiansen J. L., Hall J. R., Seader S. E., 2011a, MNRAS, 413, 2651

Balona L. A., Cunha M. S., Kurtz D. W., Brandão I. M., Gruberbauer M., Saio H., Østensen R., Elkin V. G., Borucki W. J., Christensen-Dalsgaard J., Kjeldsen H., Koch D. G., Bryson S. T., 2011b, MNRAS, 410, 517

Balona L. A., Guzik J. A., Uytterhoeven K., Smith J. C., Tenenbaum P., Twicken J. D., 2011c, MNRAS, 415, 3531

Balona L. A., Ripepi V., Catanzaro G., Kurtz D. W., Smalley B., De Cat P., Eyer L., Grigahcène A., Leccia S., Southworth J., Uytterhoeven K., van Winckel H., Christensen-Dalsgaard J., Kjeldsen H., Caldwell D. A., van Cleve J., Girouard F. R., 2011d, MNRAS, 414, 792

Balona L. A., Breger M., Catanzaro G., Cunha M. S., Handler G., Kołaczkowski Z., Kurtz D. W., Murphy S., Niemczura E., Paparó M., Smalley B., Szabó R., Uytterhoeven K., Christiansen J. L., Uddin K., Stumpe M. C., 2012a, MNRAS, 424, 1187

Balona L. A., Lenz P., Antoci V., Bernabei S., Catanzaro G., Daszyńska-Daszkiewicz J., di Criscienzo M., Grigahcène A., Handler G., Kurtz D. W., Marconi M., Molenda-Żakowicz J., Moya A., Nemec J. M., Pigulski A., Pricopi D., Ripepi V., Smalley B., Suárez J. C., Suran M., Hall J. R., Kinemuchi K., Klaus T. C., 2012b, MNRAS, 419, 3028

Balona L. A., Catanzaro G., Abedigamba O. P., Ripepi V., Smalley B., 2015, MNRAS, 448, 1378

Balona L. A., Krisciunas K., Cousins A. W. J., 1994, MNRAS, 270, 905

Baran A., Oreiro R., Pigulski A., Pérez Hernández F., Ulla A., Reed M. D., Rodríguez-López C., Moskalik P., Kim S.-L., Chen W.-P., Crowe R., Siwak M., Armendarez L., Binder P. M., Choo K.-J., Dye A., Eggen J. R., Garrido R., González Pérez J. M., Harms S. L., Huang F.-Y., Kozieł D., Lee H.-T., MacDonald J., Fox Machado L., Monserrat T., Stevick J., Stewart S., Terry D., Zhou A.-Y., Zoła S., 2009, MNRAS, 392, 1092

Baran A., Pigulski A., O'Toole S. J., 2008, MNRAS, 385, 255

Barclay T., Ramsay G., Hakala P., Napiwotzki R., Nelemans G., Potter S., Todd I., 2011, MNRAS, 413, 2696

Barnes J. W., Linscott E., Shporer A., 2011, ApJS, 197, 10

Beauchamp A., Wesemael F., Bergeron P., Liebert J., Saffer R. A., 1996, in Jeffery C. S., Heber U., eds, Hydrogen Deficient Stars, ASPC Vol. 96, p. 295

Belkacem K., Samadi R., Goupil M.-J., Dupret M.-A., 2008, A&A, 478, 163

Bergeron P., Wesemael F., Dufour P., Beauchamp A., Hunter C., Saffer R. A., Gianninas A., Ruiz M. T., Limoges M.-M., Dufour P., Fontaine G., Liebert J., 2011, ApJ, 737, 28

Bertelli G., Girardi L., Marigo P., Nasi E., 2008, A&A, 484, 815

Beust H., Lagrange A.-M., Plazy F., Mouillet D., 1996, A&A, 310, 181

Bevington P. R., 1969, Data reduction and error analysis for the physical sciences, New York: McGraw-Hill, 1969

Bidelman W. P., MacConnell D. J., 1973, AJ, 78, 687

Biermann L., 1948, Z. Astrophys, 25, 135

Bigot L., Dziembowski W. A., 2002, A&A, 391, 235

Bigot L., Kurtz D. W., 2011, A&A, 536, A73

Blažko S., 1907, Astron. Nachr., 175, 325

Blazère A., Petit P., Lignières F., Aurière M., Böhm T., Wade G., 2014, in Ballet J., Martins F., Bournaud F., Monier R., Reylé C., eds, SF2A-2014: Proceedings of the Annual meeting of the French Society of Astronomy and Astrophysics, p. 463

Böhm-Vitense E., 2006, PASP, 118, 419

Bord D. J., Cowley C. R., Ryabchikova T. A., Mathys G., 1998, American Astronomical Society Meeting Abstracts, Bulletin of the American Astronomical Society Vol. 30, p. 1318

Borucki W. J., Koch D., Basri G., Batalha N., Brown T., Caldwell D., Caldwell J., Christensen-Dalsgaard J., Cochran W. D., DeVore E., Dunham E. W., Dupree A. K., Gautier T. N., Geary J. C., Gilliland R., Gould A., Howell S. B., Jenkins J. M., Kondo Y., Latham D. W., Marcy G. W., Meibom S., Kjeldsen H., Lissauer J. J., Monet D. G., Morrison D., Sasselov D., Tarter J., Boss A., Brownlee D., Owen T., Buzasi D., Charbonneau D., Doyle L., Fortney J., Ford E. B., Holman M. J., Seager S., Steffen J. H., Welsh W. F., Rowe J., Anderson H., Buchhave L., Ciardi D., Walkowicz L., Sherry W., Horch E., Isaacson H., Everett M. E., Fischer

D., Torres G., Johnson J. A., Endl M., MacQueen P., Bryson S. T., Dotson J., Haas M., Kolodziejczak J., Van Cleve J., Chandrasekaran H., Twicken J. D., Quintana E. V., Clarke B. D., Allen C., Li J., Wu H., Tenenbaum P., Verner E., Bruhweiler F., Barnes J., Prsa A., 2010, Science, 327, 977

Bowman D. M., Kurtz D. W., 2014, MNRAS, 444, 1909

Bowman D. M., Holdsworth D. L., Kurtz D. W., 2015, MNRAS, 449, 1004

Bradley P. A., 1995, Baltic Astron., 4, 311

Bradley P. A., 1998, Baltic Astron., 7, 111

Bradley P. A., Guzik J. A., Miles L. F., Uytterhoeven K., Jackiewicz J., Kinemuchi K., 2015, AJ, 149, 68

Braithwaite J., Cantiello M., 2013, MNRAS, 428, 2789

Breger M., Montgomery M. H., 2014, ApJ, 783, 89

Breger M., 1970, ApJ, 162, 597

Breger M., 2000, in Breger M., Montgomery M., eds, Delta Scuti and Related Stars, Astron. Soc. Pac. Conf. Ser. Vol. 210, p. 3

Breger M., Stich J., Garrido R., Martin B., Jiang S. Y., Li Z. P., Hube D. P., Ostermann W., Paparo M., Scheck M., 1993, A&A, 271, 482

Breger M., Balona L., Lenz P., Hollek J. K., Kurtz D. W., Catanzaro G., Marconi M., Pamyatnykh A. A., Smalley B., Suárez J. C., Szabo R., Uytterhoeven K., Ripepi V., Christensen-Dalsgaard J., Kjeldsen H., Fanelli M. N., Ibrahim K. A., Uddin K., 2011, MNRAS, 414, 1721

Breger M., Hareter M., Endl M., Kuschnig R., Weiss W. W., Matthews J. M., Guenther D. B., Moffat A. F. J., Rowe J. F., Rucinski S. M., Sasselov D., 2012, Astron. Nachr., 333, 131

Bruntt H., De Cat P., Aerts C., 2008, A&A, 478, 487

Bruntt H., Kurtz D. W., Cunha M. S., Brandão I. M., Handler G., Bedding T. R., Medupe T., Buzasi D. L., Mashigo D., Zhang I., van Wyk F., 2009, MNRAS, 396, 1189

Buldgen G., Reese D. R., Dupret M. A., Samadi R., 2015, A&A, 574, A42

Burgh E. B., Nordsieck K. H., Kobulnicky H. A., Williams T. B., O'Donoghue D., Smith M. P., Percival J. W., 2003, in Iye M., Moorwood A. F. M., eds, Instrument Design and Performance for Optical/Infrared Ground-based Telescopes, SPIE Conference Series Vol. 4841, p. 1463

Bychkov V. D., Bychkova L. V., Madej J., 2006, MNRAS, 365, 585

Cannon A. J., Pickering E. C., 1901, Ann. Astro. Obs. Harvard, 28, 129

Cannon A. J., Pickering E. C., 1912a, Ann. Astro. Obs. Harvard, 56, 115

Cannon A. J., Pickering E. C., 1912b, Ann. Astro. Obs. Harvard, 56, 65

Cardelli J. A., Clayton G. C., Mathis J. S., 1989, ApJ, 345, 245

Carquillat J. M., Prieur J. L., 2007, MNRAS, 380, 1064

Carrier F., North P., Udry S., Babel J., 2002, A&A, 394, 151

Casey M. P., Zwintz K., Guenther D. B., Weiss W. W., Amado P. J., Díaz-Fraile D., Rodriguez E., Kuschnig R., Matthews J. M., Moffat A. F. J., Rowe J. F., Rucinski S. M., Sasselov D., 2013, MNRAS, 428, 2596

Castelli F., Gratton R. G., Kurucz R. L., 1997, A&A, 318, 841

Chaplin W. J., Miglio A., 2013, Annu. Rev. Astron. Astrophys., 51, 353

Chaplin W. J., Basu S., Huber D., Serenelli A., Casagrande L., Silva Aguirre V., Ball W. H., Creevey O. L., Gizon L., Handberg R., Karoff C., Lutz R., Marques J. P., Miglio A., Stello D., Suran M. D., Pricopi D., Metcalfe T. S., Monteiro M. J. P. F. G., Molenda-Żakowicz J., Appourchaux T., Christensen-Dalsgaard J., Elsworth Y., García R. A., Houdek G., Kjeldsen H., Bonanno A., Campante T. L., Corsaro E., Gaulme P., Hekker S., Mathur S., Mosser B., Régulo C., Salabert D., 2014, ApJS, 210, 1

Chevalier C., 1971, A&A, 14, 24

Christensen-Dalsgaard J., 2003, Lecture Notes on Stellar Oscillations, `http://users-phys.au.dk/jcd/oscilnotes/index-bw.html`

Christensen-Dalsgaard J., Kjeldsen H., Mattei J. A., 2001, ApJL, 562, L141

Christian D. J., Pollacco D. L., Skillen I., Street R. A., Keenan F. P., Clarkson W. I., Collier Cameron A., Kane S. R., Lister T. A., West R. G., Enoch B., Evans A., Fitzsimmons A., Haswell C. A., Hellier C., Hodgkin S. T., Horne K., Irwin J., Norton A. J., Osborne J., Ryans R., Wheatley P. J., Wilson D. M., 2006, MNRAS, 372, 1117

Clarke D., 2002, A&A, 386, 763

Collier Cameron A., Pollacco D., Street R. A., Lister T. A., West R. G., Wilson D. M., Pont F., Christian D. J., Clarkson W. I., Enoch B., Evans A., Fitzsimmons A., Haswell C. A., Hellier C., Hodgkin S. T., Horne K., Irwin J., Kane S. R., Keenan F. P., Norton A. J., Parley N. R., Osborne J., Ryans R., Skillen I., Wheatley P. J., 2006, MNRAS, 373, 799

Collier Cameron A., Guenther E., Smalley B., McDonald I., Hebb L., Andersen J., Augusteijn T., Barros S. C. C., Brown D. J. A., Cochran W. D., Endl M., Fossey S. J., Hartmann M., Maxted P. F. L., Pollacco D., Skillen I., Telting J., Waldmann I. P., West R. G., 2010, MNRAS, 407, 507

Conti P. S., 1970, PASP, 82, 781

Cousins A. W. J., Caldwell J. A. R., Menzies J. W., 1989, IBVS, 3412, 1

Cowley C. R., Mathys G., 1998, A&A, 339, 165

Cowley C. R., 1991, in Michaud G., Tutukov A. V., eds, Evolution of Stars: the Photospheric Abundance Connection, IAU Symposium Vol. 145, p. 183

Cowley C. R., Ryabchikova T., Kupka F., Bord D. J., Mathys G., Bidelman W. P., 2000, MNRAS, 317, 299

Cowley C. R., Hubrig S., Ryabchikova T. A., Mathys G., Piskunov N., Mittermayer P., 2001, A&A, 367, 939

Cowley C. R., Bidelman W. P., Hubrig S., Mathys G., Bord D. J., 2004, A&A, 419, 1087

Cunha M. S., Gough D., 2000, MNRAS, 319, 1020

Cunha M. S., 1998, Co. Ska., 27, 272

Cunha M. S., 2002, MNRAS, 333, 47

Cunha M. S., Aerts C., Christensen-Dalsgaard J., Baglin A., Bigot L., Brown T. M., Catala C., Creevey O. L., Domiciano de Souza A., Eggenberger P., Garcia P. J. V., Grundahl F., Kervella P., Kurtz D. W., Mathias P., Miglio A., Monteiro M. J. P. F. G., Perrin G., Pijpers F. P., Pourbaix D., Quirrenbach A., Rousselet-Perraut K., Teixeira T. C., Thévenin F., Thompson M. J., 2007, Annu. Rev. Astron. Astrophys., 14, 217

Cunha M. S., Alentiev D., Brandão I. M., Perraut K., 2013, MNRAS, 436, 1639

Debosscher J., Blomme J., Aerts C., De Ridder J., 2011, A&A, 529, A89

Deeming T. J., 1975, Ap&SS, 36, 137

Degroote P., Aerts C., Ollivier M., Miglio A., Debosscher J., Cuypers J., Briquet M., Montalbán J., Thoul A., Noels A., De Cat P., Balaguer-Núñez L., Maceroni C., Ribas I., Auvergne M., Baglin A., Deleuil M., Weiss W. W., Jorda L., Baudin F., Samadi R., 2009, A&A, 506, 471

Díaz-Fraile D., Rodríguez E., Amado P. J., 2014, A&A, 568, A32

Dorokhova T. N., Dorokhov N. I., 1998, Co. Ska., 27, 338

Doyle A. P., Smalley B., Maxted P. F. L., Anderson D. R., Cameron A. C., Gillon M., Hellier C., Pollacco D., Queloz D., Triaud A. H. M. J., West R. G., 2013, MNRAS, 428, 3164

Dravins D., Lindegren L., Mezey E., Young A. T., 1997a, PASP, 109, 173

Dravins D., Lindegren L., Mezey E., Young A. T., 1997b, PASP, 109, 725

Droege T. F., Richmond M. W., Sallman M. P., Creager R. P., 2006, PASP, 118, 1666

Dupret M. A., Grigahcène A., Garrido R., Gabriel M., Scuflaire R., 2004, A&A, 414, L17

Dupret M. A., Grigahcène A., Garrido R., Gabriel M., Scuflaire R., 2005, A&A, 435, 927

Dupret M. A., Théado S., Noels A., 2008, J. Phys.: Conf.Ser., 118(1), 012052

Durán-Rojas M. C., Watson A. M., Stapelfeldt K. R., Hiriart D., 2009, AJ, 137, 4330

Dziembowski W. A., Moskalik P., Pamyatnykh A. A., 1993, MNRAS, 265, 588

Eddington A. S., 1919, MNRAS, 79, 177

Eddington A. S., 1926, The Internal Constitution of the Stars, Cambridge University Press

Eggen O. J., 1956, PASP, 68, 238

Eisenstein D. J., Liebert J., Harris H. C., Kleinman S. J., Nitta A., Silvestri N., Anderson S. A., Barentine J. C., Brewington H. J., Brinkmann J., Harvanek M., Krzesiński J., Neilsen, Jr. E. H., Long D., Schneider D. P., Snedden S. A., 2006, ApJS, 167, 40

Elkin V. G., Kurtz D. W., Mathys G., Wade G. A., Romanyuk I. I., Kudryavtsev D. O., Smolkin S., 2005, MNRAS, 358, 1100

Elkin V. G., Kurtz D. W., Mathys G., Freyhammer L. M., 2010a, MNRAS, 404, L104

Elkin V. G., Mathys G., Kurtz D. W., Hubrig S., Freyhammer L. M., 2010b, MNRAS, 402, 1883

Elkin V. G., Kurtz D. W., Worters H. L., Mathys G., Smalley B., van Wyk F., Smith A. M. S., 2011, MNRAS, 411, 978

Elkin V., Kurtz D. W., Mathys G., 2008, Co. Ska., 38, 317

Evans D. W., Irwin M. J., Helmer L., 2002, A&A, 395, 347

Everett M. E., Howell S. B., Kinemuchi K., 2012, PASP, 124, 316

Eyer L., Bartholdi P., 1999, A&AS, 135, 1

Eyer L., Mowlavi N., 2008, J. Phys.: Conf. Ser., 118(1), 012010

Eyles C. J., Harrison R. A., Davis C. J., Waltham N. R., Shaughnessy B. M., Mapson-Menard H. C. A., Bewsher D., Crothers S. R., Davies J. A., Simnett G. M., Howard R. A., Moses J. D., Newmark J. S., Socker D. G., Halain J.-P., Defise J.-M., Mazy E., Rochus P., 2009, Sol. Phys., 254, 387

Feast M. W., 1996, MNRAS, 278, 11

Ferrario L., Pringle J. E., Tout C. A., Wickramasinghe D. T., 2009, MNRAS, 400, L71

Fontaine G., Brassard P., 2008, PASP, 120, 1043

Fossati L., Bagnulo S., Monier R., Khan S. A., Kochukhov O., Landstreet J., Wade G., Weiss W., 2007, A&A, 476, 911

Fouqué P., Chevallier L., Cohen M., Galliano E., Loup C., Alard C., de Batz B., Bertin E., Borsenberger J., Cioni M. R., Copet E., Dennefeld M., Derriere S., Deul E., Duc P.-A., Egret D., Epchtein N., Forveille T., Garzón F., Habing H. J., Hron J., Kimeswenger S., Lacombe F., Le Bertre T., Mamon G. A., Omont A., Paturel G., Pau S., Persi P., Robin A. C., Rouan D., Schultheis M., Simon G., Tiphène D., Vauglin I., Wagner S. J., 2000, A&AS, 141, 313

Frolov M. S., Irkaev B. N., 1984, IBVS, 2462, 1

Fulbright J. P., 2000, AJ, 120, 1841

Gautschy A., Saio H., 1995, Annu. Rev. Astron. Astrophys., 33, 75

Geier S., Heber U., 2012, A&A, 543, A149

Geier S., Heber U., Edelmann H., Morales-Rueda L., Kilkenny D., O'Donoghue D., Marsh T. R., Copperwheat C., 2013, A&A, 557, A122

Gerbaldi M., Floquet M., Hauck B., 1985, A&A, 146, 341

Gilliland R. L., Jenkins J. M., Borucki W. J., Bryson S. T., Caldwell D. A., Clarke B. D., Dotson J. L., Haas M. R., Hall J., Klaus T., Koch D., McCauliff S., Quintana E. V., Twicken J. D., van Cleve J. E., 2010, ApJ, 713, L160

Goldreich P., Keeley D. A., 1977, ApJ, 212, 243

Gonzalez G., 1998, A&A, 334, 221

González J. F., Hubrig S., Kurtz D. W., Elkin V., Savanov I., 2008, MNRAS, 384, 1140

Graham J. A., Slettebak A., 1973, AJ, 78, 295

Gray R. O., Corbally C. J., 2002, AJ, 124, 989

Gray R. O., Corbally, J. C., 2009, Stellar Spectral Classification, Princeton University Press

Gray R. O., Garrison R. F., 1989, ApJS, 69, 301

Gray R. O., Kaye A. B., 1999, AJ, 118, 2993

Gray D. F., 1992, The observation and analysis of stellar photospheres, Cambridge University Press

Gray R. O., 1997, in Philip A. G. D., Liebert J., Saffer R., Hayes D. S., eds, The Third Conference on Faint Blue Stars, p. 237

Gray D. F., 2008, The Observation and Analysis of Stellar Photospheres, Cambridge University Press

Gray R. O., 2014, in Niemczura E., Smalley B., Pych W., eds, Lectures from the School of Spectroscopic Data Analyses, Springer-Verlag, p. 75

Gray R. O., Corbally C. J., Garrison R. F., McFadden M. T., Robinson P. E., 2003, AJ, 126, 2048

Green D. A., Stephenson F. R., 2003, in Weiler K., ed., Supernovae and Gamma-Ray Bursters, Lecture Notes in Physics, Berlin Springer Verlag Vol. 598, p. 7

Greiss S., Steeghs D., Gänsicke B. T., Martín E. L., Groot P. J., Irwin M. J., González-Solares E., Greimel R., Knigge C., Østensen R. H., Verbeek K., Drew J. E., Drake J., Jonker P. G., Ripepi V., Scaringi S., Southworth J., Still M., Wright N. J., Farnhill H., van Haaften L. M., Shah S., 2012, AJ, 144, 24

Grigahcène A., Antoci V., Balona L., Catanzaro G., Daszyńska-Daszkiewicz J., Guzik J. A., Handler G., Houdek G., Kurtz D. W., Marconi M., Monteiro M. J. P. F. G., Moya A., Ripepi V., Suárez J.-C., Uytterhoeven K., Borucki W. J., Brown T. M., Christensen-Dalsgaard J., Gilliland R. L., Jenkins J. M., Kjeldsen H., Koch D., Bernabei S., Bradley P., Breger M., Di Criscienzo M., Dupret M.-A., García R. A., García Hernández A., Jackiewicz J., Kaiser A., Lehmann H., Martín-Ruiz S., Mathias P., Molenda-Żakowicz J., Nemec J. M., Nuspl J., Paparó M., Roth M., Szabó R., Suran M. D., Ventura R., 2010, ApJL, 713, L192

Guzik J. A., Kaye A. B., Bradley P. A., Cox A. N., Neuforge C., 2000, ApJL, 542, L57

Handler G., Paunzen E., 1999, A&AS, 135, 57

Handler G., 2009, MNRAS, 398, 1339

Hareter M., 2012, Astron. Nachr., 333, 1048

Hareter M., Paparó M., Weiss W., García Hernández A., Borkovits T., Lampens P., Rainer M., De Cat P., Marcos-Arenal P., Vos J., Poretti E., Baglin A., Michel E., Baudin F., Catala C., 2014, A&A, 567, A124

Hatzes A. P., Mkrtichian D. E., 2004, MNRAS, 351, 663

Heber U., Hunger K., Jonas G., Kudritzki R. P., 1984, A&A, 130, 119

Hekker S., Debosscher J., Huber D., Hidas M. G., De Ridder J., Aerts C., Stello D., Bedding T. R., Gilliland R. L., Christensen-Dalsgaard J., Brown T. M., Kjeldsen H., Borucki W. J., Koch D., Jenkins J. M., Van Winckel H., Beck P. G., Blomme J., Southworth J., Pigulski A., Chaplin W. J., Elsworth Y. P., Stevens I. R., Dreizler S., Kurtz D. W., Maceroni C., Cardini D., Derekas A., Suran M. D., 2010, ApJL, 713, L187

Heller C. H., Kramer K. S., 1988, IBVS, 3247, 1

Henry G. W., Fekel F. C., 2005, AJ, 129, 2026

Hoffleit D., 1997, JAAVSO, 25, 115

Høg E., Bässgen G., Bastian U., Egret D., Fabricius C., Großmann V., Halbwachs J. L., Makarov V. V., Perryman M. A. C., Schwekendiek P., Wagner K., Wicenec A., 1997, A&A, 323, L57

Holdsworth D. L., Rushton M. T., Bewsher D., Walter F. M., Eyres S. P. S., Hounsell R., Darnley M. J., 2014a, MNRAS, 438, 3483

Holdsworth D. L., Smalley B., Gillon M., Clubb K. I., Southworth J., Maxted P. F. L., Anderson D. R., Barros S. C. C., Cameron A. C., Delrez L., Faedi F., Haswell C. A., Hellier C., Horne K., Jehin E., Norton A. J., Pollacco D., Skillen I., Smith A. M. S., West R. G., Wheatley P. J., 2014b, MNRAS, 439, 2078

Holdsworth D. L., Smalley B., Kurtz D. W., Southworth J., Cunha M. S., Clubb K. I., 2014c, MNRAS, 443, 2049

Horne J. H., Baliunas S. L., 1986, ApJ, 302, 757

Houdek G., 1996, PhD thesis, University of Vienna

Houdek G., 2006, Proceedings of SOHO 18/GONG 2006/HELAS I, Beyond the spherical Sun, ESA Special Publication Vol. 624, p. 28

Houdek G., Balmforth N. J., Christensen-Dalsgaard J., Gough D. O., 1999, A&A, 351, 582

Houk N., 1978, Michigan catalogue of two-dimensional spectral types for the HD stars, University of Michigan

Huber P. J., 1981, Robust statistics, Wiley Series in Probability and Mathematical Statistics

Hubrig S., Nesvacil N., Schöller M., North P., Mathys G., Kurtz D. W., Wolff B., Szeifert T., Cunha M. S., Elkin V. G., 2005, A&A, 440, L37

Hubrig S., North P., Mathys G., 2000, ApJ, 539, 352

Jaschek C., Gómez A. E., 1970, PASP, 82, 809

Jaschek M., Jaschek C., 1958, Z. Astrophys., 45, 35

Jeffery C. S., Saio H., 2006, MNRAS, 372, L48

Jehin E., Gillon M., Queloz D., Magain P., Manfroid J., Chantry V., Lendl M., Hutsemékers D., Udry S., 2011, The Messenger, 145, 2

Jiang C., Jiang B. W., Christensen-Dalsgaard J., Bedding T. R., Stello D., Huber D., Frandsen S., Kjeldsen H., Karoff C., Mosser B., Demarque P., Fanelli M. N., Kinemuchi K., Mullally F., 2011, ApJ, 742, 120

Johnson H. L., Morgan W. W., 1953, ApJ, 117, 313

Johnson J. A., 2002, ApJS, 139, 219

Joshi S., Girish V., Sagar R., Kurtz D. W., Martinez P., Kumar B., Seetha S., Ashoka B. N., Zhou A., 2003, MNRAS, 344, 431

Kaiser M. L., Kucera T. A., Davila J. M., St. Cyr O. C., Guhathakurta M., Christian E., 2008, Sp. Sci. Rev., 136, 5

Kalas P., Graham J. R., Chiang E., Fitzgerald M. P., Clampin M., Kite E. S., Stapelfeldt K., Marois C., Krist J., 2008, Science, 322, 1345

Kallinger T., Matthews J. M., 2010, ApJL, 711, L35

Kaye A. B., Handler G., Krisciunas K., Poretti E., Zerbi F. M., 1999, PASP, 111, 840

Kennelly E. J., Brown T. M., Kotak R., Sigut T. A. A., Horner S. D., Korzennik S. G., Nisenson P., Noyes R. W., Walker A., Yang S., 1998, ApJ, 495, 440

Kilkenny D., 2002, in Aerts C., Bedding T. R., Christensen-Dalsgaard J., eds, IAU Colloq. 185: Radial and Nonradial Pulsationsn as Probes of Stellar Physics, Astronomical Society of the Pacific Conference Series Vol. 259, p. 356

Kilkenny D., 2007, Commun. Asteroseismol., 150, 234

Kilkenny D., Koen C., O'Donoghue D., Stobie R. S., 1997, MNRAS, 285, 640

Kiss L. L., Csák B., Szatmáry K., Furész G., Sziládi K., 2000, A&A, 364, 199

Kitchin C. R., 2003, Astrophysical techniques, 4th ed. Bristol; Philadelphia: Institute of Physics Publishing

Kjeldsen H., Bedding T. R., Viskum M., Frandsen S., 1995, AJ, 109, 1313

Kobulnicky H. A., Nordsieck K. H., Burgh E. B., Smith M. P., Percival J. W., Williams T. B., O'Donoghue D., 2003, in Iye M., Moorwood A. F. M., eds, Instrument Design and Performance for Optical/Infrared Ground-based Telescopes, SPIE Conference Series Vol. 4841, p. 1634

Koch D. G., Borucki W. J., Basri G., Batalha N. M., Brown T. M., Caldwell D., Christensen-Dalsgaard J., Cochran W. D., DeVore E., Dunham E. W., Gautier, III T. N., Geary J. C., Gilliland R. L., Gould A., Jenkins J., Kondo Y., Latham D. W., Lissauer J. J., Marcy G., Monet D., Sasselov D., Boss A., Brownlee D., Caldwell J., Dupree A. K., Howell S. B., Kjeldsen H., Meibom S., Morrison D., Owen T., Reitsema H., Tarter J., Bryson S. T., Dotson J. L., Gazis P., Haas M. R., Kolodziejczak J., Rowe J. F., Van Cleve J. E., Allen C., Chandrasekaran

H., Clarke B. D., Li J., Quintana E. V., Tenenbaum P., Twicken J. D., Wu H., 2010, ApJ, 713, L79

Kochukhov O., 2003, A&A, 404, 669

Kochukhov O., 2006, A&A, 454, 321

Kochukhov O., 2011, in Prasad Choudhary D., Strassmeier K. G., eds, Physics of Sun and Star Spots, IAU Symposium Vol. 273, p. 249

Kochukhov O., Bagnulo S., Barklem P. S., 2002, ApJL, 578, L75

Kochukhov O., Bagnulo S., Wade G. A., Sangalli L., Piskunov N., Landstreet J. D., Petit P., Sigut T. A. A., 2004, A&A, 414, 613

Kochukhov O., Tsymbal V., Ryabchikova T., Makaganyk V., Bagnulo S., 2006, A&A, 460, 831

Kochukhov O., Ryabchikova T., Bagnulo S., Lo Curto G., 2008, A&A, 479, L29

Kochukhov O., Bagnulo S., Lo Curto G., Ryabchikova T., 2009, A&A, 493, L45

Kochukhov O., Alentiev D., Ryabchikova T., Boyko S., Cunha M., Tsymbal V., Weiss W., 2013, MNRAS, 431, 2808

Kochukhov O., Rusomarov N., Valenti J. A., Stempels H. C., Snik F., Rodenhuis M., Piskunov N., Makaganiuk V., Keller C. U., Johns-Krull C. M., 2015, A&A, 574, A79

Koen C., 2010, Ap&SS, 329, 267

Koen C., Kurtz D. W., Gray R. O., Kilkenny D., Handler G., Van Wyk F., Marang F., Winkler H., 2001, MNRAS, 326, 387

Kreidl T. J., 1985, IBVS, 2739, 1

Kreidl T. J., 1990, IBVS, 3539, 1

Kumar C. K., Davila J. M., Rajan R. S., 1989, ApJ, 337, 414

Kupka F., Piskunov N., Ryabchikova T. A., Stempels H. C., Weiss W. W., 1999, A&AS, 138, 119

Kurtz D. W., Cropper M. S., 1981, IBVS, 1987, 1

Kurtz D. W., Kreidl T. J., 1985, MNRAS, 216, 987

Kurtz D. W., Martinez P., 1987, MNRAS, 226, 187

Kurtz D. W., Martinez P., 1993, IBVS, 3966, 1

Kurtz D. W., Martinez P., 1995, IBVS, 4209, 1

Kurtz D. W., Medupe R., 1996, Bull. Astron. Soc. India, 24, 291

Kurtz D. W., 1981, IBVS, 1915, 1

Kurtz D. W., 1982, MNRAS, 200, 807

Kurtz D. W., 1983a, MNRAS, 202, 1

Kurtz D. W., 1983b, MNRAS, 205, 3

Kurtz D. W., 1984, MNRAS, 209, 841

Kurtz D. W., 2000, in Breger M., Montgomery M., eds, Delta Scuti and Related Stars, Astronomical Society of the Pacific Conference Series Vol. 210, p. 287

Kurtz D. W., 2005, JA&A, 26, 123

Kurtz D. W., Martinez P., van Wyk F., Marang F., Roberts G., 1994, MNRAS, 268, 641

Kurtz D. W., Garrison R. F., Koen C., Hofmann G. F., Viranna N. B., 1995, MNRAS, 276, 199

Kurtz D. W., Martinez P., Koen C., Sullivan D. J., 1996, MNRAS, 281, 883

Kurtz D. W., van Wyk F., Roberts G., Marang F., Handler G., Medupe R., Kilkenny D., 1997, MNRAS, 287, 69

Kurtz D. W., Elkin V. G., Cunha M. S., Mathys G., Hubrig S., Wolff B., Savanov I., 2006, MNRAS, 372, 286

Kurtz D. W., Cunha M. S., Saio H., Bigot L., Balona L. A., Elkin V. G., Shibahashi H., Brandão I. M., Uytterhoeven K., Frandsen S., Frimann S., Hatzes A., Lueftinger T., Gruberbauer M., Kjeldsen H., Christensen-Dalsgaard J., Kawaler S. D., 2011, MNRAS, 414, 2550

Kurtz D. W., Saio H., Takata M., Shibahashi H., Murphy S. J., Sekii T., 2014, MNRAS, 444, 102

Kurtz D. W., Shibahashi H., Goode P. R., 1990, MNRAS, 247, 558

Kurucz R., 1993, ATLAS9 Stellar Atmosphere Programs and 2 km/s grid. Kurucz CD-ROM No. 13. Cambridge, Mass.: Smithsonian Astrophysical Observatory, 1993., 13

Lafler J., Kinman T. D., 1965, ApJS, 11, 216

Lagrange A.-M., Gratadour D., Chauvin G., Fusco T., Ehrenreich D., Mouillet D., Rousset G., Rouan D., Allard F., Gendron É., Charton J., Mugnier L., Rabou P., Montri J., Lacombe F., 2009, A&A, 493, L21

Lanz T., Mathys G., 1993, A&A, 280, 486

Leavitt H. S., Pickering E. C., 1912, Harvard College Observatory Circular, 173, 1

Ledoux P., 1951, ApJ, 114, 373

Lehmann H., Southworth J., Tkachenko A., Pavlovski K., 2013, A&A, 557, A79

Lenz P., Breger M., 2005, Commun. Asteroseismol., 146, 53

Lignières F., Petit P., Böhm T., Aurière M., 2009, A&A, 500, L41

Lignières F., Petit P., Aurière M., Wade G. A., Böhm T., 2014, in Petit P., Jardine M., Spruit H. C., eds, Magnetic Fields throughout Stellar Evolution, IAU Symposium Vol. 302, p. 338

Lomb N. R., 1976, Ap&SS, 39, 447

Lüftinger T., Fröhlich H.-E., Weiss W. W., Petit P., Aurière M., Nesvacil N., Gruberbauer M., Shulyak D., Alecian E., Baglin A., Baudin F., Catala C., Donati J.-F., Kochukhov O., Michel E., Piskunov N., Roudier T., Samadi R., 2010, A&A, 509, A43

Maceroni C., Lehmann H., da Silva R., Montalbán J., Lee C.-U., Ak H., Deshpande R., Yakut K., Debosscher J., Guo Z., Kim S.-L., Lee J. W., Southworth J., 2014, A&A, 563, A59

Martin D. C., Fanson J., Schiminovich D., Morrissey P., Friedman P. G., Barlow T. A., Conrow T., Grange R., Jelinsky P. N., Milliard B., Siegmund O. H. W., Bianchi L., Byun Y.-I., Donas J., Forster K., Heckman T. M., Lee Y.-W., Madore B. F., Malina R. F., Neff S. G., Rich R. M., Small T., Surber F., Szalay A. S., Welsh B., Wyder T. K., 2005, ApJL, 619, L1

Martinez P., Kauffmann G., 1990, IBVS, 3507, 1

Martinez P., Kurtz D. W., 1990a, IBVS, 3509, 1

Martinez P., Kurtz D. W., 1990b, IBVS, 3510, 1

Martinez P., Kurtz D. W., 1991a, IBVS, 3553, 1

Martinez P., Kurtz D. W., 1991b, IBVS, 3611, 1

Martinez P., Kurtz D. W., 1992, IBVS, 3750, 1

Martinez P., Kurtz D. W., 1994, MNRAS, 271, 118

Martinez P., 1991, IBVS, 3621, 1

Martinez P., 1996, IBVS, 4348, 1

Martinez P., Kurtz D. W., Kauffmann G., Jonson A. C., 1990, IBVS, 3506, 1

Martinez P., Girish V., Joshi S., Kurtz D. W., Ashoka B. N., Chaubey U. S., Gupta S. K., Sagar R., Seetha S., 2000, IBVS, 4853, 1

Martinez P., Kurtz D. W., Ashley R., 1993, IBVS, 3844, 1

Martinez P., Kurtz D. W., Kauffmann G. M., 1991, MNRAS, 250, 666

Martinez P., Kurtz D. W., van Wyk F., 1994, MNRAS, 271, 305

Martinez P., Meintjes P. J., Ratcliff S. J., 1997, IBVS, 4507, 1

Mary D. L., 2006, A&A, 452, 715

Mason B. D., Wycoff G. L., Hartkopf W. I., Douglass G. G., Worley C. E., 2001, AJ, 122, 3466

Mathys G., Lanz T., 1992, A&A, 256, 169

Mathys G., 1988, in Adelman S. J., Lanz T., eds, Elemental Abundance Analyses, p. 101

Mathys G., 1990, A&A, 232, 151

Mathys G., 2014, in Mathys G., Griffin E. R., Kochukhov O., Monier R., Wahlgren G. M., eds, Putting A Stars into Context: Evolution, Environment, and Related Stars, p. 112

Matthews J. M., Wehlau W. H., Rice J., Walker G. A. H., 1996, ApJ, 459, 278

Maury A. C., Pickering E. C., 1897, Ann. Astron. Obs. Harvard, 28, 1

Maxted P. F. L., Marsh T. R., Heber U., Morales-Rueda L., North R. C., Lawson W. A., 2002, MNRAS, 333, 231

Maxted P. F. L., Anderson D. R., Collier Cameron A., Hellier C., Queloz D., Smalley B., Street R. A., Triaud A. H. M. J., West R. G., Gillon M., Lister T. A., Pepe F., Pollacco D., Ségransan D., Smith A. M. S., Udry S., 2011, PASP, 123, 547

McDonald I., Zijlstra A. A., Boyer M. L., 2012, MNRAS, 427, 343

McNamara D. H., 2000, in Breger M., Montgomery M., eds, Delta Scuti and Related Stars, Astronomical Society of the Pacific Conference Series Vol. 210, p. 373

Medupe R., Kurtz D. W., 1998, MNRAS, 299, 371

Michaud G., 1970, ApJ, 160, 641

Michaud G., Tarasick D., Charland Y., Pelletier C., 1983, ApJ, 269, 239

Miglio A., Montalbán J., Noels A., Eggenberger P., 2008, MNRAS, 386, 1487

Mkrtichian D. E., Kusakin A. V., Lopez de Coca P., Krisciunas K., Akan C., Malanushenko V. P., Paparo M., Percy J., Rolland A., Costa V., Olivares J. I., Koval V. A., Hobart M. A., Ibanoglu C., Ozturk A., Thompson S., Paunzen E., Handler G., Burnashev V., Weiss W. W., Kuratov K. S., Kang Y. W., 2007, AJ, 134, 1713

Monet D. G., Levine S. E., Canzian B., Ables H. D., Bird A. R., Dahn C. C., Guetter H. H., Harris H. C., Henden A. A., Leggett S. K., Levison H. F., Luginbuhl C. B., Martini J., Monet A. K. B., Munn J. A., Pier J. R., Rhodes A. R., Riepe B., Sell S., Stone R. C., Vrba F. J., Walker R. L., Westerhout G., Brucato R. J., Reid I. N., Schoening W., Hartley M., Read M. A., Tritton S. B., 2003, AJ, 125, 984

Montgomery M. H., Odonoghue D., 1999, Delta Scuti Star Newsletter, 13, 28

Montgomery S. L., Welsh B., Bukoski B., Strausbaugh S., 2015, American Astronomical Society Meeting Abstracts, American Astronomical Society Meeting Abstracts Vol. 225, p. 349.19

Morgan W. W., 1933, ApJ, 77, 330

Morgan W. W., Keenan P. C., Kellman E., 1943, An atlas of stellar spectra, with an outline of spectral classification, The University of Chicago Press

Moskalik P., Dziembowski W. A., 1992, A&A, 256, L5

Munari U., Zwitter T., 1997, A&A, 318, 269

Murphy S. J., 2012, MNRAS, 422, 665

Murphy S. J., 2014, PhD thesis, University of Central Lancashire

Murphy S. J., Bedding T. R., Shibahashi H., Kurtz D. W., Kjeldsen H., 2014, MNRAS, 441, 2515

Murphy S. J., Bedding T. R., Niemczura E., Kurtz D. W., Smalley B., 2015, MNRAS, 447, 3948

Murphy S. J., Shibahashi H., Kurtz D. W., 2013, MNRAS, 430, 2986

Neilson H. R., Ignace R., 2014, A&A, 563, L4

Németh P., Kawka A., Vennes S., 2012, MNRAS, 427, 2180

Niemczura E., Smalley B., Murphy S., Catanzaro G., Uytterhoeven K., Drobek D., Briquet M., De Cat P., Marcos-Arenal P., Pápics P. I., Gameiro J. F. S., 2014, in Guzik J. A., Chaplin W. J., Handler G., Pigulski A., eds, Precision Asteroseismology, IAU Symposium Vol. 301, p. 467

North P., Ginestet N., Carquillat J.-M., Carrier F., Udry S., 1998, Contributions of the Astronomical Observatory Skalnate Pleso, 27, 179

O'Donnell J. E., 1994, ApJ, 422, 158

O'Donoghue D., Bauermeister E., Carter D. B., Evans G. P., Koorts W. P., O'Connor J., Osman F., van der Merwe S., Bigelow B. C., 2003, in Iye M., Moorwood A. F. M., eds, Instrument Design and Performance for Optical/Infrared Ground-based Telescopes, SPIE Conference Series Vol. 4841, p. 465

Ohshima O., Narusawa S.-y., Akazawa H., Arai K., Fujii M., Kawabata T., Morikawa K., Ohkura N., Takeuti M., 2001, AJ, 122, 418

Osawa K., 1965, Ann. Tokyo Astron. Obs., 9, 121

Østensen R. H., 2010, Astron. Nachr., 331, 1026

Østensen R. H., Oreiro R., Solheim J.-E., Heber U., Silvotti R., González-Pérez J. M., Ulla A., Pérez Hernández F., Rodríguez-López C., Telting J. H., 2010, A&A, 513, A6

Ostlie D. A., Cox A. N., 1986, ApJ, 311, 864

O'Toole S. J., Heber U., Benjamin R. A., 2004, A&A, 422, 1053

Padmanabhan T., 2001, Theoretical Astrophysics - Volume 2, Stars and Stellar Systems, Cambridge University Press

Pamyatnykh A. A., 1999, AcA, 49, 119

Pamyatnykh A. A., 2000, in Breger M., Montgomery M., eds, Delta Scuti and Related Stars, Astronomical Society of the Pacific Conference Series Vol. 210, p. 215

Paunzen E., Netopil M., Rode-Paunzen M., Handler G., Božić H., Ruždjak D., Sudar D., 2012, A&A, 542, A89

Paunzen E., Handler G., Netopil M., Fossati L., Iliev I. K., Rode-Paunzen M., Luftinger T., Ryabchikova T., Bozic H., 2013a, IBVS, 6058, 1

Paunzen E., Wraight K. T., Fossati L., Netopil M., White G. J., Bewsher D., 2013b, MNRAS, 429, 119

Paunzen E., Skarka M., Holdsworth D. L., Smalley B., West R. G., 2014, MNRAS, 440, 1020

Paxton B., Bildsten L., Dotter A., Herwig F., Lesaffre P., Timmes F., 2011, ApJS, 192, 3

Paxton B., Cantiello M., Arras P., Bildsten L., Brown E. F., Dotter A., Mankovich C., Montgomery M. H., Stello D., Timmes F. X., Townsend R., 2013, ApJS, 208, 4

Pedersen M. G., 2013, Bachelor project, Aarhus University

Pesnell W. D., 1990, ApJ, 363, 227

Petersen J. O., 1973, A&A, 27, 89

Petit P., Lignières F., Wade G. A., Aurière M., Böhm T., Bagnulo S., Dintrans B., Fumel A., Grunhut J., Lanoux J., Morgenthaler A., Van Grootel V., 2010, A&A, 523, A41

Petit P., Lignières F., Aurière M., Wade G. A., Alina D., Ballot J., Böhm T., Jouve L., Oza A., Paletou F., Théado S., 2011, A&A, 532, L13

Pickles A., Depagne É., 2010, PASP, 122, 1437

Pöhnl H., Maitzen H. M., Paunzen E., 2003, A&A, 402, 247

Pojmanski G., 1997, AcA, 47, 467

Pollacco D. L., Skillen I., Collier Cameron A., Christian D. J., Hellier C., Irwin J., Lister T. A., Street R. A., West R. G., Anderson D. R., Clarkson W. I., Deeg H., Enoch B., Evans A., Fitzsimmons A., Haswell C. A., Hodgkin S., Horne K., Kane S. R., Keenan F. P., Maxted P. F. L., Norton A. J., Osborne J., Parley N. R., Ryans R. S. I., Smalley B., Wheatley P. J., Wilson D. M., 2006, PASP, 118, 1407

Press W. H., Rybicki G. B., 1989, ApJ, 338, 277

Press W. H., Teukolsky S. A., Vetterling W. T., Flannery B. P., 1992, Numerical recipes in FORTRAN. The art of scientific computing, Cambridge University Press, —c1992, 2nd ed.

Przybylski A., 1961, Nature, 189, 739

Reed M. D., Kawaler S. D., Østensen R. H., Bloemen S., Baran A., Telting J. H., Silvotti R., Charpinet S., Quint A. C., Handler G., Gilliland R. L., Borucki W. J., Koch D. G., Kjeldsen H., Christensen-Dalsgaard J., 2010, MNRAS, 409, 1496

Reegen P., 2007, A&A, 467, 1353

Reiners A., Royer F., 2004, A&A, 415, 325

Renson P., Manfroid J., 2009, A&A, 498, 961

Ripepi V., Moretti M. I., Marconi M., Clementini G., Cioni M.-R. L., de Grijs R., Emerson J. P., Groenewegen M. A. T., Ivanov V. D., Muraveva T., Piatti A. E., Subramanian S., 2015, MNRAS, 446, 3034

Rodríguez E., Breger M., 2001, A&A, 366, 178

Rodríguez E., García J. M., Mkrtichian D. E., Costa V., Kim S.-L., López-González M. J., Hintz E., Kusakin A. V., Gamarova A. Y., Lee J. W., Youn J.-H., Janiashvili E. B., Garrido R., Moya A., Kang Y. W., 2004, MNRAS, 347, 1317

Rodríguez-López C., Gizis J. E., MacDonald J., Amado P. J., Carosso A., 2015, MNRAS, 446, 2613

Roman N. G., Morgan W. W., Eggen O. J., 1948, ApJ, 107, 107

Rowe J., Borucki W. J., Howell S. B., Gilliland R. L., Buchhave L. A., Batalha N. M., Latham D. W., Kepler Science Team, 2011, American Astronomical Society Meeting Abstracts 217, Bulletin of the American Astronomical Society Vol. 43, p. 103.04

Royer F., 2009, in Rozelot J.-P., Neiner C., eds, The Rotation of Sun and Stars, Lecture Notes in Physics, Berlin Springer Verlag Vol. 765, p. 207

Royer F., Gebran M., Monier R., Adelman S., Smalley B., Pintado O., Reiners A., Hill G., Gulliver A., 2014, A&A, 562, A84

Royer F., Zorec J., Gómez A. E., 2004, in Zverko J., Ziznovsky J., Adelman S. J., Weiss W. W., eds, The A-Star Puzzle, IAU Symposium Vol. 224, p. 109

Rusomarov N., Kochukhov O., Piskunov N., Jeffers S. V., Johns-Krull C. M., Keller C. U., Makaganiuk V., Rodenhuis M., Snik F., Stempels H. C., Valenti J. A., 2013, A&A, 558, A8

Saio H., Gautschy A., 2004, MNRAS, 350, 485

Saio H., 2005, MNRAS, 360, 1022

Saio H., Kurtz D. W., Takata M., Shibahashi H., Murphy S. J., Sekii T., Bedding T. R., 2015, MNRAS, 447, 3264

Samadi R., Goupil M.-J., Houdek G., 2002, A&A, 395, 563

Santos N. C., Israelian G., Mayor M., 2000, A&A, 363, 228

Scargle J. D., 1982, ApJ, 263, 835

Schlegel D. J., Finkbeiner D. P., Davis M., 1998, ApJ, 500, 525

Schneider H., Weiss W. W., 1990, IBVS, 3520, 1

Schöller M., Correia S., Hubrig S., Kurtz D. W., 2012, A&A, 545, A38

Schuh S., Huber J., Dreizler S., Heber U., O'Toole S. J., Green E. M., Fontaine G., 2006, A&A, 445, L31

Shapley H., 1914, ApJ, 40, 448

Shibahashi H., Kurtz D. W., 2012, MNRAS, 422, 738

Shibahashi H., Saio H., 1985, PASJ, 37, 245

Shorlin S. L. S., Wade G. A., Donati J.-F., Landstreet J. D., Petit P., Sigut T. A. A., Strasser S., 2002, A&A, 392, 637

Shortridge K., Meyerdierks H., Currie M., Clayton C., Lockley J., Charles A., Davenhall C., Taylor M., Ash T., Wilkins T., Axon D., Palmer J., Holloway A., Graffagnino V., Bridger A., Fuller N. M., 2004, Starlink User Note, 86

Skrutskie M. F., Cutri R. M., Stiening R., Weinberg M. D., Schneider S., Carpenter J. M., Beichman C., Capps R., Chester T., Elias J., Huchra J., Liebert J., Lonsdale C., Monet D. G., Price S., Seitzer P., Jarrett T., Kirkpatrick J. D., Gizis J. E., Howard E., Evans T., Fowler J., Fullmer L., Hurt R., Light R., Kopan E. L., Marsh K. A., McCallon H. L., Tam R., Van Dyk S., Wheelock S., 2006, AJ, 131, 1163

Smalley B., Kurtz D. W., Smith A. M. S., Fossati L., Anderson D. R., Barros S. C. C., Butters O. W., Collier Cameron A., Christian D. J., Enoch B., Faedi F., Haswell C. A., Hellier C., Holmes S., Horne K., Kane S. R., Lister T. A., Maxted P. F. L., Norton A. J., Parley N., Pollacco D., Simpson E. K., Skillen I., Southworth J., Street R. A., West R. G., Wheatley P. J., Wood P. L., 2011, A&A, 535, A3

Smalley B., Southworth J., Pintado O. I., Gillon M., Holdsworth D. L., Anderson D. R., Barros S. C. C., Collier Cameron A., Delrez L., Faedi F., Haswell C. A., Hellier C., Horne K., Jehin E., Maxted P. F. L., Norton A. J., Pollacco D., Skillen I., Smith A. M. S., West R. G., Wheatley P. J., 2014, A&A, 564, A69

Smalley B., Niemczura E., Murphy S. J., Lehmann H., Kurtz D. W., Holdsworth D. L., Cunha M. S., Balona L. A., Briquet M., Bruntt H., De Cat P., Lampens P., Thygesen A. O., Uytterhoeven K., 2015, MNRAS, 452, 3334

Smalley B., Smith K. C., Dworetsky M. M., 2001, UCLSYN *Userguide,* `http://www.astro.keele.ac.uk/~bs/uclsyn.pdf`

Smeyers P., Moya A., 2007, A&A, 465, 509

Smith K. C., Dworetsky M. M., 1988, in Adelman S. J., Lanz T., eds, Elemental Abundance Analyses, p. 32

Smith M. A., 1973, ApJS, 25, 277

Smith K. C., 1992, PhD thesis, University of London

Smith H. A., Catelan M., Kuehn C., 2011, in McWilliam A., ed., RR Lyrae Stars, Metal-Poor Stars, and the Galaxy Vol. 5, p. 17

Smith A. M. S., Collier Cameron A., Christian D. J., Clarkson W. I., Enoch B., Evans A., Haswell C. A., Hellier C., Horne K., Irwin J., Kane S. R., Lister T. A., Norton A. J., Parley N., Pollacco D. L., Ryans R., Skillen I., Street R. A., Triaud A. H. M. J., West R. G., Wheatley P. J., Wilson D. M., 2006, MNRAS, 373, 1151

Southworth J., 2013, A&A, 557, A119

Southworth J., Zima W., Aerts C., Bruntt H., Lehmann H., Kim S.-L., Kurtz D. W., Pavlovski K., Prša A., Smalley B., Gilliland R. L., Christensen-Dalsgaard J., Kawaler S. D., Kjeldsen H., Cote M. T., Tenenbaum P., Twicken J. D., 2011, MNRAS, 414, 2413

Stankov A., Handler G., 2005, ApJS, 158, 193

Stępień K., 2000, A&A, 353, 227

Stellingwerf R. F., 1978, ApJ, 224, 953

Stibbs D. W. N., 1950, MNRAS, 110, 395

Stoehr F., White R., Smith M., Kamp I., Thompson R., Durand D., Freudling W., Fraquelli D., Haase J., Hook R., Kimball T., Kümmel M., Levay K., Lombardi M., Micol A., Rogers T., 2008, in Argyle R. W., Bunclark P. S., Lewis J. R., eds, Astronomical Data Analysis Software and Systems XVII, Astronomical Society of the Pacific Conference Series Vol. 394, p. 505

Takata M., Shibahashi H., 1995, PASJ, 47, 219

Tamuz O., Mazeh T., Zucker S., 2005, MNRAS, 356, 1466

Tassoul M., 1980, ApJS, 43, 469

Telting J. H., Geier S., Østensen R. H., Heber U., Glowienka L., Nielsen T., Oreiro R., Frandsen S., 2008, A&A, 492, 815

Théado S., Cunha M., 2006, Commun. Asteroseismo., 147, 101

Théado S., Dupret M.-A., Noels A., Ferguson J. W., 2009, A&A, 493, 159

Théado S., Vauclair S., Cunha M. S., 2005, A&A, 443, 627

Thompson M. J., Christensen-Dalsgaard J., Miesch M. S., Toomre J., 2003, Annu. Rev. Astron. Astrophys., 41, 599

Tian Z. J., Bi S. L., Yang W. M., Chen Y. Q., Liu Z. E., Liu K., Li T. D., Ge Z. S., Yu J., 2014, MNRAS, 445, 2999

Titus J., Morgan W. W., 1940, ApJ, 92, 256

Tokunaga A. T., 2000, in Cox A. N., ed., Allen's Astrophysical Quantities, Springer, p. 143

Torres G., Andersen J., Giménez A., 2010, Annu. Rev. Astron. Astrophys., 18, 67

Tutukov A. V., Fedorova A. V., 2010, Astronomy Reports, 54, 156

Udalski A., Szymanski M., Kaluzny J., Kubiak M., Mateo M., 1992, AcA, 42, 253

Uytterhoeven K., Mathias P., Poretti E., Rainer M., Martín-Ruiz S., Rodríguez E., Amado P. J., Le Contel D., Jankov S., Niemczura E., Pollard K. R., Brunsden E., Paparó M., Costa V., Valtier J.-C., Garrido R., Suárez J. C., Kilmartin P. M., Chapellier E., Rodríguez-López C., Marin A. J., Aceituno F. J., Casanova V., Rolland A., Olivares I., 2008, A&A, 489, 1213

Uytterhoeven K., Moya A., Grigahcène A., Guzik J. A., Gutiérrez-Soto J., Smalley B., Handler G., Balona L. A., Niemczura E., Fox Machado L., Benatti S., Chapellier E., Tkachenko A., Szabó R., Suárez J. C., Ripepi V., Pascual J., Mathias P., Martín-Ruíz S., Lehmann H., Jackiewicz J., Hekker S., Gruberbauer M., García R. A., Dumusque X., Díaz-Fraile D., Bradley P., Antoci V., Roth M., Leroy B., Murphy S. J., De Cat P., Cuypers J., Kjeldsen H., Christensen-Dalsgaard J., Breger M., Pigulski A., Kiss L. L., Still M., Thompson S. E., van Cleve J., 2011, A&A, 534, A125

van Heerden P., Martinez P., Kilkenny D., 2012, MNRAS, 426, 969

van Leeuwen F., 2007, A&A, 474, 653

Vogt S. S., 1987, PASP, 99, 1214

Waelkens C., 1991, A&A, 246, 453

Walkowicz L. M., Basri G., Batalha N., Gilliland R. L., Jenkins J., Borucki W. J., Koch D., Caldwell D., Dupree A. K., Latham D. W., Meibom S., Howell S., Brown T. M., Bryson S., 2011, AJ, 141, 50

Wang J., 1993, IBVS, 3836, 1

Weiss W. W., Schneider H., 1984, A&A, 135, 148

Wolff S. C., 1968, PASP, 80, 281

Wolff S. C., 1983, The A-type stars: problems and perspectives., Monograph series on nonthermal phenomena in stellar atmospheres. NASA SP–463.

Wood P. R., 2000, PASA, 17, 18

Wraight K. T., Bewsher D., White G. J., Nowotny W., Norton A. J., Paladini C., 2012a, MNRAS, 426, 816

Wraight K. T., Fossati L., Netopil M., Paunzen E., Rode-Paunzen M., Bewsher D., Norton A. J., White G. J., 2012b, MNRAS, 420, 757

Zacharias N., Monet D. G., Levine S. E., Urban S. E., Gaume R., Wycoff G. L., 2005, VizieR Online Data Catalog, 1297, 0

Zerbi F. M., Rodríguez E., Garrido R., Martín S., Arellano Ferro A., Sareyan J. P., Krisciunas K., Akan M. C., Evren S., Ibanoğlu C., Keskin V., Pekunlu R., Tunca Z., Luedeke K., Paparo M., Nuspl J., Guerrero G., 1999, MNRAS, 303, 275

Zorec J., Royer F., 2012, A&A, 537, A120

Zwintz K., 2008, ApJ, 673, 1088

Zwintz K., Lenz P., Breger M., Pamyatnykh A. A., Zdravkov T., Kuschnig R., Matthews J. M., Guenther D. B., Moffat A. F. J., Rowe J. F., Rucinski S. M., Sasselov D., Weiss W. W., 2011, A&A, 533, A133

Zwintz K., Ryabchikova T., Lenz P., Pamyatnykh A. A., Fossati L., Sitnova T., Breger M., Poretti E., Rainer M., Hareter M., Mantegazza L., 2014, A&A, 567, A4